MICRO-NANO OPTICS AND PHOTOCATALYSIS MATERIALS, DEVICES, AND APPLICATIONS

EDITED BY: Shifa Wang, Hua Yang, Zao Yi, Steven Wu and Tao Xian
PUBLISHED IN: Frontiers in Materials

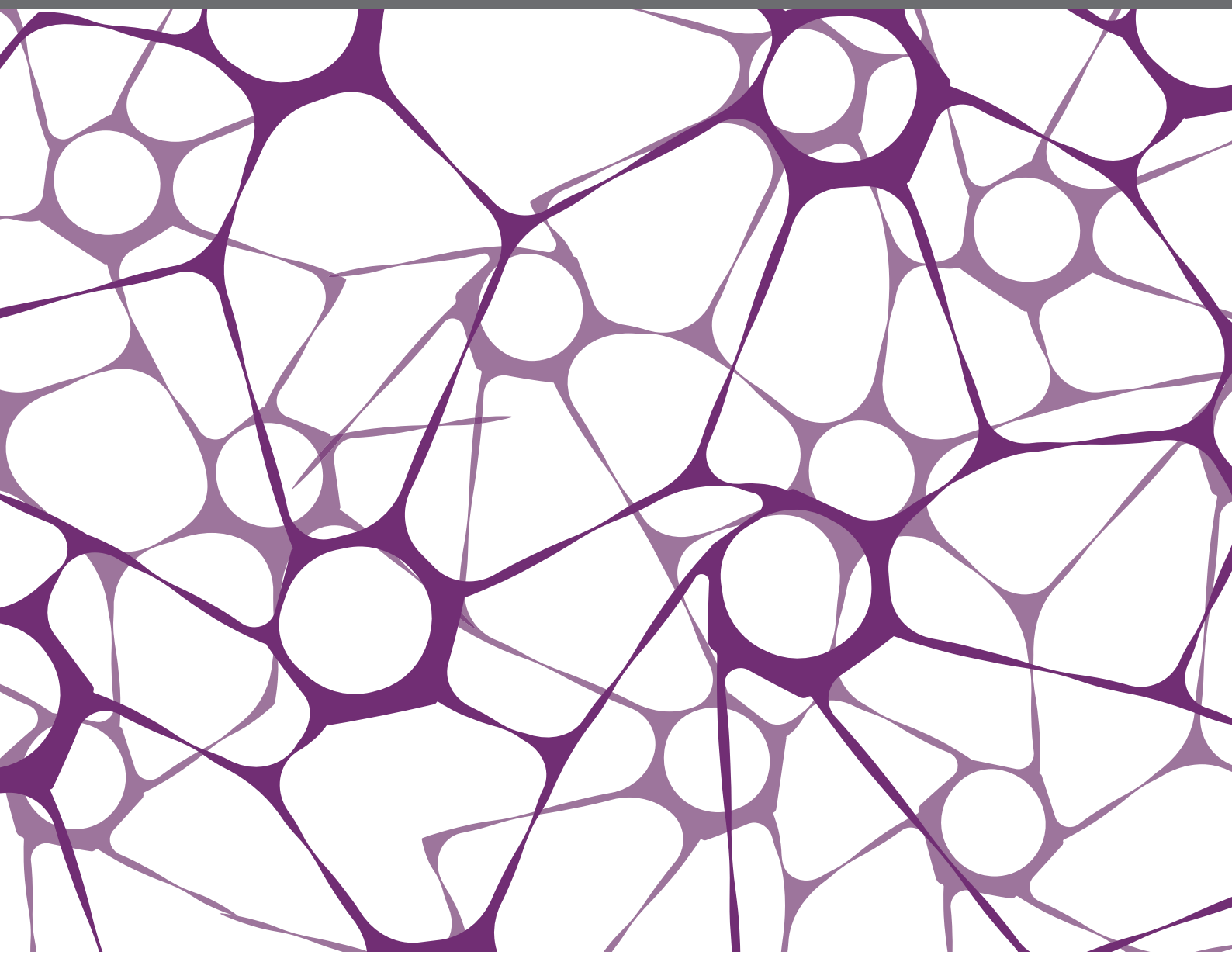

frontiers Research Topics

Frontiers eBook Copyright Statement

The copyright in the text of individual articles in this eBook is the property of their respective authors or their respective institutions or funders. The copyright in graphics and images within each article may be subject to copyright of other parties. In both cases this is subject to a license granted to Frontiers.

The compilation of articles constituting this eBook is the property of Frontiers.

Each article within this eBook, and the eBook itself, are published under the most recent version of the Creative Commons CC-BY licence. The version current at the date of publication of this eBook is CC-BY 4.0. If the CC-BY licence is updated, the licence granted by Frontiers is automatically updated to the new version.

When exercising any right under the CC-BY licence, Frontiers must be attributed as the original publisher of the article or eBook, as applicable.

Authors have the responsibility of ensuring that any graphics or other materials which are the property of others may be included in the CC-BY licence, but this should be checked before relying on the CC-BY licence to reproduce those materials. Any copyright notices relating to those materials must be complied with.

Copyright and source acknowledgement notices may not be removed and must be displayed in any copy, derivative work or partial copy which includes the elements in question.

All copyright, and all rights therein, are protected by national and international copyright laws. The above represents a summary only. For further information please read Frontiers' Conditions for Website Use and Copyright Statement, and the applicable CC-BY licence.

ISSN 1664-8714
ISBN 978-2-88976-984-1
DOI 10.3389/978-2-88976-984-1

About Frontiers

Frontiers is more than just an open-access publisher of scholarly articles: it is a pioneering approach to the world of academia, radically improving the way scholarly research is managed. The grand vision of Frontiers is a world where all people have an equal opportunity to seek, share and generate knowledge. Frontiers provides immediate and permanent online open access to all its publications, but this alone is not enough to realize our grand goals.

Frontiers Journal Series

The Frontiers Journal Series is a multi-tier and interdisciplinary set of open-access, online journals, promising a paradigm shift from the current review, selection and dissemination processes in academic publishing. All Frontiers journals are driven by researchers for researchers; therefore, they constitute a service to the scholarly community. At the same time, the Frontiers Journal Series operates on a revolutionary invention, the tiered publishing system, initially addressing specific communities of scholars, and gradually climbing up to broader public understanding, thus serving the interests of the lay society, too.

Dedication to Quality

Each Frontiers article is a landmark of the highest quality, thanks to genuinely collaborative interactions between authors and review editors, who include some of the world's best academicians. Research must be certified by peers before entering a stream of knowledge that may eventually reach the public - and shape society; therefore, Frontiers only applies the most rigorous and unbiased reviews.
Frontiers revolutionizes research publishing by freely delivering the most outstanding research, evaluated with no bias from both the academic and social point of view. By applying the most advanced information technologies, Frontiers is catapulting scholarly publishing into a new generation.

What are Frontiers Research Topics?

Frontiers Research Topics are very popular trademarks of the Frontiers Journals Series: they are collections of at least ten articles, all centered on a particular subject. With their unique mix of varied contributions from Original Research to Review Articles, Frontiers Research Topics unify the most influential researchers, the latest key findings and historical advances in a hot research area! Find out more on how to host your own Frontiers Research Topic or contribute to one as an author by contacting the Frontiers Editorial Office: frontiersin.org/about/contact

MICRO-NANO OPTICS AND PHOTOCATALYSIS MATERIALS, DEVICES, AND APPLICATIONS

Topic Editors:
Shifa Wang, Chongqing Three Gorges University Wanzhou District, China
Hua Yang, Lanzhou University of Technology, China
Zao Yi, Southwest University of Science and Technology, China
Steven Wu, University of South Dakota Vermillion, United States
Tao Xian, Qinghai Normal University, China

Citation: Wang, S., Yang, H., Yi, Z., Wu, S., Xian, T., eds. (2022). Micro-Nano Optics and Photocatalysis Materials, Devices, and Applications.
Lausanne: Frontiers Media SA. doi: 10.3389/978-2-88976-984-1

Table of Contents

frontiers | Frontiers in Materials

TYPE Editorial
PUBLISHED 08 August 2022
DOI 10.3389/fmats.2022.978059

Check for updates

OPEN ACCESS

EDITED AND REVIEWED BY
Peide Ye,
Purdue University, United States

*CORRESPONDENCE
Shifa Wang,
wangshifa2006@yeah.net

SPECIALTY SECTION
This article was submitted to Semiconducting Materials and Devices, a section of the journal Frontiers in Materials

RECEIVED 25 June 2022
ACCEPTED 04 July 2022
PUBLISHED 08 August 2022

CITATION
Wang S (2022), Editorial: Micro-nano optics and photocatalysis materials, devices, and applications. *Front. Mater.* 9:978059. doi: 10.3389/fmats.2022.978059

COPYRIGHT
© 2022 Wang. This is an open-access article distributed under the terms of the Creative Commons Attribution License (CC BY). The use, distribution or reproduction in other forums is permitted, provided the original author(s) and the copyright owner(s) are credited and that the original publication in this journal is cited, in accordance with accepted academic practice. No use, distribution or reproduction is permitted which does not comply with these terms.

Editorial: Micro-nano optics and photocatalysis materials, devices, and applications

Shifa Wang*

School of Electronic and Information Engineering, Chongqing Three Gorges University, Chongqing, China

KEYWORDS

photocatalytic technology, hall thruster, ilicon grating absorbers, environmental pollution, heterojunction photocatalysts

Editorial on the Research Topic
Micro-nano optics and photocatalysis materials, devices, and applications

Nowadays, the environmental pollution is becoming more and more serious in the world. Micro-nano optics and photocatalysis technology has demonstrated excellent ability in solving this problem. In the process of solving this critical problem, many new technologies have emerged and can be applied to optical communication, information storage, biological transport, drug carrier, sensing, display, luminescence, electronics and other fields. To effectively utilize sunlight, many novel techniques have been developed to synthesize photocatalysts or construct multiple heterojunction composite photocatalysts, and many related emerging technologies have also emerged. The vigorous development of these technologies is conducive to promoting the rapid take-off of the global economy and providing strong technical guarantee for solving environmental problems.

This volume deals with an absorbers for photon detection, optical filtering and spectral sensing, Hall thrusters for aerospace and deep space exploration, photocatalysts for orthopedic implants, photocatalysts for hydrogen production from water decomposition, and special synthesis of special heterojunction photocatalysts. From simulation calculation to experimental research, this study provides an in-depth insight into the core technologies used in optics, aerospace, photocatalysis and medical fields, and points out the direction for subsequent research. Simultaneously, some synthesis methods of novel photocatalysts are also explored, which provides a technical route for constructing new heterojunction photocatalysts.

To effectively use solar energy, (Xu et al.) proposed a design method of asymmetric silicon grating absorbers based on surface plasmon resonance and Fabry-Perot (FP) cavity and used finite difference time domain (FDTD) to simulate the calculation. The influences of geometric parameters, incident and polarization angles on the performance of silicon grating absorbers were discussed in detail. The designed absorber can be potentially used in the field of photon detection, optical filtering and spectral sensing. To achieve solar energy collection, light heat conversion, high sensitive sensing and other functions,

(Huang et al.) designed an ultra-broadband solar absorber on the basis of metal tungsten and semiconductor GaAs structure. By adjusting the geometric parameters, the high efficiency surface plasmon resonance is excited and the ultra-wideband absorption of up to 2,350 nm is realized. Similarly, (Liu et al.) proposed a perfect broadband solar absorber with the structure of GaAs grating-GaAs film-W substrate. The model have been simulated by the finite time domain difference method (FDTD). This structure is thought to be very simple and easy to operate, and can be used in photothermal conversion, collection and utilization of solar energy.

In the past, deep space exploration mainly carried chemical propellant to provide energy for spacecraft, while Hall thruster has gradually replaced the traditional chemical thruster to provide a new technological replacement for the space field. The design of the new Hall thruster has become an indispensable trend to help the new development of space industry. (Yang et al.) designed a new 5 kW Hall thruster, which can be used for deep space exploration, this technology providing reference for the design of Hall thrusters in space industry.

Photocatalytic technology is a green technology which has been developed as the environment is polluted and highly valued all over the world. (Han et al.) reviewed the application of MAl_2O_4 (M = Mg, Sr, Ba) based photocatalysts in the field of photocatalysis, and summarized the development trend of this kind of catalyst in the future, which can be applied to the synthesis and application of other photocatalysts. Photocatalysts can be used in medicine, especially orthopedic implants, in addition to efficiently degrading dyes, drugs and hard-to-degrade pollutants in the process of efficient utilization of sunlight. (Qi et al.) studied the application of different types of TiO_2-based photocatalysts in the field of photocatalysis and orthopedic implants based on the preparation of TiO_2-based photocatalysts. These technologies provide technical support for the study of other semiconductor based photocatalysts for orthopedic implants. (Tong et al.) constructed $ZnFe_2O_4$ based heterojunction photocatalyst by sol-gel method, which showed high photocatalytic activity in photocatalytic degradation of dyes, refractory pollutants and drugs. (Pu et al.; Wang et al.; Zhang et al.) and his research group synthesized a variety of semiconductor composites using special preparation methods and investigated their photocatalytic activities of water decomposition to produce hydrogen and dye degradation. The application of these techniques in the field of photocatalysis will promote the further development of photocatalysis.

Author contributions

SW performed the paper writing.

Conflict of interest

The authors declare that the research was conducted in the absence of any commercial or financial relationships that could be construed as a potential conflict of interest.

Publisher's note

All claims expressed in this article are solely those of the authors and do not necessarily represent those of their affiliated organizations, or those of the publisher, the editors and the reviewers. Any product that may be evaluated in this article, or claim that may be made by its manufacturer, is not guaranteed or endorsed by the publisher.

frontiers in Materials

ORIGINAL RESEARCH
published: 09 September 2021
doi: 10.3389/fmats.2021.752745

An Asymmetric Silicon Grating Dual-Narrow-Band Perfect Absorber Based on Dielectric-Metal-Dielectric Structure

*Feng Xu, Lixia Lin, Dongwei Wei, Jing Xu and Jun Fang**

College of Chemical Engineering and Materials Science, Quanzhou Normal University, Quanzhou, China

With the exhaustion of world energy, new energy has become the most important content of each country's development strategy. How to efficiently use solar energy has become a research hotspot in current scientific research. Based on surface plasmon resonance and Fabry-Perot (FP) cavity, this paper proposes a design method of asymmetric silicon grating absorber, and uses finite difference time domain (FDTD) method for simulation calculation. By adjusting the geometric parameters, the asymmetric silicon grating absorber realizes two narrow-band absorption peaks with absorption greater than 99% in the optical wavelength range of 3,000–5,000 nm, and the absorption peak wavelengths are λ_1 = 3,780 nm and λ_2 = 4,135 nm, respectively. When the electromagnetic wave is incident on the surface of the metamaterial, it will excite the plasmon resonance of the metal to form a surface plasmon (SP) wave. When the SP wave propagates along the *x* axis, the silicon grating can reflect the SP wave back and forth. When the frequency of the SP wave and the incident light are equal, it will cause horizontal FP coupling resonance, resulting in different resonance wavelengths. This paper also discusses the influence of geometric parameters, incident angle and polarization angle on the performance of silicon grating absorbers. Finally, the sensing performance of the structure as a refractive index sensor is studied. The absorber can be used for various spectral applications such as photon detection, optical filtering and spectral sensing.

Keywords: surface plasmon resonance, fabry-perot resonance, asymmetric silicon grating, dual-narrow-band, perfect absorption

OPEN ACCESS

Edited by:
Zao Yi,
Southwest University of Science and Technology, China

Reviewed by:
Yougen Yi,
Central South University, China
Weitang Yao,
Chengdu University, China
Yongzhi Cheng,
Wuhan University of Science and Technology, China

****Correspondence:***
Jun Fang
fangjun_qztc@163.com

Specialty section:
This article was submitted to Semiconducting Materials and Devices, a section of the journal Frontiers in Materials

Received: *03 August 2021*
Accepted: *27 August 2021*
Published: *09 September 2021*

Citation:
Xu F, Lin L, Wei D, Xu J and Fang J (2021) An Asymmetric Silicon Grating Dual-Narrow-Band Perfect Absorber Based on Dielectric-Metal-Dielectric Structure. Front. Mater. 8:752745. doi: 10.3389/fmats.2021.752745

INTRODUCTION

Surface plasmon resonance (SPR) is a non-radiative electromagnetic mode formed by the coupling of incident photons and free electrons on the metal surface (Cao et al., 2014). It is an excited state that locally propagates on the medium and metal surface. It is limited to the surface of the medium and metal, where the surface intensity is the highest, and it gradually attenuates to both sides in the direction perpendicular to the surface (Deng et al., 2015; Chen et al., 2021a; Li-Ying et al., 2021). Its propagation characteristics are related to the incident light source, the metal medium material and the surrounding refractive index (Jiang et al., 2021a). SPR provides a foundation for micro-nano applications due to its unique advantages, including biosensing, light field enhancement, solar cells, photocatalysis, Raman enhanced detection, and photodetectors (Liu et al., 2017; Xiao et al., 2017; Li et al., 2018; Chen et al., 2019; Li et al., 2020a; Zhao et al., 2021).

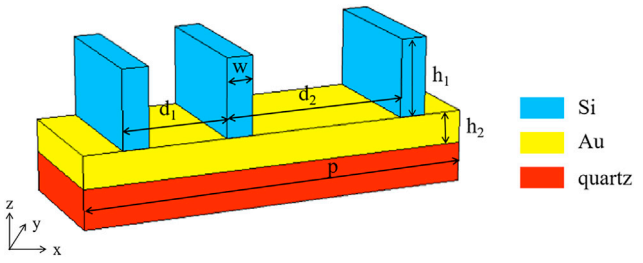

FIGURE 1 | Three-dimensional structure diagram of asymmetric silicon grating.

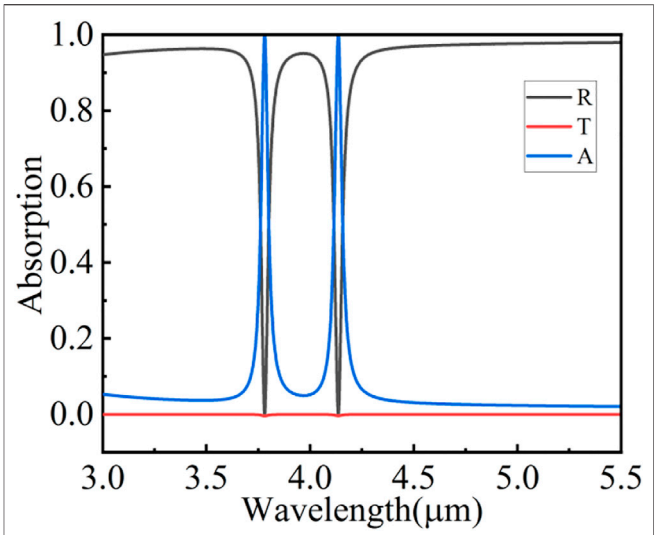

FIGURE 2 | Spectra of reflection (R), transmission (T) and absorption (A) under normal incidence of TM polarized light.

Resonance in subwavelength periodic structures has been studied extensively in the last decade. The resonance mode can be excited by the plasmon to affect the transmission, reflection and absorption characteristics of the structure (Ding and Magnusson, 2004; Deng et al., 2018; Jiang et al., 2021b). The near unit absorption of waves is called perfect absorption, and researchers have carried out many studies on perfect metamaterial absorbers (Cheng and Du, 2019; Cheng et al., 2019; Cheng et al., 2020; Cheng et al., 2021). They have many potential applications. Perfect absorbers with wide operating bandwidth are conducive to the application in photon detection, solar energy collection and other fields (Zhu et al., 2014; Rosenberg et al., 2019; Li et al., 2020b; Li et al., 2021a; Li et al., 2021b; Zhou et al., 2021), while perfect absorbers with narrow operating bandwidth have great advantages in sensing, filtering and selective thermal emission (Liu et al., 2010; Mason et al., 2011; Yi et al., 2020; Chen et al., 2021b; Wang et al., 2021). In addition, the ultra-narrow bandwidth refractive index sensor based on the perfect absorber has large figure of merit (FOM), and many researchers have proposed such a sensor with good performance (Vafapour and Ghahraloud, 2018; Keshavarz and Vafapour, 2019; Vafapour, 2019; Zhang et al., 2021). Usually, an all-metal structure or a three-layer or multi-layer metal insulator metal (MIM) structure is used to achieve perfect absorption in a narrow band (El-Gohary et al., 2014; Long et al., 2015; Zhang et al., 2015; Long et al., 2016; Elshorbagy et al., 2017). However, due to the incompatibility of these structures with complementary metal oxide semiconductor (CMOS) manufacturing processes, the manufacturing costs are high (Kuznetsov et al., 2016). Therefore, people are paying more and more attention to the realization of narrow-band perfect absorber through the dielectric structure on the metal system (Sharon et al., 1997; Liao and Zhao, 2017; Ren et al., 2019). Compared with the perfect metal absorber, this absorber can save manufacturing costs (Cui et al., 2014). This type of absorber usually has a dielectric waveguide layer. They can produce ultra-narrow absorption, but the structures are complex. Therefore, in order to optimize the structure, we can place the dielectric waveguide layer on the metal substrate or metal base film. For example, in 2016, Callewaert et al. proposed a narrow-band absorber based on a silver film dielectric nanodisk array (Callewaert et al., 2016).

In this paper, an asymmetric silicon grating absorber is designed based on the medium-metal-medium structure. Through the adjustment of geometric parameters, the dual-narrow-band perfect absorption is finally achieved. Asymmetric silicon grating is designed by using three unevenly spaced silicon strips in each cell. This asymmetric structure makes the absorber support horizontal FP resonance. The plane plasmon wave excited by the TM polarization (incident electric field polarized along the *x*-axis) incident can produce different FP coupling resonances with the incident light, resulting in two absorption peaks. When the incident angle is changed, the two absorption peaks show insensitive characteristics in the range of 0°–20°. In addition, the influence of geometric parameters and polarization angle on the performance of the absorber are briefly discussed. Finally, when this structure is used as a sensor, it has high sensitivity and quasi-linear response. It can be used in a variety of multi-spectral applications, such as filtering, photon detection, and spectral sensing.

MATERIALS AND METHODS

Figure 1 shows the structure of the dual-narrow-band grating absorber we designed. It is made of a quartz substrate and a silicon grating on the surface of a gold film. Incident light source is TM plane light wave, and the direction of light source is perpendicular to grating plane. The period of the grating is A, and there are three silicon gratings with unequal spacing in each period. The three silicon grating structures in a unit period make the grating as a whole asymmetrical structure. h_1 represents the height of the silicon grating, h_2 represents the height of the gold thin layer, w represents the width of the silicon grating, and d_1 and d_2 represent the center spacing of adjacent silicon gratings. The parameters of gold and silicon come from Palik (Palik, 1998),

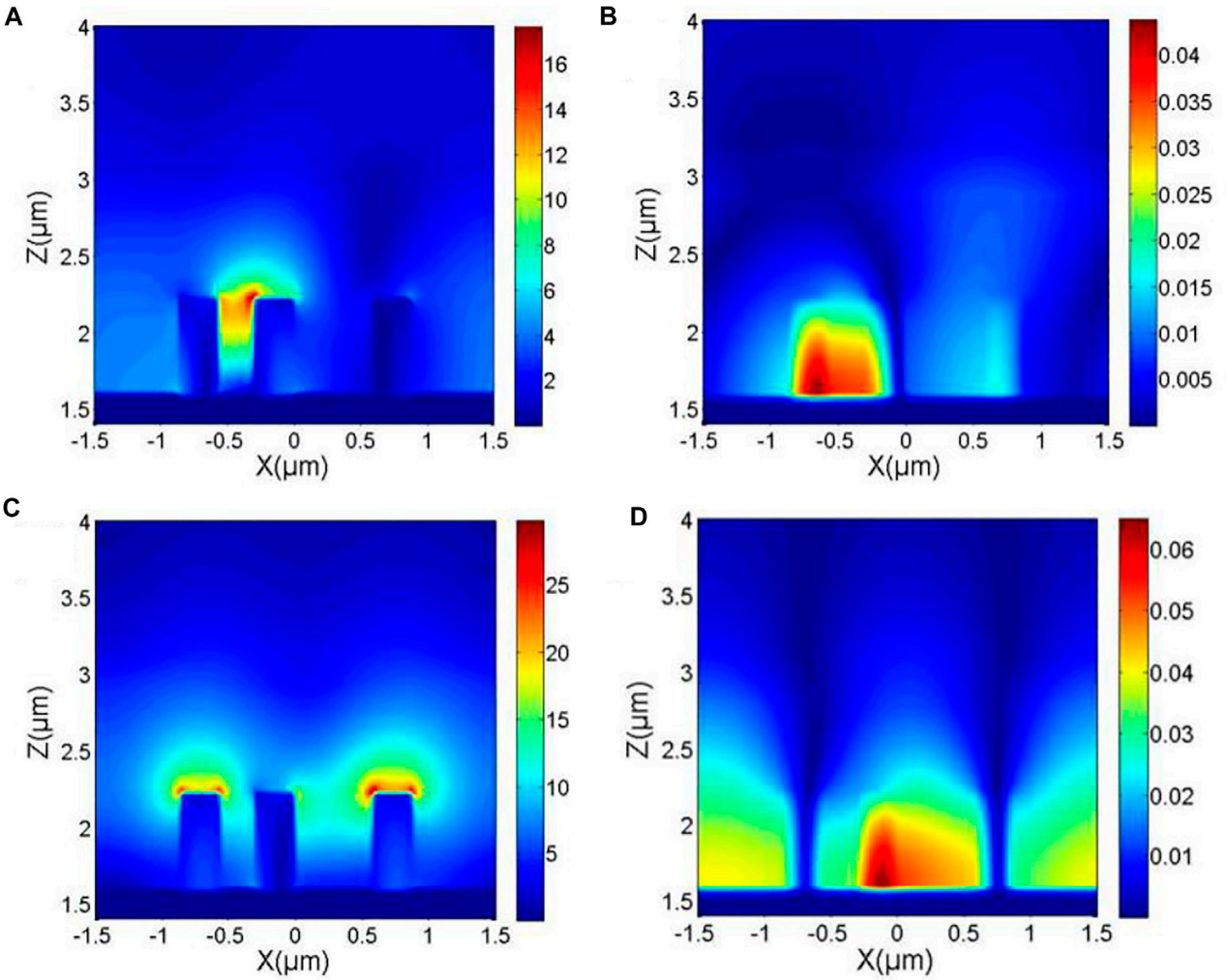

FIGURE 3 | (A) and **(B)** represent the electric and magnetic field diagrams at λ_1 = 3780 nm, respectively. **(C)** and **(D)** represent the electric and magnetic field diagrams at λ_2 = 4135 nm, respectively.

and the refractive index of quartz is 1.45. In the case of normal light wave incidence, we calculate the reflection (R), transmission (T) and absorption (A) as shown in **Figure 2**. The geometric parameters of the structure are A = 3,000 nm, h_1 = 630 nm, h_2 = 90 nm, w = 300 nm, d_1 = 560 nm, and d_2 = 880 nm, respectively. We can notice from **Figure 2** that the range of the light waveband is 3,000–5,000 nm, where the T is basically zero. The first absorption peak that appears is named λ_1 (λ_1 = 3,780 nm), and its full width at half maximum (FWHM) is 40 nm. The second absorption peak, we named λ_2 (λ_2 = 4,135 nm, FWHM = 39 nm). The absorption of the two resonance peak wavelengths exceeds 99%.

RESULTS AND DISCUSSION

In order to analyze the physical mechanism of resonance, we simulated and calculated the electric and magnetic field distributions at λ_1 = 3,780 nm and λ_2 = 4,135 nm on the XOZ plane. **Figures 3A,B** respectively show the electric field and magnetic field distribution at λ_1. We have observed that the electric field is distributed at the top corners of the slits with small silicon grating spacing, and the magnetic field is mainly distributed between the slits with small silicon grating spacing. **Figures 3C,D** respectively show the electric field and magnetic field distribution at λ_2. The difference from λ_1 is that the electric field is distributed on the surface of the three silicon gratings, and the magnetic field is mainly distributed in the slits of the two silicon gratings with a larger silicon grating spacing. This indicates that these two resonance peaks are derived from the coupling between the SPR of the metal and the resonance of the FP cavity (Cheng et al., 2015; Lv et al., 2018; He et al., 2020). The resonant peak at λ_1 is mainly related to the FP resonance between gratings with a short pitch (d_1), and the resonant peak at λ_2 is mainly derived from the FP resonance between gratings with a large pitch (d_2).

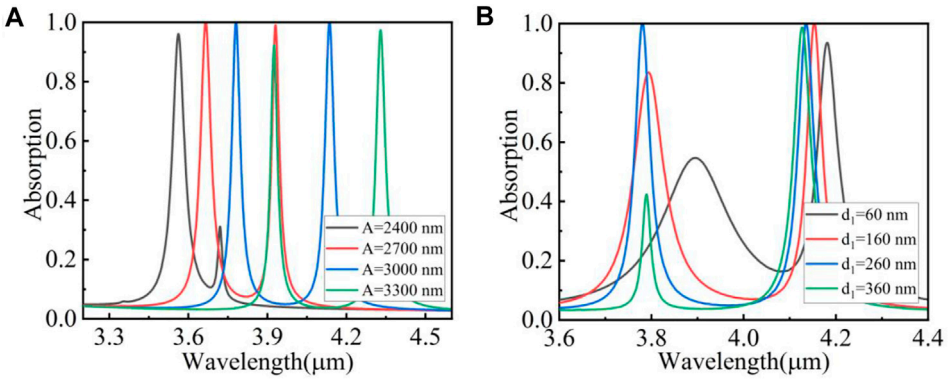

FIGURE 4 | (A) The effect of changing the grating period on the absorption spectrum. **(B)** The effect of changing the smaller silicon pitch of the grating on the absorption spectrum.

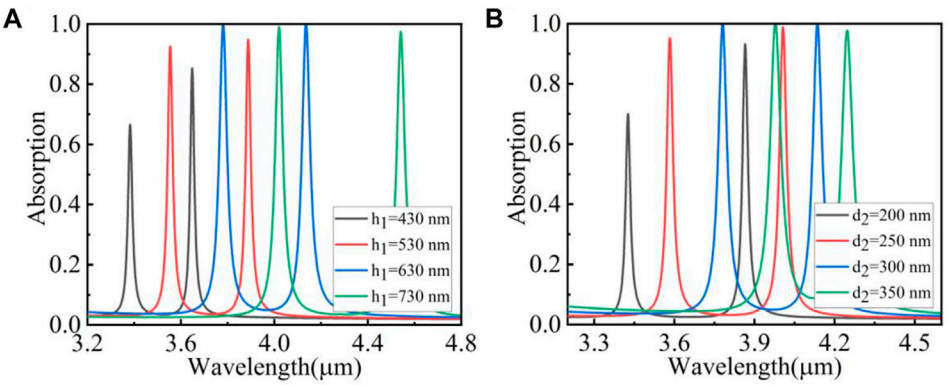

FIGURE 5 | (A) The effect of changing the thickness of the grating silicon on the absorption spectrum. **(B)** The effect of changing the silicon width of the grating on the absorption spectrum.

Then in order to explore the influence of the asymmetric silicon grating structure on the absorption performance, we used the controlled variable method to change the geometric parameters. **Figures 4A,B** respectively show the influence of the change of the period and the geometric parameters of the silicon grating pitch on the absorption performance of the silicon grating. From **Figure 4A**, we can observe that as the period length increases, the first absorption peak (λ_1) of the silicon grating gradually increases. With the increase of the period length, the two absorption peaks show red shift, and the longer the period length is, the farther the wavelength distance of the two absorption peaks is. At the same time, we noticed that the FWHM slowly decreases with the increase of the period. **Figure 5B** shows that we change the smaller silicon pitch of the asymmetric silicon grating (d_1) as the geometric parameter variable. Through **Figure 4B**, we found that when the silicon grating pitch is 60 nm, the absorption of the two absorption peaks is not high, and the FWHM is large. As the spacing of the silicon grating increases, the absorption gradually increases, the FWHM gradually decreases, and the two absorption peaks appear blue shift. At the same time, we can observe that the change of the silicon grating pitch has a greater influence on the first absorption peak, indicating that the λ_1 peak is sensitive to the change of the grating pitch, that is, the absorption peak is sensitive to the cavity length change.

Figures 5A,B respectively show the influence of asymmetric silicon grating thickness and silicon grating width geometric parameters (d_2) on the absorption performance of the silicon grating. From **Figure 5A**, we can observe that as the thickness of the silicon grating increases, the absorption of the two absorption peaks shows a trend of first increasing and then decreasing. This is because when the thickness of the silicon grating is small, it weakens the FP resonance and reduces the absorption of light. When the thickness increases to a certain size (630 nm), that is, when the thickness reaches the critical value, the absorption will no longer increase. At the same time, both absorption peaks appear red shift. And the distance between the two absorption peaks gradually increases, because each silicon grating plays a different role in the FP cavity. From **Figure 5B**, we also found that as the width of the silicon grating increases, the two absorption peaks first increase and then decrease, the resonance wavelength appears red-shifted, and the FWHM gradually increases.

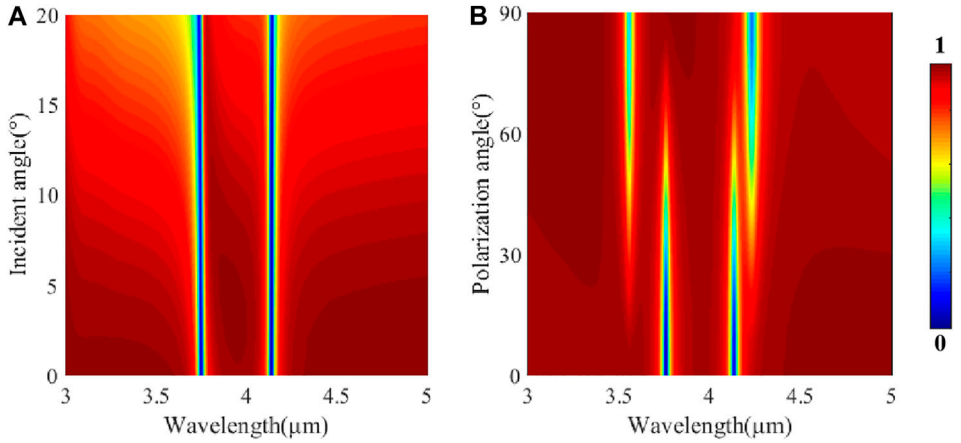

FIGURE 6 | (A) The relation between resonance wavelength and incident angle under TM polarization. **(B)** The effect of changing the polarization angle of incident light on the reflection spectrum.

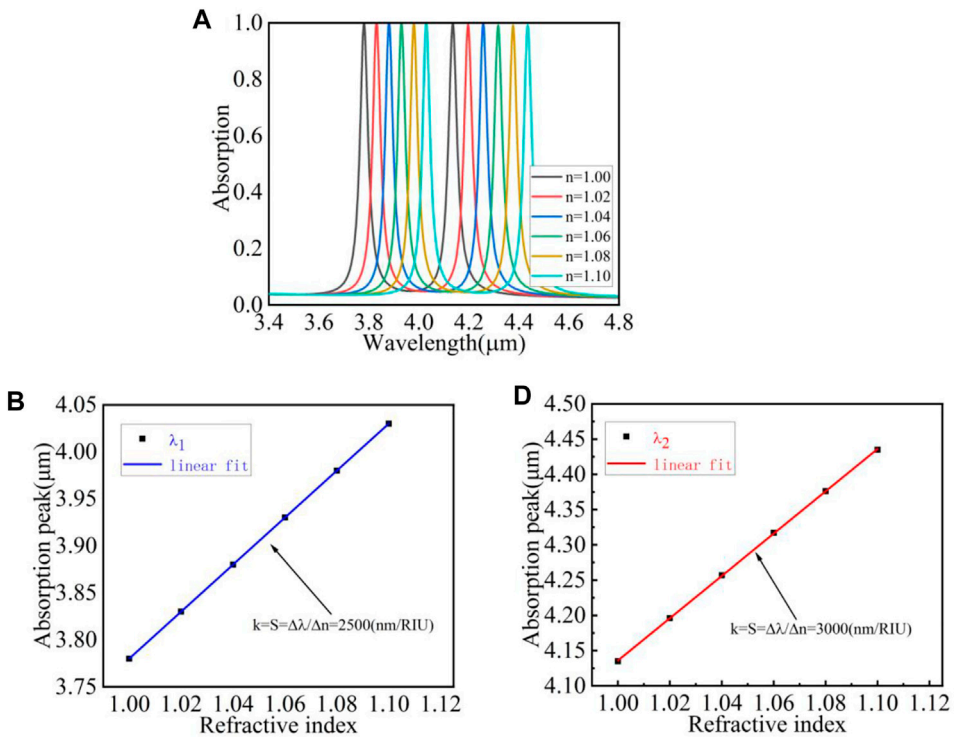

FIGURE 7 | (A) When changing the environmental background refractive index, the absorption spectrum of the grating. **(B)** For the wavelength λ_1, the peak wavelength relationship diagram corresponding to the refractive index change. **(C)** For the wavelength λ_2, the peak wavelength relationship diagram corresponding to the refractive index change.

However, unlike the trend of silicon grating thickness changes, as the silicon thickness changes, the distance between the two absorption peaks becomes smaller and smaller. The reason is the same as the thickness of the silicon grating: each silicon grating acts as a mirror, and their role is different.

In addition, we also studied the spectral response of the asymmetric silicon grating structure under different incident angles and polarization angles, and the results are shown in **Figure 6**. It can be seen that the intensity and position of the absorption peaks in the range of 0°–20° incident angle do not change, which indicates that the absorber is not sensitive to the incident angle in this range. When the incident angle exceeds 20°, the absorption will be greatly reduced due to the wave vector mismatch. When changing the polarization angle of the beam

from 0°(TM polarization) to 90° (TE polarization), the results are shown in **Figure 6B**. It can be clearly found that the extinction intensity of the two peaks decreases with the increase of the polarization angle. At the same time, we also noticed that when the incident plane wave is TE polarization, two new resonance peaks appear, which are caused by phase resonance (Qin et al., 2020; Su et al., 2021). The electric field generated at this time has a phase difference of π, which causes the far field to produce coherent cancellation, thereby generating two new peaks.

Finally, in order to explore the performance of asymmetric silicon grating as a refractive index sensor, we conduct research by changing its environmental refractive index. **Figure 7A** shows the absorption spectrum of the silicon grating when the refractive index of the surrounding environment changes. Since our silicon grating structure belongs to narrow-band absorption, we set the refractive index to change from 1.0 to 1.1 with a gradient of 0.02. From the figure, we can observe that as the refractive index of the environment increases, the two absorption peaks appear red-shifted, but the peaks of the two absorption peaks remain basically stable. At the same time, we found that the FWHM of the two absorption peaks did not change much, the change range was between 1 and 2nm, and we took the average value of the FWHM. **Figures 7B,C** show the corresponding absorption peak wavelengths of the two absorption peaks of λ_1 and λ_2 under the change of refractive index. The oblique line data is obtained by our linear fitting process. According to the formula $S = \Delta\lambda/\Delta n$ and FOM = S/FWHM, the sensitivity (S) and FOM of the silicon grating can be calculated (Chen et al., 2013; Cai et al., 2014; Tang et al., 2018; Wu et al., 2020; Chen et al., 2021c). According to the formula, we can find that the slope of the straight line is the S. The S of the absorption peaks at λ_1 and λ_2 are 2,500 nm/RIU and 3,000 nm/RIU. The FWHM are 40 nm and 39 nm. FOM are 62.5 and 76.9. It can be found that this structure has high sensitivity, so it can be applied in the field of refractive index sensors.

CONCLUSION

In conclusion, we fully demonstrate the absorption of dielectric structures on metal systems, based on the gold mold. By adjusting the geometric parameters, the asymmetric silicon grating absorber achieves the best absorption efficiency, two narrow-band absorption peaks in the range 3,000–5,000 nm light wave segments, the absorption peaks are λ_1 = 3,780 nm and λ_2 = 4,135 nm. And the absorption value is over 99%. We find that the distance between asymmetric gratings and the length of periods are changed, the absorption and FWHM of the absorption peak are the most affected. At the same time, it is found that the extinction intensity of the two peaks decreases with the increase of polarization angle. The structure has good sensing performance and high sensitivity. For the absorption peak of λ_1, S = 2,500 nm/RIU and FOM = 62.5. For the absorption peak of λ_2, S = 3,000 nm/RIU and FOM = 76.9.

DATA AVAILABILITY STATEMENT

The original contributions presented in the study are included in the article/Supplementary Material, further inquiries can be directed to the corresponding author.

AUTHOR CONTRIBUTIONS

FX: Conceptualization, Formal analysis, Investigation, Data curation, Writing-original draft, Writing-review and editing. LL: Conceptualization, Formal analysis, Investigation, Data curation, funding acquisition. DW: Conceptualization, Formal analysis, Investigation, Data curation, Writing-original draft, Writing-review and editing. JX: Conceptualization, Formal analysis, Revision. JF: Conceptualization, Formal analysis, Revision.

FUNDING

This work was supported by the National Natural Science Foundation of China (21676222, U175252), the Natural Science Foundation of Fujian Province (2019J01732, JT180365), the Quanzhou high level Talents Innovation and Entrepreneurship Project (2020C044R).

REFERENCES

Cai, R., Rao, W., Zhang, Z., Long, F., and Yin, Y. (2014). An Imprinted Electrochemical Sensor for Bisphenol A Determination Based on Electrodeposition of a Graphene and Ag Nanoparticle Modified Carbon Electrode. *Anal. Methods* 6, 1590–1597. doi:10.1039/c3ay42125b

Callewaert, F., Chen, S., Butun, S., and Aydin, K. (2016). Narrow Band Absorber Based on a Dielectric Nanodisk Array on Silver Film. *J. Opt.* 18 (7), 075006. doi:10.1088/2040-8978/18/7/075006

Cao, G., Li, H., Deng, Y., Zhan, S., He, Z., and Li, B. (2014). Systematic Theoretical Analysis of Selective-Mode Plasmonic Filter Based on Aperture-Side-Coupled Slot Cavity. *Plasmonics* 9, 1163–1169. doi:10.1007/s11468-014-9727-y

Chen, H.-J., Zhang, Z.-H., Cai, R., Kong, X.-Q., Chen, X., Liu, Y.-N., et al. (2013). Molecularly Imprinted Electrochemical Sensor Based on a Reduced Graphene Modified Carbon Electrode for Tetrabromobisphenol A Detection. *Analyst* 138, 2769–2776. doi:10.1039/c3an00146f

Chen, P., Liu, F., Ding, H., Chen, S., Chen, L., Li, Y.-J., et al. (2019). Porous Double-Shell CdS@C3N4 Octahedron Derived by *In Situ* Supramolecular Self-Assembly for Enhanced Photocatalytic Activity. *Appl. Catal. B: Environ.* 252, 33–40. doi:10.1016/j.apcatb.2019.04.006

Chen, X., Wu, W., Zhang, W., Wang, Z., Fu, Z., Zhou, L., et al. (2021). Blue and green Double Band Luminescent Carbon Quantum Dots: Synthesis, Origin of Photoluminescence, and Application in white Light-Emitting Devices. *Appl. Phys. Lett.* 118, 153102. doi:10.1063/5.0046495

Chen, Z., Chen, H., Jile, H., Xu, D., Yi, Z., Lei, Y., et al. (2021). Multi-band Multi-Tunable Perfect Plasmon Absorber Based on L-Shaped and Double-Elliptical Graphene Stacks. *Diamond Relat. Mater.* 115, 108374. doi:10.1016/j.diamond.2021.108374

Chen, Z., Chen, H., Yin, J., Zhang, R., Jile, H., Xu, D., et al. (2021). Multi-band, Tunable, High Figure of merit, High Sensitivity Single-Layer Patterned Graphene-Perfect Absorber Based on Surface Plasmon Resonance. *Diamond Relat. Mater.* 116, 108393. doi:10.1016/j.diamond.2021.108393

Cheng, Y., Chen, F., and Luo, H. (2021). Plasmonic Chiral Metasurface Absorber Based on Bilayer Fourfold Twisted Semicircle Nanostructure at Optical Frequency. *Nanoscale Res. Lett.* 16, 12. doi:10.1186/s11671-021-03474-6

Cheng, Y., Chen, F., and Luo, H. (2020). Triple-Band Perfect Light Absorber Based on Hybrid Metasurface for Sensing Application. *Nanoscale Res. Lett.* 15 (1), 103. doi:10.1186/s11671-020-03332-x

Cheng, Y., and Du, C. (2019). Broadband Plasmonic Absorber Based on All Silicon Nanostructure Resonators in Visible Region. *Opt. Mater.* 98, 109441. doi:10.1016/j.optmat.2019.109441

Cheng, Y., Luo, H., Chen, F., and Gong, R. (2019). Triple Narrow-Band Plasmonic Perfect Absorber for Refractive index Sensing Applications of Optical Frequency. *OSA Continuum* 2 (7), 2113. doi:10.1364/osac.2.002113

Cheng, Z., Liao, J., He, B., Zhang, F., Zhang, F., Huang, X., et al. (2015). One-Step Fabrication of Graphene Oxide Enhanced Magnetic Composite Gel for Highly Efficient Dye Adsorption and Catalysis. *ACS Sust. Chem. Eng.* 3, 1677–1685. doi:10.1021/acssuschemeng.5b00383

Cui, Y., He, Y., Jin, Y., Ding, F., Yang, L., Ye, Y., et al. (2014). Plasmonic and Metamaterial Structures as Electromagnetic Absorbers. *Laser Photon. Rev.* 8, 495–520. doi:10.1002/lpor.201400026

Deng, Y., Cao, G., Wu, Y., Zhou, X., and Liao, W. (2015). Theoretical Description of Dynamic Transmission Characteristics in MDM Waveguide Aperture-Side-Coupled with Ring Cavity. *Plasmonics* 10, 1537–1543. doi:10.1007/s11468-015-9971-9

Deng, Y., Cao, G., Yang, H., Zhou, X., and Wu, Y. (2018). Dynamic Control of Double Plasmon-Induced Transparencies in Aperture-Coupled Waveguide-Cavity System. *Plasmonics* 13, 345–352. doi:10.1007/s11468-017-0519-z

Ding, Y., and Magnusson, R. (2004). Resonant Leaky-Mode Spectral-Band Engineering and Device Applications. *Opt. Express* 12 (23), 5661–5674. doi:10.1364/opex.12.005661

El-Gohary, S. H., Choi, J. M., Kim, N.-H., and Byun, K. M. (2014). Plasmonic Metal-Dielectric-Metal Stack Structure with Subwavelength Metallic Gratings for Improving Sensor Sensitivity and Signal Quality. *Appl. Opt.* 53, 2152–2157. doi:10.1364/ao.53.002152

Elshorbagy, M. H., Cuadrado, A., and Alda, J. (2017). High-sensitivity Integrated Devices Based on Surface Plasmon Resonance for Sensing Applications. *Photon. Res.* 5, 654–661. doi:10.1364/prj.5.000654

He, X., Jie, J., Yang, J., Han, Y., and Zhang, S. (2020). Asymmetric Dielectric Grating on Metallic Film Enabled Dual- and Narrow-Band Absorbers. *Opt. Express* 28 (4), 4594–4602. doi:10.1364/oe.386742

Jiang, L., Yi, Y., Tang, Y., Li, Z., Yi, Z., Liu, L., et al. (2021). A High Quality Factor Ultra-narrow Band Perfect Metamaterial Absorber for Monolayer Molybdenum Disulfide. *Chin. Phys. B* 19, 103415. doi:10.1088/1674-1056/ac1e11

Jiang, L., Yuan, C., Li, Z., Su, J., Yi, Z., Yao, W., et al. (2021). Multi-band and High-Sensitivity Perfect Absorber Based on Monolayer Graphene Metamaterial. *Diamond Relat. Mater.* 111, 108227. doi:10.1016/j.diamond.2020.108227

Keshavarz, A., and Vafapour, Z. (2019). Thermo-optical Applications of a Novel Terahertz Semiconductor Metamaterial Design. *J. Opt. Soc. Am. B* 36, 35–41. doi:10.1364/josab.36.000035

Kuznetsov, A. I., Miroshnichenko, A. E., Brongersma, M. L., Kivshar, Y. S., and Luk'yanchuk, B. (2016). Optically Resonant Dielectric Nanostructures. *Science* 354, 846. doi:10.1126/science.aag2472

Li, J., Chen, X., Yi, Z., Yang, H., Tang, Y., Yi, Y., et al. (2020). Broadband Solar Energy Absorber Based on Monolayer Molybdenum Disulfide Using Tungsten Elliptical Arrays. *Mater. Today Energ.* 16, 100390. doi:10.1016/j.mtener.2020.100390

Li, J., Jiang, J., Xu, Z., Liu, M., Tang, S., Yang, C., et al. (2018). Facile Synthesis of Ag@Cu2O Heterogeneous Nanocrystals Decorated N-Doped Reduced Graphene Oxide with Enhanced Electrocatalytic Activity for Ultrasensitive Detection of H2O2. *Sensors Actuators B: Chem.* 260, 529–540. doi:10.1016/j.snb.2018.01.068

Li, J., Jiang, J., Zhao, D., Xu, Z., Liu, M., Liu, X., et al. (2020). Novel Hierarchical Sea Urchin-like Prussian Blue@palladium Core-Shell Heterostructures Supported on Nitrogen-Doped Reduced Graphene Oxide: Facile Synthesis and Excellent Guanine Sensing Performance. *Electrochimica Acta* 330, 135196. doi:10.1016/j.electacta.2019.135196

Li, Z., Yi, Y., Xu, D., Yang, H., Yi, Z., Chen, X., et al. (2021). A Multi-Band and Polarization-independent Perfect Absorber Based on Dirac Semimetals Circles and Semi-ellipses Array. *Chin. Phys. B* 30, 098104. doi:10.1088/1674-1056/abfb57

Li, Z., Yi, Z., Liu, T., Liu, L., Chen, X., Zheng, F., et al. (2021). Three-band Perfect Absorber with High Refractive index Sensing Based on an Active Tunable Dirac Semimetal. *Phys. Chem. Chem. Phys.* 23, 17374–17381. doi:10.1039/D1CP01375K

Li-Ying, J., Yi, Y. T., Ying-Ting, Y., Zao, Y., Hua, Y., Zhi-You, L., et al. (2021). A Four-Band Perfect Absorber Based on High Quality Factor and High Quality Factor of Monolayer Molybdenum Disulfide. *Acta Physica Sinica* 70, 128101. doi:10.7498/aps.70.20202163

Liao, Y.-L., and Zhao, Y. (2017). An Ultra-narrowband Absorber with a Dielectric-Dielectric-Metal Structure Based on Guide-Mode Resonance. *Opt. Commun.* 382, 307–310. doi:10.1016/j.optcom.2016.08.008

Liu, N., Mesch, M., Weiss, T., Hentschel, M., and Giessen, H. (2010). Infrared Perfect Absorber and its Application as Plasmonic Sensor. *Nano Lett.* 10, 2342–2348. doi:10.1021/nl9041033

Liu, Y., Bo, M., Yang, X., Zhang, P., Sun, C. Q., and Huang, Y. (2017). Size Modulation Electronic and Optical Properties of Phosphorene Nanoribbons: DFT-BOLS Approximation. *Phys. Chem. Chem. Phys.* 19, 5304–5309. doi:10.1039/c6cp08011a

Long, F., Zhang, Z. H., Wang, J., Yan, L., Lu, P. P., and Yang, Z. X. (2016). Magnetic Graphene Modified Imprinted Electrochemical Sensor for Detection of 4-Octylphenol. *Chin. J. Anal. Chem.* 44, 908–914. doi:10.11895/j.issn.0253.3820.160016

Long, F., Zhang, Z., Wang, J., Yan, L., and Zhou, B. (2015). Cobalt-nickel Bimetallic Nanoparticles Decorated Graphene Sensitized Imprinted Electrochemical Sensor for Determination of Octylphenol. *Electrochimica Acta* 168, 337–345. doi:10.1016/j.electacta.2015.04.054

Lv, P., Xie, D., and Zhang, Z. (2018). Magnetic Carbon Dots Based Molecularly Imprinted Polymers for Fluorescent Detection of Bovine Hemoglobin. *Talanta* 188, 145–151. doi:10.1016/j.talanta.2018.05.068

Mason, J. A., Smith, S., and Wasserman, D. (2011). Strong Absorption and Selective thermal Emission from a Midinfrared Metamaterial. *Appl. Phys. Lett.* 98, 241105. doi:10.1063/1.3600779

Palik, E. D. (1998). *Handbook of Optical Constants of Solids*. Academic Press.

Qin, F., Chen, X., Yi, Z., Yao, W., Yang, H., Tang, Y., et al. (2020). Ultra-broadband and Wide-Angle Perfect Solar Absorber Based on TiN Nanodisk and Ti Thin Film Structure. *Solar Energ. Mater. Solar Cell* 211, 110535. doi:10.1016/j.solmat.2020.110535

Ren, Z., Sun, Y., Lin, Z., and Wang, C. (2019). Ultra-narrow Band Perfect Metamaterial Absorber Based on Dielectric-Metal Periodic Configuration. *Opt. Mater.* 89, 308–315. doi:10.1016/j.optmat.2019.01.020

Rosenberg, J., Shenoi, R. V., Vandervelde, T. E., Krishna, S., and Painter, O. (2019). A Multispectral and Polarization-Selective Surface-Plasmon Resonant Midinfrared Detector. *Appl. Phys. Lett.* 95, 161101. doi:10.1063/1.3244204

Sharon, A., Glasberg, S., Rosenblatt, D., and Friesem, A. A. (1997). Metal-based Resonant Grating Waveguide Structures. *J. Opt. Soc. Am. A.* 14, 588–595. doi:10.1364/josaa.14.000588

Su, J., Yang, H., Xu, Y., Tang, Y., Yi, Z., Zheng, F., et al. (2021). Based on Ultrathin PEDOT:PSS/c-Ge Solar Cells Design and Their Photoelectric Performance. *Coatings* 11 (7), 748. doi:10.3390/coatings11070748

Tang, N., Li, Y., Chen, F., and Han, Z. (2018). *In Situ* fabrication of a Direct Z-Scheme Photocatalyst by Immobilizing CdS Quantum Dots in the Channels of Graphene-Hybridized and Supported Mesoporous Titanium Nanocrystals for High Photocatalytic Performance under Visible Light. *RSC Adv.* 8, 42233–42245. doi:10.1039/c8ra08008a

Vafapour, Z., and Ghahraloud, H. (2018). Semiconductor-based Far-Infrared Biosensor by Optical Control of Light Propagation Using THz Metamaterial. *J. Opt. Soc. Am. B* 35, 1192–1199. doi:10.1364/josab.35.001192

Vafapour, Z. (2019). Polarization-independent Perfect Optical Metamaterial Absorber as a Glucose Sensor in Food Industry Applications. *IEEE Trans.on Nanobioscience* 18, 622–627. doi:10.1109/tnb.2019.2929802

Wang, Y., Yi, Y., Xu, D., Yi, Z., Li, Z., Chen, X., et al. (2021). Terahertz Tunable Three Band Narrowband Perfect Absorber Based on Dirac Semimetal. *Physica E: Low-dimensional Syst. Nanostructures* 131, 114750. doi:10.1016/j.physe.2021.114750

Wu, P., Zhang, C., Tang, Y., Liu, B., and Lv, L. (2020). A Perfect Absorber Based on Similar Fabry-Perot Four-Band in the Visible Range. *Nanomaterials* 10 (3), 488. doi:10.3390/nano10030488

Xiao, L., Youji, L., Feitai, C., Peng, X., and Ming, L. (2017). Facile Synthesis of Mesoporous Titanium Dioxide Doped by Ag-Coated Graphene with Enhanced Visible-Light Photocatalytic Performance for Methylene Blue Degradation. *RSC Adv.* 7, 25314–25324. doi:10.1039/c7ra02198d

Yi, Z., Li, J., Lin, J., Qin, F., Chen, X., Yao, W., et al. (2020). Broadband Polarization-Insensitive and Wide-Angle Solar Energy Absorber Based on Tungsten Ring-Disc Array. *Nanoscale* 12, 23077–23083. doi:10.1039/d0nr04502k

Zhang, Y., Yi, Z., Wang, X., Chu, P., Yao, W., Zhou, Z., et al. (2021). Dual Band Visible Metamaterial Absorbers Based on Four Identical Ring Patches. *Physica E: Low-dimensional Syst. Nanostructures* 127, 114526. doi:10.1016/j.physe.2020.114526

Zhang, Z., Cai, R., Long, F., and Wang, J. (2015). Development and Application of Tetrabromobisphenol A Imprinted Electrochemical Sensor Based on Graphene/carbon Nanotubes Three-Dimensional Nanocomposites Modified Carbon Electrode. *Talanta* 134, 435–442. doi:10.1016/j.talanta.2014.11.040

Zhao, F., Yi, Y., Lin, J., Yi, Z., Qin, F., Zheng, Y., et al. (2021). The Better Photoelectric Performance of Thin-Film TiO2/c-Si Heterojunction Solar Cells Based on Surface Plasmon Resonance. *Results Phys.* 28, 104628. doi:10.1016/j.rinp.2021.104628

Zhou, F., Qin, F., Yi, Z., Yao, W., Liu, Z., Wu, X., et al. (2021). Ultra-wideband and Wide-Angle Perfect Solar Energy Absorber Based on Ti Nanorings Surface Plasmon Resonance. *Phys. Chem. Chem. Phys.* 23, 17041–17048. doi:10.1039/D1CP03036A

Zhu, J., Ma, Z., Sun, W., Ding, F., He, Q., Zhou, L., et al. (2014). Ultra-broadband Terahertz Metamaterial Absorber. *Appl. Phys. Lett.* 105 (2), 021102. doi:10.1063/1.4890521

Conflict of Interest: The authors declare that the research was conducted in the absence of any commercial or financial relationships that could be construed as a potential conflict of interest.

Publisher's Note: All claims expressed in this article are solely those of the authors and do not necessarily represent those of their affiliated organizations, or those of the publisher, the editors and the reviewers. Any product that may be evaluated in this article, or claim that may be made by its manufacturer, is not guaranteed or endorsed by the publisher.

Copyright © 2021 Xu, Lin, Wei, Xu and Fang. This is an open-access article distributed under the terms of the Creative Commons Attribution License (CC BY). The use, distribution or reproduction in other forums is permitted, provided the original author(s) and the copyright owner(s) are credited and that the original publication in this journal is cited, in accordance with accepted academic practice. No use, distribution or reproduction is permitted which does not comply with these terms.

frontiers in Materials

ORIGINAL RESEARCH
published: 25 October 2021
doi: 10.3389/fmats.2021.781803

Design of Grating Type GaAs Solar Absorber and Investigation of Its Photoelectric Characteristics

*Meihong Huang[1], Kaihua Wei[2], Pinghui Wu[3], Danyang Xu[4] and Yan Xu[5]**

[1]College of Transportation and Navigation, Quanzhou Normal University, Quanzhou, China, [2]School of Automation, Hangzhou Dianzi University, Hangzhou, China, [3]Fujian Provincial Key Laboratory for Advanced Micro-nano Photonics Technology and Devices, Quanzhou Normal University, Quanzhou, China, [4]College of Science, Zhejiang University of Technology, Hangzhou, China, [5]School of Science, Huzhou University, Huzhou, China

In recent years, as a renewable clean energy with many excellent characteristics, solar energy has been widely concerned. In this paper, we propose an ultra-broadband solar absorber based on metal tungsten and semiconductor GaAs structure. A multilayer metal semiconductor composite structure composed of W-Ti-GaAs three-layer films and GaAs gratings is proposed. The finite difference time domain method is used to simulate the performance of the proposed model. High efficiency surface plasmon resonance is excited by adjusting the geometric parameters, and the broadband absorption of up to 2,350 nm in 500–2850 nm is realized. The spectrum of the structure can be changed by adjusting the geometric parameters to meet different needs. The proposed absorber has good oblique incidence characteristics (0–60°) and high short-circuit current characteristics. The geometry of the absorber is clear, easy to manufacture, and has good photoelectric performance. It can realize solar energy collection, light heat conversion, high sensitive sensing and other functions.

Keywords: solar absorber, finite difference time domain method, broadband absorption, GaAs gratings, photoelectric characteristics

OPEN ACCESS

Edited by:
Shifa Wang,
Chongqing Three Gorges University, China

Reviewed by:
Yougen Yi,
Central South University, China
Chao Liu,
Northeast Petroleum University, China
Chen Zhiquan,
Hunan University, China

****Correspondence:***
Yan Xu
xuyanhzu@126.com

Specialty section:
This article was submitted to Semiconducting Materials and Devices, a section of the journal Frontiers in Materials

Received: *23 September 2021*
Accepted: *11 October 2021*
Published: *25 October 2021*

Citation:
Huang M, Wei K, Wu P, Xu D and Xu Y (2021) Design of Grating Type GaAs Solar Absorber and Investigation of Its Photoelectric Characteristics. Front. Mater. 8:781803. doi: 10.3389/fmats.2021.781803

INTRODUCTION

From the beginning of the 21st century, with the improvement of people's living standards, there are more and more kinds of household appliances, and the demand for traditional fossil energy is also increasing, which is in contradiction with the characteristics of non-renewable resources. According to the existing data, if energy consumption can not be controlled before the end of this century, oil and natural gas energy will be exhausted, and coal reserves will be exhausted. With the decrease of these conventional non-renewable resources, how to effectively and reasonably use conventional energy, and develop and utilize new energy, especially renewable energy, is a major event in front of all mankind (Xiao et al., 2017; Tang et al., 2018; Cai et al., 2019; Sivák et al., 2020; Xie et al., 2020; Zhao et al., 2021).

Among all kinds of energy, as a renewable energy, solar energy is considered to be the most potential energy, because it is inexhaustible, reliable, less pollution and so on. As an important energy collection device, solar absorber has attracted more and more attention in recent years (Li et al., 2016; Chen et al., 2019a; Xiao et al., 2019; Li et al., 2020a; Roostaei et al., 2021). For an ideal absorber, it must have high efficiency light absorption and many other excellent physical properties, such as polarization stability and tunability (Li et al., 2020b; Wu et al., 2020; Yi et al., 2020; Chen et al., 2021a; Jiang et al., 2021a; Li et al., 2021a; Li et al., 2021b; Li-Ying et al., 2021; Zhou et al., 2021). However, the

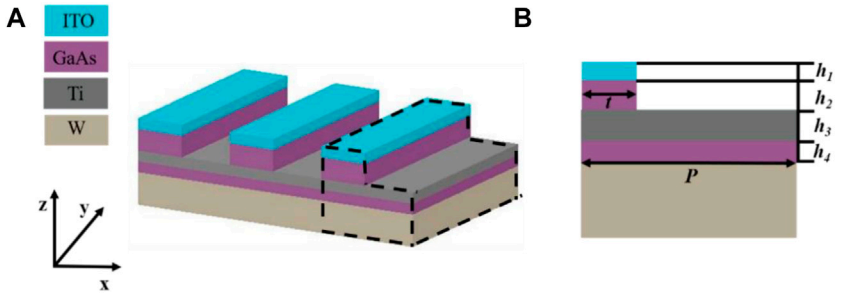

FIGURE 1 | (A) Schematic diagram of multilayer metal semiconductor structure **(B)** Side view.

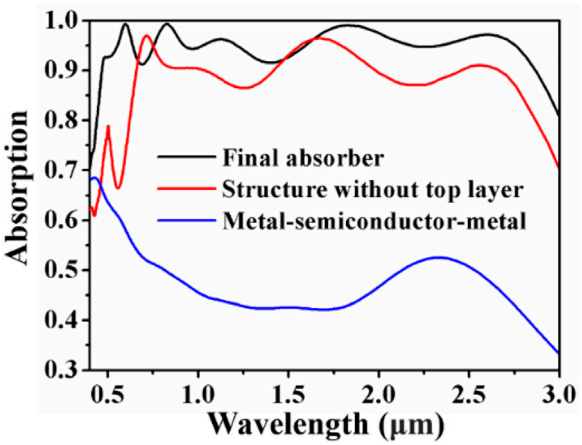

FIGURE 2 | Absorption spectra of multilayer broadband absorber with different configurations.

existing absorbers are generally limited by low temperature tolerance, low light absorption efficiency and materials (Chen et al., 2020; Chen et al., 2021b; Jiang et al., 2021b; Wang et al., 2021; Zhang et al., 2021). Therefore, a new type of broadband solar energy which can solve the above problems needs to be proposed. According to the actual situation of solar radiation in the range of 295–2,500 nm, the key to realize the efficient utilization of solar energy is to design a solar device which can match the band perfectly.

The research on broadband absorber has been carried out for many years in the world, and it has been used in solar cells, solar heating devices and photothermal converters (Liu et al., 2017; Keshavarz and Vafapour, 2019; Yu et al., 2020; Chen et al., 2021c; Su et al., 2021). For the design and improvement of broadband absorber, we should pay attention to the following aspects: the first is to select the appropriate material. Traditional precious metal materials such as gold and silver were used in the original broadband absorbers. However, due to its high cost and poor high temperature resistance, people began to pay attention to high melting point materials such as titanium nitride. They not only have high melting point, but also can excite effective plasmon. Secondly, the nanostructure design of broadband absorber is also very important. The multi-layer metal-insulator structure was first used, and then turned to simpler MIM or IMI nanostructures. Finally, the working area of broadband absorber, especially from ultraviolet to near-infrared, has been studied and improved. Efforts in these directions are to obtain ideal broadband absorbers for practical applications. For instance, Lei proposed an ultra-broadband absorber based on a thin metamaterial nanostructure composed of Ti-SiO_2 cubes and Al bottom film. The proposed structure can achieve nearly perfect absorption with an average absorbance of 97% from 354 to 1,066 nm (Lei et al., 2018). Huang proposed a broadband absorber with near-unity absorption in the terahertz regime based on a target-patterned graphene sheet, the absorption bandwidth (more than 90%) is 1.57 THz with a central frequency of 1.83 THz under normal incidence (Huang et al., 2018). Although the characteristics of these absorbers are superior enough, their complex nanostructures and a variety of complex materials make the proposed absorbers difficult to apply. Therefore, an absorber with simple structure and excellent high absorptivity should be proposed.

In this paper, we propose a broadband solar absorber composed of W-Ti-GaAs three-layer thin film and GaAs grating, as shown in **Figure 1**. The proposed structure uses W metal as the substrate and GaAs semiconductor grating as the auxiliary structure. There is a layer of metal Ti between the w base and the GaAs film, and the top layer is a layer of ITO (refractive index is 2.0) film to reduce the reflection of the whole structure and improve the overall absorptivity. The electromagnetic field in different wavebands, the influence of structure parameters on the overall absorptivity and the distribution of solar absorption characteristics are simulated. The results show that its high absorptivity band width (>90%) can reach 2,350 nm, which matches the solar radiation range on the earth (about 295–2,500 nm), and can perfectly meet the actual work requirements.

MATERIALS AND METHODS

In the simulation process, we define the grating period as p and its width as t. The thickness from ITO layer to GaAs layer is defined as h_1-h_4. The thickness of W base is much larger than the penetration depth of light, so that the light transmittance T of the whole structure is approximately zero. The TM polarized

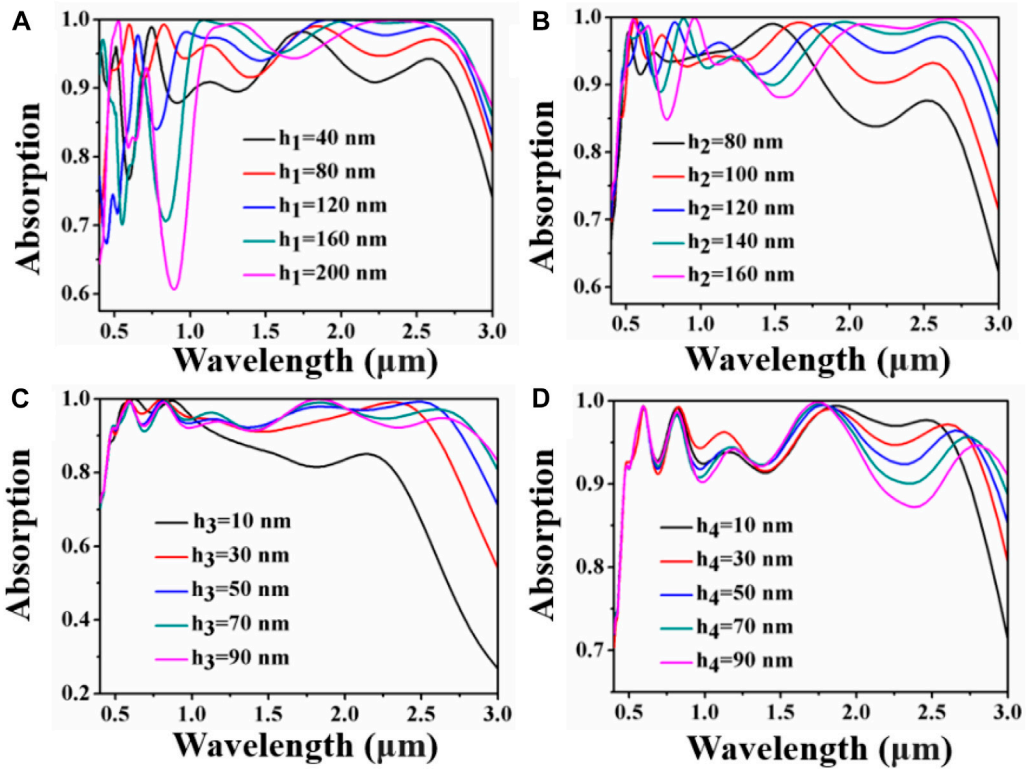

FIGURE 3 | (A–D) Absorption spectra corresponding to different geometric parameters.

plane wave is used as the light source to project vertically into the structure. The periodic boundary condition is set in the *x* direction and the perfectly matched layer is set in the *z* direction. The specific parameters of all materials are from the material library of FDTD solution software (Cao et al., 2014; Deng et al., 2015; Deng et al., 2018; Xu et al., 2021). The light absorption is still calculated by the formula $A = 1\text{-}T\text{-}R$, where T represents transmission rate and R represents reflection (Zhang et al., 2015; Long et al., 2016; Lv et al., 2018).

The simulation results are shown in **Figure 2**. In order to verify the rationality of our proposed five-layer structure, we also calculate the absorption without top layer ITO (shown by the red line in the figure) and the absorption with only three layers of Ti-GaAs-W (shown by the blue line in the figure). It can be seen from the figure that when there are only three layers of film structure, the overall absorptivity is very low, and the highest absorptivity in the whole band is less than 70%. For the case of adding GaAs grating without ITO film, the absorption rate has been greatly improved compared with the three-layer film structure, but the absorptivity is less than 90% in 1,030–1,410 nm and 2000–2,450 nm, which is still unsatisfactory. In our final five-layer structure, the absorption is more than 90% in the wavelength range of about 500–2,850 nm, which is up to 2,350 nm. Through calculation, the average absorption is 95% in the bandwidth of 2,350 nm, which meets the requirements of practical application perfectly.

RESULTS AND DISCUSSION

First, we explore the influence of the main geometric parameters of the structure on the overall absorption, and the results are shown in **Figure 3** Figure (a) shows the influence of the thickness of the top ITO film on the overall absorption. In the short wavelength range, the absorption changes greatly with the increase of the thickness, but at the long wavelength, it will gradually become better with the increase of the thickness and finally tend to remain unchanged. Considering the absorption of the whole band, we choose h_1 = 80 nm as the optimal parameter. Figure (c) shows the effect of Ti film thickness on the structural absorptivity. When the thickness of Ti film is low, the absorptivity of the whole structure is poor, but with the increase of the thickness, it has a significant increase, and has a good absorption effect at h_3 = 70–90 nm. The main reason is that the better impedance matching condition is met at this time. Figures (b) and (d) show the effects of the thickness of the two layers on the overall absorption. In figure (b), with the increase of h_2, the long band absorption has been significantly improved. This is because the guided mode resonance of the grating layer is mainly related to its effective refractive index (Chen et al., 2013; Cai et al., 2014; Long et al., 2015), and the change of h_2 will significantly change the effective refractive index of the waveguide layer. In figure (d), with the increase of the thickness, the absorption in the long band decreases gradually, while the absorption in the short band is almost unchanged. This is

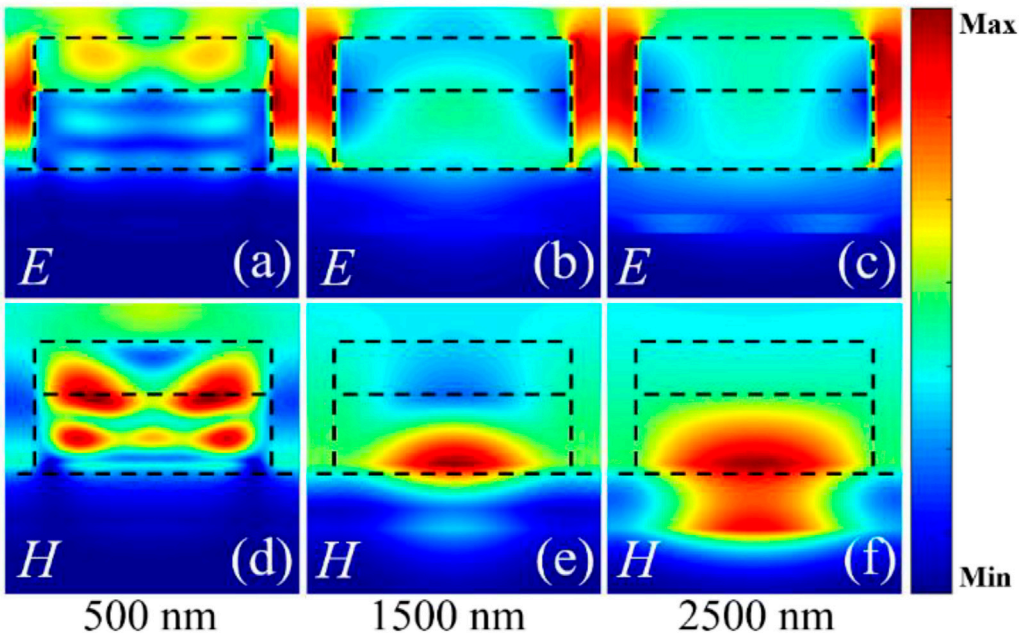

FIGURE 4 | (A-F) Electromagnetic field distribution of structures at incident wavelengths of 500 nm, 1,500 nm and 2,500 nm (*xoz* plane).

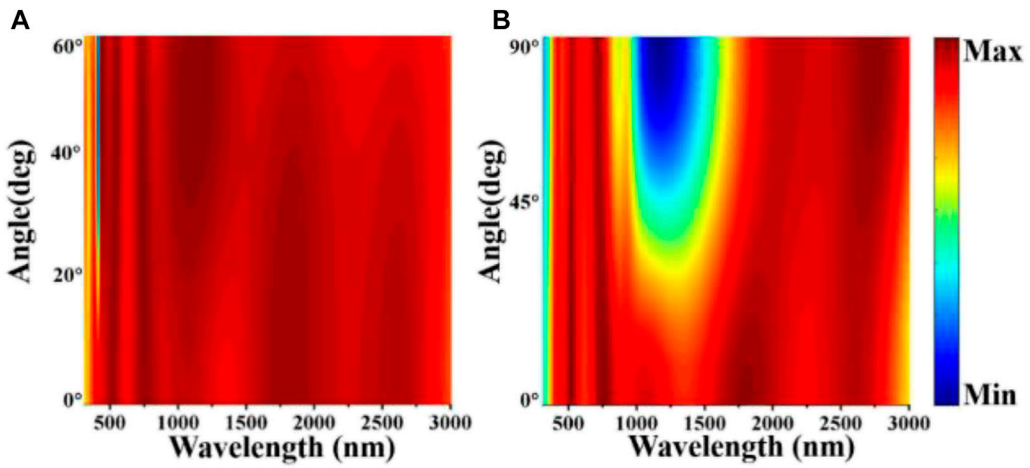

FIGURE 5 | (A) Absorption spectra at different oblique incidence angle. **(B)** Absorption spectra at different polarization angles.

because the change of the film thickness will cause a weak change in the number of dielectric cavities.

Next, in order to more clearly and deeply explore the specific physical mechanism behind the broadband absorption phenomenon, we made a detailed analysis of its electromagnetic field distribution, and the results are shown in the **Figure 4**. The distribution of electric field and magnetic field at the wavelength of 500 nm, 1,500 nm and 2,500 nm of the incident light are plotted with the interval of 1,000 nm. The selected plane is *xoz* plane, and the top layer of ITO antireflection layer and GaAs grating layer are indicated with black dotted line. When the incident light wavelength is 500 nm, it can be seen from figures (a) and (d) that the electric field is mainly concentrated on both sides of the top structure and the interface with the air, and the magnetic field is distributed in the top two-layer structure, which indicates that in this case, the cavity film and GMRs mode are excited, and the joint effect of the two greatly enhances the overall absorptivity of the structure (Xu et al., 2020). Furthermore, it can be seen from figures (c) and (f) that the light penetrates further to the bottom layer and stronger SPPs are excited. From the corresponding electromagnetic fields of these three bands, we can draw the following conclusion: it is the

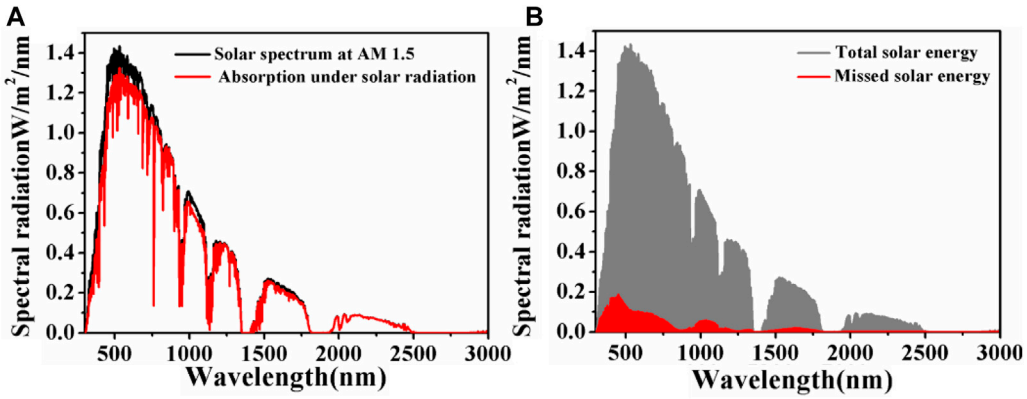

FIGURE 6 | (A) Solar energy absorption spectrum **(B)** Comparison of energy absorption and loss.

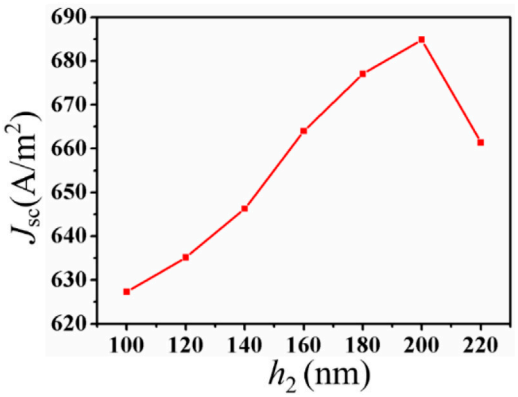

FIGURE 7 | Influence of different grating layer thickness on short circuit current.

coupling effect of GMRs, cavity film and SPPs that makes the broadband absorption possible.

After the mechanism of broadband absorption of the proposed absorber has been proved, we have further analyzed its other photoelectric characteristics. Similar to the three-layer absorber mentioned above, we simulate the absorption spectrum when the incident angle is 0°–60° and the polarization angle changes from 0° to 90° as shown in the **Figure 5**. It can be seen from the figure that the designed absorbers have high absorptivity in the range of 0–60° and can withstand large incident angle changes, so the effect is very ideal; For the polarization angle, because the structure is not highly geometrically symmetric, the absorptivity inevitably decreases in the wavelength range of 1,000 nm–1500 nm, but it still maintains a high absorption in the whole wavelength range, and the effect is acceptable. In general, the absorption effect of the proposed absorber is much better than that of the previous absorber, which has better oblique incidence and polarization insensitive characteristics (Cheng et al., 2015; Callewaert et al., 2016; Vafapour, 2019).

Subsequently, as a solar absorber, the absorption capacity of the actual solar radiation is a very important index (Elshorbagy et al., 2017; Li et al., 2018; Nie et al., 2021; Xie et al., 2021). In order to explore its solar absorption in real situation, we selected AM1.5 spectrum to test its performance, and the results are shown in the **Figure 6**. In **Figure 6A**, the black line represents the solar spectrum at AM 1.5, and the red line represents the absorption of the proposed absorber under this solar radiation. It can be clearly seen that the red line and the black line coincide approximately in the whole 400–3000 nm band, which indicates that the efficiency of the absorber is very high and the absorption effect is very ideal. **Figure 6B** illustrates the previous conclusion more intuitively from the angle of how much energy is absorbed and lost. In the figure, the gray part represents the absorbed energy, and the red part represents the lost part. We can see that there is only a little energy loss in the short band, and it is insignificant compared with the area of the absorbed part. From these two aspects, it is easy to see that the proposed absorber has good practical effect.

We also explore the ideal short-circuit current of the multilayer structure, and the results are shown in **Figure 7**. It can be seen that the short circuit current of the structure is high. When h_2 = 200 nm, the short-circuit current is up to 684.851 A/m^2. It can be predicted that the absorber will have a high photoelectric conversion efficiency, making the solar cell have more excellent performance (Mason et al., 2011; El-Gohary et al., 2014; Chen et al., 2019b).

CONCLUSION

In this paper, we propose a solar absorber composed of three-layer W-Ti-GaAs films and multi-layer metal semiconductor composite structure of GaAs grating. By adjusting the geometric parameters for many times, the broadband absorption at 500–2,850 nm, up to 2,350 nm, is realized, which greatly broadens the absorption bandwidth of the original simple structure. At the same time, the electromagnetic field distribution of the structure is given, which explains the reason of broadband absorption in physical essence. The spectrum, solar absorption and loss spectrum, ideal short circuit current and other parameters of oblique incidence and polarization angle change are studied, respectively. The results show that our solar

absorber can meet the requirements of practical application. The proposed absorber provides theoretical basis for the design of perfect broadband solar absorber.

DATA AVAILABILITY STATEMENT

The original contributions presented in the study are included in the article/Supplementary Material, further inquiries can be directed to the corresponding author.

AUTHOR CONTRIBUTIONS

MH: Conceptualization, Formal analysis, Investigation, Data curation, Writing - original draft, Writing - review & editing. KW: Conceptualization, Formal analysis, Investigation, Data curation, Funding acquisition. PW: Conceptualization, Formal analysis, Investigation, Data curation, Writing - original draft, Writing - review & editing. DX: Conceptualization, Formal analysis, Revision. YX: Conceptualization, Formal analysis, Revision.

FUNDING

This work was supported by the National Natural Science Foundation of China (NSFC) (11704223 and 61705056), Zhejiang Provincial Natural Science Foundation of China (LGF20F050004), Research Project of Zhejiang Provincial Department of Education (Y202146019), Research Project of Fujian Provincial Department of Education (JAT190534), Science and Technology Project of Zhejiang University of Technology (KYY-HX-20210657).

REFERENCES

Cai, R., Rao, W., Zhang, Z., Long, F., and Yin, Y. (2014). An Imprinted Electrochemical Sensor for Bisphenol A Determination Based on Electrodeposition of a Graphene and Ag Nanoparticle Modified Carbon Electrode. *Anal. Methods* 6, 1590–1597. doi:10.1039/c3ay42125b

Cai, Y., Huang, D., Ma, Z., Wang, H., Huang, Y., Wu, X., et al. (2019). Construction of Highly Conductive Network for Improving Electrochemical Performance of Lithium Iron Phosphate. *Electrochimica Acta* 305, 563–570. doi:10.1016/j.electacta.2019.02.114

Callewaert, F., Chen, S., Butun, S., and Aydin, K. (2016). Narrow Band Absorber Based on a Dielectric Nanodisk Array on Silver Film. *J. Opt.* 18 (7), 075006. doi:10.1088/2040-8978/18/7/075006

Cao, G., Li, H., Deng, Y., Zhan, S., He, Z., and Li, B. (2014). Systematic Theoretical Analysis of Selective-Mode Plasmonic Filter Based on Aperture-Side-Coupled Slot Cavity. *Plasmonics* 9, 1163–1169. doi:10.1007/s11468-014-9727-y

Chen, H.-J., Zhang, Z.-H., Cai, R., Kong, X.-Q., Chen, X., Liu, Y.-N., et al. (2013). Molecularly Imprinted Electrochemical Sensor Based on a Reduced Graphene Modified Carbon Electrode for Tetrabromobisphenol A Detection. *Analyst* 138, 2769–2776. doi:10.1039/c3an00146f

Chen, P., Liu, F., Ding, H., Chen, S., Chen, L., Li, Y.-J., et al. (2019). Porous Double-Shell CdS@C3N4 Octahedron Derived by *In Situ* Supramolecular Self-Assembly for Enhanced Photocatalytic Activity. *Appl. Catal. B: Environ.* 252, 33–40. doi:10.1016/j.apcatb.2019.04.006

Chen, X., Zhou, Y., Han, H., Wang, X., Zhou, L., Yi, Z., et al. (2021). Optical and Magnetic Properties of Small-Size Core-Shell Fe3O4@C Nanoparticles. *Mater. Today Chem.* 22, 100556. doi:10.1016/j.mtchem.2021.100556

Chen, Z., Chen, H., Jile, H., Xu, D., Yi, Z., Lei, Y., et al. (2021). Multi-band Multi-Tunable Perfect Plasmon Absorber Based on L-Shaped and Double-Elliptical Graphene Stacks. *Diamond Relat. Mater.* 115, 108374. doi:10.1016/j.diamond.2021.108374

Chen, Z., Chen, H., Yin, J., Zhang, R., Jile, H., Xu, D., et al. (2021). Multi-band, Tunable, High Figure of merit, High Sensitivity Single-Layer Patterned Graphene-Perfect Absorber Based on Surface Plasmon Resonance. *Diamond Relat. Mater.* 116, 108393. doi:10.1016/j.diamond.2021.108393

Chen, Z., Li, P., Zhang, S., Chen, Y., Liu, P., and Duan, H. (2019). Enhanced Extraordinary Optical Transmission and Refractive-index Sensing Sensitivity in Tapered Plasmonic Nanohole Arrays. *Nanotechnology* 30, 335201. doi:10.1088/1361-6528/ab1b89

Chen, Z., Zhang, S., Chen, Y., Liu, Y., Li, P., Wang, Z., et al. (2020). Double Fano Resonances in Hybrid Disk/rod Artificial Plasmonic Molecules Based on Dipole-Quadrupole Coupling. *Nanoscale* 12 (17), 9776–9785. doi:10.1039/d0nr00461h

Cheng, Z., Liao, J., He, B., Zhang, F., Zhang, F., Huang, X., et al. (2015). One-Step Fabrication of Graphene Oxide Enhanced Magnetic Composite Gel for Highly Efficient Dye Adsorption and Catalysis. *ACS Sustainable Chem. Eng.* 3, 1677–1685. doi:10.1021/acssuschemeng.5b00383

Deng, Y., Cao, G., Wu, Y., Zhou, X., and Liao, W. (2015). Theoretical Description of Dynamic Transmission Characteristics in MDM Waveguide Aperture-Side-Coupled with Ring Cavity. *Plasmonics* 10, 1537–1543. doi:10.1007/s11468-015-9971-9

Deng, Y., Cao, G., Yang, H., Zhou, X., and Wu, Y. (2018). Dynamic Control of Double Plasmon-Induced Transparencies in Aperture-Coupled Waveguide-Cavity System. *Plasmonics* 13, 345–352. doi:10.1007/s11468-017-0519-z

El-Gohary, S. H., Choi, J. M., Kim, N.-H., and Byun, K. M. (2014). Plasmonic Metal-Dielectric-Metal Stack Structure with Subwavelength Metallic Gratings for Improving Sensor Sensitivity and Signal Quality. *Appl. Opt.* 53, 2152–2157. doi:10.1364/AO.53.002152

Elshorbagy, M. H., Cuadrado, A., and Alda, J. (2017). High-sensitivity Integrated Devices Based on Surface Plasmon Resonance for Sensing Applications. *Photon. Res.* 5, 654–661. doi:10.1364/PRJ.5.000654

Huang, X., He, W., Yang, F., Ran, J., Gao, B., and Zhang, W.-L. (2018). Polarization-independent and Angle-Insensitive Broadband Absorber with a Target-Patterned Graphene Layer in the Terahertz Regime. *Opt. Express* 26 (20), 25558–25566. doi:10.1364/OE.26.025558

Jiang, L., Yi, Y., Tang, Y., Li, Z., Yi, Z., Liu, L., et al. (2021). A High Quality Factor Ultra-narrow Band Perfect Metamaterial Absorber for Monolayer Molybdenum Disulfide. *Chin. Phys. B* 19, 103415. doi:10.1088/1674-1056/ac1e11

Jiang, L., Yuan, C., Li, Z., Su, J., Yi, Z., Yao, W., et al. (2021). Multi-band and High-Sensitivity Perfect Absorber Based on Monolayer Graphene Metamaterial. *Diamond Relat. Mater.* 111, 108227. doi:10.1016/j.diamond.2020.108227

Keshavarz, A., and Vafapour, Z. (2019). Thermo-optical Applications of a Novel Terahertz Semiconductor Metamaterial Design. *J. Opt. Soc. Am. B* 36, 35–41. doi:10.1364/JOSAB.36.000035

Lei, L., Li, S., Huang, H., Tao, K., and Xu, P. (2018). Ultra-broadband Absorber from Visible to Near-Infrared Using Plasmonic Metamaterial. *Opt. Express* 26 (5), 5686. doi:10.1364/OE.26.005686

Li, J., Chen, X., Yi, Z., Yang, H., Tang, Y., Yi, Y., et al. (2020). Broadband Solar Energy Absorber Based on Monolayer Molybdenum Disulfide Using Tungsten Elliptical Arrays. *Mater. Today Energ.* 16, 100390. doi:10.1016/j.mtener.2020.100390

Li, J., Jiang, J., Xu, Z., Liu, M., Tang, S., Yang, C., et al. (2018). Facile Synthesis of Ag@Cu2O Heterogeneous Nanocrystals Decorated N-Doped Reduced Graphene Oxide with Enhanced Electrocatalytic Activity for Ultrasensitive Detection of H2O2. *Sensors Actuators B: Chem.* 260, 529–540. doi:10.1016/j.snb.2018.01.068

Li, J., Jiang, J., Zhao, D., Xu, Z., Liu, M., Liu, X., et al. (2020). Novel Hierarchical Sea Urchin-like Prussian Blue@palladium Core-Shell Heterostructures Supported on Nitrogen-Doped Reduced Graphene Oxide: Facile Synthesis and Excellent Guanine Sensing Performance. *Electrochimica Acta* 330, 135196. doi:10.1016/j.electacta.2019.135196

Li, Y., Li, M., Xu, P., Tang, S., and Liu, C. (2016). Efficient Photocatalytic Degradation of Acid orange 7 over N-Doped Ordered Mesoporous Titania on Carbon Fibers under Visible-Light Irradiation Based on Three Synergistic Effects. *Appl. Catal. A: Gen.* 524, 163–172. doi:10.1016/j.apcata.2015.01.050

Li, Z., Yi, Y., Xu, D., Yang, H., Yi, Z., Chen, X., et al. (2021). A Multi-Band and Polarization-independent Perfect Absorber Based on Dirac Semimetals Circles and Semi-ellipses Array*. *Chin. Phys. B* 30, 098102. doi:10.1088/1674-1056/abfb57

Li, Z., Yi, Z., Liu, T., Liu, L., Chen, X., Zheng, F., et al. (2021). Three-band Perfect Absorber with High Refractive index Sensing Based on an Active Tunable Dirac Semimetal. *Phys. Chem. Chem. Phys.* 23 (32), 17374–17381. doi:10.1039/D1CP01375K

Li-Ying, J., Yi, Y. T., Ying-Ting, Y., Zao, Y., Hua, Y., Zhi-You, L., et al. (2021). A Four-Band Perfect Absorber Based on High Quality Factor and High Quality Factor of Monolayer Molybdenum Disulfide. *Acta Physica Sinica* 70, 128101. doi:10.7498/aps.70.20202163

Liu, Y., Bo, M., Yang, X., Zhang, P., Sun, C. Q., and Huang, Y. (2017). Size Modulation Electronic and Optical Properties of Phosphorene Nanoribbons: DFT-BOLS Approximation. *Phys. Chem. Chem. Phys.* 19, 5304–5309. doi:10.1039/c6cp08011a

Long, F., Zhang, Z. H., Wang, J., Yan, L., Lu, P. P., and Yang, Z. X. (2016). Magnetic Graphene Modified Imprinted Electrochemical Sensor for Detection of 4-Octylphenol. *Chin. J. Anal. Chem.* 44, 908–914. doi:10.11895/j.issn.0253.3820.160016

Long, F., Zhang, Z., Wang, J., Yan, L., and Zhou, B. (2015). Cobalt-nickel Bimetallic Nanoparticles Decorated Graphene Sensitized Imprinted Electrochemical Sensor for Determination of Octylphenol. *Electrochimica Acta* 168, 337–345. doi:10.1016/j.electacta.2015.04.054

Lv, P., Xie, D., and Zhang, Z. (2018). Magnetic Carbon Dots Based Molecularly Imprinted Polymers for Fluorescent Detection of Bovine Hemoglobin. *Talanta* 188, 145–151. doi:10.1016/j.talanta.2018.05.068

Mason, J. A., Smith, S., and Wasserman, D. (2011). Strong Absorption and Selective thermal Emission from a Midinfrared Metamaterial. *Appl. Phys. Lett.* 98, 241105. doi:10.1063/1.3600779

Nie, Y., Xie, Y., Zheng, Y., Luo, Y., Zhang, J., Yi, Z., et al. (2021). Preparation of ZnO/Bi2O3 Composites as Heterogeneous Thin Film Materials with High Photoelectric Performance on FTO Base. *Coatings* 11, 1140. doi:10.3390/coatings11091140

Roostaei, N., Mbarak, H., Monfared, S. A., and Hamidi, S. M. (2021). Plasmonic Wideband and Tunable Absorber Based on Semi Etalon Nano Structure in the Visible Region. *Phys. Scr.* 96 (3), 035805. doi:10.1088/1402-4896/abdbf6

Sivák, P., Tauš, P., Rybár, R., Beer, M., Šimková, Z., Baník, F., et al. (2020). Analysis of the Combined Ice Storage (PCM) Heating System Installation with Special Kind of Solar Absorber in an Older House. *Energies* 13 (15), 3878. doi:10.3390/en13153878

Su, J., Yang, H., Xu, Y., Tang, Y., Yi, Z., Zheng, F., et al. (2021). Based on Ultrathin PEDOT:PSS/c-Ge Solar Cells Design and Their Photoelectric Performance. *Coatings* 11 (7), 748. doi:10.3390/coatings11070748

Tang, N., Li, Y., Chen, F., and Han, Z. (2018). *In Situ* fabrication of a Direct Z-Scheme Photocatalyst by Immobilizing CdS Quantum Dots in the Channels of Graphene-Hybridized and Supported Mesoporous Titanium Nanocrystals for High Photocatalytic Performance under Visible Light. *RSC Adv.* 8, 42233–42245. doi:10.1039/c8ra08008a

Vafapour, Z. (2019). Polarization-independent Perfect Optical Metamaterial Absorber as a Glucose Sensor in Food Industry Applications. *IEEE Trans.on Nanobioscience* 18, 622–627. doi:10.1109/TNB.2019.2929802

Wang, Y., Yi, Y., Xu, D., Yi, Z., Li, Z., Chen, X., et al. (2021). Terahertz Tunable Three Band Narrowband Perfect Absorber Based on Dirac Semimetal. *Physica E: Low-dimensional Syst. Nanostructures* 131, 114750. doi:10.1016/j.physe.2021.114750

Wu, P., Zhang, C., Tang, Y., Liu, B., and Lv, L. (2020). A Perfect Absorber Based on Similar Fabry-Perot Four-Band in the Visible Range. *Nanomaterials* 10 (3), 488. doi:10.3390/nano10030488

Xiao, L., Youji, L., Feitai, C., Peng, X., and Ming, L. (2017). Facile Synthesis of Mesoporous Titanium Dioxide Doped by Ag-Coated Graphene with Enhanced Visible-Light Photocatalytic Performance for Methylene Blue Degradation. *RSC Adv.* 7, 25314–25324. doi:10.1039/c7ra02198d

Xiao, L., Zhang, Q., Chen, P., Chen, L., Ding, F., Tang, J., et al. (2019). Copper-mediated Metal-Organic Framework as Efficient Photocatalyst for the Partial Oxidation of Aromatic Alcohols under Visible-Light Irradiation: Synergism of Plasmonic Effect and Schottky junction. *Appl. Catal. B: Environ.* 248, 380–387. doi:10.1016/j.apcatb.2019.02.012

Xie, X., Liang, S., Gao, J., Guo, S., Guo, J., Wang, C., et al. (2020). Manipulating the Ion-Transfer Kinetics and Interface Stability for High-Performance Zinc Metal Anodes. *Energy Environ. Sci.* 13 (2), 503–510. doi:10.1039/c9ee03545a

Xie, Y., Nie, Y., Zheng, Y., Luo, Y., Zhang, J., Yi, Z., et al. (2021). The Influence of β-Ga2O3 Film Thickness on the Optoelectronic Properties of β-Ga2O3@ZnO Nanocomposite Heterogeneous Materials. *Mater. Today Commun.* 29, 102873. doi:10.1016/j.mtcomm.2021.102873

Xu, F., Lin, L., Wei, D., Xu, J., and Fang, J. (2021). An Asymmetric Silicon Grating Dual-Narrow-Band Perfect Absorber Based on Dielectric-Metal-Dielectric Structure. *Front. Mater.* 8, 752745. doi:10.3389/fmats.2021.752745

Xu, H., Chen, Z., He, Z., Nie, G., and Li, D. (2020). Terahertz Tunable Optical Dual-Functional Slow Light Reflector Based on Gold-Graphene Metamaterials. *New J. Phys.* 22 (12), 123009. doi:10.1088/1367-2630/abcc1c

Yi, Z., Li, J., Lin, J., Qin, F., Chen, X., Yao, W., et al. (2020). Broadband Polarization-Insensitive and Wide-Angle Solar Energy Absorber Based on Tungsten Ring-Disc Array. *Nanoscale* 12, 23077–23083. doi:10.1039/d0nr04502k

Yu, P., Yang, H., Chen, X., Yi, Z., Yao, W., Chen, J., et al. (2020). Ultra-wideband Solar Absorber Based on Refractory Titanium Metal. *Renew. Energ.* 158, 227–235. doi:10.1016/j.renene.2020.05.142

Zhang, Y., Yi, Z., Wang, X., Chu, P., Yao, W., Zhou, Z., et al. (2021). Dual Band Visible Metamaterial Absorbers Based on Four Identical Ring Patches. *Physica E: Low-dimensional Syst. Nanostructures* 127, 114526. doi:10.1016/j.physe.2020.114526

Zhang, Z., Cai, R., Long, F., and Wang, J. (2015). Development and Application of Tetrabromobisphenol A Imprinted Electrochemical Sensor Based on Graphene/carbon Nanotubes Three-Dimensional Nanocomposites Modified Carbon Electrode. *Talanta* 134, 435–442. doi:10.1016/j.talanta.2014.11.040

Zhao, F., Yi, Y., Lin, J., Yi, Z., Qin, F., Zheng, Y., et al. (2021). The Better Photoelectric Performance of Thin-Film TiO2/c-Si Heterojunction Solar Cells Based on Surface Plasmon Resonance. *Results Phys.* 28, 104628. doi:10.1016/j.rinp.2021.104628

Zhou, F., Qin, F., Yi, Z., Yao, W., Liu, Z., Wu, X., et al. (2021). Ultra-wideband and Wide-Angle Perfect Solar Energy Absorber Based on Ti Nanorings Surface Plasmon Resonance. *Phys. Chem. Chem. Phys.* 23 (31), 17041–17048. doi:10.1039/D1CP03036A

Conflict of Interest: The authors declare that the research was conducted in the absence of any commercial or financial relationships that could be construed as a potential conflict of interest.

Publisher's Note: All claims expressed in this article are solely those of the authors and do not necessarily represent those of their affiliated organizations, or those of the publisher, the editors and the reviewers. Any product that may be evaluated in this article, or claim that may be made by its manufacturer, is not guaranteed or endorsed by the publisher.

Copyright © 2021 Huang, Wei, Wu, Xu and Xu. This is an open-access article distributed under the terms of the Creative Commons Attribution License (CC BY). The use, distribution or reproduction in other forums is permitted, provided the original author(s) and the copyright owner(s) are credited and that the original publication in this journal is cited, in accordance with accepted academic practice. No use, distribution or reproduction is permitted which does not comply with these terms.

frontiers in Materials

ORIGINAL RESEARCH
published: 02 November 2021
doi: 10.3389/fmats.2021.776817

Synthesis and Photocatalytic Degradation of Water to Produce Hydrogen from Novel Cerium Dioxide and Silver-Doped Cerium Dioxide Fiber Membranes by the Electrospinning Method

Xingyu Pu[1,2], *Chencheng Wang*[1], *Xingwang Chen*[1], *Jing Jin*[1], *Wanfei Li*[1] *and Feng Chen*[1,2]*

[1]School of Materials Science and Engineering, Suzhou University of Science and Technology, Suzhou, China, [2]Tianping Collage of Suzhou University of Science and Technology, Suzhou, China

OPEN ACCESS

Edited by:
Hua Yang,
Lanzhou University of Technology, China

Reviewed by:
Fang Leiming,
China Academy of Engineering Physics, China
Guangzhuang Sun,
Chongqing Three Gorges University, China

***Correspondence:**
Feng Chen
ujschenfeng@163.com

Specialty section:
This article was submitted to Semiconducting Materials and Devices, a section of the journal Frontiers in Materials

Received: 14 September 2021
Accepted: 20 September 2021
Published: 02 November 2021

Citation:
Pu X, Wang C, Chen X, Jin J, Li W and Chen F (2021) Synthesis and Photocatalytic Degradation of Water to Produce Hydrogen from Novel Cerium Dioxide and Silver-Doped Cerium Dioxide Fiber Membranes by the Electrospinning Method. Front. Mater. 8:776817. doi: 10.3389/fmats.2021.776817

The sol-gel method combined with the electrospinning technique were used to synthesize CeO_2 nanofiber membranes and CeO_2 fiber membranes doped with different contents of nano-silver. The thermal degradation behavior, phase structure, morphology, and optical and photocatalytic hydrogen production efficiency of CeO_2 nanofiber membranes and CeO_2 fiber membranes doped with different contents of nano-silver were studied. X-ray diffraction (XRD) results indicate that the increase of silver concentration can inhibit the formation of CeO_2 crystal. Scanning electron microscopy (SEM) and transmission electron microscopy (TEM) observations show that in the prepared CeO_2 with a diameter of about 100 nm and fiber membrane material doped with nano-silver, the fiber is made of a large number of accumulating grains. Analysis of optical properties found that the doped nano–silver CeO_2 fiber membranes enhance the absorption of visible light and reduce the band gap of the material. Photocatalytic experiments show that the cerium dioxide nanofibers doped with nano-silver can greatly improve the photocatalytic performance of materials than that of pure CeO_2. The Ag/CeO_2 fiber membrane with the Ag/CeO_2 molar ratio of 3:50 possesses the highest photocatalytic hydrogen production efficiency because of its high electron hole transfer and separation efficiency. This novel synthesis strategy can be used to prepare other broad band gap semiconductor oxides and enhance their photocatalytic activity.

Keywords: photocatalytic degradation of water, cerium dioxide, silver, fiber membranes, electrospinning

INTRODUCTION

With the rapid development of the global economy, the demand for energy continues to grow, while the concern of greenhouse gas and aerosol emissions is increasing, the development of clean, renewable new energy has become the most urgent task for countries all over the world (Chen et al., 2020). As a secondary energy source, hydrogen energy has the advantages of being abundant, economical, clean, efficient, storable, and transportable, and is generally regarded as one of the most ideal pollution-free green energy sources in the 21st century (Prekob et al., 2020). At present, one of

the main means of hydrogen production is photocatalytic decomposition of water to produce hydrogen, and the key of this is to choose a good photocatalyst (Bashiri et al., 2020; Abd-Rabboh et al., 2021; Hamdy et al., 2021). Therefore, it is interesting to develop new photocatalysts to construct specific defect structures and to study their photocatalytic activity.

As the one of the most abundant rare elements in nature, cerium has a unique 4f electronic structure which makes its compounds widely used in optical, electrical, and magnetic fields (Rajesh et al., 2020; Abd-Rabboh et al., 2021; Wang et al., 2021a; Wang et al., 2021b; Syed et al., 2021). Cerium dioxide is a promising semiconductor photocatalyst, because it has the properties of n–type semiconductors such as good light–resistant corrosivity and excellent storage and release of oxygen, and its unique Ce^{3+}/Ce^{4+} valence activity makes it highly oxidative and gives it a reducing ability (Mishra et al., 2018; Wen et al., 2018; Xing et al., 2020; Wang et al., 2021c; Wang et al., 2021d). Nano–cerium dioxide possesses more special properties and applications than cerium dioxide, so researchers have more stringent requirements about morphology, size, and others (Gao et al., 2018; Gong et al., 2019; Li et al., 2021). However, research on cerium dioxide nanofibers is relatively rare. Generally, the single component CeO_2 photocatalyst has a large band gap and is difficult to respond to visible light, which greatly limits its application in the field of photocatalytic decomposition of water to produce hydrogen (Li et al., 2021). Up to now, there are three methods to improve the photocatalytic activity of CeO_2 photocatalysts (Gao et al., 2018; Malyukin et al., 2018; Mohammadiyan et al., 2018; Wen et al., 2018; Xing et al., 2020; Wang et al., 2021d; Mikheeva et al., 2021): 1) using special preparation methods to synthesize CeO_2 photocatalysts with special defect structures, 2) combining other metal oxides with a small band gap value to construct special heterojunction structure composites to enhance their light response ability, and 3) a CeO_2 photocatalyst was modified by noble metal particles to enhance the charge transfer and migration ability of the system, thus improving the photocatalytic activity of CeO_2. Noble metal particles-doped cerium dioxide is expected to show excellent physical and chemical properties (Mikheeva et al., 2021). Therefore, the preparation of cerium dioxide and noble metal particles-doped cerium dioxide by special technology and the study of their photocatalytic decomposition of water to produce hydrogen has important research significance.

In this paper, cerium dioxide composite fiber membranes and CeO_2 fiber membranes doped with different contents of nano-silver were prepared by the sol-gel method combined with electrospinning technology. The thermal decomposition behavior, phase structure, morphology, and optical and photocatalytic decomposition of water to produce hydrogen of cerium dioxide composite fiber membranes and CeO_2 fiber membranes doped with different contents of nano-silver were studied by various characterization methods. Based on the energy band theory and photocatalytic experiment results, a photocatalytic mechanism is proposed.

MATERIALS AND METHODS

Materials

All reagents were analytical grade and were used without further treatment. Hexahydrate nitrate and polyvinylpyrrolidone (PVP) were purchased from Aladdin Reagent (China) Co., Ltd. Anhydrous ethanol, silver nitrate, and acetic acid were purchased from Sinopharm Group Chemical Reagent Co., Ltd.

Preparation of Cerium Dioxide Fiber Membranes

A total of 3 g of polyvinylpyrrolidone (PVP) was weighed and added to 50 ml of ethanol, then the mixture, known as solution A, was stirred for 3 h until completely dissolved. In total, 2.171 g of cerium nitrate hexahydrate was dissolved in 10 ml of ethanol. After stirring, the solution was slowly added dropwise to solution A and stirred for about 6 h. The solution was spray–coated by the electrospinning method with a temperature of 20°C and a relative humidity of 50%. The film was dried in a vacuum oven at 40°C for 12 h. The dried film was then calcined in a muffle furnace at 550°C and incubated for 0.5 h. And finally a pale yellow cerium dioxide film was obtained.

Preparation of Cerium Dioxide Fiber Membrane Doped With Nano-Silver

Solution A and the cerium source solution were prepared under the same conditions and the two solutions were mixed under stirring. A total of 0.017 g of $AgNO_3$ was added to 5 ml of deionized water and stirred for 20 min. The silver source solution was slowly added dropwise to the above mixed solution and stirred for 2 h. In addition, by changing the content of $AgNO_3$ in the spinning solution, the morphological characteristics and properties of the spinning film under different silver contents were investigated. The solution of 0.051 and 0.085 g of silver nitrate was prepared by the same method, which means that the molar ratios of $AgNO_3$/Ce $(NO_3)_3$ in the spinning solution were 1:50, 3:50, and 5:50. The film was prepared by an electrospinning method. After drying under the same conditions, the film was calcined in a muffle furnace to 600°C for 1 h. Finally, cerium dioxide nanofiber membranes doped with nano-silver were obtained.

Materials Characterization

The products were characterized by thermogravimetric analysis (TG) and differential scanning calorimetry (DSC). The heating rate, the air flow rate, the injection volume, and the temperature range were 20 K/min, 100 ml/min, 2 mg and 25–800°C, respectively. The composition of membranes was characterized by a Brook D8 Advance X-Ray diffractometer with a scanning angle of 20–80°, a scanning step length of 0.02°, and using Cu target Kα (λ = 0.154056 nm) radiation with a working voltage of 40 kV and a current of 40 mA. The microstructures of membranes were observed by scanning electron microscopy, while the fibers and particles constituting membranes were

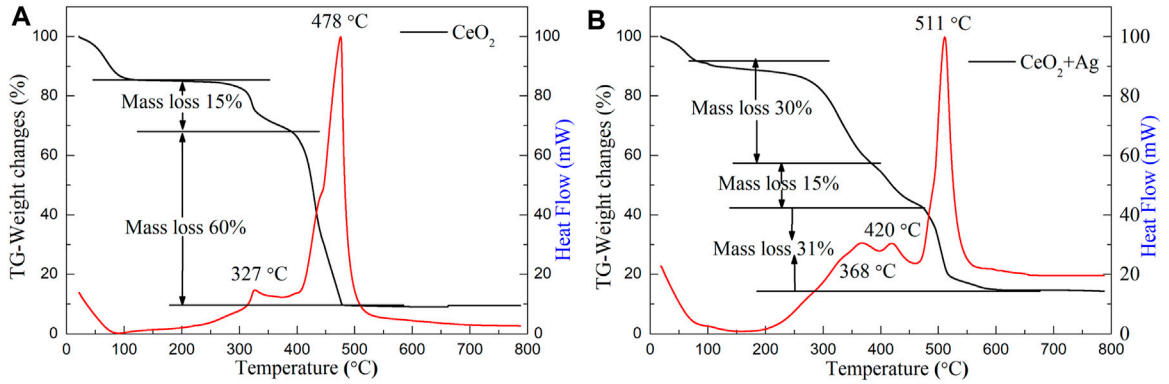

FIGURE 1 | Thermogravimetric analysis of **(A)** PVP/Ce $(NO_3)_3$ and **(B)** PVP/Ce $(NO_3)_3$/$AgNO_3$ composite fiber membranes with the Ag/CeO_2 molar ratios of 3:50 prepared by the electrospinning method.

characterized by scanning electron microscopy (SEM) and transmission electron microscopy (TEM). UV-visible absorption spectra of prepared samples were measured by an ultraviolet and visible spectrophotometer.

Photocatalytic Experiments

In order to investigate the photocatalytic properties of the prepared cerium dioxide fiber membranes and the cerium dioxide fibers doped with different proportions of nano-silver, they were applied to the reaction of photocatalytic degradation of water to produce hydrogen and compared with the bulk pure cerium oxide. The Labsolar H_2 photolysis system was developed by Beijing Prefectlight Technology Co., Ltd., and the detection device was a Shanghai Tianmei GC7900 Gas Chromatograph, with a Microsolar300 high performance analog daylight xenon lamp used as the simulation light source. A 100-mg sample was added to 100 ml of deionized water, and sodium sulfite was added as the sacrificial agent to carry out photocatalytic hydrogen production. The hydrogen production of each material was compared after 6 h of illumination.

RESULTS AND DISCUSSION

Thermogravimetric Analysis-Differential Scanning Calorimetry Analysis

Figure 1A shows the TG-DSC curves of PVP/Ce $(NO_3)_3$ composite membranes prepared by the electrospinning method. It can be seen from the figure that the sample has a large weight loss process at room temperature to 100°C, and the weight loss process is the elimination of the moisture absorbed by the sample and the possible residual solvent (Wang et al., 2013). It can be also proved that membranes have certain water absorption capacities. After that there are two large weight loss processes which correspond to two distinct exothermic peaks, especially the second exothermic peak. The first exothermic peak appears at 327°C, which indicates that from 100 to 400°C, the sample first absorbs heat, and the outer layer of the composite fiber PVP begins to decompose, then the cerium nitrate in the fiber is decomposed into cerium dioxide; the weight loss of the system during this decomposition is 15% (Mohammadiyan et al., 2018). After 550°C, the reaction is basically completed, the sample weight and heat flow curve are stable, and the final quality is about 10% of the original quality. Thus, the calcination temperature of the PVP/Ce $(NO_3)_3$ composite film can be set at 550°C.

Figure 1B shows the TG-DSC analysis of PVP/Ce$(NO_3)_3$/$AgNO_3$ for composite membrane materials. It can be seen from the figure that the final mass of the sample is about 14% of the original mass throughout the reaction. The weight loss phase from room temperature to 100°C is the residual solvent and moisture contained in the sample. There are three exothermic peaks since then, with two adjacent exothermic peaks from 100 to 450°C, then the process undergoes a more complex reaction. As can be seen from **Figure 1B**, the exothermic peak at 368°C corresponds to the initial decomposition of the polymer template, then cerium nitrate decomposes and oxidizes to cerium oxide. and the weight loss is about 30%. The exothermic peak at 420°C is a sign that the silver nitrate is thermally decomposed into silver nanoparticles with a weight loss ratio of 15%. The complete decomposition of PVP occurs between 450 and 600°C. From the TG-DSC curve, it can be seen that the thermal decomposition has been basically completed at 600°C. After the sample stabilizes, the heat flow curve tends to be smooth. The calcination temperature of the PVP/Ce $(NO_3)_3$/$AgNO_3$ composite film can be set at 600°C. When silver nitrate is introduced, a higher sintering temperature is needed to obtain the target product.

X-Ray Diffraction Analysis

Figure 2A shows the XRD pattern of PVP/Ce$(NO_3)_3$ composite fiber membranes and the membranes after calcination at 550°C in air and incubated for 0.5 h. The result indicates that the membranes after calcination have obvious diffraction peaks at $2\theta = 28.4°$, 33.0°, 47.4°, 56.1°, 59.0°, 69.2°, 76.4°, and 78.8°, corresponding to the (111), (200), (220), (311), (222), (400), (331), and (420) crystal faces of cubic fluorite crystal CeO_2, which is consistent with the standard

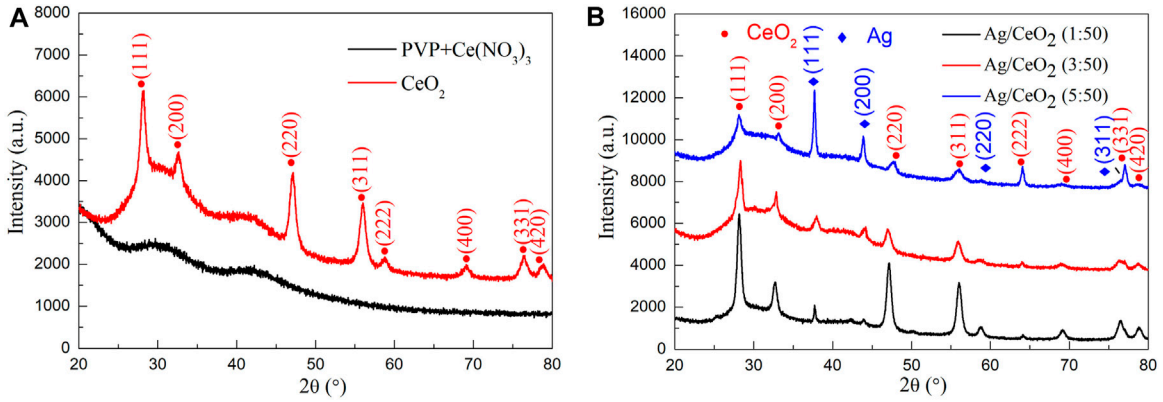

FIGURE 2 | (A) XRD pattern of PVP/Ce $(NO_3)_3$ composite fiber membrane and CeO_2 nanofiber membrane calcined at 550°C. **(B)** XRD pattern of the cerium oxide fiber doped with nano-silver with the Ce $(NO_3)_3/AgNO_3$ molar ratios of 1:50, 3:50, and 5: 50.

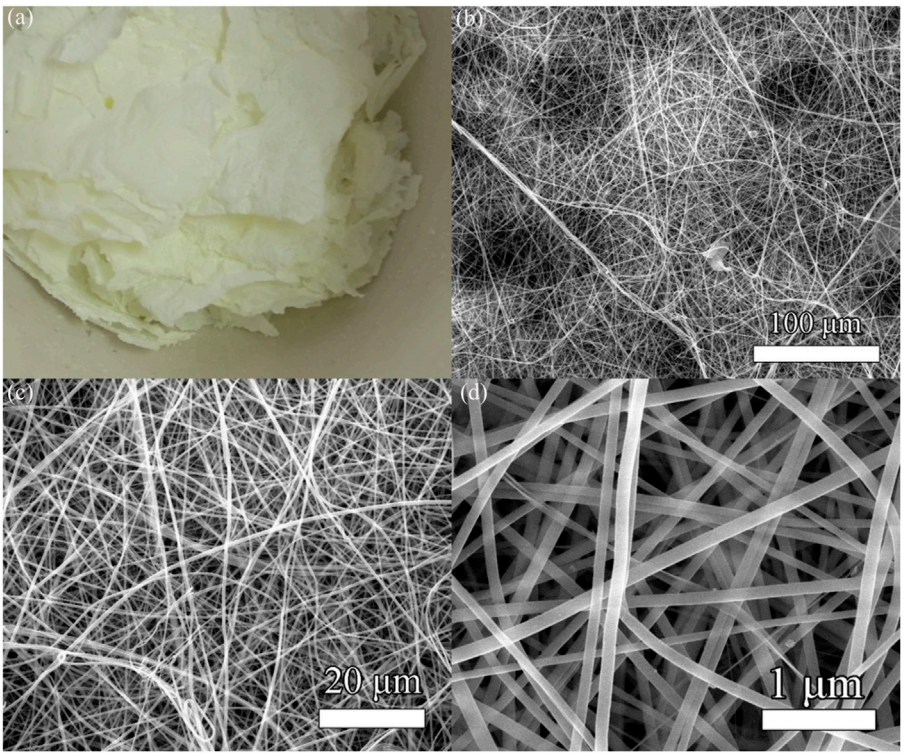

FIGURE 3 | (A) Real photographs of CeO_2 nanofiber membranes. **(B–D)** SEM images of CeO_2 nanofiber membranes at different magnifications.

card of cerium dioxide (JCPDS card no. 43 -1002). Because the fibers in membranes are covered and encapsulated by a large number of polymer PVPs, two amorphous bread peaks appear in the XRD pattern which are the diffraction peaks of the polymer. In addition, there were no other sharp diffraction peaks, and it was found that the composite fiber membrane synthesized by the electrospinning method was formed into a face-centered cubic cerium dioxide with standard card JCPDS card no. 21-1272 after calcination.

Figure 2B shows the XRD pattern of PVP/Ce $(NO_3)_3/AgNO_3$ composite fiber membranes with different silver content after calcination at 600°C for 1 h in muffle furnace, which contains the molar ratios of $AgNO_3$/Ce $(NO_3)_3$ of 1:50, 3:50, and 5:50 respectively. From the XRD curve, it can be seen that at 2θ = 28.4°, 33.0°, 47.4°, 56.1°, 59.0°, 69.2°, 76.4°, and 78.8°, the diffraction peaks correspond to (111), (200), (220), (311), (222), (400), (331), and (420) planes of the cubic fluorite crystal CeO_2. At diffraction angles of 2θ = 37.98°, 44.18°, 64.42°, and 77.26°, the diffraction

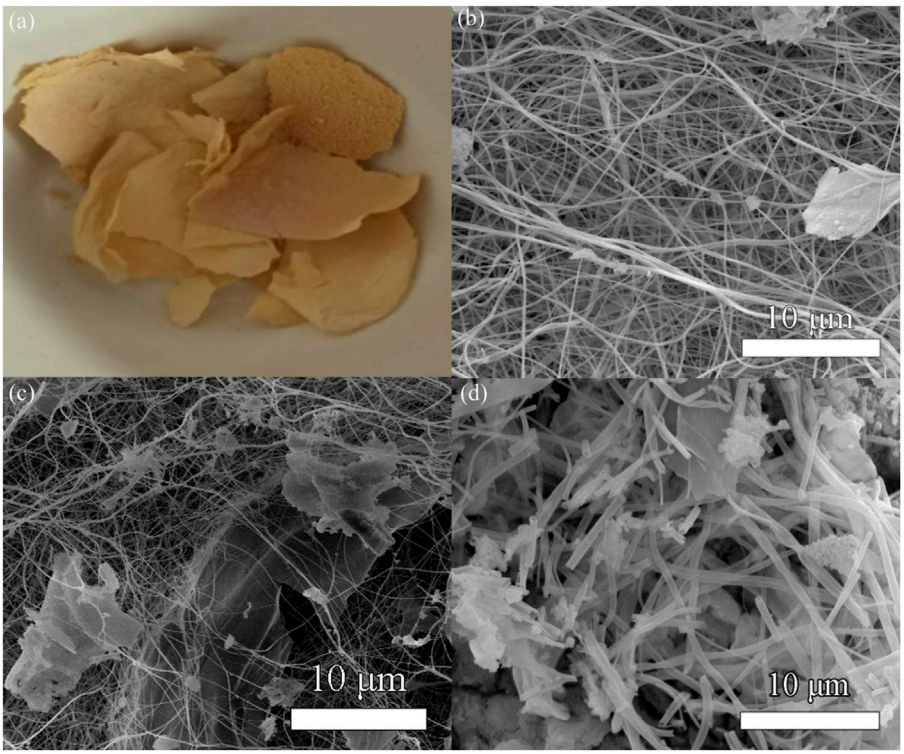

FIGURE 4 | (A) Real photographs of Ag/CeO_2 fiber membranes. SEM images of the cerium oxide fiber doped with nano-silver with the Ag/CeO_2 molar ratios of **(B)** 1:50, **(C)** 3:50, and **(D)** 5: 50.

signals correspond to the (111), (200), (220), and (311) planes of silver, which match the standard card of the nano-silver cubic crystal structure (JCPDS card no. 04-0783). All the diffraction peaks for the three samples are cerium dioxide and nano-silver. And with the increase of the relative content of silver, the peak of nano-silver shows more strongly, while the diffraction peak of cerium dioxide is weakened. All of these have proven that the prepared material is a thin cerium dioxide fiber film material loaded with nano-silver.

Scanning Electron Microscopy Analysis

Figure 3 shows the real photographs and SEM images of the PVP/$Ce(NO_3)_3$ composite fiber membranes and the membranes after calcination at 550°C in air. **Figure 3A** shows the real photographs of cerium dioxide after calcination. Obviously, the membrane has a greater degree of contraction and is pale yellow, the weight is very light and fragile, but still retains the structure of lamellae. **Figure 3B** shows the SEM image at a magnification of 100 μm, which shows that the sample is relatively flat and compact and has a high porosity. **Figure 3C** shows the SEM image at a magnification of 20 μm. It can be seen that the sample consists of a large number of nanofibers, and the fibers are disordered, within layers, and with no accumulation of fibers. **Figure 3D** shows the high resolution FESEM picture, the scale is 1 μm, the fiber is straight, the thickness and the distribution are uniform, the fiber diameter is about 100 nm, and has a very high aspect ratio.

Figure 4 shows the real photographs and SEM images of the Ag/CeO_2 fiber membrane prepared at different molar ratios of $Ce(NO_3)_3/AgNO_3$ including 1:50, 3:50, and 5:50. **Figure 4A** shows the real photographs of the sample after calcination at 600°C. It can be seen that the sample still retains the morphology of the membranes, and the addition of silver ions significantly increases the color of the sample which presents as brownish yellow when compared to the CeO_2 fiber membrane. **Figures 4B–D** show the SEM images of the Ag/CeO_2 fiber membrane prepared at different molar ratios of $Ce(NO_3)_3/AgNO_3$ including 1:50, 3:50, and 5:50. It can be seen that the sample still retains the fiber morphology. The fiber thickness of the Ag/CeO_2 membranes loaded with nano-silver is relatively uneven and the fiber distribution is more cluttered compared with the pure cerium oxide fiber. There is a phenomenon of heap and fracture in the microstructure of the membranes. Because of the introduction of metallic silver ions in the spinning solution, the introduction of this inorganic salt changes the electrostatic parameters of the spinning solution, making the electrospinning process of the spinning fluid become more complex and changeable and making fibers of uneven thickness. With the increase of silver ions, the overall morphology of the fiber becomes more uneven, and agglomeration is becoming more and more serious.

Transmission Electron Microscopy Analysis

Figure 5 shows the TEM and HRTEM images of the nano-cerium dioxide membrane material. From **Figure 5A**, it can be observed that the cerium dioxide is a fibrous structure and the diameter of

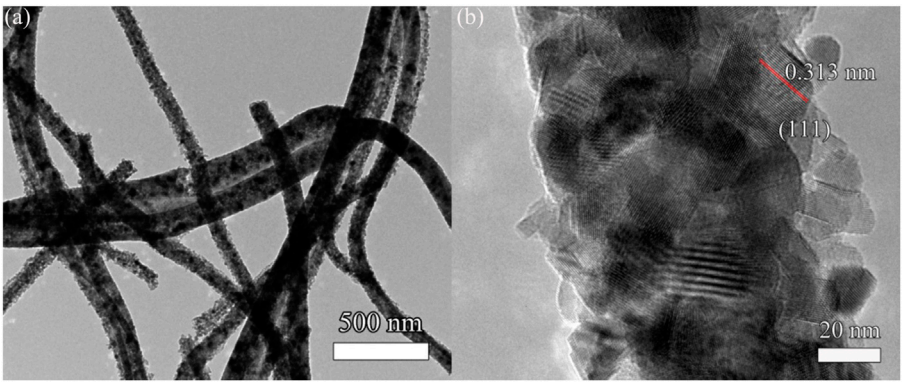

FIGURE 5 | (A) TEM image and **(B)** high-resolution transmission electron microscopy (HRTEM) of cerium dioxide fiber membranes.

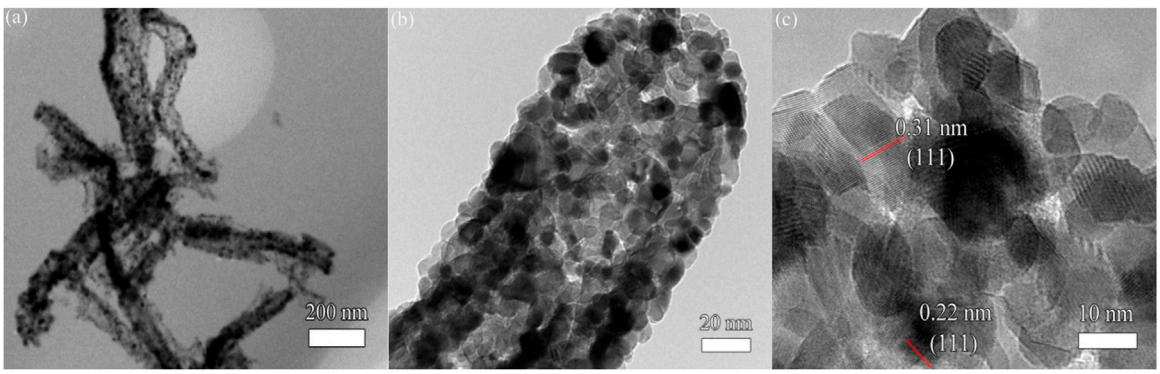

FIGURE 6 | (A) TEM image, **(B)** enlarged TEM image, and **(C)** HRTEM image of Ag/CeO_2 fiber membrane with an Ag/CeO_2 molar ratio of 3:50.

the fiber is about 100 nm. The morphology is well preserved and has a large aspect ratio. **Figure 5B** shows the high–resolution transmission electron microscopy (HRTEM) image. It can be seen that the fiber is actually made of nano–sized cerium dioxide grains. The cerium dioxide grains forming the fibers have a grain size of 15 nm, and there is a large number of lattice lines of cerium dioxide crystals. By measuring the interplanar spacing, it can be seen that the exposed active surface is a (111) plane and $d_{(111)}$ = 0.313 nm.

Figure 6 shows the TEM and HRTEM images of the Ag/CeO_2 fiber membrane with an Ag/CeO_2 molar ratio of 3:50. **Figure 6A** shows the TEM image of the sample at a 200-nm scale. It can be seen from the figure that the fibrous Ag/CeO_2 has a diameter of about 100 nm. **Figure 6B** shows an enlarged TEM image at 20 nm, and it can be clearly seen that the fibers are deposited from a large number of crystal particles with a grain size of about 10 nm. **Figure 6C** shows the HRTEM image, at 10 nm, of the Ag/CeO_2 fiber membrane with the Ag/CeO_2 molar ratio of 3:50. A large number of lattice lines are shown in which the spacing of most of the lattice lines is 0.31 nm corresponding to the (111) plane of the cerium dioxide cubic crystal structure, and there is also a lattice line with a crystal plane spacing of 0.22 nm corresponding to the (111) crystal face of Ag nanoparticles. All of the above analyses prove that the material is cerium dioxide fiber material doped with nano-silver, which corresponds to the XRD result.

Optical Properties

Figure 7 shows the UV-Vis absorption spectra and its corresponding forbidden band width calculation for the pure cerium oxide fiber membrane and the cerium oxide fiber membrane with different amounts of loaded silver. As can be seen from **Figure 7A**, the light absorption of the pure cerium dioxide fiber membrane in the wavelength range of 400–800 nm is weak, and gradually increases before 400 nm. While compared with the nano–silver-loaded material, the absorption of nano-silver-loaded material in the visible light area has significantly improved. This is because the nano–silver loaded in the CeO_2 semiconductor brings defects, resulting in changes in the band structure and reduction of the band gap width. And the nano-silver particles have the capability to absorb light, so the

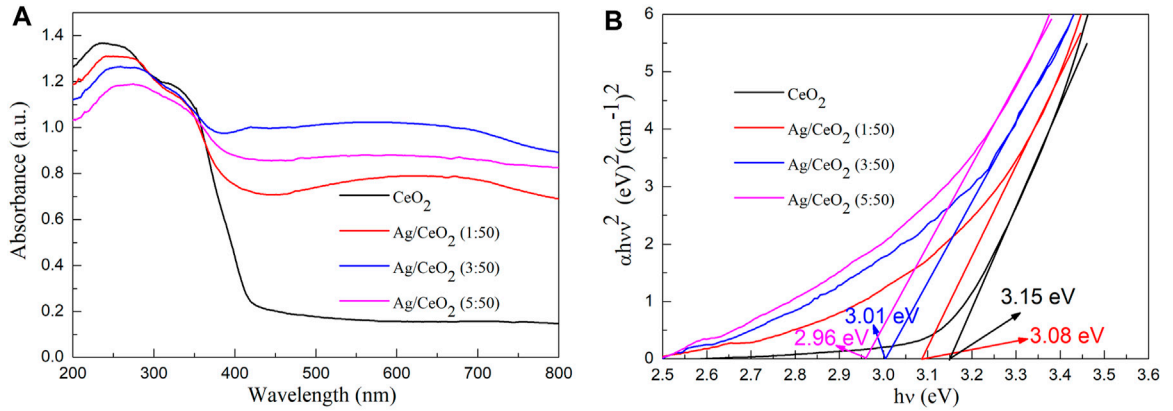

FIGURE 7 | (A) UV-Vis diffuse scattering spectra of pure cerium dioxide nanofiber membranes and cerium dioxide nanofiber membranes doped with different amounts of nano-silver. **(B)** The optical band gap (Eg) values of pure cerium dioxide nanofiber membranes and cerium dioxide nanofiber membranes doped with different amounts of nano-silver.

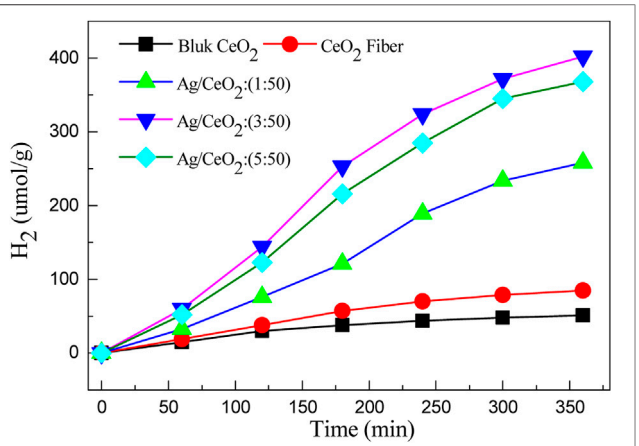

FIGURE 8 | Hydrogen evolution of different materials under visible light irradiation.

material on the absorption of visible light intensity is significantly enhanced.

The band gap energy (Eg) values of pure cerium dioxide nanofiber membranes and cerium dioxide nanofiber membranes doped with different amounts of nano-silver were obtained by absorbance spectra using the Tauc relation (Tang et al., 2020; Wang et al., 2020; Wang and Tian, 2020; Wang et al., 2021e; Gao et al., 2021).

$$(F(R)h\nu)^n = A\left(h\nu - E_g\right) \quad (1)$$

Where ν is the frequency, A is the absorption coefficient, and n is equal to 2. The band gap of the samples are obtained by a simple intercept method. In **Figure 7B**, the band gap width of pure cerium oxide fibers is consistent with the literature (Gao et al., 2018) (3.15 eV). When the molar ratios of Ag/CeO_2 are 1:50, 3:50, and 5:50, the corresponding band gap values are 3.08, 3.01, and 2.96 eV, respectively. It can be seen that the band gap of the Ag/CeO_2 fiber membrane decreases gradually with the increase of the relative content of metallic silver. After modification of the CeO_2 fiber membrane by Ag nanoparticles, the band gap of the CeO_2 fiber membrane is reduced.

Photocatalytic Decomposition of Water to Produce Hydrogen

Figure 8 shows the hydrogen production of bulk cerium dioxide, cerium dioxide nanofibers, and three different silver-doped cerium dioxide nanofiber membranes. It can be seen from the figure that the hydrogen production of the sample is increasing with the progress of the reaction, but the efficiency of hydrogen production decreases with the consumption of the sacrificial agent and the decrease of the catalyst activity. The hydrogenation efficiency of bulk cerium dioxide and cerium dioxide nanofibers are very low because the cerium dioxide only absorbs ultraviolet light, which leads to low photocatalytic activity. The photocatalytic hydrogen production efficiency of the noble metal nano-silver-doped cerium dioxide fiber material has been greatly improved due to the nano-silver as it is in contact with the cerium dioxide crystal to form a heterojunction, and the band of the semiconductor is bent at the interface. Then, the electrons shift from a high Fermi level to a low Fermi level, forming a Schottky barrier in the materials. Comparing 3 M ratios of Ag/CeO_2, the photocatalytic hydrogen is the highest when the molar ratio of Ag/CeO_2 is 3:50, and the hydrogen production is about 402 μmol/g after 6 h of illumination. The photocatalytic activity of CeO_2 fiber increases with the addition of nano-silver, but the photocatalytic activity decreases when the doped noble metal nano-silver goes over a certain limit. This is because the excess of nano-silver particles will become the recombination center of the carrier, which will capture the hole on the surface of the CeO_2 fiber, leading to a decrease of photogenerated carrier density and

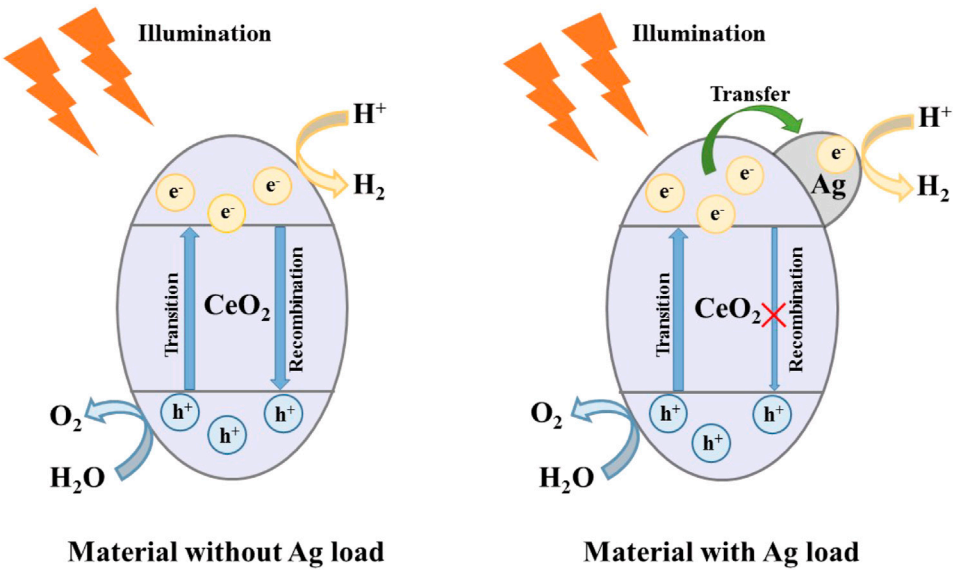

FIGURE 9 | Photocatalytic mechanism of CeO_2 and Ag/CeO_2 photocatalysts.

a reduction in photocatalytic performance. While too much precious metal particles will cover the active center of CeO_2, which will also reduce the photocatalytic performance of the system. Moreover, it can be seen from the SEM image that CeO_2 has a tendency to accumulate into blocks as the amount of silver increases which can make the specific surface area reduce.

Photocatalytic Mechanism

Based on band theory and experimental results, **Figure 9** shows the photocatalytic mechanism of CeO_2 and Ag/CeO_2 photocatalysts. When visible light irradiates on the surface of CeO_2, because the band gap of CeO_2 is large, it can only respond to ultraviolet light, so the probability of valence band electron transition to the conduction band is small. At the same time, the photocatalytic hydrogen production efficiency is low because a small number of electrons in the conduction band are easily recombined with the holes in the valence band. When Ag is loaded on the surface of CeO_2, the electron transition from the valence band of CeO_2 to its conduction band is accelerated, so that the Ag/CeO_2 photocatalyst can respond to visible light. The electrons that transition to the CeO_2 conduction band will accelerate the transfer to Ag particles, preventing the electron from recombination with the holes of the CeO_2 conduction band. The transfer and separation of electrons and holes play an important role in the whole process of photocatalytic hydrogen production. Ag particles act as the carrier of charge carrier transfer during the whole process.

CONCLUSION

CeO_2 nanofiber membranes and CeO_2 fiber membranes doped with different contents of nano-silver were prepared by the sol-gel method and electrospinning technique. The CeO_2 and Ag/CeO_2 nanofiber membranes were characterized by TG-DSC, XRD, SEM, TEM, and UV-Vis, and their photocatalytic activity was investigated by the photocatalytic decomposition of water. The electrospinning method successfully prepared CeO_2 with a diameter of about 100 nm and fiber membrane materials doped with nano-silver; the fiber is made of a large number of accumulated grains. The increase of silver concentration can inhibit formation of CeO_2 crystal. With the increase of the relative content of silver ions, the difficulty of spinning increases, the morphology of the fibers becomes more and more cluttered, and the accumulation phenomenon becomes more and more serious. The doped nano–silver CeO_2 fiber membrane enhances the absorption of visible light and reduces the band gap of the material, so its photocatalytic performance is significantly improved. In the photocatalytic hydrogen production, the cerium dioxide nanofibers doped with nano-silver can greatly improve the photocatalytic performance of materials. The Ag/CeO_2 fiber membrane with the Ag/CeO_2 molar ratio of 3:50 exhibits the highest photocatalytic hydrogen production efficiency, and the hydrogen production after irradiation for 6 h is about 402 μmol/g due to its high electron hole transfer and separation efficiency.

DATA AVAILABILITY STATEMENT

The original contributions presented in the study are included in the article/Supplementary Material, further inquiries can be directed to the corresponding authors.

AUTHOR CONTRIBUTIONS

XP was responsible for synthesis experiments, performance tests and data analysis. CW and XC were responsible for material characterization. JJ was responsible for the analysis and guidance of XRD and UV tests. WL is responsible for analyzing the reaction mechanism. FC was responsible for experimental design and paper revision.

FUNDING

This work was supported by National Natural Science Foundation of China (21773291); Natural Science Foundation of Jiangsu Province (BK20180103); Qing Lan Project of Jiangsu Province; Suzhou Key Laboratory for Nanophotonic and Nanoelectronic Materials and Its Devices.

REFERENCES

Abd-Rabboh, H. S. M., Benaissa, M., Hamdy, M. S., Ahmed, M. A., and Glal, M. (2021). Synthesis of an Efficient, and Recyclable Mesoporous BiVO4/TiO2 Direct Z-Scheme Heterojunction by Sonochemical Route for Photocatalytic Hydrogen Production and Photodegradation of Rhodamine B Dye in the Visible Region. *Opt. Mater.* 114, 110761. doi:10.1016/j.optmat.2020.110761

Bashiri, R., Mohamed, N. M., Sufian, S., and Kait, C. F. (2020). Improved Photoelectrochemical Hydrogen Production over Decorated Titania with Copper and Nickel Oxides by Optimizing the Photoanode and Reaction Characteristics. *Mater. Today Chem.* 16, 100241. doi:10.1016/j.mtchem.2020.100241

Chen, S., Skordos, A., and Thakur, V. K. (2020). Functional Nanocomposites for Energy Storage: Chemistry and New Horizons. *Mater. Today Chem.* 17, 100304. doi:10.1016/j.mtchem.2020.100304

Gao, H., Wang, Y., Gao, Q., Pan, X., Wang, S., Yang, H., et al. (2021). Phase Evolution and Photoluminescence Behavior of MMoO4 (M = Mg, Ca, Sr) Phosphors. *Optik* 241, 167040. doi:10.1016/j.ijleo.2021.167040

Gao, H., Yang, H., Yang, G., and Wang, S. (2018). Effects of Oxygen Vacancy and Sintering Temperature on the Photoluminescence Properties and Photocatalytic Activity of CeO2 Nanoparticles with High Uniformity. *Mater. Technol.* 33, 321–332. doi:10.1080/10667857.2018.1438222

Gong, X., Gao, X., Du, W., Zhang, H., Zhang, S., Nguyen, T. T., et al. (2019). Wood Powder-Derived Quantum Dots for CeO2 Photocatalytic and Anti-counterfeit Applications. *Opt. Mater.* 96, 109302. doi:10.1016/j.optmat.2019.109302

Hamdy, M. S., Abd-Rabboh, H. S. M., Benaissa, M., Al-Metwaly, M. G., Galal, A. H., and Ahmed, M. A. (2021). Fabrication of Novel polyaniline/ZnO Heterojunction for Exceptional Photocatalytic Hydrogen Production and Degradation of Fluorescein Dye through Direct Z-Scheme Mechanism. *Opt. Mater.* 117, 111198. doi:10.1016/j.optmat.2021.111198

Li, J., Wang, S., Sun, G., Gao, H., Yu, X., Tang, S., et al. (2021). Facile Preparation of MgAl2O4/CeO2/Mn3O4 Heterojunction Photocatalyst and Enhanced Photocatalytic Activity. *Mater. Today Chem.* 19, 100390. doi:10.1016/j.mtchem.2020.100390

Malyukin, Y., Seminko, V., Maksimchuk, P., Okrushko, E., Sedyh, O., and Zorenko, Y. (2018). Hydrogen Peroxide Sensing Using Ce3+ Luminescence of Cerium Oxide (CeO2-X) Nanoparticles. *Opt. Mater.* 85, 303–307. doi:10.1016/j.optmat.2018.08.063

Mikheeva, N. N., Zaikovskii, V. I., Larichev, Y. V., and Mamontov, G. V. (2021). Toluene Abatement on Ag-CeO2/SBA-15 Catalysts: Synergistic Effect of Silver and Ceria. *Mater. Today Chem.* 21, 100530. doi:10.1016/j.mtchem.2021.100530

Mishra, S., Soren, S., Debnath, A. K., Aswal, D. K., Das, N., and Parhi, P. (2018). Rapid Microwave - Hydrothermal Synthesis of CeO2 Nanoparticles for Simultaneous Adsorption/photodegradation of Organic Dyes under Visible Light. *Optik* 169, 125–136. doi:10.1016/j.ijleo.2018.05.045

Mohammadiyan, E., Ghafuri, H., and Kakanejadifard, A. (2018). Synthesis and Characterization of a Magnetic Fe3O4@CeO2 Nanocomposite Decorated with Ag Nanoparticle and Investigation of Synergistic Effects of Ag on Photocatalytic Activity. *Optik* 166, 39–48. doi:10.1016/j.ijleo.2018.03.044

Prekob, Á., Hajdu, V., Muránszky, G., Fiser, B., Sycheva, A., Ferenczi, T., et al. (2020). Application of Carbonized Cellulose-Based Catalyst in Nitrobenzene Hydrogenation. *Mater. Today Chem.* 17, 100337. doi:10.1016/j.mtchem.2020.100337

Rajesh, K., Sakthivel, P., Santhanam, A., and Venugobal, J. (2020). Incorporation of Silver Ion on Structural and Optical Characteristics of CeO2 Nanoparticles: White LED Applications. *Optik* 216, 164800. doi:10.1016/j.ijleo.2020.164800

Syed, A., Elgorban, A. M., and Al Kheraif, A. A. (2021). High Performance Nanohybrid CeO2@2D CdO Plates with Suppressed Charge Recombination: Insights of Photoluminescence, Visible-Light Photocatalysis, Intrinsic Mechanism and Antibacterial Activity. *Opt. Mater.* 121, 111510. doi:10.1016/j.optmat.2021.111510

Tang, S., Wang, S., Yu, X., Gao, H., Niu, X., Wang, Y., et al. (2020). Gamma-Ray Irradiation Assisted Polyacrylamide Gel Synthesis of Scheelite Type BaWO 4 Phosphors and its Colorimetric, Optical and Photoluminescence Properties. *ChemBioChem* 5, 10599–10606. doi:10.1002/slct.202002429

Wang, S.-F., Zhang, C., Sun, G., Chen, B., Xiang, X., Wang, H., et al. (2013). Fabrication of a Novel Light Emission Material AlFeO3 by a Modified Polyacrylamide Gel Route and Characterization of the Material. *Opt. Mater.* 36, 482–488. doi:10.1016/j.optmat.2013.10.014

Wang, S. F., Chen, X. Y., Gao, H. J., Fang, L. M., Hu, Q. W., Sun, G. A., et al. (2021a). A Comparative Study on the Phase Structure, Optical and NIR Reflectivity of BaFe12O19 Nano-Pigments by the Traditional and Modified Polyacrylamide Gel Method. *J. Nano Res.* 67, 1–14. doi:10.4028/www.scientific.net/jnanor.67.1

Wang, S., Gao, H., Fang, L., Hu, Q., Sun, G., Chen, X., et al. (2021b). Synthesis of Novel CQDs/CeO2/SrFe12O19 Magnetic Separation Photocatalysts and Synergic Adsorption-Photocatalytic Degradation Effect for Methylene Blue Dye Removal. *Chem. Eng. J. Adv.* 6, 100089. doi:10.1016/j.ceja.2021.100089

Wang, S., Gao, H., Li, J., Wang, Y., Chen, C., Yu, X., et al. (2021c). Comparative Study of the Photoluminescence Performance and Photocatalytic Activity of CeO2/MgAl2O4 Composite Materials with an N-N Heterojunction Prepared by One-step Synthesis and Two-step Synthesis Methods. *J. Phys. Chem. Sol.* 150, 109891. doi:10.1016/j.jpcs.2020.109891

Wang, S., Gao, H., Yu, H., Li, P., Li, Y., Chen, C., et al. (2020). Optical and Photoluminescence Properties of the MgAl2O4:M (M = Ti, Mn, Co, Ni) Phosphors: Calcination Behavior and Photoluminescence Mechanism. *Trans. Indian Ceram. Soc.* 79, 221–231. doi:10.1080/0371750X.2020.1817789

Wang, S., Tang, S., Gao, H., Chen, X., Liu, H., Yu, C., et al. (2021d). Microstructure, Optical, Photoluminescence Properties and the Intrinsic Mechanism of Photoluminescence and Photocatalysis for the BaTiO3, BaTiO3/TiO2 and BaTiO3/TiO2/CeO2 Smart Composites. *Opt. Mater.* 118, 111273. doi:10.1016/j.optmat.2021.111273

Wang, S., Tang, S., Gao, H., Fang, L., Hu, Q., Sun, G., et al. (2021e). Modified Polyacrylamide Gel Synthesis of CeO2 Nanoparticles by Using Cerium Sulfate as Metal Source and its Optical and Photoluminescence Properties. *J. Mater. Sci. Mater. Electron.* 32, 10820–10834. doi:10.1007/s10854-021-05740-w

Wang, Y., and Tian, H. (2020). Study on the Construction of YMnO3/CeO2 Composite Photocatalyst Heterostructure and Photocatalytic Degradation of Methyl Red. *Optik* 201, 163524. doi:10.1016/j.ijleo.2019.163524

Wen, X.-J., Niu, C.-G., Zhang, L., Liang, C., and Zeng, G.-M. (2018). A Novel Ag2O/CeO2 Heterojunction Photocatalysts for Photocatalytic Degradation of Enrofloxacin: Possible Degradation Pathways, Mineralization Activity and an

in Depth Mechanism Insight. *Appl. Catal. B: Environ.* 221, 701–714. doi:10.1016/j.apcatb.2017.09.060

Xing, S., Song, S., and Xiang, J. (2020). Study on Magnetic, Optical and Photocatalytic Activities of TbMnO3@CeO2 Composite Multiferroic Materials. *Optik* 220, 165144. doi:10.1016/j.ijleo.2020.165144

Conflict of Interest: The authors declare that the research was conducted in the absence of any commercial or financial relationships that could be construed as a potential conflict of interest.

Publisher's Note: All claims expressed in this article are solely those of the authors and do not necessarily represent those of their affiliated organizations, or those of the publisher, the editors and the reviewers. Any product that may be evaluated in this article, or claim that may be made by its manufacturer, is not guaranteed or endorsed by the publisher.

Copyright © 2021 Pu, Wang, Chen, Jin, Li and Chen. This is an open-access article distributed under the terms of the Creative Commons Attribution License (CC BY). The use, distribution or reproduction in other forums is permitted, provided the original author(s) and the copyright owner(s) are credited and that the original publication in this journal is cited, in accordance with accepted academic practice. No use, distribution or reproduction is permitted which does not comply with these terms.

frontiers in Materials

ORIGINAL RESEARCH
published: 16 November 2021
doi: 10.3389/fmats.2021.754479

Performance Simulation of a 5 kW hall Thruster

L. Yang, P. Y. Wang and T. Wang*

School of Electrical Engineering, Northwest University for Nationalities, Lanzhou, China

Hall thruster is a kind of plasma optics device, which is used mainly in space propulsion. To simulate the discharge process of plasma and the performance of a 5 kW hall thruster, a two-dimensional PIC-MCC model in the R-Z plane is built. In the model, the anomalous diffusion of the electrons including Bohm diffusion and near-wall conduction is modeled. The Bohm diffusion is modeled by using a Brownian motion instead of the Bohm collision method and the near-wall conduction is modeled by a secondary electron emission model. In addition to the elastic, excitation, and ionization collisions between electrons and neutral atoms, the Coulomb collisions are included. The plasma discharge process including the transient oscillation and steady state oscillation is well reproduced. First, the influence of the discharge voltage and magnetic field on the steady state oscillation is simulated. The oscillation amplitude increases as the discharge voltage gets larger at first, and then decreases. While the oscillation amplitude decreases as the magnetic field gets stronger at first, and then increases. Later, the influence of the discharge voltage and mass flow rate on the performance of the thruster is simulated. When the mass flow rate is constant, the total efficiency initially increases with the discharge voltage, reaches the maximum at 600 V, and then declined. When the discharge voltage is constant, the total efficiency increases as the mass flow rate rises from 10 to 15 mg/s. Finally, a comparison between simulated and experimental performance reveals that the largest deviation is within 15%, thereby indirectly validating the accuracy of the model.

Keywords: hall thruster, plasma optics device, particle-in-cell, performance simulation, plasma oscillation

OPEN ACCESS

Edited by:
Shifa Wang,
Chongqing Three Gorges University, China

Reviewed by:
Yanan Wang,
Xi'an Jiaotong University, China
Jianfei Long,
University of South China, China
Xianggeng Wei,
Northwestern Polytechnical University, China
Xinfeng Sun,
Lanzhou institute of physics (LIP), China

****Correspondence:***
L. Yang
yangle_23737@sina.com

Specialty section:
This article was submitted to Semiconducting Materials and Devices, a section of the journal Frontiers in Materials

Received: *06 August 2021*
Accepted: *22 September 2021*
Published: *16 November 2021*

Citation:
Yang L, Wang PY and Wang T (2021) Performance Simulation of a 5 kW hall Thruster. Front. Mater. 8:754479. doi: 10.3389/fmats.2021.754479

INTRODUCTION

Hall electric propulsion is one of the most mature and widely used electric propulsion technologies (Pidgeon, 2006; Mathers et al., 2009). LHT-140 (**Figure 1**) is a 5 kW hall thruster developed by the Lanzhou Institute of Physics. At present, the discharge characteristics of the plasma and the performance of a hall thruster are evaluated mainly by conducting high–cost and time–consuming experiments. As research on plasma discharge mechanism becomes in depth and numerical methods improve continuously, simulation plays an increasely important role in understanding the micro physical process of hall thruster (Arkhipov and Bishaev, 2007; Hofer, 2008; Zhang et al., 2011; Zhang et al., 2014). Lentz built a one-dimensional particle-in-cell (PIC) model (Lentz, 1993) and simulated the plasma characteristics and performance of a Japanese hall thruster. Noguchi, Martinez–Sanchez and Ahedo studied axial plasma discharge oscillation by using a one-dimensional PIC model (Noguchi et al., 1999). Hirakawa built a two-dimensional PIC model (Hirakawa and Arakawa, 1996) and simulated the electron diffusion. Later, Beidler (1999), Szabo (2001), Sullivan (2004) and Adam et al. (2004) improved the simulation method continuously.

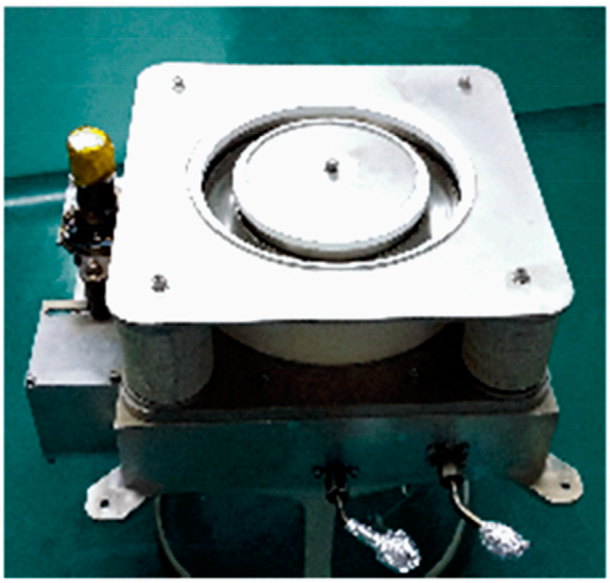

FIGURE 1 | LHT-140 hall thruster.

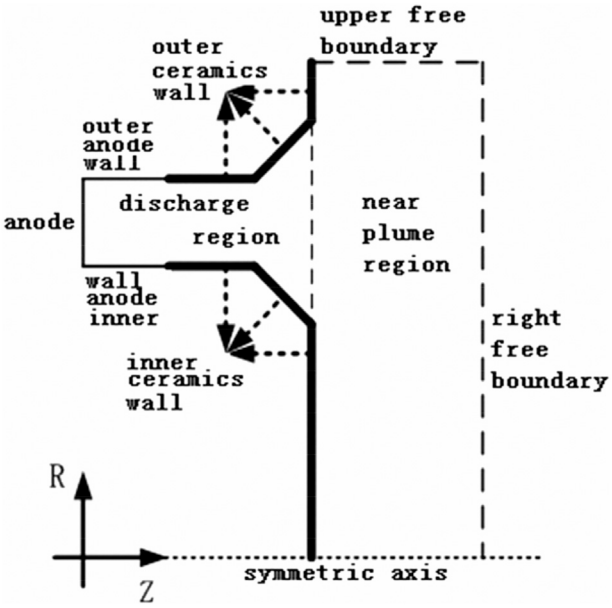

FIGURE 2 | Simulation region.

In most PIC models, Bohm collision was applied to simulate the anomalous diffusion of electrons (Koo and Boyd, 2006; Cho et al., 2013). The limitation is that not all the probable diffusion magnitudes can be simulated. In this paper, we applied the method of Vincent (2002) to simulate Bohm diffusion, to allow the simulation of any diffusion magnitude. In addition, in most present models, the Coulomb collisions between electrons and ions, as well as electrons and electrons, are excluded, we simulated the Coulomb collisions by using the method of Szabo (2001).

This paper aims to evaluate the performance and discharge characteristics of LHT-140 by using the built PIC model. First, the numerical methods applied in the building process of the model are introduced. Second, the plasma discharge characteristics and thruster performance are simulated. Finally, the simulated and experimental performance results are compared.

NUMERICAL METHODS

Simulation Region

The simulation region (**Figure 2**) consists of the discharge channel and the near plume region. The length and width of the near plume region is 1.5 and 4.5 times that of the discharge channel, respectively. The boundary of the discharge channel consists of a metal anode wall, ceramics wall, symmetric axis, and free space.

Model Simplification

Lightening ions using an artificial mass ratio and increasing the vacuum permittivity using artificial permittivity are conventional methods to simplify the particle-in-cell (PIC) model (Szabo, 2001). Speeding up the ions could shorten the time of convergence. In this study, we apply an artificial mass ratio of $f = M_{real}/M_{comp} = 1{,}000$, which indicates that the ions are 1,000 times lighter than they should be. Increasing the vacuum permittivity enables us to use a coarser grid. In this study, we increase the vacuum permittivity by 2,500 times. Consequently, the size of rectangular grid applied in our model could be magnified by 50 times (Szabo, 2001). The LHT-140 Hall thruster is similar to the 5 kW P5 Hall thruster (Vincent, 2002), and the Debye length of 0.02 mm in reference (Vincent, 2002) is used in our model. Finally, the mesh size becomes 1 mm after increasing the vacuum permittivity.

Potential and Electric Field Solving

The potential was acquired by solving the Poisson equation. The boundary conditions of the potential are as follows:

- At the anode surface, the potential is set to discharge voltage.
- At the symmetric axis, the normal electric field $E_\perp = 0$.
- At the free space boundary, the potential is set to 0 V.
- At the boron nitride ceramic wall surface, the boundary condition is (Vincent, 2002):

$$E_\perp^{plasma} - \varepsilon_{dieletric} E_\perp^{dielectric} = \frac{\sigma}{\varepsilon_0}. \tag{1}$$

For LHT-140 hall thruster, both in and outside the discharge channel, $\varepsilon_{dieletric} E_\perp^{dielectric}$ is negligible compared with $E_\perp^{plasma}$, similar to the situation for the P5 thruster (Vincent, 2002). Thus, $\varepsilon_{dieletric} E_\perp^{dielectric}$ could be neglected, and **Eq. 2** becomes:

$$E_\perp^{plasma} = \frac{\sigma}{\varepsilon_0}. \tag{2}$$

The electric field was solved by **Eqs 4**, **5** (Birdsall and Langdon, 1991):

$$E_{x_{j,k}} = \frac{1}{3}\left(\frac{1}{2}\frac{\phi_{k+1,j-1} - \phi_{k+1,j+1}}{2\Delta x} + \frac{\phi_{k,j-1} - \phi_{k,j+1}}{\Delta x} + \frac{1}{2}\frac{\phi_{k-1,j-1} - \phi_{k-1,j+1}}{2\Delta x} \right), \quad (3)$$

$$E_{y_{j,k}} = \frac{1}{3}\left(\frac{1}{2}\frac{\phi_{k-1,j-1} - \phi_{k+1,j-1}}{2\Delta x} + \frac{\phi_{k-1,j} - \phi_{k+1,j}}{\Delta x} + \frac{1}{2}\frac{\phi_{k-1,j+1} - \phi_{k+1,j+1}}{2\Delta x} \right), \quad (4)$$

where $E_{x_{j,k}}$ and $E_{y_{j,k}}$ are the electric field on the grid point (j, k) in the x and y directions, respectively, and $\phi_{k+1,j-1}$, $\phi_{k+1,j+1}$, $\phi_{k,j-1}$, $\phi_{k,j+1}$, $\phi_{k-1,j-1}$, $\phi_{k-1,j+1}$, $\phi_{k-1,j}$ and $\phi_{k+1,j}$ are the electric potential on the grid points around (k, j), and Δx is the width of the square grid.

Moving the Particles

Both neutrals and charged particles were modeled by PIC-MCC method. After the electric filed was determined, electrons and ions moved by the electric and magnetic fields were simulated using the leapfrog method (Birdsall and Langdon, 1991). The neutrals were not affected by the electric and magnetic fields, and there's no need to update their velocity during each time step if there's no collision. Because the density of neutrals is much larger than that of charged particles, a larger weight should be used for neutrals, which was 60 in our model.

Cathode Modeling

The cathode is modeled by injecting electrons from the upper free boundary with 0.1 eV of kinetic energy. The number of electrons injected in each time step is determined by current balance.

$$I_c = I_{cb} + I_{cd}. \quad (5)$$

Cathode current getting into the discharge region I_{cd}, ion current leaving from the free boundaryI_b^+, and electron current leaving from the free boundary I_{az} satisfy the following constraints:

$$I_{cd} = I_c - I_b^+ + I_{az}. \quad (6)$$

From **Eq. 7**, the number of electrons injected in each time step could be determined.

Anomalous Diffusion

The Bohm diffusion and near-wall conduction are the main factors that lead to the anomalous diffusion of electrons. Usually, a virtual collision called "Bohm collision" is introduced to simulate the Bohm diffusion. The Bohm collision frequency ν_β, is acquired by solving the following equation:

$$\frac{1}{16}\frac{kT_e}{eB} = \frac{kT_e}{m_e}\frac{1}{\omega_c}\frac{\beta}{1+\beta^2} \quad (7)$$

$\beta = \omega_c/(\nu_c + \nu_\beta)$ is the hall parameter that indicates the magnetization of electrons. Two limitations occur. Within one time step, the direction of electron velocity can be randomized only once, thus, $\nu_\beta < 1/\Delta t$. When $\beta = 1$, ν_β reaches the maximum in **Eq. 8**.

Thus, not all the probable diffusion magnitudes can be simulated. Vincent (2002) applied a Brownian motion to simulate the Bohm diffusion. After the electron was moved by the leapfrog algorithm, it was then moved in the two-dimensional plane perpendicular to the local magnetic field

$$\Delta X = \sqrt{-2\ln R_1}\sqrt{2D\Delta t}\cos R_2, \quad (8)$$

$$\Delta Y = \sqrt{-2\ln R_1}\sqrt{2D\Delta t}\sin R_2, \quad (9)$$

where D is the electron diffusion coefficient; Δt is the time step; and R_1 and R_2 are uniform random numbers between 0 and 1. Through this approach, any Bohm diffusion magnitude can be simulated.

Coulomb Collision

According to J. J. Szabo's method (Szabo, 2001), the Coulomb collision frequency can be calculated as follows:

$$\nu_{ei} = n_i Q_{ei}|v_e|, \quad (10)$$

$$\nu_{ee} = n_e Q_{ee}|v_e|. \quad (11)$$

The collision section can be calculated as follows:

$$Q_{ei} = \frac{6.5\times10^{-14}}{E_e^2}\ln\Lambda cm^2, \quad (12)$$

$$Q_{ee} = \frac{4.34\times10^{-14}}{T_e^2}\ln\Lambda cm^2, \quad (13)$$

where $\ln\Lambda$ is the Coulomb logarithm.

Near-Wall Conduction

A secondary electron emission model of Richard R. Hofer (Hofer et al., 2007) was applied to simulate the near-wall conduction of electrons.

$$\delta_w(T_e) = \Gamma[2+b]aT_e^b, \quad (14)$$

where Γ is the gamma function (a = 0.123, b = 0.528). The number of secondary electrons emitted from the ceramics wall after an electron collision is

$$N_s = \lceil\delta_w\rceil + \left\{R_f < \left(\delta_w - \lceil\delta_w\rceil\right)\right\}, \quad (15)$$

where $\lceil\delta_w\rceil$ means rounding δ_w down to an integer, and R_f is a random number between 0 and 1. If $R_f < \left(\delta_w - \lceil\delta_w\rceil\right)$, the primary electron is reflected back into the plasma, otherwise accumulates on the ceramics wall. The velocities of the secondary electrons after colliding against the wall are determined as follows:

$$v_1 = \beta_2 \times \sin\theta \times \beta_1, \quad (16)$$

$$v_2 = \beta_2 \times \cos\theta \times \beta_1, \quad (17)$$

$$v_3 = \beta_3 \times \beta_1, \quad (18)$$

where v_1 and v_2 are perpendicular to the direction of effusion and v_3 is in the direction of effusion.

$$\beta_1 = \sqrt{\frac{2kT_e}{M_e}}, \quad (19)$$

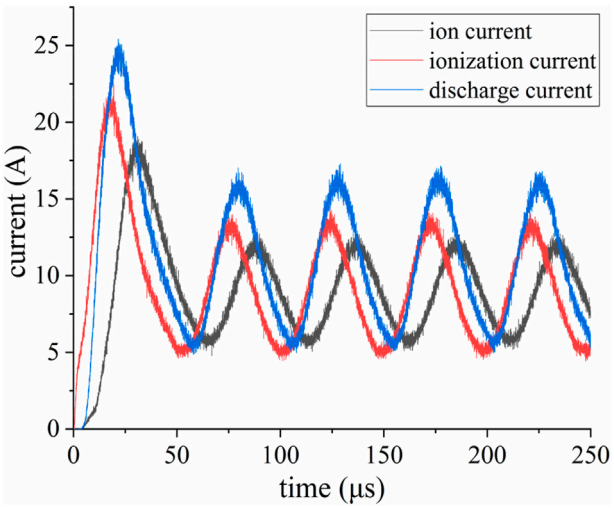

FIGURE 3 | Time history of current.

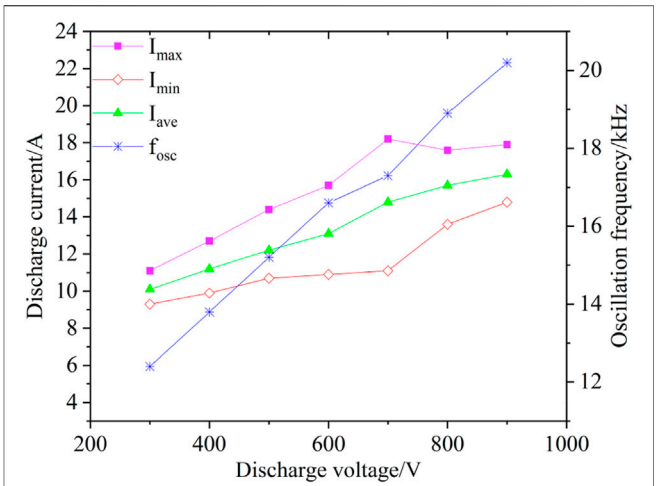

FIGURE 4 | Simulated oscillation amplitude and frequency of discharge currentwith different discharge voltages.

$$\beta_2 = \sqrt{-\log(R_1)}, \tag{20}$$

$$\beta_3 = \sqrt{-\log(R_2)}, \tag{21}$$

$$\theta = 2\pi R_3. \tag{22}$$

R_1, R_2, and R_3 are random numbers between 0 and 1.

Performance Model

The main performance of a hall thruster includes thrust, specific impulse and efficiency. The thrust is calculated by summing the product of mass flow rate and axial speed of ions that leave from the thruster exit.

$$T = \sum_{\alpha} T_i^{\alpha} = \sum_{\alpha} \dot{m}_i^{\alpha} v_i^{\alpha}, \tag{23}$$

αrepresents the charge state of ions, $\alpha = 1$ represents single-charged ions, and $\alpha = 2$ represents double-charged ions. The anode efficiency of the thruster is

$$\eta = T^2/2\dot{m}_a P_d, \tag{24}$$

where $P_d = V_d I_c$ is the discharge power, and $\dot{m}_a$ is the anode mass flow rate. The acceleration efficiency of ions is defined as the ratio of the ion current to the discharge current

$$\eta_\alpha = I_i/I_c. \tag{25}$$

The utilization efficiency of propellant is defined as the ratio of the mass flow rate of ions leaving the discharge channel to that of propellant atoms entering the discharge channel

$$\eta_u = \sum_{\alpha} \dot{m}_i^{\alpha}/\dot{m}_a. \tag{26}$$

The efficiency of electrical energy converted into kinetic energy of ions is defined as:

$$\eta_E = E_e/eV_d. \tag{27}$$

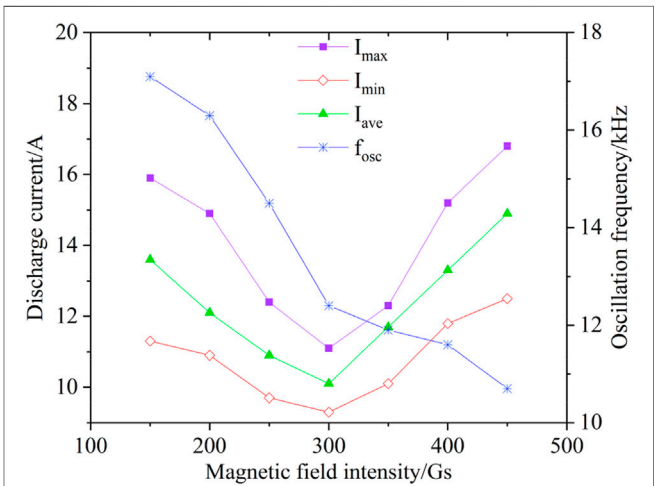

FIGURE 5 | Simulated oscillation amplitude and frequency of discharge current with different magnetic field intensities.

The relationship between the total efficiency and other efficiencies is

$$\eta = \eta_\alpha \eta_u \eta_E \gamma^2, \tag{28}$$

where γ is the thrust loss factor.

RESULTS AND DISCUSSION

Plasma Discharge

The plasma discharge process of LHT-140 when the discharge voltage is 300 V and the propellant mass flow rate is 10 mg/s is simulated. **Figure 3** shows the change of currents with time. The process consists of transient oscillation and steady-state periodic oscillation. During the transient oscillation, the discharge and ion

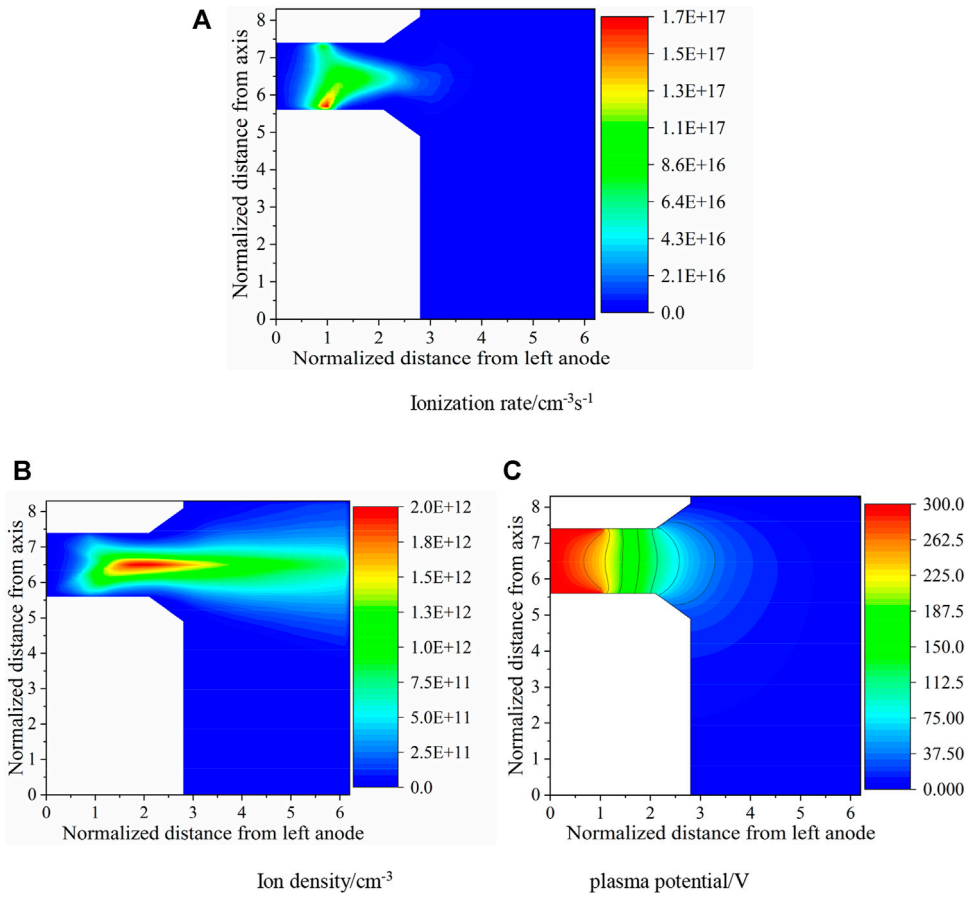

FIGURE 6 | Two-dimensional distributions of the plasma characteristics. **(A)** Ionization rate/cm^{-3}s^{-1}. **(B)** Ion density/cm^{-3} **(C)** plasma potential/V.

currents increase quickly, reaching a maximum, which is far larger than the steady-state value at approximately 15 μs. **Figure 3** shows that the transient maximum value of the discharge current is twice that in the steady state. After the transient reached the maximum value, the currents decreased and then oscillated periodically, which indicated the beginning of the so-called "breathing oscillation" (Fife et al., 1997; Boeuf and Garrigues, 1998).

Figure 4 presents the change of maximum value (I_{max}), minimum value (I_{min}), and average value (I_{ave}) of the discharge current and the oscillation frequency (f_{osc}) with discharge voltage. The discharge voltage significantly affected the oscillation. When the discharge voltage increased from 300 to 700 V, the oscillation amplitude (I_{max}–I_{min}) increased from 1.8 to 7.1 A. When the discharge voltage increased from 700 to 900 V, the oscillation amplitude decreases from 7.1 to 3.1 A. The oscillation frequency increased from 12 to 20 kHz.

Figure 5 displays the change of I_{max}, I_{min}, I_{ave}, and f_{osc} with magnetic field intensity. We can see that the magnetic field also exhibited a great influence on the oscillation. The oscillation amplitude decreased from 4.6 to 1.8 A when the magnetic field increased from 150 to 300 Gs and increased from 1.8 to 4.3 A when the magnetic field increased from 300 to 450 Gs. The oscillation frequency decreased from 17 to 10 kHz.

Figures 6A–C show the time-averaged two-dimensional distributions of the plasma potential, density, and ionization rate during 1,000 steps (almost 1/5 of the oscillation period), respectively. As shown in **Figure 6A**, the ionization region is located at one to two normalized distances from the anode. **Figure 6B** indicates that the largest plasma density is 2 × 10^{12}cm^{-3} and 0.6 normalized distance upstream of the thruster exit. **Figure 6C** illustrates that the potential drop occurs mainly in the ionization region, where the magnetic field is strong and the electron conductivity is low. The strength of the electric field must be high to compensate for the low electron conductivity, and to guarantee the continuity of the discharge current.

Thruster Performance

Performance experiments (**Figure 7**) with different discharge voltages and propellant mass flow rates of LHT-140 were conducted in a large vacuum chamber TS-7 with a diameter and a length of 3.8 and 8.5 m, respectively. The pumping speed of TS-7 can reach 1.8 × 10^5 L per second, providing a background pressure of around 2.0 × 10^{-3} Pa during testing. The discharge voltage ranged from 300 to 900 V, and the propellant mass flow

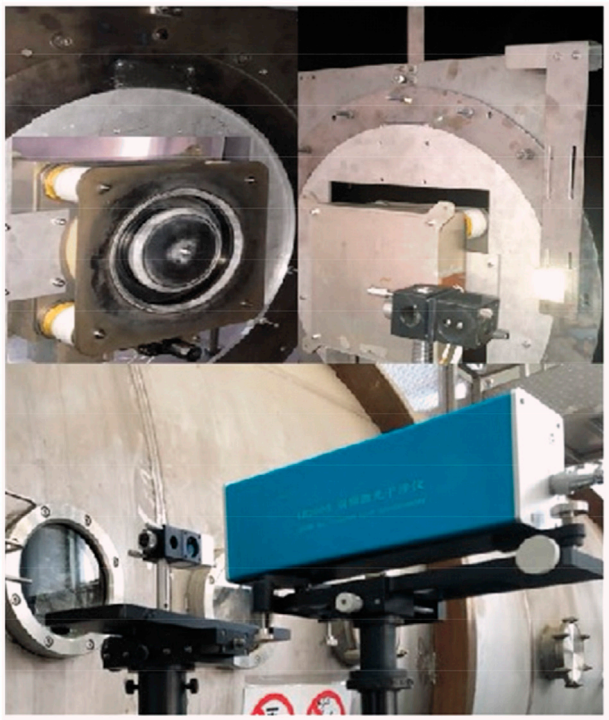

FIGURE 7 | Performance test of LHT-140.

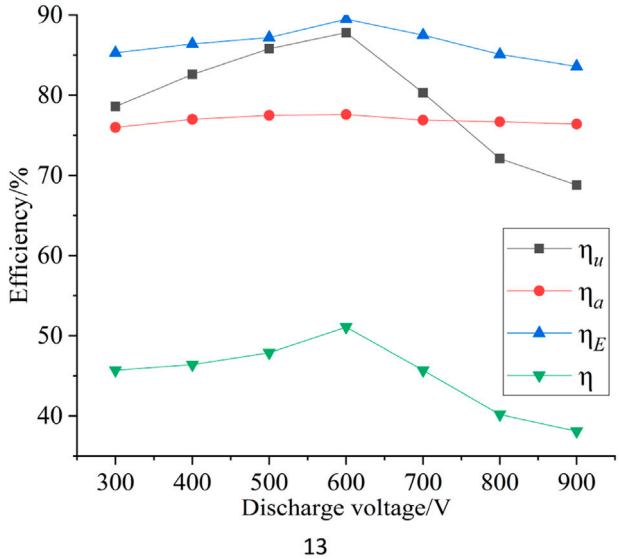

FIGURE 8 | Simulated results of efficiency for different discharge voltages.

rate which was regulated by a flowmeter ranged from 10 to 15 mg/s, while the magnetic field remained unchanged.

Thrust was measured by a laser interferometer (showed in **Figure 7**) through the relationship between thrust and displacement. Thrust measurements were conducted in intervals of about 40 min to minimize the thermal drift. Considering the thermal drift and repeatability, the average variation in thrust for a given point was estimated to be about ±2%. Given the uncertainty of the thrust, mass flow rate, current and voltage, the uncertainty for efficiency was about ±3.1%.

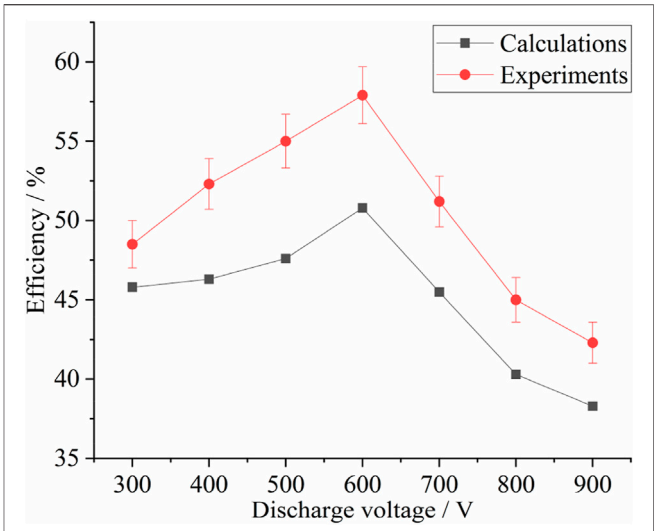

FIGURE 9 | Comparison of simulated and experimental results of total efficiency for different discharge voltages.

The simulated results of the total, acceleration, utilization, and energy conversion efficiencies are shown in **Figure 8** The total efficiency initially increased with the discharge voltage, reached the maximum at 600 V, and then declined. Blateau's simulation study (Vincent et al., 2001) showed that the magnetic field and discharge voltage require a reasonable match. After the discharge voltage increased to a certain value, the magnetic field must increase as well. However, **Figure 8** shows that the magnetic field remained unchanged. After the discharge voltage increased to 600 V, the magnetic field was not large enough to constrain the electrons, which indicated that the electrons were absorbed by the anode before the ionization collisions with the propellant atoms. Thus, the total efficiency declined after the discharge voltage increased to 600 V. The acceleration efficiency is insensitive to the change in discharge voltage, and remains at 77%. A similar relationship is found in experiments (Ashkenazy et al., 1998) for a hall thruster with a diameter of 70 mm. Moreover, with the increasing discharge voltage, the ionization of propellant atoms becomes increasingly adequate, thereby increasing the utilization efficiency. Once the magnetic field is no longer large enough to constrain the electrons, the utilization efficiency starts to decline.

Figure 9 shows a comparison of the experimental and simulated results of total efficiency when the discharge voltage ranged from 300 to 900 V and the propellant mass flow rate was 10 mg/s. The tested maximum value is 58%, and

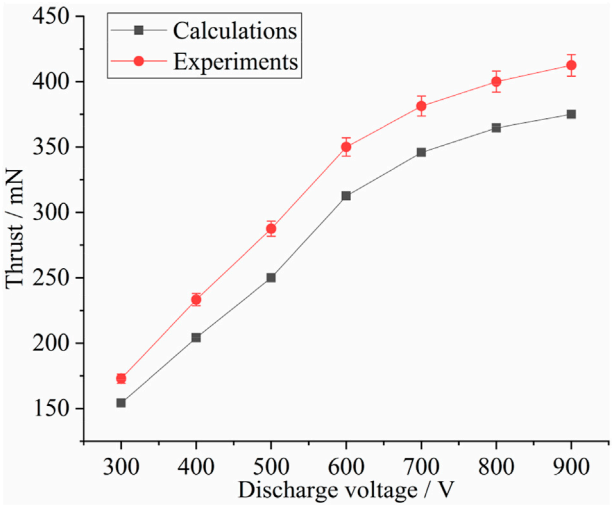

FIGURE 10 | Comparison of simulated and experimental results of thrus for different discharge voltages.

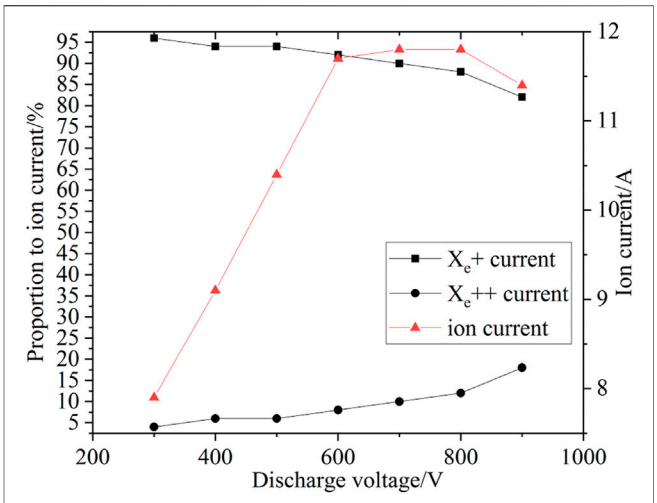

FIGURE 12 | Proportion of x_e+ and x_e++ current to the total ion current for various discharge voltages.

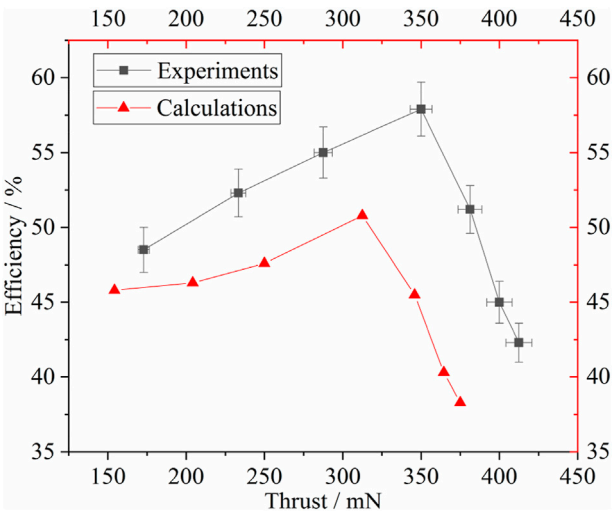

FIGURE 11 | Relationship between efficiency and thrust.

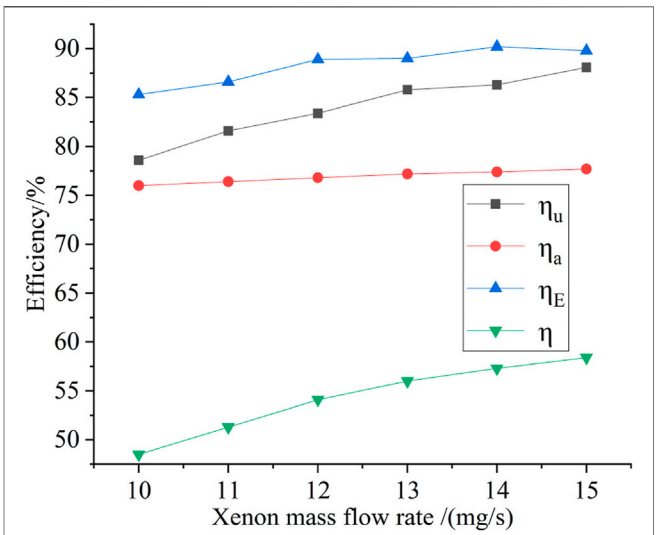

FIGURE 13 | Simulated results of efficiency for different mass flow rate.

the simulated maximum value is 51%. When the discharge voltage increased from 300 to 600 V, ηincreased with η_u. When the discharge voltage increased from 600 to 900 V, η decreased with η_u. The simulated results are smaller than the experimental results by 9–13% because the influence of background pressure in the vacuum chamber is not included.

Figure 10 shows a comparison of the experimental and simulated results of thrust when the discharge voltage ranged from 300 to 900 V and the propellant mass flow rate was 10 mg/s. As in the previous analysis, when the discharge voltage increased from 300 to 600 V, the ionization became increasingly adequate, the amount of produced ions increased, and the speed of the ejected ions became increasingly fast. Thus, the thrust increased with the discharge voltage. When the discharge voltage increased from 600 to 900 V, the ionization efficiency decreased dramatically and the number of produced ions decreased, but the speed of the ejected ions still increased. Thus, the thrust still increased with a slower speed. The simulated results are smaller than the experimental results by 8–14%. As mentioned earlier, the influence of background pressure in the vacuum chamber is not included.

Figure 11 shows the relationship between thrust and efficiency. The maximum simulated efficiency is 51.1%, and the corresponding thrust is 315 mN. The maximum experimental efficiency is 58%, and the corresponding thrust is 350 mN. The trend demonstrated that efficiency increased as

thrust increased initially and then decreased as thrust increased continuously.

Only single-charged ions Xe^{+} and double-charged ions Xe^{++} are included. **Figure 12** shows the ratio of Xe^{+} current and Xe^{++} current to the total ion current when the discharge voltage ranged from 300 to 900 V and the mass flow rate is 10 mg/s. The ratio of Xe^{+} current decreased from 96 to 82%, while the ratio of Xe^{++} current increased from 4 to 18%. In accordance with the variance of propellant utilization efficiency or ionization efficiency, the ion current increased when the discharge voltage increased from 300 to 600 V and then decreased when the discharge voltage increased from 600 to 900 V. The trend of beam current, Xe^{+} and Xe^{++} fractions were similar to that in reference (Vincent et al., 2001; Vincent, 2002), in which, the Xe^{++} fraction increased from 20.2 to 30.3% when the discharge voltage ranged from 300 to 1200 V, and the beam current increased at first, then started to decrease.

The frequency of ionization collisions increased with the increase in the propellant mass flow rate. Consequently, the utilization or ionization efficiency increased as well, as shown in **Figure 13**.

CONCLUSION

The discharge process of the plasma, including transient and steady-state oscillations, is well reproduced. During transient oscillation, the discharge current increases rapidly to a value that is far larger than the steady-state value. These characteristics must be considered when designing the power processing unit. During steady-state oscillation, the discharge amplitude increased first and then decreased as the discharge voltage increased, while it decreased first and then increased as the magnetic field became stronger. The performance of LHT-140 was well predicted by the built model with a deviation of less than 15% compared with the experimental results, while the deviation was mainly caused by the background pressure of the vacuum chamber. Both discharge voltage and propellant mass flow rate have a great influence on the performance of the thruster. The trend of the total efficiency was consistent with either the propellant utilization efficiency or the ionization efficiency. As the discharge voltage increased, the thrust became larger and the specific impulse became higher, but the efficiency of the thruster decreased. The research results of this paper is helpful to determine a reasonable range of discharge voltage. This paper is helpful for the optimization of the performance and selection of ideal operating points for the LHT-140 hall thruster.

DATA AVAILABILITY STATEMENT

The original contributions presented in the study are included in the article/Supplementary Material, further inquiries can be directed to the corresponding author.

AUTHOR CONTRIBUTIONS

PW and TW help to design and do the experiment.

REFERENCES

Adam, J. C., Héron, A., and Laval, G. (2004). Study of Stationary Plasma Thrusters Using Two-Dimensional Fully Kinetic Simulations. *Phys. Plasmas* 11, 295–305. doi:10.1063/1.1632904

Arkhipov, A. S., and Bishaev, A. M. (2007). Three-dimensional Numerical Simulation of the Plasma Plume from a Stationary Plasma Thruster. *Comput. Math. Math. Phys.* 47, 472–486. doi:10.1134/s0965542507030116

Ashkenazy, J., Raitses, Y., and Appelbaum, G. (1998). Parametric Studies of the Hall Current Plasma Thruster. *Phys. Plasmas* 5, 2055–2063. doi:10.1063/1.872877

Beidler, P. (1999). *Master's Thesis* (Cambridge: Massachusetts Institute of Technology).

Birdsall, C. K., and Langdon, A. B. (1991). *Plasma Physics via Computer Simulation*. Philadelphia: Institute of Physics Publishing.

Boeuf, J. P., and Garrigues, L. (1998). Low Frequency Oscillations in a Stationary Plasma Thruster. *J. Appl. Phys.* 84, 3541–3554. doi:10.1063/1.368529

Cho, S., Komurasaki, K., and Arakawa, Y. (2013). Kinetic Particle Simulation of Discharge and wall Erosion of a Hall Thruster. *Phys. Plasmas* 20, 063501. doi:10.1063/1.4810798

Hirakawa, M., and Arakawa, Y. (1996), "Numerical Simulation of Plasma Particle Behavior in a Hall Thruster," AIAA Paper No. 1996-3195. doi:10.2514/6.1996-3195

Fife, J., Martinez-Sanchez, M., and Szabo, J. (1997), "A Numerical Study of Low-Frequency Discharge Oscillation in Hall Thrusters," AIAA Paper No. 1997-3051, In 33rd Joint Propulsion Conference and Exhibit. doi:10.2514/6.1997-3052

Koo, J. W., and Boyd, I. D. (2006). Modeling of Anomalous Electron Mobility in Hall Thrusters. *Phys. Plasmas* 13, 033501. doi:10.1063/1.2172191

Lentz, C. A. (1993). *Master's Thesis* (Cambridge: Massachusetts Institute of Technology).

Mathers, Alex., de Grys, Kristi., and Paisley, Jonathan. (2009). Performance Variation in BPT-4000 Hall Thrusters. *IEPC* 09-144.

Noguchi, R., Martinez-Sanchez, M., and Ahedo, E. (1999). Linear 1-D Analysis of Oscillations in Hall Thrusters. *IEPC* 99-105.

Pidgeon, D. J. (2006), "Two Years On-Orbit Performance of the SPT-100 Electric Propulsion," AIAA Paper No. 2006-5353. doi:10.2514/6.2006-5353

Hofer, R. R., "Efficacy of Electron Mobility Models in Hybrid-PIC Hall Thruster Simulations," AIAA Paper No. 2008-4924, 2008. doi:10.2514/6.2008-4924

Hofer, R. R., Mikellides, I. G., Katz, Ira., and Goebel, D., "Wall Sheath and Electron Mobility Modeling in Hybrid-PIC Hall Thruster Simulations," AIAA Paper No. 2007-5267, 2007. doi:10.2514/6.2007-5267

Sullivan, Kay. Ueda. (2004). *PhD Thesis* (Cambridge: Massachusetts Institute of Technology).

Szabo, J. J. (2001). *PhD Thesis* (Cambridge: Massachusetts Institute of Technology).

Vincent, Blateau., Martinez-Sanchez, Manuel., Batishchev, Oleg., and Szabo, James. (2001). PIC Simulation of High Specific Impulse Hall Thruster. *IEPC* 01-037.

Vincent, Blateau. (2002). *Master's Thesis* (Cambridge: Massachusetts Institute of Technology).

Zhang, F., Ding, Y., Li, H., Wu, X., and Yu, D. (2011). Effect of Anisotropy of Electron Velocity Distribution Function on Dynamic Characteristics of Sheath in Hall Thrusters. *Phys. Plasmas* 18, 103512. doi:10.1063/1.3654052

Zhang, F., Kong, L., Li, C., Yang, H., and Li, W. (2014). Sheath Oscillation Characteristics and Effect on Near-wall Conduction in a Krypton Hall Thruster. *Phys. Plasmas* 21, 113501. doi:10.1063/1.4900764

Conflict of Interest: The authors declare that the research was conducted in the absence of any commercial or financial relationships that could be construed as a potential conflict of interest.

Publisher's Note: All claims expressed in this article are solely those of the authors and do not necessarily represent those of their affiliated organizations, or those of the publisher, the editors and the reviewers. Any product that may be evaluated in this article, or claim that may be made by its manufacturer, is not guaranteed or endorsed by the publisher.

Copyright © 2021 Yang, Wang and Wang. This is an open-access article distributed under the terms of the Creative Commons Attribution License (CC BY). The use, distribution or reproduction in other forums is permitted, provided the original author(s) and the copyright owner(s) are credited and that the original publication in this journal is cited, in accordance with accepted academic practice. No use, distribution or reproduction is permitted which does not comply with these terms.

NOMENCLATURE

ϕ electric potential

ρ volume charge density

ε_0 vacuum permittivity

$E_{\perp}^{plasma}$ normal electric field in the plasma

$E_{\perp}^{dielectric}$ normal electric field in boron nitride

$\varepsilon_{dielectric}$ dielectric constant of boron nitride

σ surface charge density

E electric field

Δx size of the square grids

I_c cathode current

I_{cb} cathode current getting into the plume

I_{cd} cathode current getting into the channel

I_b^+ ion current

I_{az} electron current leaving from free boundary

e electron charge

B magnetic field

k Boltzmann constant

T_e electron temperature

ω_c cyclotron frequency

ν_β Bohm collision frequency

ν_c electron collision frequency

Δt time step

v_e electron velocity

n_e electron density

n_i ion density

E_e electron kinetic energy

$\dot{m}_a$ anode mass flow rate

V_d discharge voltage

$\dot{m}_i$ ion mass flow rate

v_i ion velocity

M_{real} real mass of Xe

M_{comp} computational mass of Xe

frontiers in Materials

ORIGINAL RESEARCH
published: 18 January 2022
doi: 10.3389/fmats.2021.821431

Design and Photoelectric Performance of Perfect Solar Absorber Based on GaAs Grating

Bin Liu[1,2], Pinghui Wu[3], Yan Li[4], Hongyang Zhu[4] and Li Lv[4]**

[1]Rural Revitalization Institute, Linyi University, Linyi, China, [2]Center for International Education, Philippine Christian University, Manila, Philippines, [3]Fujian Provincial Key Laboratory for Advanced Micro-Nano Photonics Technology and Devices, Quanzhou Normal University, Quanzhou, China, [4]School of Physics and Electronic Engineering, Linyi University, Linyi, China

In recent years, solar energy has received extensive attention as a clean and renewable energy. We present a perfect broadband solar absorber based on tungsten and semiconductor GaAs in this paper. The structure of GaAs grating-GaAs film-W substrate has been proposed. And the finite time domain difference method (FDTD) has been used for the numerical simulation of the model. Broadband absorption has been realized in the 500–1,850 nm, by adjusting the parameters of geometry to excite high-efficiency surface plasmon resonance. The absorption spectrum of the structure can be changed by adjusting the geometric parameters to meet different needs. The proposed absorber has incidence insensitive (0–60°) and high short-circuit current characteristics. The structure is simple and easy to manufacture, and has superior photoelectric properties to be application in photothermal conversion, collection and utilization of solar energy.

Keywords: solar energy absorber, ultra-broadband perfect absorption, GaAs grating, photoelectric performance, surface plasmon resonance

OPEN ACCESS

Edited by:
Hua Yang,
Lanzhou University of Technology, China

Reviewed by:
Chao Liu,
Northeast Petroleum University, China
Jing Chen,
Nanjing University of Posts and Telecommunications, China
Yougen Yi,
Central South University, China

****Correspondence:***
Hongyang Zhu
zhuhongyang@lyu.edu.cn
Li Lv
lb_lyu@163.com

Specialty section:
This article was submitted to Semiconducting Materials and Devices, a section of the journal Frontiers in Materials

Received: *24 November 2021*
Accepted: *06 December 2021*
Published: *18 January 2022*

Citation:
Liu B, Wu P, Li Y, Zhu H and Lv L (2022) Design and Photoelectric Performance of Perfect Solar Absorber Based on GaAs Grating. Front. Mater. 8:821431. doi: 10.3389/fmats.2021.821431

INTRODUCTION

Solar energy is inexhaustible, reliable and less polluting, which is why it is considered the most potential energy (Zhao et al., 2020). As a green energy, solar energy is widely used in many fields (Xiong et al., 2013; Yang et al., 2014; Zhang et al., 2014; Li et al., 2016; Xiao et al., 2017; Li et al., 2018; Tang et al., 2018; Chen P. et al., 2019; Cheng et al., 2022). These advantages have always made how to collect and use solar energy a hot and important issue. The actual solar radiation in the range of about 295–2,500 nm, the design can be perfectly matched to the wavelength band of the solar device is a key to efficient use of solar energy.

In recent years, solar absorbers have attracted more and more attention as an important energy collect device (Kimpton et al., 2020; Yi et al., 2020; Yu et al., 2020; Li et al., 2021a; Zhou et al., 2021). For an ideal absorber must have a high efficiency of light absorption and many other physical properties, such as polarization stability and adjustability etc. (Jiang et al., 2021a; Li et al., 2021b; Li R. et al., 2021c; Li-Ying et al., 2021; Wu et al., 2021). However, the existing absorbers are generally limited by low temperature tolerance, low light absorption efficiency and materials (Briggs et al., 2010; Li et al., 2020a; Chen et al., 2021a; Chen et al., 2021b; Jiang et al., 2021b). Therefore, a new broadband solar absorber needs to be proposed to solve these problems.

Broadband absorber is an old concept that was proposed many years ago. Over the years, it has been widely used in the fields of solar heating devices, solar cells and photothermal converters (Sobhani et al., 2013; Xiao et al., 2019; Li et al., 2020b; Wang et al., 2021; Zhao et al., 2021). The improvement of broadband absorbers has three main directions. Firstly, it is important to find the

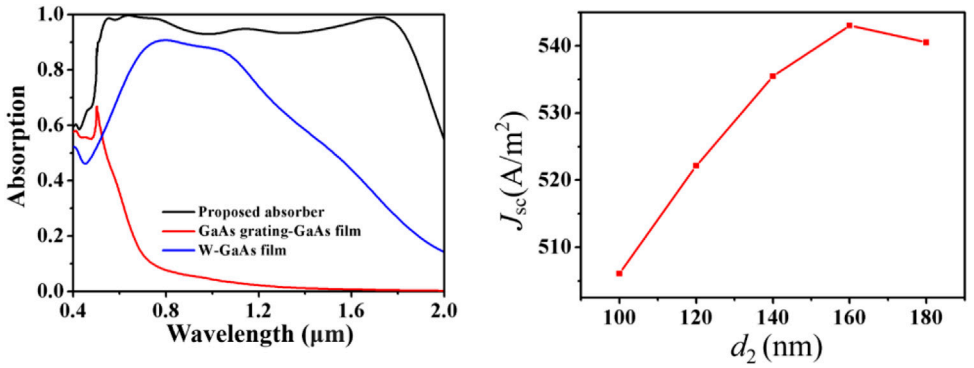

GRAPHICAL ABSTRACT | A perfect broadband solar absorber based on tungsten and grating-GaAs was proposed. Broadband absorption has been realized in the 500–1,850 nm. The proposed absorber has incidence insensitive (0–60°). The proposed absorber has high short-circuit current characteristics.

most suitable material. Because of the obvious shortcomings of traditional metal materials such as gold and silver, such as high cost and poor heat resistance, people began to pay attention to materials with high melting points such as TiN, tungsten and other, which are different from the original broadband absorber. They not only have a high melting point, but also can be used as effective plasmon excitation materials. Secondly, the nanostructure design of the broadband absorber is also very critical. The multi-layer-metal-insulator (MMI) structure is first used, and then turned to a simpler MIM or IMI nanostructures. Finally, the working range of the broadband absorber was investigated and continuously improved, especially in the ultraviolet to near infrared range. In order to obtain an ideal broadband absorber in practical applications, it is necessary that the proposed absorber can fulfill the requirements mentioned above. For example, Lei et al. (2016) modulated the duty cycle of metal gratings. They simulated the optical characteristics of metal-insulator-metal grating nanostructures and obtained four absorption regions with absorption near 100%. Qin et al. (2020) proposed a solar absorber based on TiN and Ti. The simulation results demonstrate that broadband absorption can be achieved. Jiang et al. proposed a broadband solar absorber based on hyperbolic multilayer metamaterial (HMM) is obtained in greater than 90% absorption from 300 to 2,215 nm (Khavasi, 2015). Although the characteristics of these absorbers are sufficiently superior, their complex nanostructures and various preparations of complex materials make the proposed absorbers imperfect, and it is difficult to apply them in subsequent practical manufacturing. Accordingly, an absorber with structure simpler but also excellent high absorption is presented urgently.

Over here, we proposed a GaAs grating solar absorber which obtain bandwidth with absorption over 90% reaches 1,350 nm. The overall structure only uses two kinds of materials: metal W and semiconductor GaAs, the melting points of them are high and their thermal stabilities are great. Compared with traditional noble metals, W has higher metal loss and is easier to achieve broadband absorption. And the semiconductor GaAs has a stronger excitation effect on the structure due to its higher dielectric constant, and can also achieve broadband absorption. The proposed structure can achieve wide broadband absorption, changing the absorption spectrum by adjusting structure parameters with a certain tunability is feasible. The model was also simulated with the solar spectrum conditions in the actual environment to investigate the effect in the actual solar radiation environment.

STRUCTURAL DESIGN OF BROADBAND PERFECT SOLAR ENERGY ABSORBER

First, the broadband absorber structure based on metal W and semiconductor GaAs has been proposed. **Figure 1** shows this structure. W has been selected as the substrate. There is a thin layer of GaAs film on the W film, and the top layer is a GaAs grating arranged periodically. The period of the grating is represented by P, and the width is t. d_1 and d_2 are the thicknesses of the GaAs film and the top grating, respectively. In order to ensure that the transmittance is almost zero, the thickness of W metal substrate needs to be much greater than the skin depth of light. The overall structure is very simple and clear, and can be manufactured using traditional magnetron sputtering and photolithography processes. The optimal parameters of the structure: P = 500 nm, t = 240 nm, d_1 = 30 nm, d_2 = 120 nm. The parameters of W and GaAs are both from the database of FDTD solutions (Cao et al., 2014; Deng et al., 2015; Deng et al., 2018).

Our simulations and calculations use the finite-difference time-domain (FDTD)methods. The software used is FDTD solutions of Lumerical Company. Compared with other commercial simulation software, its calculation time is shorter and the accuracy is higher, which is very suitable for the simulation of nanostructure. In the actual simulation parameter setting, the incident light source is vertically incident from above the structure and adopts TM polarized plane wave. The boundary conditions are set by using periodic boundary conditions in the x-direction and perfect matched layer to cut off the boundary in the z direction. The division precision of the grid is 10 nm × 10 nm × 5 nm. The material parameters of metal W and semiconductor GaAs are used in the material library of the FDTD solutions software. The global absorption of the structure can be calculated with the formula $A = 1\text{-}T\text{-}R$, where the

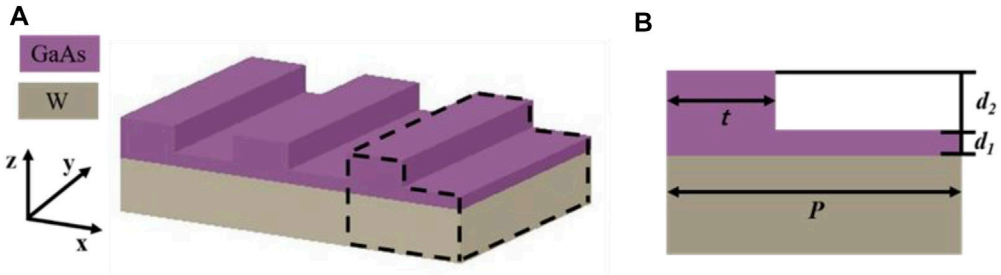

FIGURE 1 | (A) Schematic of metal W-semiconductor GaAs structure of broadband absorber. **(B)** Cross-sectional view.

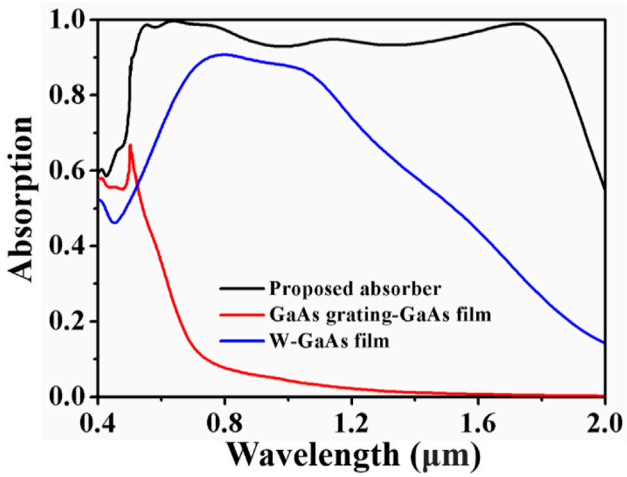

FIGURE 2 | Absorption of broadband absorber in several different configurations.

absorption is A, T and R represent the transmission and reflection, respectively (Long et al., 2016; Liu et al., 2017; Cai et al., 2019; Liu et al., 2021).

RESULTS AND DISCUSSION

Figure 2 presents the simulation results of the structure. Obviously, the absorption effect of the proposed absorber is excellent, the absorption is higher than 90% at 500–1,850 nm. In order to reflect the rationality of the designed structure, we also calculated the other two similar configurations as a comparison. The absorption when there is no top grating and there is only a layer of W substrate and GaAs film is indicated by the blue line, and the red line represents the absorption when there is no W substrate and only GaAs film and grating. Clearly, when there is no top layer of GaAs grating, the structure only got a higher absorption at the wavelength from 700 to 1,100 nm, but there is almost no part higher than 90%, and the absorption at the wavelength after 1,100 nm drops rapidly; In the case of a non-metal W substrate, as shown by the red line, there is an absorption of about 60% only at the beginning of the curve, and thereafter it continues to decrease until it approaches zero. Through the comparison of the two, we can fully realize that the light reflection effect of the metal substrate and the LSPR mode excited by the top semiconductor grating have a huge effect on the improvement of the overall absorber, and the loss of any part of the component will lead to the collapse of the overall structure (Lv et al., 2018; Huang et al., 2021; Xu et al., 2021).

There are many choices of metal and semiconductor materials. As a comparison, we listed the absorption of several other very common metal materials and semiconductors, as shown in **Figure 3**. **Figure 3A** presents the effect of choosing different metals when GaAs is used as the top layer material. In order to make a comprehensive comparison, we not only chose to use traditional noble metals such as gold and silver, but also selected Ti and V, which are the same refractory metals as W. It is very clear that the high absorption part of traditional noble metals is concentrated in the short wavelength region and the bandwidth is very narrow, and the absorption in the whole band is very unsatisfactory. This result is mainly caused by the small metal loss of noble metals (Cai et al., 2014). **Figure 3B** is the absorption spectrum of several different semiconductor materials when metal W is used as the bottom layer. It shows that GaAs is the best choice because of the widest absorption bandwidth and the best absorption. This is mainly because GaAs has a higher dielectric constant and the electromagnetic field has a strong excitation effect on the structure, so it has a good absorption effect.

Further, we have investigated the influences of several main geometric parameters on the overall absorption effect one by one, which explains the reasons for the selection of geometric parameters of the proposed absorber, and we also simulated the tuning according to the needs of the actual use. First, we studied the influence of the total structure period P on absorption, as shown in **Figure 4A**. We calculated in the range of 400–600 nm with 50 nm steps. It is clear that with the increase of the period, in the main absorption band (>90% part), the overall absorption of the structure continues to increase, and the bandwidth does not change significantly. However, this increase is not unlimited. At P = 550 nm, the total absorption begins to decrease. This is because the excessively large period greatly increases the intensity of the surface plasmon resonance (Chen et al., 2019a; Chen et al., 2019b; Chen et al., 2018), which narrows the absorption bandwidth slightly and decreases the absorption. Therefore,

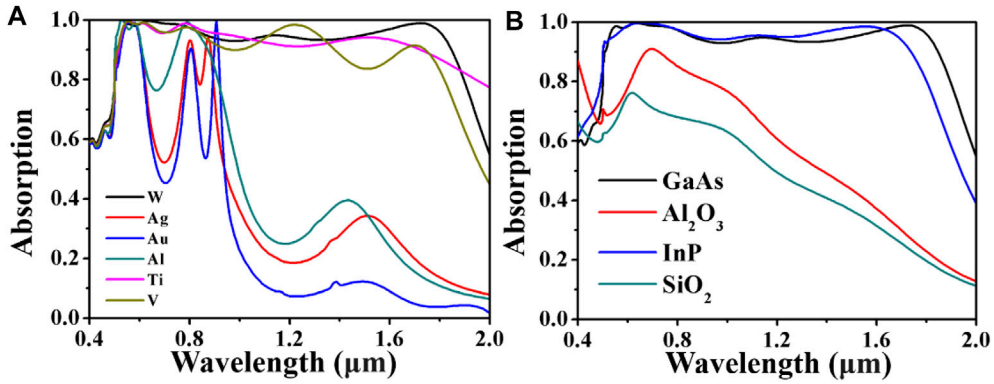

FIGURE 3 | (A) Absorbance spectrum of different metal materials. **(B)** Absorbance spectrum of different semiconductor materials.

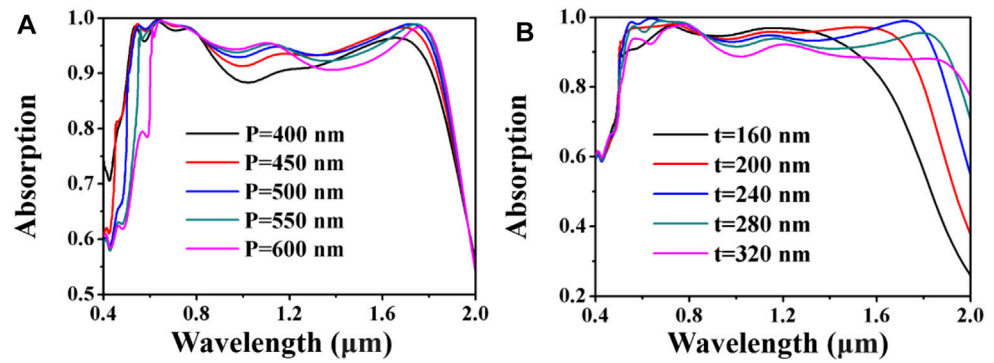

FIGURE 4 | (A) Absorption spectrum under different periods. **(B)** Absorption spectrum under different grating widths.

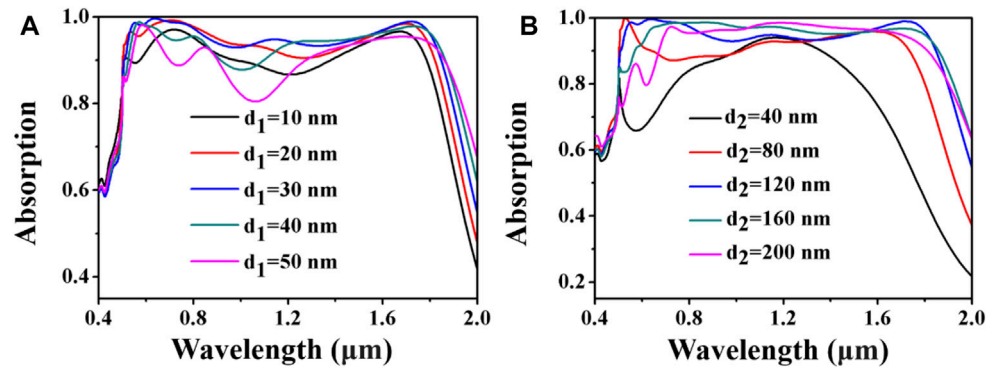

FIGURE 5 | (A) Absorption spectrum with different semiconductor layer thicknesses. **(B)** Absorption spectrum with different grating layer thicknesses.

after comprehensive consideration, we selected P = 500 nm, which is an ideal parameter. Subsequently, we simulated the influence of the width t of the grating on the absorption of the structure, and the result is presented in **Figure 4B**. Obviously, its main influence on the spectrum is reflected in the long wavelength range. When the width of the grating becomes wider, the global absorption bandwidth becomes obviously wider, but the change of the absorption rate is not same, it is a trend of first increasing and then decreasing. After exhaustive consideration, we finally select the middle parameter as the optimal value, so that a wider absorption bandwidth can be obtained without making the overall absorption too low.

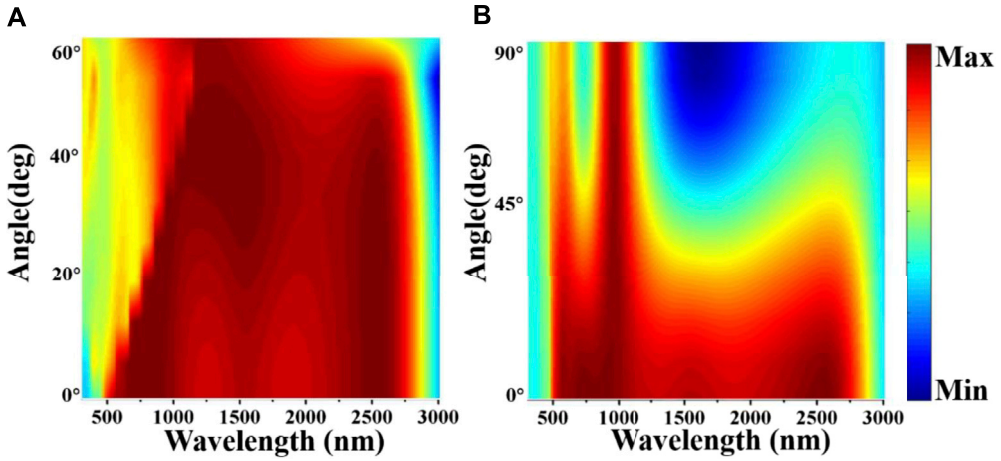

FIGURE 6 | (A) Absorption at different incident angles. **(B)** Absorption at different polarization angles.

After having investigated the influences of period and grating width on the whole absorption of the proposed absorber, we also studied the influence of grating layer and semiconductor layer thickness parameters on absorption, as results shown in **Figure 5**. First, we have changed the thickness of the semiconductor layer from 10 to 50 nm, and 10 nm as the step. We can see that the total absorption first rises from 10 nm, and reaches a maximum at 30 nm, then decreases as the height increases. The whole bandwidth is slightly widened as the height increases. 30 nm is selected as the optimal parameter on balance, so as not to make the bandwidth too narrow, but also to obtain the highest absorbance. Next, we also studied the influence of the different top grating layer thickness on absorption, and the results are presented in **Figure 5B**. The absorption of the structure is very low and the bandwidth is narrow when d_2 = 40 nm; when it is increased to 80 nm, there is a big improvement. By comparison, we selected the optimal parameters 120 nm. In conclusion, whether it is the period of the structure, the width of the grating or the thickness of the semiconductor GaAs layer, the change of these parameters directly affects the surface plasmon resonance characteristics of the entire structure, or make it strengthen, or make it weaken, which in turn leads to a corresponding change in the absorption of the proposed absorber and the bandwidth of the spectrum (Chen et al., 2013; Liu et al., 2020; An et al., 2021; Cheng T. et al., 2021). The width of the top grating will not only affect the surface plasmon resonance, but also the change of its geometric parameters will have a certain effect on the cavity film of the structure, which will not be described in detail here.

As a solar absorber will be applied in the actual environment, it can be expected that the light in nature cannot be incident perpendicularly as in the ideal case (Cheng et al., 2015). Therefore, we must take these factors into consideration when simulating. In fact, the absorption under oblique incidence and different polarization angles are also two important parameters for examining the structural design of the solar absorber. **Figure 6A** is the absorption spectrum when the incidence angle changes from 0 to 60°, and **Figure 6B** is the absorption spectrum when the polarization angle changes from 0 to 90°. It is obviously from **Figure 6A** that the total absorption effect of the proposed absorber is good at the long wavelength range. The absorption starts to decrease significantly as the incident angle is close to 60°. However, the result is not very ideal in the short wavelength range. When the incident angle begins to increase, not only the absorption decreases, but the high-efficiency absorption bandwidth also becomes narrow. As for the situation when the polarization angle is changed as shown in **Figure 6B**, when the rotation angle exceeds about 30°, the absorption and bandwidth of the structure will decrease significantly. This is because the structure is not completely symmetrical, and when switching to the TE polarization mode, the surface plasmon resonance cannot be excited. The simulation results are consistent with the theoretical explanation.

The proposed absorber is mainly used for solar energy collection. Therefore, its absorption characteristics in actual solar radiation are very important. We simulated carefully to test the performance in actual situation of the proposed absorber. The solar energy absorption efficiency equation with AM 1.5 is:

$$\eta_A = \frac{\int_{\lambda_{min}}^{\lambda_{max}} (1 - R(\omega)) \cdot I_{AM1.5}(\omega) \cdot d\omega}{\int_{\lambda_{min}}^{\lambda_{max}} I_{AM1.5}(\omega) \cdot d\omega} \quad (1)$$

Where η_A is the absorption efficiency, $R(\omega)$ is the reflection of the structure, ω is the frequency of the incident source, and $I_{AM\,1.5}$ is solar radiation (Long et al., 2015; Zhang et al., 2015; Fu et al., 2021; Su et al., 2021). The results are presented in **Figure 7**.

In the **Figure 7A**, black line is the solar spectrum at AM 1.5, red line is the absorption spectrum for the proposed absorber under solar radiation. It is very clear that the red line is much lower than the black line at the wavelength of 400–750 nm, which means the absorption of light in this range is relatively low. Also, the red line does not match the black line at the wavelength of 1,500–2,500 nm, which represents the low energy absorption

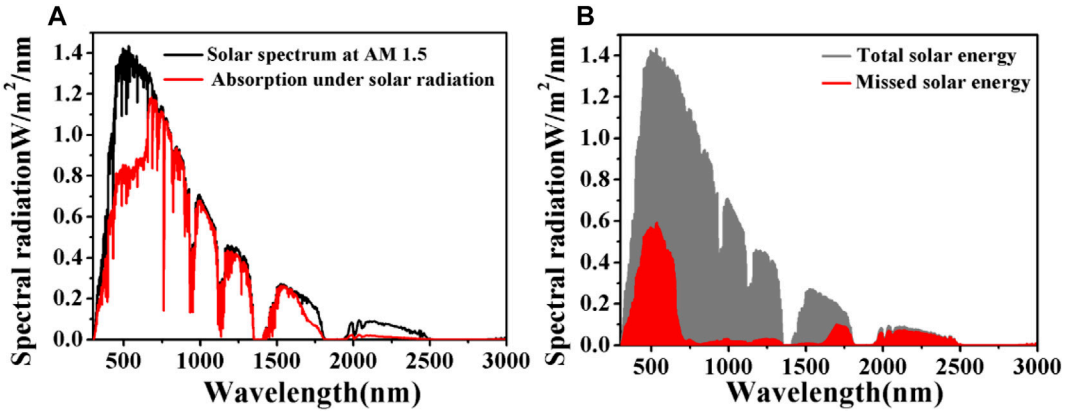

FIGURE 7 | (A) Absorption spectrum under a solar spectrum at AM 1.5. **(B)** Total solar energy and missed energy at AM 1.5.

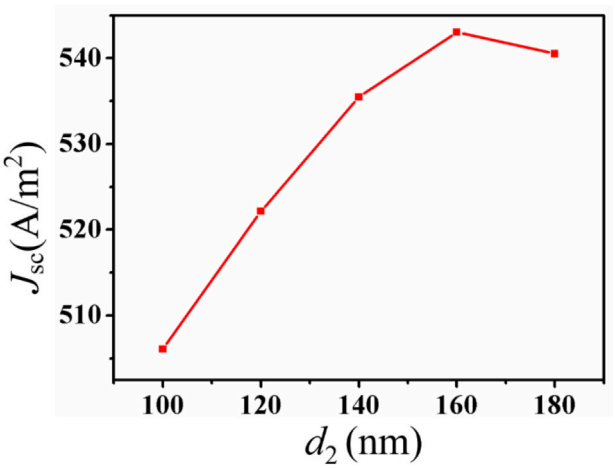

FIGURE 8 | The influence of different grating layer thickness on short-circuit current.

same. In order to present this phenomenon intuitively, we made a schematic diagram showing the relationship between energy missed and total energy, as shown in **Figure 7B**. The gray area is the total solar energy, and the red area is the energy missed by the proposed absorber. We can see that the area of energy missed is also mainly concentrated in the two bands mentioned earlier, and the area is larger, which represents a greater loss of energy. Nevertheless, the global absorption effect of the proposed absorber is good and acceptable.

In practical applications, the proposed absorber can be used as a main component of a solar cell. Since it is a solar cell, the photoelectric conversion efficiency is a matter of great concern to us, and the photoelectric conversion efficiency is directly related to the ideal short-circuit current and directly proportional, which means that in order to achieve higher photoelectric conversion efficiency, higher short-circuit current is the basis (Ghasemi et al., 2014; Ni et al., 2016). Therefore, we studied the ideal short-circuit current of the structure and simulated with different grating layer thicknesses, as shown in **Figure 8**. When the grating layer thickness d_2 = 160 nm, the short-circuit current reaches the maximum value, which is 543.027 A/m^2.

DISCUSSION

A broadband absorber structure based on metal W and semiconductor material GaAs is proposed in this paper. Its structure is very simple, consisting only of metal W substrate, GaAs film layer and grating layer. We have achieved broadband absorption at the wavelength of 500–1,850 nm by repeatedly adjusting the geometric parameters. Subsequently, the rationality of its structure design and materials selection, the influences of several geometric parameters on the global structure, the spectrum when incident and polarization angle change, the solar absorption and loss spectrum, and the ideal short-circuit current are analyzed one by one. We mainly drew the following conclusions:

1) The reflection effect of the metal substrate on the light and the LSPR mode excited by the top semiconductor grating have a very clear effect on the improvement of the total absorber, and the absence of any part will result in the failure of broadband absorption.
2) Selecting noble metals with less metal loss as the film will narrow the bandwidth; among semiconductor materials, GaAs has a stronger electrical excitation due to its higher dielectric constant, so the broadband absorption effect is good.
3) The change of the geometric parameters of the structure actually affects the surface plasmon resonance of the structure, and then different absorption conditions will appear.

DATA AVAILABILITY STATEMENT

The original contributions presented in the study are included in the article/Supplementary Material, further inquiries can be directed to the corresponding authors.

AUTHOR CONTRIBUTIONS

All authors listed have made a substantial, direct, and intellectual contribution to the work and approved it for publication.

FUNDING

This work is supported by the National Natural Science Foundation of China (11774128, 11704223), and the Natural Science Foundation of Shandong Province (ZR2018JL003, 2019KJJ003).

REFERENCES

An, S., Hu, C., Zhou, L., Yi, Z., Liu, C., Lv, J., et al. (2021). Design of Broadband Single-Polarization Filter Based on Simple Structure Photonic crystal Fiber with Gold-Coated Air Holes. *Mod. Phys. Lett. B.* 35 (30), 2150473. doi:10.1142/S021798492150473X

Briggs, R. M., Pryce, I. M., and Atwater, H. A. (2010). Compact Silicon Photonic Waveguide Modulator Based on the Vanadium Dioxide Metal-Insulator Phase Transition. *Opt. Express* 18 (11), 11192–11201. doi:10.1364/OE.18.011192

Cai, L., Zhang, Z., Xiao, H., Chen, S., and Fu, J. (2019). An Eco-Friendly Imprinted Polymer Based on Graphene Quantum Dots for Fluorescent Detection of P-Nitroaniline. *RSC Adv.* 9, 41383–41391. doi:10.1039/c9ra08726e

Cai, R., Rao, W., Zhang, Z., Long, F., and Yin, Y. (2014). An Imprinted Electrochemical Sensor for Bisphenol A Determination Based on Electrodeposition of a Graphene and Ag Nanoparticle Modified Carbon Electrode. *Anal. Methods* 6, 1590–1597. doi:10.1039/c3ay42125b

Cao, G., Li, H., Deng, Y., Zhan, S., He, Z., and Li, B. (2014). Systematic Theoretical Analysis of Selective-Mode Plasmonic Filter Based on Aperture-Side-Coupled Slot Cavity. *Plasmonics* 9, 1163–1169. doi:10.1007/s11468-014-9727-y

Chen, H.-J., Zhang, Z.-H., Cai, R., Kong, X.-Q., Chen, X., Liu, Y.-N., et al. (2013). Molecularly Imprinted Electrochemical Sensor Based on a Reduced Graphene Modified Carbon Electrode for Tetrabromobisphenol A Detection. *Analyst* 138, 2769–2776. doi:10.1039/c3an00146f

Chen, J., Nie, H., Tang, C., Cui, Y., Yan, B., Zhang, Z., et al. (2019a). Highly Sensitive Refractive-Index Sensor Based on strong Magnetic Resonance in Metamaterials. *Appl. Phys. Express* 12, 052015. doi:10.7567/1882-0786/ab14fa

Chen, J., Peng, C., Qi, S., Zhang, Q., Tang, C., Shen, X., et al. (2018). Photonic Microcavity-Enhanced Magnetic Plasmon Resonance of Metamaterials for Sensing Applications. *IEEE Photon. Technol. Lett.* 31 (2), 113–116. doi:10.1109/LPT.2018.2881989

Chen, J., Qi, S., Hong, X., Gu, P., Wei, R., Tang, C., et al. (2019b). Highly Sensitive 3D Metamaterial Sensor Based on Diffraction Coupling of Magnetic Plasmon Resonances. *Results Phys.* 15, 102791. doi:10.1016/j.rinp.2019.102791

Chen, P., Liu, F., Ding, H., Chen, S., Chen, L., Li, Y.-J., et al. (2019). Porous Double-Shell CdS@C3N4 Octahedron Derived by *In Situ* Supramolecular Self-Assembly for Enhanced Photocatalytic Activity. *Appl. Catal. B Environ.* 252, 33–40. doi:10.1016/j.apcatb.2019.04.006

Chen, Z., Chen, H., Jile, H., Xu, D., Yi, Z., Lei, Y., et al. (2021b). Multi-band Multi-Tunable Perfect Plasmon Absorber Based on L-Shaped and Double-Elliptical Graphene Stacks. *Diamond Relat. Mater.* 115, 108374. doi:10.1016/j.diamond.2021.108374

Chen, Z., Chen, H., Yin, J., Zhang, R., Jile, H., Xu, D., et al. (2021a). Multi-band, Tunable, High Figure of merit, High Sensitivity Single-Layer Patterned Graphene-Perfect Absorber Based on Surface Plasmon Resonance. *Diamond Relat. Mater.* 116, 108393. doi:10.1016/j.diamond.2021.108393

Cheng, T., Gao, H., Li, R., Wang, S., Yi, Z., and Yang, H. (2021). Flexoelectricity-induced Enhancement in Carrier Separation and Photocatalytic Activity of a Photocatalyst. *Appl. Surf. Sci.* 566, 150669. doi:10.1016/j.apsusc.2021.150669

Cheng, T., Gao, H., Liu, G., Pu, Z., Wang, S., Yi, Z., et al. (2022). Preparation of Core-Shell Heterojunction Photocatalysts by Coating CdS Nanoparticles onto Bi4Ti3O12 Hierarchical Microspheres and Their Photocatalytic Removal of Organic Pollutants and Cr(VI) Ions. *Colloids Surf. A Physicochem. Eng. Asp.* 633 (2), 127918. doi:10.1016/j.colsurfa.2021.127918

Cheng, Z., Liao, J., He, B., Zhang, F., Zhang, F., Huang, X., et al. (2015). One-Step Fabrication of Graphene Oxide Enhanced Magnetic Composite Gel for Highly Efficient Dye Adsorption and Catalysis. *ACS Sust. Chem. Eng.* 3, 1677–1685. doi:10.1021/acssuschemeng.5b00383

Deng, Y., Cao, G., Wu, Y., Zhou, X., and Liao, W. (2015). Theoretical Description of Dynamic Transmission Characteristics in MDM Waveguide Aperture-Side-Coupled with Ring Cavity. *Plasmonics* 10, 1537–1543. doi:10.1007/s11468-015-9971-9

Deng, Y., Cao, G., Yang, H., Zhou, X., and Wu, Y. (2018). Dynamic Control of Double Plasmon-Induced Transparencies in Aperture-Coupled Waveguide-Cavity System. *Plasmonics* 13, 345–352. doi:10.1007/s11468-017-0519-z

Fu, H., Yi, Z., Shi, Y., Liu, C., Lv, J., Yang, L., et al. (2021). Circular Anti-resonance Fibre Supporting Orbital Angular Momentum Modes with Flat Dispersion, High Purity and Low Confinement Loss. *J. Mod. Opt.* 68 (15), 784–791. doi:10.1080/09500340.2021.1947533

Ghasemi, H., Ni, G., Marconnet, A. M., Loomis, J., Yerci, S., Miljkovic, N., et al. (2014). Solar Steam Generation by Heat Localization. *Nat. Commun.* 5, 4449. doi:10.1038/ncomms5449

Huang, M., Wei, K., Wu, P., Xu, D., and Xu, Y. (2021). Design of Grating Type GaAs Solar Absorber and Investigation of its Photoelectric Characteristics. *Front. Mater.* 8, 781803. doi:10.3389/fmats.2021.781803

Jiang, L., Yi, Y., Tang, Y., Li, Z., Yi, Z., Liu, L., et al. (2021a). A High Quality Factor Ultra-narrow Band Perfect Metamaterial Absorber for Monolayer Molybdenum Disulfide. *Chin. Phys. B.* 19, 103415. doi:10.1088/1674-1056/ac1e11

Jiang, L., Yuan, C., Li, Z., Su, J., Yi, Z., Yao, W., et al. (2021b). Multi-Band and High-Sensitivity Perfect Absorber Based on Monolayer Graphene Metamaterial. *Diamond Relat. Mater.* 111, 108227. doi:10.1016/j.diamond.2020.108227

Khavasi, A. (2015). Design of Ultra-Broadband Graphene Absorber Using Circuit Theory. *J. Opt. Soc. Am. B.* 32 (9), 1941. doi:10.1364/JOSAB.32.001941

Kimpton, H., Stulz, E., and Zhang, X. (2020). Silver Nanofluids Based Broadband Solar Absorber Through Tuning Nanosilver Geometries. *Solar Energy* 208, 515–526. doi:10.1016/j.solener.2020.08.018

Lei, J., Ji, B., and Lin, J. (2016). High-Performance Tunable Plasmonic Absorber Based on the Metal-Insulator-Metal Grating Nanostructure. *Plasmonics* 12 (1), 151–156. doi:10.1007/s11468-016-0242-1

Li, J., Chen, X., Yi, Z., Yang, H., Tang, Y., Yi, Y., et al. (2020a). Broadband Solar Energy Absorber Based on Monolayer Molybdenum Disulfide Using Tungsten Elliptical Arrays. *Mater. Today Energ.* 16, 100390. doi:10.1016/j.mtener.2020.100390

Li, J., Jiang, J., Xu, Z., Liu, M., Tang, S., Yang, C., et al. (2018). Facile Synthesis of Ag@Cu2O Heterogeneous Nanocrystals Decorated N-Doped Reduced Graphene Oxide with Enhanced Electrocatalytic Activity for Ultrasensitive Detection of H2O2. *Sens. Actuators B: Chem.* 260, 529–540. doi:10.1016/j.snb.2018.01.068

Li, J., Jiang, J., Zhao, D., Xu, Z., Liu, M., Liu, X., et al. (2020b). Novel Hierarchical Sea Urchin-Like Prussian Blue@palladium Core-Shell Heterostructures Supported on Nitrogen-Doped Reduced Graphene Oxide: Facile Synthesis and Excellent Guanine Sensing Performance. *Electrochim. Acta* 330, 135196. doi:10.1016/j.electacta.2019.135196

Li, R., Zheng, Y., Luo, Y., Zhang, J., Yi, Z., Liu, L., et al. (2021). Multi-Peak Narrow-Band Perfect Absorber Based on Two-Dimensional Graphene Array. *Diamond Relat. Mater.* 120, 108666. doi:10.1016/j.diamond.2021.108666

Li, Y., Li, M., Xu, P., Tang, S., and Liu, C. (2016). Efficient Photocatalytic Degradation of Acid orange 7 over N-Doped Ordered Mesoporous Titania on Carbon Fibers under Visible-Light Irradiation Based on Three Synergistic Effects. *Appl. Catal. A: Gen.* 524, 163–172. doi:10.1016/j.apcata.2015.01.050

Li, Z., Yi, Y., Xu, D., Yang, H., Yi, Z., Chen, X., et al. (2021b). A Multi-Band and Polarization-Independent Perfect Absorber Based on Dirac Semimetals Circles and Semi-ellipses Array. *Chin. Phys. B.* 30, 098102. doi:10.1088/1674-1056/abfb57

Li, Z., Yi, Z., Liu, T., Liu, L., Chen, X., Zheng, F., et al. (2021a). Three-Band Perfect Absorber with High Refractive Index Sensing Based on an Active Tunable Dirac Semimetal. *Phys. Chem. Chem. Phys.* 23 (32), 17374–17381. doi:10.1039/D1CP01375K

Li-Ying, J., Yi, Y. T., Ying-Ting, Y., Zao, Y., Hua, Y., Zhi-You, L., et al. (2021). A Four-Band Perfect Absorber Based on High Quality Factor and High Quality

Factor of Monolayer Molybdenum Disulfide. *Acta Phys. Sin.* 70, 128101. doi:10.7498/aps.70.20202163

Liu, H., Wang, Q., and Zhang, F. (2020). Preparation of Fe3O4@SiO2@ P(AANa-co-AM) Composites and Their Adsorption for Pb(II). *ACS Omega* 5, 8816–8824. doi:10.1021/acsomega.0c00403

Liu, W., Shi, Y., Yi, Z., Liu, C., Wang, F., Li, X., et al. (2021). Surface Plasmon Resonance Chemical Sensor Composed of a Microstructured Optical Fiber for the Detection of an Ultra-Wide Refractive index Range and Gas-Liquid Pollutants. *Opt. Express* 29 (25), 40734–40747. doi:10.1364/oe.444323

Liu, Y., Bo, M., Yang, X., Zhang, P., Sun, C. Q., and Huang, Y. (2017). Size Modulation Electronic and Optical Properties of Phosphorene Nanoribbons: DFT-BOLS Approximation. *Phys. Chem. Chem. Phys.* 19, 5304–5309. doi:10.1039/c6cp08011a

Long, F., Zhang, Z. H., Wang, J., Yan, L., Lu, P. P., and Yang, Z. X. (2016). Magnetic Graphene Modified Imprinted Electrochemical Sensor for Detection of 4-Octylphenol. *Chin. J. Anal. Chem.* 44, 908–914. doi:10.11895/j.issn.0253.3820.160016

Long, F., Zhang, Z., Wang, J., Yan, L., and Zhou, B. (2015). Cobalt-nickel Bimetallic Nanoparticles Decorated Graphene Sensitized Imprinted Electrochemical Sensor for Determination of Octylphenol. *Electrochimica Acta* 168, 337–345. doi:10.1016/j.electacta.2015.04.054

Lv, P., Xie, D., and Zhang, Z. (2018). Magnetic Carbon Dots Based Molecularly Imprinted Polymers for Fluorescent Detection of Bovine Hemoglobin. *Talanta* 188, 145–151. doi:10.1016/j.talanta.2018.05.068

Ni, G., Li, G., Boriskina, S. V., Li, H., Yang, W., Zhang, T., et al. (2016). Steam Generation under One Sun Enabled by a Floating Structure with thermal Concentration. *Nat. Energ.* 1, 16126. doi:10.1038/NENERGY.2016.126

Qin, F., Chen, X., Yi, Z., Yao, W., Yang, H., Tang, Y., et al. (2020). Ultra-Broadband and Wide-Angle Perfect Solar Absorber Based on TiN Nanodisk and Ti Thin Film Structure. *Solar Energ. Mater. Solar Cell* 211, 110535. doi:10.1016/j.solmat.2020.110535

Sobhani, A., Knight, M. W., Wang, Y., Zheng, B., King, N. S., Brown, L. V., et al. (2013). Narrowband Photodetection in the Near-Infrared with a Plasmon-Induced Hot Electron Device. *Nat. Commun.* 4, 1643. doi:10.1038/ncomms2642

Su, J., Yang, H., Xu, Y., Tang, Y., Yi, Z., Zheng, F., et al. (2021). Based on Ultrathin PEDOT:PSS/c-Ge Solar Cells Design and Their Photoelectric Performance. *Coatings* 11 (7), 748. doi:10.3390/coatings11070748

Tang, N., Li, Y., Chen, F., and Han, Z. (2018). *In Situ* fabrication of a Direct Z-Scheme Photocatalyst by Immobilizing CdS Quantum Dots in the Channels of Graphene-Hybridized and Supported Mesoporous Titanium Nanocrystals for High Photocatalytic Performance under Visible Light. *RSC Adv.* 8, 42233–42245. doi:10.1039/c8ra08008a

Wang, Y., Yi, Y., Xu, D., Yi, Z., Li, Z., Chen, X., et al. (2021). Terahertz Tunable Three Band Narrowband Perfect Absorber Based on Dirac Semimetal. *Phys. E: Low-Dimens. Syst. Nanostructures* 131, 114750. doi:10.1016/j.physe.2021.114750

Wu, X., Zheng, Y., Luo, Y., Zhang, J., Yi, Z., Wu, X., et al. (2021). A Four-Band and Polarization-Independent BDS-Based Tunable Absorber with High Refractive index Sensitivity. *Phys. Chem. Chem. Phys.* 23, 26864–26873. doi:10.1039/D1CP04568G

Xiao, L., Youji, L., Feitai, C., Peng, X., and Ming, L. (2017). Facile Synthesis of Mesoporous Titanium Dioxide Doped by Ag-Coated Graphene with Enhanced Visible-Light Photocatalytic Performance for Methylene Blue Degradation. *RSC Adv.* 7, 25314–25324. doi:10.1039/c7ra02198d

Xiao, L., Zhang, Q., Chen, P., Chen, L., Ding, F., Tang, J., et al. (2019). Copper-Mediated Metal-Organic Framework as Efficient Photocatalyst for the Partial Oxidation of Aromatic Alcohols under Visible-Light Irradiation: Synergism of Plasmonic Effect and Schottky junction. *Appl. Catal. B: Environ.* 248, 380–387. doi:10.1016/j.apcatb.2019.02.012

Xiong, S., Yin, Z., Zhou, Y., Peng, X., Yan, W., Liu, Z., et al. (2013). The Dual-Frequency (20/40 kHz) Ultrasound Assisted Photocatalysis with the Active Carbon Fiber-Loaded Fe3+-TiO2as Photocatalyst for Degradation of Organic Dye. *Bull. Korean Chem. Soc.* 34, 3039–3045. doi:10.5012/bkcs.2013.34.10.3039

Xu, F., Lin, L., Wei, D., Xu, J., and Fang, J. (2021). An Asymmetric Silicon Grating Dual-Narrow-Band Perfect Absorber Based on Dielectric-Metal-Dielectric Structure. *Front. Mater.* 8, 752745. doi:10.3389/fmats.2021.752745

Yang, X., Zhang, F., Hu, Y. J., Chen, D. Z., He, Z. Q., and Xiong, L. Z. (2014). Gold Nanoparticals Doping Graphene Sheets Nanocomposites Sensitized Screen-Printed Carbon Electrode as a Disposable Platform for Voltammetric Determination of Guaiacol in Bamboo Juice. *Int. J. Electrochem. Sci.* 9, 5061–5072.

Yi, Z., Li, J., Lin, J., Qin, F., Chen, X., Yao, W., et al. (2020). Broadband Polarization-Insensitive and Wide-Angle Solar Energy Absorber Based on Tungsten Ring-Disc Array. *Nanoscale* 12, 23077–23083. doi:10.1039/d0nr04502k

Yu, P., Yang, H., Chen, X., Yi, Z., Yao, W., Chen, J., et al. (2020). Ultra-Wideband Solar Absorber Based on Refractory Titanium Metal. *Renew. Energ.* 158, 227–235. doi:10.1016/j.renene.2020.05.142

Zhang, F., Wang, B., and Shen, Y. (2014). Blue Luminescent ZnO Nanoclusters Stabilized by Esterifiable Polyamidoamine Dendrimers and Their UV-Shielding Applications. *Asian J. Chem.* 26, 3467–3470. doi:10.14233/ajchem.2014.15942

Zhang, Z., Cai, R., Long, F., and Wang, J. (2015). Development and Application of Tetrabromobisphenol A Imprinted Electrochemical Sensor Based on Graphene/carbon Nanotubes Three-Dimensional Nanocomposites Modified Carbon Electrode. *Talanta* 134, 435–442. doi:10.1016/j.talanta.2014.11.040

Zhao, F., Chen, X., Yi, Z., Qin, F., Tang, Y., Yao, W., et al. (2020). Study on the Solar Energy Absorption of Hybrid Solar Cells with Trapezoid-Pyramidal Structure Based PEDOT:PSS/c-Ge. *Solar Energy* 204, 635–643. doi:10.1016/j.solener.2020.05.030

Zhao, F., Yi, Y., Lin, J., Yi, Z., Qin, F., Zheng, Y., et al. (2021). The Better Photoelectric Performance of Thin-Film TiO2/c-Si Heterojunction Solar Cells Based on Surface Plasmon Resonance. *Results Phys.* 28, 104628. doi:10.1016/j.rinp.2021.104628

Zhou, F., Qin, F., Yi, Z., Yao, W., Liu, Z., Wu, X., et al. (2021). Ultra-wideband and Wide-Angle Perfect Solar Energy Absorber Based on Ti Nanorings Surface Plasmon Resonance. *Phys. Chem. Chem. Phys.* 23 (31), 17041–17048. doi:10.1039/D1CP03036A

Conflict of Interest: The authors declare that the research was conducted in the absence of any commercial or financial relationships that could be construed as a potential conflict of interest.

Publisher's Note: All claims expressed in this article are solely those of the authors and do not necessarily represent those of their affiliated organizations, or those of the publisher, the editors and the reviewers. Any product that may be evaluated in this article, or claim that may be made by its manufacturer, is not guaranteed or endorsed by the publisher.

Copyright © 2022 Liu, Wu, Li, Zhu and Lv. This is an open-access article distributed under the terms of the Creative Commons Attribution License (CC BY). The use, distribution or reproduction in other forums is permitted, provided the original author(s) and the copyright owner(s) are credited and that the original publication in this journal is cited, in accordance with accepted academic practice. No use, distribution or reproduction is permitted which does not comply with these terms.

frontiers in Materials

ORIGINAL RESEARCH
published: 21 January 2022
doi: 10.3389/fmats.2021.775027

Synthesis of Fibrous Micro-nano Hierarchical Porous Cerium Dioxide Materials by the Impregnation and Thermal Decomposition Method and Its Enhanced Photocatalytic Activity

Meng Zhang[1], *Xingwang Chen*[1], *Min Zu*[1], *Yuanzheng Tang*[1], *Chengbao Liu*[1], *Wanfei Li*[2]* *and Feng Chen*[1]*

[1]*Jiangsu Key Laboratory for Environment Functional Materials, School of Materials Science and Engineering, Suzhou University of Science and Technology, Suzhou, China,* [2]*Suzhou Key Laboratory for Nanophotonic and Nanoelectronic Materials and Its Devices, Suzhou University of Science and Technology, Suzhou, China*

OPEN ACCESS

Edited by:
Tao Xian,
Qinghai Normal University, China

Reviewed by:
Zuming He,
Changzhou University, China
Yuxiang Yan,
Nanjing University, China

***Correspondence:**
Wanfei Li
wfli2018@mail.usts.edu.cn
Feng Chen
ujschenfeng@163.com

Specialty section:
This article was submitted to Semiconducting Materials and Devices, a section of the journal Frontiers in Materials

Received: *13 September 2021*
Accepted: *29 October 2021*
Published: *21 January 2022*

Citation:
Zhang M, Chen X, Zu M, Tang Y, Liu C, Li W and Chen F (2022) Synthesis of Fibrous Micro-nano Hierarchical Porous Cerium Dioxide Materials by the Impregnation and Thermal Decomposition Method and Its Enhanced Photocatalytic Activity. Front. Mater. 8:775027. doi: 10.3389/fmats.2021.775027

Fibrous micro-nano hierarchical porous cerium dioxide materials were prepared from oriental paperbush flower stems by impregnation and thermal decomposition methods. Thermogravimetric analyzer (TG, DSC), field emission scanning electron microscopy (FESEM), X-ray diffraction (XRD), transmission electron microscopy (TEM), N_2 adsorption-desorption isothermals, temperature-programmed reduction (TPR), and UV-Vis spectrophotometer were used to characterize the thermal decomposition behavior, microstructure and photocatalytic properties of fibrous micro-nano hierarchical porous cerium dioxide materials. The results proved that the achieved products retained a fibrous morphology similar to oriental paperbush flower stems with the original biotemplate in material completely removed. The average diameter of CeO_2 particles on the surface of the material is about 9 nm, and the large specific surface area is around 55.6 m^2/g. UV-Vis absorption spectra showed that the fibrous micro-nano hierarchical porous cerium dioxide materials have high light absorption capacity and can respond to simulated sunlight. The effects of initial dye concentration, catalyst concentration, pH value, cycle number, and irradiation time on the photocatalytic activity of fibrous micro-nano hierarchical porous cerium dioxide materials for the photo-degradation of methylene blue under simulated solar irradiation were systematically studied. A reasonable photocatalytic mechanism is proposed based on the experimental results and theoretical analysis. This strategy can be extended to synthesize other broad bandgap semiconductor oxides with high photocatalytic activity for the photo-degradation of organic dyes under simulated solar irradiation.

Keywords: fibrous, cerium dioxide, photocatalytic activity, photocatalytic mechanism, organic dye

INTRODUCTION

With the development of society and the progress of industry, the pollution caused by varied organic dyes is becoming worse, which results in more attention being paid to environmental and energy issues (Chen et al., 2020; Ge et al., 2021). Scientists are committed to enhancing the living environment of mankind and creating better living conditions, and it is imperative to solve the environmental problems caused by industrial development (Chenab et al., 2020; Pooja and Chowdhury, 2021). Recently, pollution, especially organic dyes afecting water resources, has become quite serious. With the background of energy utilization and environmental protection, the photo-degradation of organic pollutants has been actively studied (Medda et al., 2020; Cheng et al., 2021a; Wang et al., 2021a). To reduce the pressure on the environment caused by organic pollutants, many processes including ozone-oxidation method, photo-degradation method, activated-carbon adsorption method, and so on have been designed to degrade the organic pollutants (Caballero-Espitia et al., 2020; Wang et al., 2021b; Wang et al., 2021c). Among these methods, the photo-degradation method is an efficient method to degrade organic dyes from wastewater. Therefore, using the photo-degradation method to study the degradation of organic pollutants from wastewater has important research significance.

The core of the photo-degradation method is to select suitable photocatalysts to degrade organic dyes from wastewater (Wang et al., 2020a; Cheng et al., 2021b; Jiménez-Almarza et al., 2021). Cerium dioxide (CeO_2) is a highly efficient photocatalyst, which shows unique advantages in the degradation of various organic dyes (Gao et al., 2018a; Gong et al., 2019; Murali et al., 2019; Li et al., 2021). However, CeO_2 has a large bandgap and can only respond to ultraviolet light, which greatly restricts its application in the field of photocatalysis. (Wang et al., 2021d; Han et al., 2021). Therefore, it is of great significance to develop a new synthesis route to synthesize the CeO_2 photocatalyst with a special defect structure and study its photocatalytic activity. Lately, the biological template method prepared by inorganic functional materials has become a novel technology to produce the inorganic materials used as photocatalysts (Ai et al., 2021; Kulshrestha et al., 2021). Compared with other preparation methods, the biological template method has the advantages of green environmental protection, a simple process, low cost, and easy mass production. The technique is inspired by the development of biological mineralization and it is the method for preparing inorganic materials with controllable structures. The natural existence and special micromorphology of various biological matters are used as a template, with the introduction of inorganic particles by immersion and the removal of the template by calcination, which is aimed to prepare nano-materials with unique bionic morphology. The structure and properties of the inorganic materials synthesized by the biological template method are highly dependent on the structure and properties of the original biological template. The biological materials possess an inherent hierarchical porous structure, large surface area, light weight, high permeability, and any number of other properties. The chemical composition of the organism and the special microstructure can provide a stable environment for the synthesis of CeO_2 photocatalyst. However, no researchers have yet used the natural biological structure as a template to synthesize a CeO_2 photocatalyst and study its photocatalytic activity. Therefore, the selection of a suitable natural biological structure as a template can be prepared for the industrial production of high-performance CeO_2 photocatalyst.

In this paper, oriental paperbush flower stems were utilized to synthesize the CeO_2 materials with a micro-nano hierarchical structure with high photocatalytic activity for the photo-degradation of methylene blue dye under simulated solar irradiation. The phase purity, microstructure, morphology, optical properties, and photocatalytic activity of micro-nano hierarchical porous cerium dioxide materials were systematically studied. The effects of catalyst concentration, dye concentration, pH value, and stability on the photocatalytic activity of micro-nano hierarchical porous cerium dioxide materials were also studied. The results showed that the prepared micro-nano hierarchical porous cerium dioxide materials can preserve and duplicate the microstructure of the original biological template and exhibit excellent photocatalytic activity for the photo-degradation of methylene blue dye under simulated solar irradiation.

EXPERIMENTAL PROCEDURES

Materials Preparation

All the reagents including $Ce(NO_3)_3{\cdot}6H_2O$, hydrochloric acid anhydrous, and ethanol were purchased from Sinopharm Chemical Reagent Co. Ltd. and the oriental paperbush flower stems were picked from the campus. After being washed by deionized water three times or more, the oriental paperbush flower stems were put in a percentage of anhydrous ethanol solution which to was added a certain amount of hydrochloric acid and were left to stand for 24 h, then this step was repeated three times to get experimental available biological templates. Next, the right amount of oriental paperbush flower stems were impregnated into 0.1 mol/L $Ce(NO_3)_3{\cdot}6H_2O$ solution for 72 h and dried at room temperature, the matter obtained in this step was named the precursor for material synthesis. After repeating the above steps three times, the third drying product was heated to 600°C in a muffle furnace for 200 min. After these processes, the micro-nano hierarchical porous cerium dioxide materials were obtained. To make a comparison, with other conditions unchanged, the cerium dioxide standard samples were obtained by heating pure cerium precursor to 550°C for 200 min in the muffle furnace.

Material Characterization

A thermogravimetric analyzer (TG-DSC TG 209 F3, Netzsch) of fibrous micro-nano hierarchical porous cerium dioxide materials was used to measure the weight changes of precursor for material synthesis during the calcination process. The morphology and various other information about the fibrous micro-nano hierarchical porous cerium dioxide materials were characterized by the Hitachi S4800 type field emission scanning electron microscopy (FESEM) and JEM-2100 type

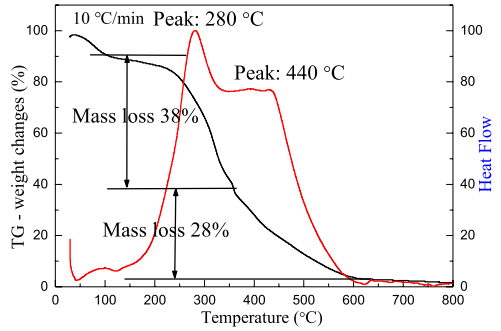

FIGURE 1 | TG-DSC curves of oriental paperbush flower stems/cerium nitrate precursor.

transmission electron microscopy (TEM). The phase structure of fibrous micro-nano hierarchical porous cerium dioxide materials was identified by a Rigaku D/max 2500 PC type X-ray diffraction by using Cu Kα radiation at 40 kV and 40 mA with a scanning rate of 5(°) at 2θ/min which ranges from 20° to 80°. The specific surface area and pore-size distribution of fibrous micro-nano hierarchical porous cerium dioxide materials were calculated by using the BET, ASAP-2010C Brunauer-Emmett-Teller method. A TP-5000 analyzer with a TCD detector (Tianjin, China) was used to determine the temperature-programmed reduction (TPR) of fibrous micro-nano hierarchical porous cerium dioxide materials. The TPR profile of the powder (about 100 mg) was recorded between 20°C and 780°C at a heating rate of 10°C/min.

Photocatalytic Experiments

Methylene blue dye, which is difficult to degrade under natural conditions, was used to detect the photocatalytic activity of fibrous micro-nano hierarchical porous cerium dioxide materials. Before the photo-degradation experiment, adsorption experiments in dark conditions for 30 min were performed to distinguish the change of dye concentration caused by adsorption. A measure of 400 ml of methylene blue solution with a concentration of 10, 50, 100, 150, 200, or 250 mg/L was poured into the photoreactor, and 0.2, 0.4, 0.6, 0.8, 1.0, 1.2, or 1.4 g/L of fibrous micro-nano hierarchical porous cerium dioxide materials was weighed and added into the reactor, and magnetic stirring was carried out simultaneously under the simulated sunlight irradiation with the wavelength of 320–780 nm. Samples were taken at intervals, and the supernatant was removed after centrifugation. The absorbance of methylene blue was measured at 642 nm by the Shimadu Company's UV-Vis spectrophotometer UV-2450. The degradation percentage (D%) of the solution was calculated by the following formula:

$$D\% = \frac{A_0 - A}{A_0} \times 100\% \quad (1)$$

A0 is the absorbance of initial dye concentration, A is the absorbance of the dye after degradation. Simultaneously, different pH values and cyclic stability experiments were performed.

RESULTS AND DISCUSSION

TG-DSC Analysis

Figure 1 shows the TG-DSC curves of oriental paperbush flower stems/cerium nitrate precursor. The black curve in the figure reflects the thermal weight loss of oriental paperbush flower stems/cerium nitrate precursor as the temperature increased, while the red curve represented the changes of the heat flow in the oriental paperbush flower stems/cerium nitrate precursor. From the differential thermal analysis curve in the figure, the weight of the sample system was observed to decrease slightly when the temperature was about 100°C, and there was an insignificant endothermic peak in the heat flow curve, which could be regarded as part of the weight loss caused by the removal of adsorbed water in the complex. (Wang et al., 2013). While two obvious exothermic peaks appeared at 280 and 440°C, and the weight loss of the composite was observed on the corresponding weight loss curves, where the rate of weight loss was 38 and 28%, respectively. The weight loss phenomenon of the composite at 250–350°C can be considered as caused by the carbonization of the organic components in the stem (Zhang et al., 2009a; Zhang et al., 2009b). The observed weight loss between 350 and 600°C was due to the reaction of carbides with oxygen to produce gases such as carbon dioxide (Wu et al., 2004; Xian et al., 2009). The sample was decomposed completely at about 600°C, the quality remained constant. Therefore, the optimum calcination temperature for the selected material is 600°C, at which point the template was completely removed to obtain the pure cerium oxide material.

Microstructure Analysis

Figure 2 presents SEM images of oriental paperbush flower stems and the micro-nano hierarchical ceria material synthesized from oriental paperbush flower stems. In **Figures 2A,B**, the products exhibited irregularly arranged long fibrous structures on the micro-morphology. The length of a single fiber was upward of 100 μm and the fiber radius was about 5–10 μm. In addition, the single fibers intertwined with each other, indicating that the prepared cerium oxide material completely retains the long fibrous structure of the pilose anthers stigma cells completely. Further observation of **Figures 2C,D** showed that the long fibers possessed a lamellar structure, and the edges of these lamellar structures underwent significant warping due to inconsistencies in the material and transverse and longitudinal shrinkage during the subsequent calcination. **Figure 2D** shows the magnified image of the area of the micro-nano hierarchical ceria materials. From the rupture of the fibrous structure in the figure, it can be seen that the inside of the material was hollow structure, which was caused by the curling of the single fiber. The outer surfaces of the fibrous structure were in the shape of burr structures. The presence of the burr structures indicated that in the cerium nitrate precursor after the impregnation–calcination progress the microstructure of the original template was perfectly reproduced. Moreover, these massive skin needles can significantly increase the BET specific surface area of the material and provide more catalytic active sites to promote adsorption of dye, thereby increasing the catalytic activity of the micro-nano hierarchical ceria materials.

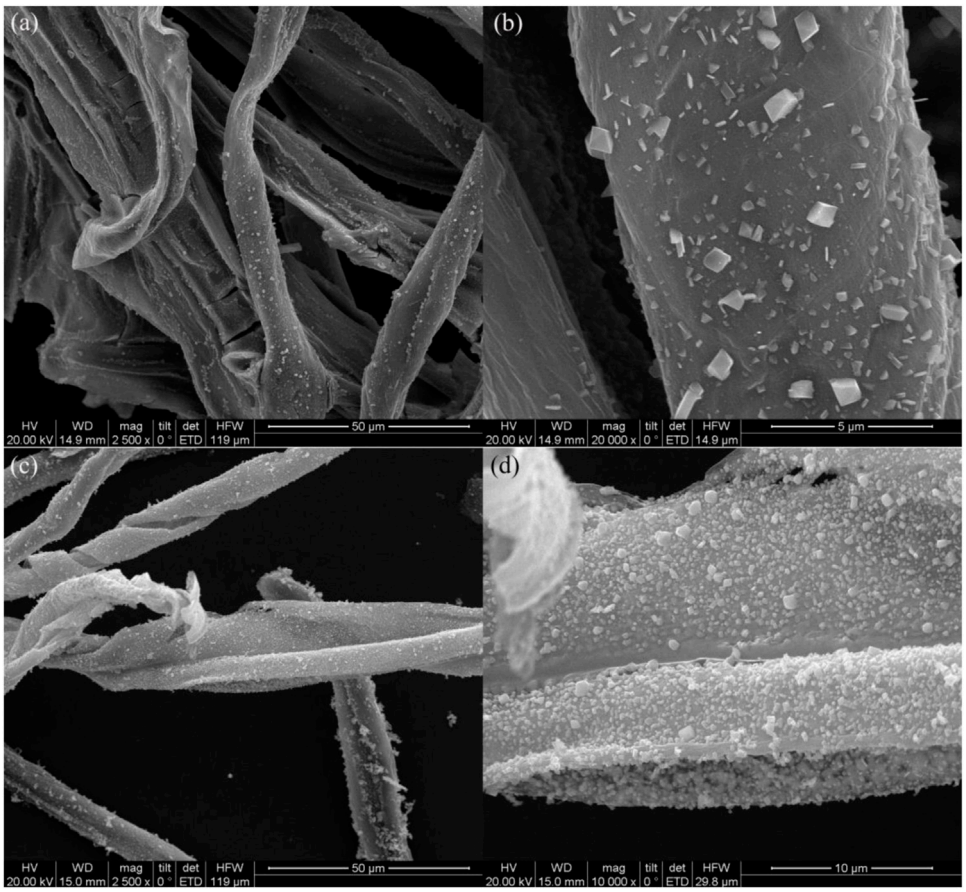

FIGURE 2 | SEM images of the biomimetic structure of oriental paperbush flower stems **(A, B)**, and the micro-nano hierarchical ceria materials **(C, D)**.

The composition of micro-nano hierarchical ceria materials can be observed from **Figures 3A,B**. The surface of micro-nano hierarchical ceria materials was like the structure of the biological cells. There were many pore structures between the particle and the nanoparticles uniformly distributed on the surface of the sample. **Figure 3B** shows the particle size of the sample was less than 20 nm, which was in accordance with the particle size calculated by JADE software. It can be seen from **Figure 3C** that the mean particle size of CeO_2 particles was about 9 nm. The selected area electron diffraction (SAED) pattern of micro-nano hierarchical ceria materials as showed in **Figure 3D**, confirmed the prepared sample was composed of ceria nanoparticles with high crystallinity and polycrystalline structure. On the surface of micro-nano hierarchical ceria materials, there were many irregular cellular structure polycrystalline particles, whose size was about 100 nm and existed plenty of pore structure. These results confirm that the micro-nano hierarchical ceria materials with the fiber structure were formed by self-assembly.

X-ray Diffraction Analysis

Figure 4 shows the XRD pattern of micro-nano hierarchical ceria materials. The six characteristic peaks of micro-nano hierarchical ceria materials sequentially correspond to (111), (200), (220), (311), (222), and (400) crystal planes of the face-centered cubic CeO_2 with standard JCPDF card No. 34-0394, indicating that the prepared product is a cerium oxide material. No extra peaks were observed, indicating that the template had been completely removed during the calcination and that the cerium nitrate precursor was thoroughly decomposed and the phase purity of the product was improved. The sharp diffraction peak and high XRD intensity of the sample indicated that the product has good crystallinity. According to the full width at half maximum (FWHM) of each diffraction peak, the grain size of micro-nano hierarchical cerium oxide material is calculated by the Scherrer formula to be 9 nm. The theoretical calculation result is consistent with the TEM observation.

Adsorption-Desorption Isotherm and Pore Size Distribution

Figure 5 shows the nitrogen adsorption-desorption isotherms and their corresponding pore size distribution curves of micro-nano hierarchical ceria materials. It can be observed that the adsorption-desorption isotherm is type IV and is a typical adsorption isotherm for both microporous and mesoporous structures. When the relative pressure increases to a certain

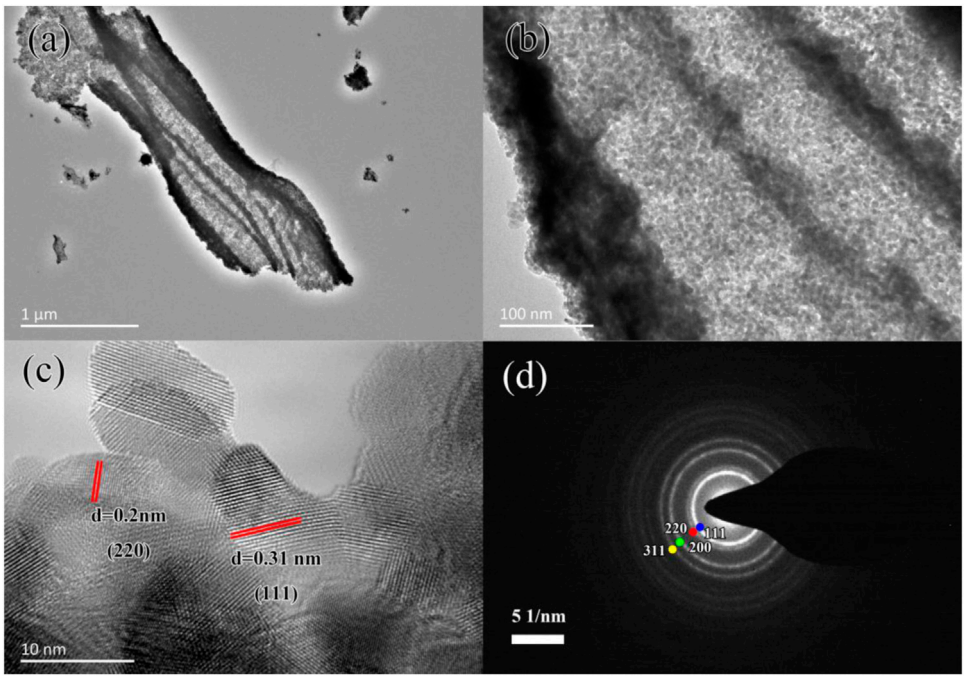

FIGURE 3 | (A) TEM image, **(B)** TEM enlargement, **(C)** HRTEM image, and **(D)** SAED pattern of micro-nano hierarchical ceria materials.

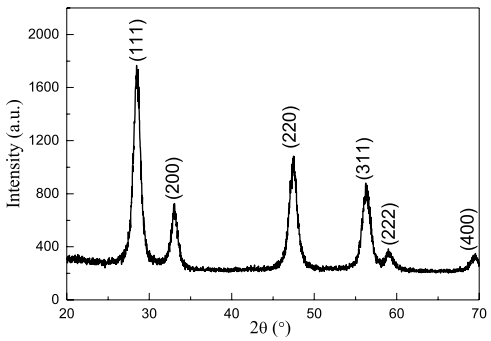

FIGURE 4 | XRD pattern of micro-nano hierarchical ceria materials.

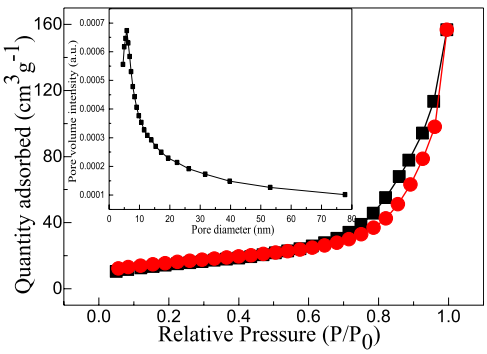

FIGURE 5 | Nitrogen adsorption-desorption isotherm of micro-nano hierarchical ceria materials. The inset shows the corresponding pore size distribution curve of micro-nano hierarchical ceria materials.

value (p/p_0 is 0.4–10), the nitrogen molecules in mesopores Capillary condensation occur, resulting in adsorption lag phenomenon, and the formation of an H3-type hysteresis ring. The position of the pressure section determines the pore size of micro-nano hierarchical ceria materials. The specific surface area of micro-nano hierarchical ceria materials calculated by the BET method was 55.6 m^2/g. The pore size distribution curve of micro-nano hierarchical ceria materials calculated by the BJH equation shows that the prepared fibrous cerium oxide material has more pore size distribution intervals and the diameters are between 4 and 20 nm, which fully shows that the sample was a rich mesoporous structure, which is consistent with the TEM observation. The existence of these mesoporous structures can increase the BET specific surface area of micro-nano hierarchical ceria materials, and then provide more active sites for the photocatalyst, and further enhance the photocatalytic activity of micro-nano hierarchical ceria materials.

Temperature-Programmed Reduction Experiments

H_2-TPR is the spectrum obtained according to the change of hydrogen concentration in the constant rate heating process, in which hydrogen in the reaction gas reacts with oxygen released in the transformation process of Ce^{4+}/Ce^{3+} to generate water. According to the peak temperature, peak type and peak area of the TPR spectrum, the catalytic, oxygen storage and release properties of micro-nano hierarchical ceria materials and bulk

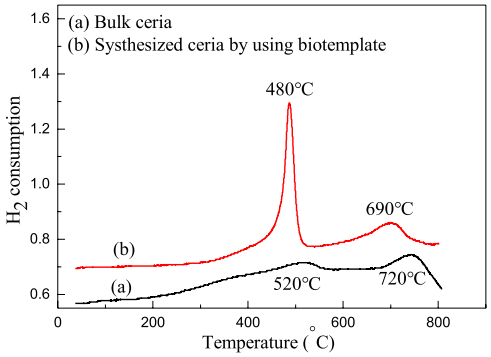

FIGURE 6 | Temperature-programmed reduction profiles of (a) micro-nano hierarchical ceria materials and (b) bulk ceria.

ceria can be qualitatively analyzed. **Figure 6** shows the temperature-programmed reduction profiles of micro-nano hierarchical ceria materials and bulk ceria. In **Figure 6**, bulk cerium oxide exhibits hydrogen consumption peaks at about 450 and 750°C, respectively, corresponding to surface and bulk oxygen consumption of cerium oxide materials. It can be clearly observed that the micro-nano hierarchical ceria materials prepared by the template method have a sharp peak type at about 480°C, and the peak area is much higher than that of bulk ceria. Simultaneously, the bulk phase oxygen consumption peak area of micro-nano hierarchical ceria materials is significantly reduced compared with the bulk ceria, indicating that the surface oxygen consumption of porous cerium oxide material is significantly increased. The results indicate that the micro-nano hierarchical ceria materials have more surface oxygen and more surface oxygen active sites. However, the hydrogen consumption peak of bulk phase oxygen appears at about 680°C, which may be caused by the crystal lattice distortion caused by the incorporation of N element in the template, which makes bulk phase oxygen overflow more easily. The above analysis results imply that the micro-nano hierarchical ceria materials have excellent photocatalytic activity.

Optical Properties

Figures 7A, B shows the UV–Vis absorption spectra of micro-nano hierarchical ceria materials and bulk ceria. As can be seen from **Figure 7A**, bulk CeO_2 has a high optical absorption coefficient before 400 nm and can respond to ultraviolet light. The micro-nano hierarchical ceria materials exhibit novel optical properties compared with those of bulk materials, and a new characteristic peak appears at about 380 nm, mainly due to special defects in the micro-nano hierarchical ceria materials. Meanwhile, the range of light absorption is extended from the ultraviolet region to the visible region. There is some weak light absorption at 600 and 700 nm, indicating that the micro-nano hierarchical ceria materials have a visible light response-ability. Based on UV-Vis absorption spectra and Tauc theory (Tang et al., 2020; Zhao et al., 2020; Gao et al., 2021a; Wang et al., 2021e), the optical band gap (Eg) value of bulk ceria and micro-nano hierarchical ceria materials can be obtained.

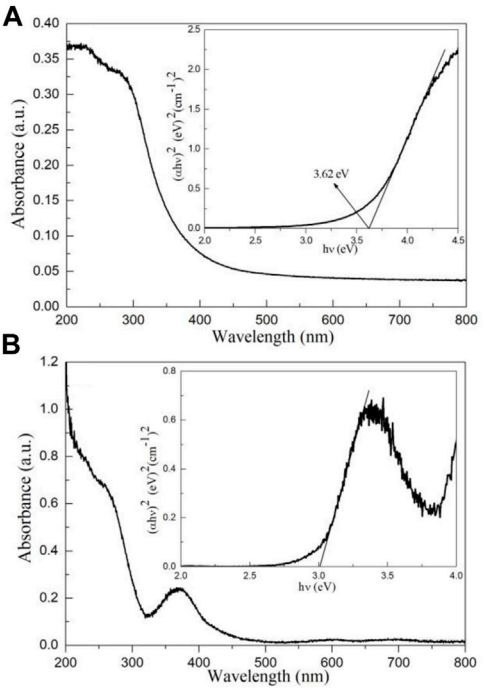

FIGURE 7 | UV–Vis absorption spectra of **(A)** bulk ceria and **(B)** micro-nano hierarchical ceria materials. The insets show the optical band gap (Eg) values of **(A)** bulk ceria and **(B)** micro-nano hierarchical ceria materials.

$$(F(R)h\nu)^n = A\left(h\nu - E_g\right) \quad (2)$$

Where ν is the frequency, A is the absorption coefficient, and $n = 2$.

The Eg values of bulk ceria and micro-nano hierarchical ceria materials as shown in **Figure 7A** inset and **Figure 7B** inset. The Eg values of bulk ceria and micro-nano hierarchical ceria materials are found to be 3.62 and 3.00 eV, respectively. The results show that the micro-nano hierarchical ceria materials can respond to visible light and is a potential visible-light photocatalyst. This conclusion will be further confirmed in the photocatalytic experiment section.

Photocatalytic Activity

To study the photocatalytic activity of micro-nano hierarchical ceria materials, methylene blue was selected as the target degradation dye (**Figure 8A**). To eliminate the influence of adsorption on the photocatalytic experiment, half an hour of adsorption experiments was carried out in a dark room before the photocatalytic experiment. Although CeO_2 forms a porous structure, the amount of methylene blue dye adsorbed is very low, only about 8%. When only the methylene blue dye solution is illuminated, the methylene blue dye hardly degrades. The results show that methylene blue dye is an organic pollutant that is difficult to degrade under natural light irradiation. To compare with the traditional CeO_2 nanoparticles (C-CeO_2), the photo-degradation of methylene blue dye by CeO_2 nanoparticles was also performed. The photocatalytic degradation rate increases

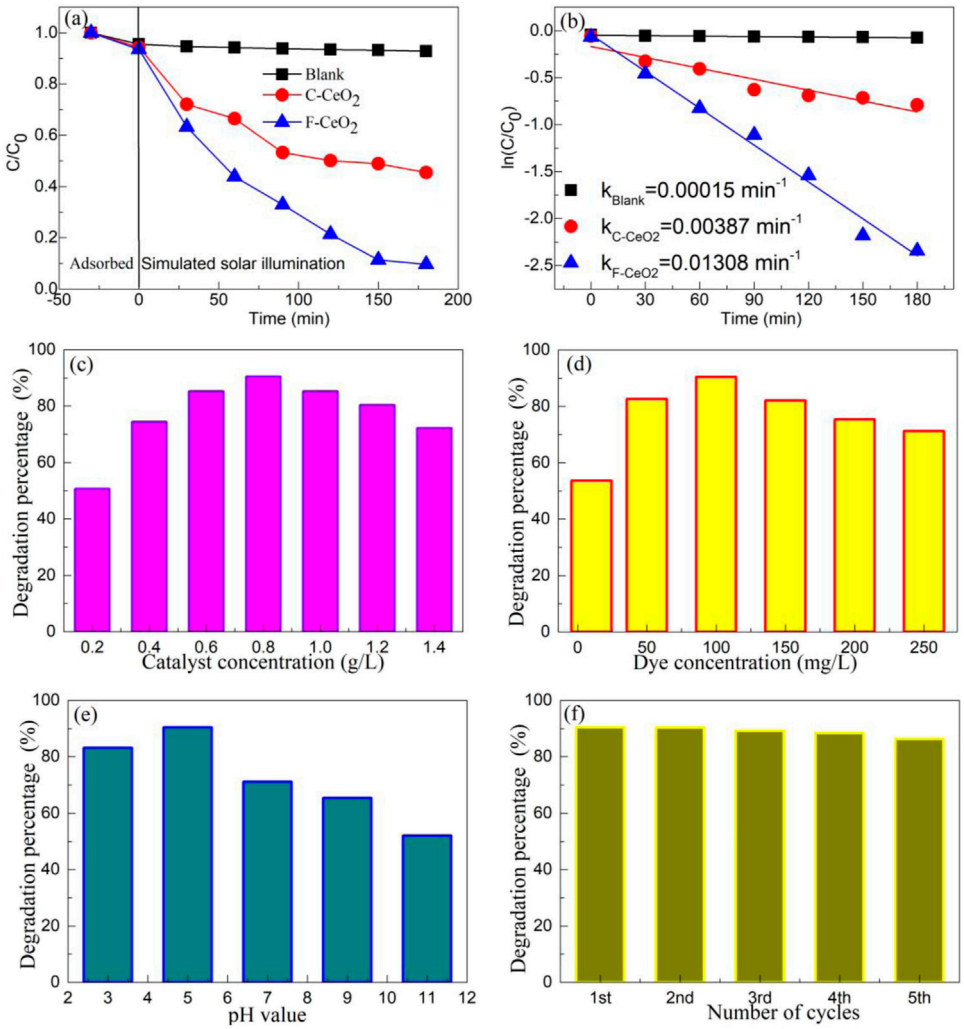

FIGURE 8 | Photocatalytic activity of micro-nano hierarchical ceria materials for the degradation of methylene blue under different parameters. **(A)** Different irradiation times, **(B)** Corresponding first-order dynamics curve, **(C)** Different catalyst concentrations, **(D)** Different dye concentrations, **(E)** Different pH values, and **(F)** Cyclic stability experiments.

with the increase of irradiation time. However, the degradation percentage of traditional CeO_2 nanoparticles was only about 50% after being exposed to light for 180 min. The photocatalytic degradation percentage of micro-nano hierarchical ceria materials can reach about 90.4%.

The degradation rate of micro-nano hierarchical ceria materials can be further expressed by first-order kinetic model (Wang et al., 2020b; Yu and Han, 2021):

$$\ln(A_t/A_0) = -kt \quad (3)$$

Where A_t, A_0, k, and t are the absorbance of dye at different irradiation times, the initial dye absorbance, the rate constant, and the irradiation time, respectively. The corresponding first-order dynamics curve of blank, the CeO_2 nanoparticles, and micro-nano hierarchical ceria materials is shown in **Figure 8B**. The k values of blank, CeO_2 nanoparticles, and micro-nano hierarchical ceria materials are 0.00015, 0.00387, and 0.01308 min^{-1}, respectively. The photocatalytic activity of micro-nano hierarchical ceria materials was about 3.38 times higher than that of CeO_2 nanoparticles. The photocatalytic activity of micro-nano hierarchical ceria materials was 2.60 times higher than that of CeO_2 nanoparticles reported in the literature (Gao et al., 2018a). The results further confirmed that the micro-nano hierarchical ceria materials exhibited high visible-light photocatalytic activity for the photo-degradation of methylene blue dye.

The effect of catalyst concentration on the photocatalytic activity of semiconductor photocatalysts is always a problem worth discussing. **Figure 8C** shows the effect of catalyst concentration on the photocatalytic activity of micro-nano hierarchical ceria materials for the photo-degradation of methylene blue under simulated solar irradiation. With the increase of catalyst concentration, the photocatalytic degradation percentage first increases and then decreases, and

the optimal catalyst concentration is 0.8 g/L. When the catalyst concentration is low, the probability of photon absorption is small, the photogenerated electron-hole pair is less, the number of catalytic active centers is correspondingly less, and the organic molecules can not be fully adsorbed to the surface of the micro-nano hierarchical ceria materials, so the photocatalytic degradation effect is poor. (Cao et al., 2018). With the increase of catalyst concentration, the utilization rate of photons increases, the number of catalytic active centers in the reaction increases, and the degradation rate increases. When the concentration of catalyst increases to a certain value (0.8 g/L), the photocatalytic degradation percentage reaches the best. When the concentration of catalyst continues to increase, the scattering effect of catalyst particles on incident light becomes prominent, and the utilization rate of photons decreases, making the degradation rate show a downward trend. (Yumei Guo et al., 2020).

Figure 8D shows the effect of dye concentration on the photocatalytic activity of micro-nano hierarchical ceria materials for the photo-degradation of methylene blue dye under simulated solar irradiation. With the increase of the methylene blue dye initial concentration, the degradation percentage first increased and then showed a downward trend, and the degradation percentage reached the maximum when the dye concentration was 100 mg/L. When the dye concentration is low, the photocatalytic reaction rate is approximately proportional to the concentration of organic matter (Konstantinou and Albanis, 2004), so the degradation percentage of dye increases with the increase of dye concentration. When the dye concentration is too high, the transmittance of the solution decreases, resulting in a decrease in the number of effective photons involved in the photocatalytic reaction, and the surface of the catalyst will reduce its active site due to the adsorption of excessive dye molecules. (Wang and Tian, 2020). When the concentration of dye molecules exceeds a certain level, its degradation rate begins to decline.

Figure 8E shows the effect of pH value on the photocatalytic activity of micro-nano hierarchical ceria materials for the photo-degradation of methylene blue dye under simulated solar irradiation. It can be seen from **Figure 8E** that the degradation percentage of methylene blue dye is higher in acidic conditions, but lower in alkaline conditions. The optimal pH value of micro-nano hierarchical ceria materials for the photo-degradation of methylene blue dye under simulated solar irradiation is 5. This result is related to the point of zero charge (PZC) of CeO_2 and the cationic dye of methylene blue. (Gao et al., 2018b; Ramirez et al., 2019).

The recyclability of a photocatalyst is another important index to evaluate its photocatalytic activity. **Figure 8F** shows the recyclability experiments of micro-nano hierarchical ceria materials for the photo-degradation of methylene blue dye under simulated solar irradiation. After each cycle, the photocatalyst in the degraded dye solution should be centrifuged, filtered, and dried before the next cycle experiment. After five cycles, the degradation rate of micro-nano hierarchical ceria materials decreased by only about 6%, indicating that the micro-nano hierarchical ceria materials can be reused many times. The results indicate that the micro-nano hierarchical ceria materials have high cyclic stability and are a potential visible-light photocatalyst.

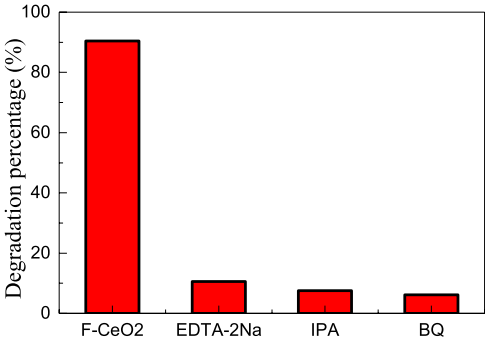

FIGURE 9 | Species trapping experiments for the degradation of methylene blue dye over micro-nano hierarchical ceria materials.

Photocatalytic Mechanism

Based on the literature (He et al., 2016; He et al., 2021), the hole (hVB+), hydroxyl radical (•OH) and superoxide radical ($\bullet O_2^-$) can be detected by using the disodium ethylenediamine tetraacetic acid (EDTA-2Na), 2-propanol (IPA), and 1, 4-benzoquinone (BQ) as scavengers, respectively. The trapping experiment was consistent with the photocatalytic experiment, except that a 1 mmol trapping agent was added to the reaction solution. **Figure 9** shows the species trapping experiments for the degradation of methylene blue dye over micro-nano hierarchical ceria materials. When EDTA-2Na, IPA, and BQ were added to the reaction solution, the photocatalytic efficiency of micro-nano hierarchical ceria materials was significantly inhibited, indicating that holes, hydroxyl radicals, and superoxide radicals played a crucial role in the photocatalytic reaction.

Based on the experimental results and band theory analysis, the photocatalytic mechanism of micro-nano hierarchical ceria materials can be discussed. The adsorption experiment results show that the effect of adsorption on micro-nano hierarchical ceria materials is very small. According to the literature (Gao et al., 2018a) and the Eg value of micro-nano hierarchical ceria materials, the conduction band potential and valence band potential of micro-nano hierarchical ceria materials were obtained. **Figure 10** shows the photocatalytic mechanism of micro-nano hierarchical ceria materials. When simulated sunlight shines on the surface of micro-nano hierarchical ceria materials, photogenerated electrons are excited to transition to the conduction band of micro-nano hierarchical ceria materials, leaving holes in the valence band.

$$\text{Ceria} + hv \rightarrow e^- + h^+ \quad (4)$$

Some of the remaining holes in the valence band react directly with the dye to form non-toxic small molecular organic matters, while the other reacts with OH^- or H_2O to form hydroxyl radicals (•OH).

$$h^+ + \text{dye} \rightarrow \text{Products} \quad (5)$$

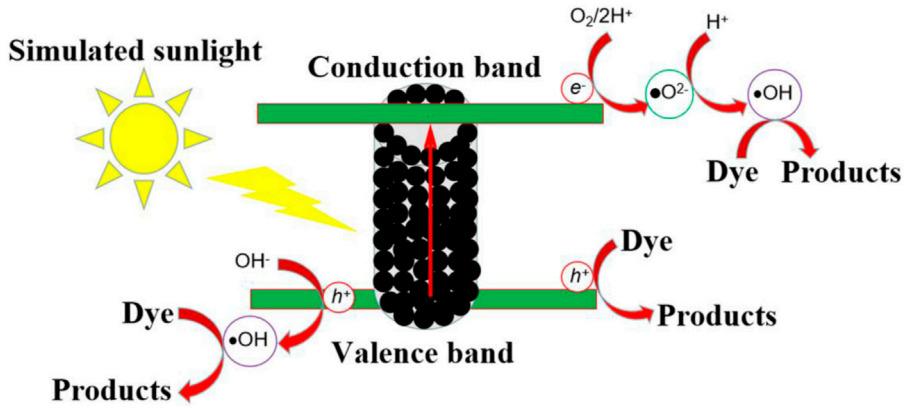

FIGURE 10 | Photocatalytic mechanism of micro-nano hierarchical ceria materials.

$$h^+ + OH^-/H_2O \rightarrow \bullet OH \quad (6)$$

The electrons that transition to the conduction band will undergo a series of reactions, forming superoxide radicals ($\bullet O^{2-}$), which in turn interact with the electrons to form •OH (Li et al., 2019; You et al., 2020; Zheng et al., 2020; Dhinagaran et al., 2021).

$$e^- + O_2 \rightarrow \bullet O^{2-} \quad (7)$$

$$\bullet O^{2-} + 2H^+ + e^- \rightarrow H_2O_2 \quad (8)$$

$$2e^- + O_2 + 2H^+ \rightarrow H_2O_2 \quad (9)$$

$$e^- + H_2O_2 \rightarrow \bullet OH + OH^- \quad (10)$$

$$\bullet O^{2-} + H_2O_2 \rightarrow \bullet OH + OH^- + O_2 \quad (11)$$

Hydroxyl radicals generated in the conduction band or valence band of micro-nano hierarchical ceria materials will interact with dye molecules to produce non-toxic and harmless products.

$$\bullet OH + \text{dye} \rightarrow \text{Products} \quad (12)$$

When the dye and micro-nano hierarchical ceria materials adsorb together by electrostatic interaction (Ayati et al., 2016; Gao et al., 2021b; Liu et al., 2022), in addition to the interaction of holes, superoxide radical, and hydroxyl radical, the special defect structure of micro-nano hierarchical ceria materials also causes the degradation of the dye. Combined with experimental analysis results and mechanism study, the special defects in the micro-nano hierarchical ceria materials also play an important role in the photo-degradation of methylene blue dye. Analysis of the results shows that the defect plays the role of electron transport carrier in the transfer and separation of charge carriers.

CONCLUSION

The micro-nano hierarchical ceria materials were prepared using the oriental paperbush flower stems as a template and cerium nitrate as a precursor. The fiber length ranged from 100 to 500 μm and the radius was about 3–8 μm. The fiber structure was warped due to inconsistent shrinkage in the subsequent calcination process and formed a hollow-like structure. The micro-nano hierarchical ceria materials have a large BET-specific surface area (55.6 m^2/g) and abundant pore structures, which can increase the BET-specific surface area and promote the mass transfer process. HRTEM imaging shows that the fiber structure is composed of uniformly distributed nano-polycrystalline cerium oxide grains. There are many active oxygen sites on the surface of micro-nano hierarchical ceria materials, but the doping of N element in the template causes the lattice distortion of cerium oxide. The micro-nano hierarchical ceria materials showed the best photocatalytic activity for the photodegradation of methylene blue under visible light irradiation, and the degradation percentage of methylene blue reached 90.4% after 180 min. The optimal irradiation time, catalyst concentration, dye concentration, and pH value were 180 min, 0.8 g/L, 100 mg/L, and 5, respectively. This method can be used to synthesize other micro-nano hierarchical metal oxides and enhance their physicochemical properties.

DATA AVAILABILITY STATEMENT

The original contributions presented in the study are included in the article/supplementary material, further inquiries can be directed to the corresponding authors.

AUTHOR CONTRIBUTIONS

MeZ was responsible for synthesis experiments, performance tests and data analysis. XC, MiZ and YT were responsible for material characterization. CL was responsible for the analysis and guidance of XRD and UV tests. WL is responsible for analyzing the reaction mechanism. FC was responsible for experimental design and paper revision.

FUNDING

This work was supported by the National key research and development plan of "air pollution causes and control technology research" (2017YFC0211903), National Natural Science Foundation of China (21773291), the Natural Science Foundation of Jiangsu Province (BK20180103), the Qing Lan Project of Jiangsu Province and Postgraduate research and innovation plan project in Jiangsu Province (KYCX20_2761).

REFERENCES

Ai, K., Huang, J., Xiao, Z., Yang, Y., Bai, Y., and Peng, J. (2021). Localized Surface Plasmon Resonance Properties and Biomedical Applications of Copper Selenide Nanomaterials. *Mater. Today Chem.* 20, 100402. doi:10.1016/j.mtchem.2020.100402

Ayati, A., Shahrak, M. N., Tanhaei, B., and Sillanpää, M. (2016). Emerging Adsorptive Removal of Azo Dye by Metal-Organic Frameworks. *Chemosphere* 160, 30–44. doi:10.1016/j.chemosphere.2016.06.065

Caballero-Espitia, D. L., Lizarraga-Medina, E. G., Borbon-Nuñez, H. A., Contreras-Lopez, O. E., Tiznado, H., and Marquez, H. (2020). Study of Al2O3 Thin Films by ALD Using H2O and O3 as Oxygen Source for Waveguide Applications. *Opt. Mater.* 109, 110370. doi:10.1016/j.optmat.2020.110370

Cao, Z., Wang, C., and Chen, J. (2018). Synthesis and Photocatalytic Property of P-N junction YMnO3/SrTiO3 Composites. *Mater. Res. Express* 5, 115512. doi:10.1088/2053-1591/aadec0/meta#

Chen, S., Skordos, A., and Thakur, V. K. (2020). Functional Nanocomposites for Energy Storage: Chemistry and New Horizons. *Mater. Today Chem.* 17, 100304. doi:10.1016/j.mtchem.2020.100304

Chenab, K. K., Sohrabi, B., Jafari, A., and Ramakrishna, S. (2020). Water Treatment: Functional Nanomaterials and Applications from Adsorption to Photodegradation. *Mater. Today Chem.* 16, 100262. doi:10.1016/j.mtchem.2020.100262

Cheng, T., Gao, H., Li, R., Wang, S., Yi, Z., and Yang, H. (2021). Flexoelectricity-induced Enhancement in Carrier Separation and Photocatalytic Activity of a Photocatalyst. *Appl. Surf. Sci.* 566, 150669. doi:10.1016/j.apsusc.2021.150669

Cheng, T., Gao, H., Sun, X., Xian, T., Wang, S., Yi, Z., et al. (2021). An Excellent Z-Scheme Ag2MoO4/Bi4Ti3O12 Heterojunction Photocatalyst: Construction Strategy and Application in Environmental Purification. *Adv. Powder Tech.* 32 (3), 951–962. doi:10.1016/j.apt.2021.01.039

Dhinagaran, M., Elakkiya, V., and Sumathi, S. (2021). Tailor Made ZnAl2O4-CeO2 Hetero Structure as an Efficient Photo Catalyst for Environmental Remediation. *Opt. Mater.* 111, 110546. doi:10.1016/j.optmat.2020.110546

Gao, H. J., Wang, S. F., Fang, L. M., Sun, G. A., Chen, X. P., Tang, S. N., et al. (2021). Nanostructured Spinel-type M(M = Mg, Co, Zn)Cr2O4 Oxides: Novel Adsorbents for Aqueous Congo Red Removal. *Mater. Today Chem.* 22, 100593. doi:10.1016/j.mtchem.2021.100593

Gao, H., Wang, Y., Gao, Q., Pan, X., Wang, S., Yang, H., et al. (2021). Phase Evolution and Photoluminescence Behavior of MMoO4 (M = Mg, Ca, Sr) Phosphors. *Optik* 241, 167040. doi:10.1016/j.ijleo.2021.167040

Gao, H., Yang, H., and Wang, S. (2018). Hydrothermal Synthesis, Growth Mechanism, Optical Properties and Photocatalytic Activity of Cubic SrTiO3 Particles for the Degradation of Cationic and Anionic Dyes. *Optik* 175, 237–249. doi:10.1016/j.ijleo.2018.09.027

Gao, H., Yang, H., Yang, G., and Wang, S. (2018). Effects of Oxygen Vacancy and Sintering Temperature on the Photoluminescence Properties and Photocatalytic Activity of CeO2 Nanoparticles with High Uniformity. *Mater. Tech.* 33, 321–332. doi:10.1080/10667857.2018.1438222

Ge, Y., Luo, H., Huang, J., and Zhang, Z. (2021). Visible-light-active TiO2 Photocatalyst for Efficient Photodegradation of Organic Dyes. *Opt. Mater.* 115, 111058. doi:10.1016/j.optmat.2021.111058

Gong, X., Gao, X., Du, W., Zhang, H., Zhang, S., Nguyen, T. T., et al. (2019). Wood Powder-Derived Quantum Dots for CeO2 Photocatalytic and Anti-counterfeit Applications. *Opt. Mater.* 96, 109302. doi:10.1016/j.optmat.2019.109302

Han, K., Wang, Y., Wang, S., Liu, Q., Deng, Z., and Wang, F. (2021). Narrowing Band gap Energy of CeO2 in (Ni/CeO2)@SiO2 Catalyst for Photothermal Methane Dry Reforming. *Chem. Eng. J.* 421, 129989. doi:10.1016/j.cej.2021.129989

He, Z., Xia, Y., Tang, B., Jiang, X., and Su, J. (2016). Fabrication and Photocatalytic Property of ZnO/Cu2O Core-Shell Nanocomposites. *Mater. Lett.* 184, 148–151. doi:10.1016/j.matlet.2016.08.020

He, Z., Yang, H., Su, J., Xia, Y., Fu, X., Kang, L., et al. (2021). Polyacrylamide Gel Synthesis and Photocatalytic Performance of CuCo2O4 Nanoparticles. *Mater. Lett.* 288, 129375. doi:10.1016/j.matlet.2021.129375

Jiménez-Almarza, A., López-Magano, A., Cano, R., Ortín-Rubio, B., Díaz-García, D., Gomez-Ruiz, S., et al. (2021). Engineering Covalent Organic Frameworks in the Modulation of Photocatalytic Degradation of Pollutants under Visible Light Conditions. *Mater. Today Chem.* 22, 100548. doi:10.1016/j.mtchem.2021.100548

Konstantinou, I. K., and Albanis, T. A. (2004). TiO2-assisted Photocatalytic Degradation of Azo Dyes in Aqueous Solution: Kinetic and Mechanistic Investigations. *Appl. Catal. B: Environ.* 49, 1–14. doi:10.1016/j.apcatb.2003.11.010

Kulshrestha, A., Gehlot, P. S., and Kumar, A. (2021). Paramagnetic Surface Active Ionic Liquids: Synthesis, Properties, and Applications. *Mater. Today ChemistryToday Chem* 21, 100522. doi:10.1016/j.mtchem.2021.100522

Li, D., Zu, X., Ao, D., Tang, Q., Fu, Y., Guo, Y., et al. (2019). High Humidity Enhanced Surface Acoustic Wave (SAW) H2S Sensors Based on Sol-Gel CuO Films. *Sensors Actuators B: Chem.* 294, 55–61. doi:10.1016/j.snb.2019.04.010

Li, J., Wang, S., Sun, G., Gao, H., Yu, X., Tang, S., et al. (2021). Facile Preparation of MgAl2O4/CeO2/Mn3O4 Heterojunction Photocatalyst and Enhanced Photocatalytic Activity. *Mater. Today Chem.* 19, 100390. doi:10.1016/j.mtchem.2020.100390

Liu, H., Wang, S., Gao, H., Yang, H., Wang, F., Chen, X., et al. (2022). A Simple Polyacrylamide Gel Route for the Synthesis of MgAl2O4 Nanoparticles with Different Metal Sources as an Efficient Adsorbent: Neural Network Algorithm Simulation, Equilibrium, Kinetics and Thermodynamic Studies. *Sep. Purif. Tech.* 281, 119855. doi:10.1016/j.seppur.2021.119855

Medda, S. K., Manna, S., and De, G. (2020). Photocatalytic Evaluation of Anatase TiO2 Coating on Ceramic Tiles by Raman Spectroscopy. *Trans. Indian Ceram. Soc.* 79, 13–17. doi:10.1080/0371750X.2019.1696233

Murali, A., Lan, Y. P., Sarswat, P. K., and Free, M. L. (2019). Synthesis of CeO2/reduced Graphene Oxide Nanocomposite for Electrochemical Determination of Ascorbic Acid and Dopamine and for Photocatalytic Applications. *Mater. Today Chem.* 12, 222–232. doi:10.1016/j.mtchem.2019.02.001

Pooja, P., and Chowdhury, P. (2021). Functionalized CdTe Fluorescence Nanosensor for the Sensitive Detection of Water Borne Environmentally Hazardous Metal Ions. *Opt. Mater.* 111, 110584. doi:10.1016/j.optmat.2020.110584

Ramirez, L., Ramseier Gentile, S., Zimmermann, S., and Stoll, S. (2019). Behavior of TiO2 and CeO2 Nanoparticles and Polystyrene Nanoplastics in Bottled Mineral, Drinking and Lake Geneva Waters. Impact of Water Hardness and Natural Organic Matter on Nanoparticle Surface Properties and Aggregation. *Water* 11 (4), 721. doi:10.3390/w11040721

Tang, S., Wang, S., Yu, X., Gao, H., Niu, X., Wang, Y., et al. (2020). Gamma-Ray Irradiation Assisted Polyacrylamide Gel Synthesis of Scheelite Type BaWO 4 Phosphors and its Colorimetric, Optical and Photoluminescence Properties. *ChemistrySelect* 5, 10599–10606. doi:10.1002/slct.202002429

Wang, S.-F., Zhang, C., Sun, G., Chen, B., Xiang, X., Wang, H., et al. (2013). Fabrication of a Novel Light Emission Material AlFeO3 by a Modified Polyacrylamide Gel Route and Characterization of the Material. *Opt. Mater.* 36, 482–488. doi:10.1016/j.optmat.2013.10.014

Wang, S. F., Chen, X. Y., Gao, H. J., Fang, L. M., Hu, Q. W., Sun, G. A., et al. (2021). A Comparative Study on the Phase Structure, Optical and NIR Reflectivity of BaFe12O19 Nano-Pigments by the Traditional and Modified Polyacrylamide Gel Method. *JNanoR* 67, 1–14. doi:10.4028/www.scientific.net/jnanor.67.1

Wang, S., Gao, H., Fang, L., Hu, Q., Sun, G., Chen, X., et al. (2021). Synthesis of Novel CQDs/CeO2/SrFe12O19 Magnetic Separation Photocatalysts and

Synergic Adsorption-Photocatalytic Degradation Effect for Methylene Blue Dye Removal. *Chem. Eng. J. Adv.* 6, 100089. doi:10.1016/j.ceja.2021.100089

Wang, S., Gao, H., Li, J., Wang, Y., Chen, C., Yu, X., et al. (2021). Comparative Study of the Photoluminescence Performance and Photocatalytic Activity of CeO2/MgAl2O4 Composite Materials with an N-N Heterojunction Prepared by One-step Synthesis and Two-step Synthesis Methods. *J. Phys. Chem. Sol.* 150, 109891. doi:10.1016/j.jpcs.2020.109891

Wang, S., Gao, H., Yu, H., Li, P., Li, Y., Chen, C., et al. (2020). Optical and Photoluminescence Properties of the MgAl2O4:M (M = Ti, Mn, Co, Ni) Phosphors: Calcination Behavior and Photoluminescence Mechanism. *Trans. Indian Ceram. Soc.* 79, 221–231. doi:10.1080/0371750X.2020.1817789

Wang, S., Gao, H., Yu, X., Tang, S., Wang, Y., Fang, L., et al. (2020). Nanostructured SrTiO3 with Different Morphologies Achieved by mineral Acid-Assisted Hydrothermal Method with Enhanced Optical, Electrochemical, and Photocatalytic Performances. *J. Mater. Sci. Mater. Electron.* 31, 17736–17754. doi:10.1007/s10854-020-04328-0

Wang, S., Tang, S., Gao, H., Chen, X., Liu, H., Yu, C., et al. (2021). Microstructure, Optical, Photoluminescence Properties and the Intrinsic Mechanism of Photoluminescence and Photocatalysis for the BaTiO3, BaTiO3/TiO2 and BaTiO3/TiO2/CeO2 Smart Composites. *Opt. Mater.* 118, 111273. doi:10.1016/j.optmat.2021.111273

Wang, S., Tang, S., Gao, H., Fang, L., Hu, Q., Sun, G., et al. (2021). Modified Polyacrylamide Gel Synthesis of CeO2 Nanoparticles by Using Cerium Sulfate as Metal Source and its Optical and Photoluminescence Properties. *J. Mater. Sci. Mater. Electron.* 32, 10820–10834. doi:10.1007/s10854-021-05740-w

Wang, Y., and Tian, H. (2020). Study on the Construction of YMnO3/CeO2 Composite Photocatalyst Heterostructure and Photocatalytic Degradation of Methyl Red. *Optik* 201, 163524. doi:10.1016/j.ijleo.2019.163524

Wu, S., Liu, Y., He, L., and Wang, F. (2004). Preparation of β-spodumene-based Glass-Ceramic Powders by Polyacrylamide Gel Process. *Mater. Lett.* 58, 2772–2775. doi:10.1016/j.matlet.2004.04.017

Xian, T., Yang, H., Shen, X., Jiang, J. L., Wei, Z. Q., and Feng, W. J. (2009). Preparation of High-Quality BiFeO3 Nanopowders via a Polyacrylamide Gel Route. *J. Alloys Comp.* 480, 889–892. doi:10.1016/j.jallcom.2009.02.068

You, J., Zhan, S., Wen, J., Ma, Y., and Zhu, Z. (2020). Construction of Heterojunction of Ag2S Modified Yttrium Manganate Visible Photocatalyst and Study on Photocatalytic Mechanism. *Optik* 217, 164900. doi:10.1016/j.ijleo.2020.164900

Yu, H., and Han, Q. (2021). Effect of Reaction Mediums on Photocatalytic Performance of BiOX (X = Cl, Br, I). *Opt. Mater.* 119, 111399. doi:10.1016/j.optmat.2021.111399

Yumei Guo, Y., Ren, C., Li, L., and Zhang, X. (2020). Comparative Study of Cobalt Ferrite and Polyacrylamide Decorated Cobalt Ferrite Microspheres in Structural, Optical, Magnetic, Photoluminescence, and Photocatalytic Properties. *Russ. J. Phys. Chem.* 94, 2614–2621. doi:10.1134/S003602442012033X

Zhang, Y., Liang, H., Zhao, C. Y., and Liu, Y. (2009). Macroporous Alumina Monoliths Prepared by Filling Polymer Foams with Alumina Hydrosols. *J. Mater. Sci.* 44, 931–938. doi:10.1007/s10853-008-3189-6

Zhang, Y., Zhao, C. Y., Liang, H., and Liu, Y. (2009). Macroporous Monolithic Pt/γ-Al2O3 and K-Pt/γ-Al2O3 Catalysts Used for Preferential Oxidation of CO. *Catal. Lett.* 127, 339–347. doi:10.1007/s10562-008-9686-z

Zhao, X., Wang, S., Guan, S., Gao, H., Wang, Y., Wang, Y., et al. (2020). Construction and Photoluminescence Mechanism of N-N Type Double Heterojunction Bi2S3/Bi4Ti3O12/Bi2MoO6 Phosphors. *Optik* 224, 165537. doi:10.1016/j.ijleo.2020.165537

Zheng, Z., Zu, X., Zhang, Y., and Zhou, W. (2020). Rational Design of Type-II Nano-Heterojunctions for Nanoscale Optoelectronics. *Mater. Today Phys.* 15, 100262. doi:10.1016/j.mtphys.2020.100262

Conflict of Interest: The authors declare that the research was conducted in the absence of any commercial or financial relationships that could be construed as a potential conflict of interest.

Publisher's Note: All claims expressed in this article are solely those of the authors and do not necessarily represent those of their affiliated organizations, or those of the publisher, the editors, and the reviewers. Any product that may be evaluated in this article, or claim that may be made by its manufacturer, is not guaranteed or endorsed by the publisher.

Copyright © 2022 Zhang, Chen, Zu, Tang, Liu, Li and Chen. This is an open-access article distributed under the terms of the Creative Commons Attribution License (CC BY). The use, distribution or reproduction in other forums is permitted, provided the original author(s) and the copyright owner(s) are credited and that the original publication in this journal is cited, in accordance with accepted academic practice. No use, distribution or reproduction is permitted which does not comply with these terms.

frontiers in Materials

REVIEW
published: 01 February 2022
doi: 10.3389/fmats.2022.845664

Progress in Synthesis and Photocatalytic Activity of MAl_2O_4(M=Mg, Sr, Ba) Based Photocatalysts

Xiulin Han[1,2], *Meijuan Sun*[1,2]*, *Xiaona Chai*[1,2], *Jun Li*[1,2], *Yanning Wu*[1,2] *and Wu Sun*[1,2]

[1]Key Laboratory of Functional Materials and Devices for Informatics of Anhui Higher Education Institutes, Fuyang Normal University, Fuyang, China, [2]School of Physics and Electronic Engineering, Fuyang Normal University, Fuyang, China

Photocatalysis is regarded as a green technology to degrade organic dyes driven by light energy. The selection of photocatalyst restricts the development of photocatalytic technology. Aluminate is a kind of potential broad-gap semiconductor photocatalyst and also an excellent phosphor substrate materials. The physical and chemical properties of aluminate are strongly dependent on the preparation method. Insight into the influence of synthesis methods on photocatalytic activity of aluminate based photocatalysts is helpful for the development of novel aluminate based photocatalysts. In this paper, the typical synthesis methods of aluminate photocatalysts, ion-doped aluminate based photocatalysts and heterojunction type aluminate photocatalysts, and their photocatalytic activities are reviewed. Based on the energy band theory, the photocatalytic mechanisms of single component aluminate photocatalyst, ion-doped aluminate based photocatalyst, and heterojunction type aluminate photocatalyst were reviewed. The future development of aluminate based photocatalyst will give priority to the salinization of aluminate modified by silver and other metal particles and the photocatalytic application of activated ion modified aluminate based phosphors.

Keywords: photocatalysis, aluminate, heterojunction, photocatalytic mechanism, photocatalytic application

OPEN ACCESS

Edited by:
Zao Yi,
Southwest University of Science and Technology, China

Reviewed by:
Fang Leiming,
China Academy of Engineering Physics, China
Fei Wang,
Sichuan University, China
Yuxiang Yan,
Nanjing University, China

***Correspondence:**
Meijuan Sun
hhj200606@126.com

Specialty section:
This article was submitted to Semiconducting Materials and Devices, a section of the journal Frontiers in Materials

Received: *30 December 2021*
Accepted: *17 January 2022*
Published: *01 February 2022*

Citation:
Han X, Sun M, Chai X, Li J, Wu Y and Sun W (2022) Progress in Synthesis and Photocatalytic Activity of MAl_2O_4(M=Mg, Sr, Ba) Based Photocatalysts. Front. Mater. 9:845664. doi: 10.3389/fmats.2022.845664

INTRODUCTION

The economic development of all countries in the world has a great impact on the environment, especially human beings' thirst for necessities such as leather, textiles, medicines, food and so on, and the increasing demand for dyes, thus causing different degrees of pollution to the environment. (Wang et al., 2021a; Piriyanon et al., 2021; Ibrahim et al., 2022; Lahiri et al., 2022). Since water is needed for all kinds of necessities, and these factories are built along rivers, direct discharge of organic dyes into rivers will cause devastating pollution to the environment. This forces mankind to consider the problem of environmental pollution while developing. To deal with the pollution of organic dyes to water resources, the countries all over the world have invested a lot of money to solve this problem. Many mature methods have been developed to solve the problem of organic dye contamination, including: 1) Thermocatalytic technique driven by thermal energy. (Bao et al., 2020; Forouzesh et al., 2021) 2) Electrocatalytic technique driven by electric field or magnetic field. (Li et al., 2017; Szroeder et al., 2019). 3) Piezoelectric catalytic technique driven by mechanical energy. (Cheng et al., 2021a; Cheng et al., 2021b) 4) Biodegradation technique (Ghalei and Handa, 2022; Mathew et al., 2022). 5) Adsorption technique (Gao et al., 2021; Liu et al., 2022). 6) Photocatalytic technique

driven by light energy (Pu et al., 2021; Gao et al., 2022; Zhang et al., 2022). 7) Multi - technology hybrid degradation of organic matter. (Wang et al., 2021b). Among these technologies, the catalyst is the key factor affecting the degradation rate of dyes.

Recently, a series of photocatalysts have been developed to degrade organic dyes. There are three main types of photocatalysts (Wang et al., 2017; Wang et al., 2020a; Rajabathar et al., 2020; Shifa Wang et al., 2020; Cheng et al., 2021c; Wang et al., 2021c; Ivashchenko et al., 2021; Kim et al., 2021; Kumar and Luxmi, 2021; Musa et al., 2021; Taazayet et al., 2021): 1) Single-component photocatalysts 2) Photocatalyst of two components 3) Ternary or multi-component photocatalysts. For a long time, single-component photocatalysts have been widely favored by researchers because of their advantages of simple composition and easy synthesis. Spinel aluminate is a kind of such single component photocatalyst, which has wide application prospect in the field of photocatalysis due to its high chemical and thermal stability, high catalytic activity, high specific surface area, and high surface defects and active sites. (Kharlanov et al., 2019; Boudiaf et al., 2020; Chen et al., 2021). Spinel aluminate generally has the structure of MB_2O_4, A is generally Mg, Ca, Sr, Ba, Co, Ni, Cu, Mn, and other bivalent metal ions, B is Al, Fe, Ga, Cr, and other trivalent metal ions. (Sharma et al., 2014; Sriram et al., 2020). Among these spinel aluminates, MAl_2O_4 (A = Mg, Sr, and Ba) has attracted extensive attention from researchers due to its excellent physicochemical properties make it can be used as long afterglow phosphor base materials, lightweight helmets, photoelectric devices, microwave dielectric capacitors, and high temperature windows, etc. (Han et al., 2018; Takebuchi et al., 2020; Basyrova et al., 2021; Kiryakov et al., 2021) Simultaneously, MAl_2O_4 is a kind of environmental friendly material, in the photocatalytic field, especially in the degradation of organic dyes has a good application. (Wang et al., 2019a; Shifa Wang et al., 2020; Liu et al., 2022). Therefore, the work of MAl_2O_4 and MAl_2O_4 based photocatalysts in the degradation of organic dyes is reviewed, which has important research significance for the development of new aluminate based photocatalysts.

It is well known that the photocatalytic activity of aluminate based photocatalysts is strongly dependent on the preparation method. Different preparation methods will produce aluminate with different morphology, which may have special defect structure, thus enhancing the photocatalytic activity of aluminate. Ion doping and heterostructure construction will accelerate the transfer and separation of electrons and holes, and improve the photocatalytic activity of the system. Therefore, the influence of ion doping and heterostructure construction on the photocatalytic activity of aluminate photocatalyst should not be underestimated. In this paper, we start from the preparation of aluminate based photocatalysts, reviewed the preparation of single-component aluminate, metal ion doped aluminate and multiple heterojunction aluminate based photocatalysts, and their applications in the field of photocatalysis. Based on electron hole pair transfer, separation and energy band theory, the photocatalytic mechanism of single component aluminate and heterojunction aluminate photocatalysts was reviewed, and which provided technical support for the development of aluminate based photocatalysts.

TABLE 1 | The conduction band potential and valence band potential of MAl_2O_4 photocatalyst.

Samples	Eg (eV)	X (V)	Conduction band potential (V)	Valence band potential (V)
$BeAl_2O_4$	6.450	5.565	−2.160	4.290
$MgAl_2O_4$	3.923	5.356	−1.106	2.817
$CaAl_2O_4$	7.400	4.963	−3.237	4.163
$SrAl_2O_4$	3.984	4.896	−1.596	2.388
$BaAl_2O_4$	3.910	5.025	−1.430	2.480
$MnAl_2O_4$	4.030	5.350	−1.165	2.865
$FeAl_2O_4$	1.780	5.417	0.027	1.807
$CoAl_2O_4$	1.948	5.462	−0.012	1.936
$NiAl_2O_4$	3.000	5.480	−0.520	2.480
$CuAl_2O_4$	2.920	5.494	−0.466	2.454
$ZnAl_2O_4$	3.800	5.489	−0.911	2.889

SYNTHESIS OF MAL_2O_4(M = MG, SR, AND BA) BASED PHOTOCATALYSTS

The photocatalytic activity of catalysts strongly depends on morphology, size, dimension, specific surface area, defec,t and impurity. Ultimately, these parameters affect the electron hole pair transfer and separation efficiency of the photocatalyst, which in turn accelerates the oxidation or reduction capacity of the electrons and holes. The dye is oxidized or reduced to form non-toxic small organic molecules. To regulate these parameters, the special synthesis methods are necessary. Currently, the MAl_2O_4(M = Mg, Sr, and Ba) based photoatalysts have been synthesized in a number of ways to construct specific defect structures.

Synthesis of MAl_2O_4(M = Mg, Sr, and Ba) Photocatalysts

Spinel aluminate is a wide-gap semiconductor, such as $BeAl_2O_4$ (6.450 eV) (Ching et al., 2001), $MgAl_2O_4$ (3.923 eV) (Wang et al., 2019a), $CaAl_2O_4$ (7.400 eV) (Moirangthem et al., 2019), $SrAl_2O_4$ (3.984 eV) (Shifa Wang et al., 2020), $BaAl_2O_4$ (3.910 eV) (Nair and Pillai, 2021), $MnAl_2O_4$ (4.030 eV) (Bhavani et al., 2018), $FeAl_2O_4$ (1.780 eV) (Mu et al., 2017), $CoAl_2O_4$ (1.948 eV) (Gao et al., 2018), $NiAl_2O_4$ (3.000 eV) (Chellammal Gayathri et al., 2021), $CuAl_2O_4$ (2.920 eV) (Potbhare et al., 2019), and $ZnAl_2O_4$ (3.800 eV) (Shang-Pan et al., 2020). Based on the obtained optical band gap value and band theory, the conduction band potential and valence band potential of MAl_2O_4 were calculated.

$$E_{CB} = X - E^e - 0.5E_g \quad (1)$$

$$E_{VB} = X - E^e + 0.5E_g \quad (2)$$

Where, X of MAl_2O_4 was estimated by **Eq. 3**, E^e is 4.5 eV and Eg is optical band gap value.

$$X(MAl_2O_4) = \sqrt[7]{X(M)X(AI)^2X(O)^4} \quad (3)$$

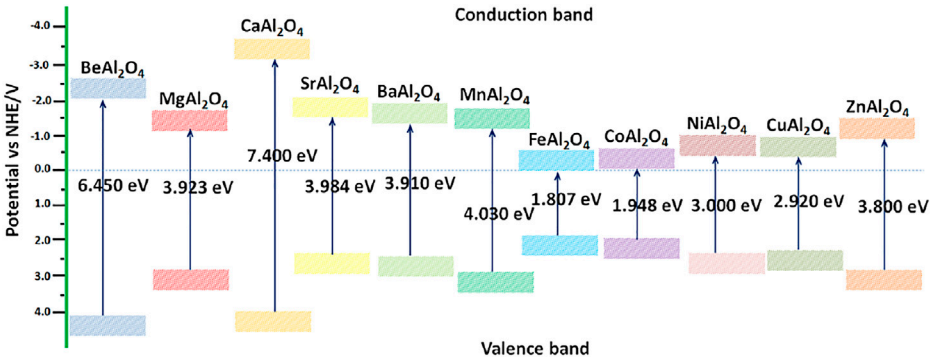

FIGURE 1 | The related energy level diagram of MAl_2O_4 photocatalyst.

Table 1 shows the X value, conduction band potential and valence band potential of MAl_2O_4 photocatalyst. The related energy level diagram of MAl_2O_4 photocatalyst can be described in **Figure 1**. As can be seen from **Figure 1**, the band gap value of MAl_2O_4 (M = Fe, Co, and Cu) is less than 3, which can easily respond to visible light and degrade organic dyes under visible light conditions (Gholami et al., 2016; Mu et al., 2017; Feng et al., 2021). Other aluminate photocatalysts must adopt special preparation methods to introduce impurities or defects if they are to respond to visible light. Wang et al. (Wang et al., 2019b) used amorphous alumina and α-alumina to modify $MnAl_2O_4$ spinel type oxides exhibits high visible light photocatalytic activity. However, these mainly introduce impurities in the form of doping or coupling to enhance the photocatalytic activity of single component aluminate. In particular, the band gap values of MAl_2O_4 (M = Mg, Sr, and Ba) are close to 4, making it difficult to respond to visible light. Traditional methods such as the solid state reaction method, (Ganesh et al., 2004; Canaza-Mamani et al., 2021), the sol-gel method, (Habibi et al., 2017; Salehabadi et al., 2017), the solvothermal method, (Zhu et al., 2012), the hydrothermal method (Sera et al., 2021), and the coprecipitation method (Zawrah et al., 2007) are difficult to make its have special defect structure. In order to make a single component aluminate photocatalytic activity, special preparation methods must be used to enhance the electron and hole pairs transfer and separation ability. Wang et al. (Wang et al., 2019a) synthesized $MgAl_2O_4$ photocatalyst with special defective structure by gamma ray irradiation assisted polyacrylamide gel method, which showed that it had high visible light photocatalytic activity for the degradation of methylene blue. However, the extreme conditions such as high energy, high pressure and high temperature are often needed to prepare aluminate photocatalyst with defective structure by special preparation process, which are very difficult to achieve in general laboratory. Therefore, other means must be found to enhance the photocatalytic activity of single component aluminate photocatalyst.

Synthesis of Metal Ion Doped MAl_2O_4(M = Mg, Sr, and Ba) Photocatalysts

Ion doping is an effective way to enhance the photocatalytic activity of a single component semiconductor photocatalyst. Generally, ion doping can change the band gap value of a single component semiconductor photocatalyst. For the MAl_2O_4, doping can choose A site substitution and Al site substitution, A site substitution of ion radius should be close to the A site ion. In the synthesis of dense ceramics, the solid state reaction method is relatively better, and the high temperature, and high pressure conditions are easy to doping ions into the lattice of a single component aluminate. However, due to the small specific surface area and porosity of dense ceramics, the photocatalytic degradation of organic dyes is not favorable, which will greatly limit the application of solid phase reaction method in the synthesis of ion doped aluminate photocatalysts. Alam et al. (Alam et al., 2022) synthesized the Cr^{3+}-doped $MgAl_2O_4$ nanoparticles by the solution combustion method exhibits excellent photocatalytic activity against Acid Red-88 (AR-88) dye. Solution combustion method is easy to control the morphology of Cr^{3+}-doped $MgAl_2O_4$, adjust the doping ratio, reduce the particle size, resulting in a single component of $MgAl_2O_4$ exhibit novel physicochemical properties. Chen et al. (Chen et al., 2009) synthesized $MgAl_2O_4$:Eu^{3+} phosphors by hydrothermal method exhibits high photoluminescence properties. Different morphologies of $MgAl_2O_4$:Eu^{3+} phosphors can be obtained by changing the ratio of precursor salts. The SEM images of $MgAl_2O_4$:Eu^{3+} phosphors as shown in **Figure 2**. The results further show that it is easy to synthesize different morphologies of ion doped aluminate photocatalysts by hydrothermal method. Wang et al. (Wang et al., 2019c) reported that the $Mg_{1-x}Co_xAl_2O_4$ photocatalysts synthesized by the irradiation assisted polyacrylamide gel route exhibits high photocatalytic activity. The method can be used to synthesize aluminate photocatalysts with different proportions and morphologies, which is beneficial to improve the photocatalytic activity of single component aluminate photocatalysts.

Synthesis of MAl_2O_4(M = Mg, Sr, and Ba) Based Multivariate Heterojunction Photocatalysts

Another way to enhance the photocatalytic activity of semiconductor photocatalysts is to construct multiple photocatalysts with special heterojunction structure. Similarly, the aluminate based phosphors can be used in a similar way to enhance

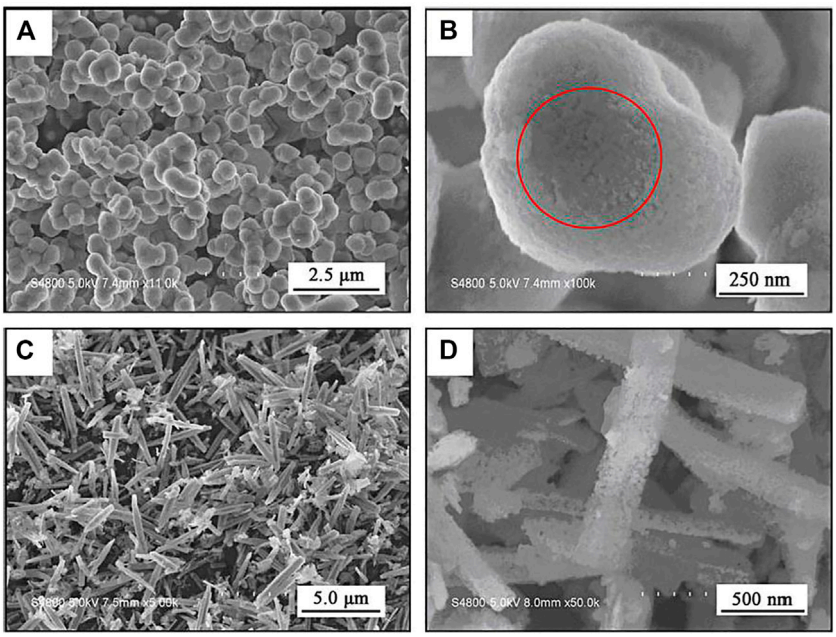

FIGURE 2 | SEM images of $MgAl_2O_4$:Eu^{3+} phosphors with different molar ratios of $Mg(NO_3)_2$● $6H_2O$, $Al(NO_3)_3$ ●$9H_2O$ and $CO(NH_2)_2$. **(A, B)** 1:2:10, and **(C, D)** 1:2:50 (Chen et al., 2009). Adapted from ref. (Chen et al., 2009). Copyright © 2009 Elsevier Inc.

the photoluminescence properties of a single component aluminate (Wang et al., 2020b; Liu et al., 2020). Surface modification of $MgAl_2O_4$ with metal particles can enhance its photoluminescence properties due to plasma resonance effect. With the increase of sintering temperature, the metal particles are oxidized, which affects the band gap value of the system. The $MgAl_2O_4$: M (M = Mg, Ti, Mn, Co, and Ni) phosphors exhibits wide visible light absorption, suggesting that they have high photocatalytic activity under visible light. Mkhalid et al. (Mkhalid, 2022) synthesized the $Ag_2O/SrAl_2O_4$/CNT ternary photocatalyst by the sol-gel method exhibits high visible-light-responsive for H_2 production. The construction of multiple heterojunctions is beneficial to enhance the electron transport, transfer and separation efficiency of $SrAl_2O_4$, and thus improving the photocatalytic activity of the system under visible light irradiation. Sol-gel method has more advantages than solid phase method and coprecipitation method because of its easy composition control and simple synthesis. Hydrothermal method is easy to synthesize the aluminate products with different morphologies, but its application in the construction of multiple heterojunctions is less. Therefore, the sol-gel method is commonly used to synthesize aluminate - based multielement heterostructures.

PHOTOCATALYTIC ACTIVITY OF MAL_2O_4(M = MG, SR, AND BA) BASED PHOTOCATALYSTS

The photocatalytic activity of aluminate photocatalyst is strongly dependent on the preparation method, ion doping and heterostructure construction.

Photocatalytic Activity of MAl_2O_4(M = Mg, Sr, and Ba) Photocatalysts

Due to the large band gap value of MAl_2O_4(M = Mg, Sr, and Ba) aluminate photocatalyst, there are relatively few studies on its use as photocatalyst alone. Except for $MgAl_2O_4$ and $BaAl_2O_4$, single component $SrAl_2O_4$ has not been used as a photocatalyst to degrade organic dyes. **Table 2** shows the photocatalytic activity of $MgAl_2O_4$ and $BaAl_2O_4$ photocatalyst. Nassar et al. (Nassar et al., 2014) reported the $MgAl_2O_4$ photocatalyst prepared by the sol–gel auto combustion method exhibits high photocatalytic activity for the degradation of Reactive Red Me 4BL dye. Qian et al. (Qian et al., 2017) synthesized $MgAl_2O_4$ photocatalyst by a simple hydrothermal route exhibits high photocatalytic activity for the degradation of Methylene bule. However, $MgAl_2O_4$ synthesized by this method is inadequate in degrading phenol. Li et al. (2011) prepared the mixed amorphous and crystalline $MgAl_2O_4$ nanopowders by a simple solution combustion method using glycine and urea as fuel mixtures exhibits high visible light-induced photocatalytic activity for the degradation of Methylene bule. Jiang et al. (2014) synthesized the $MgAl_2O_4$ photocatalyst by a sol-gel method exhibits a poor photocatalytic activity for the degradation of various dyes including methyl orange, acid red B and reactive brilliant red K-2G. Parvarinezhad et al. (2019) synthesized the $MgAl_2O_4$ nanopowders by one-step solid state reaction method possessed strong light absorption properties in the ultraviolet-visible region. Wang et al. (2019d) synthesized the $MgAl_2O_4$ and $BaAl_2O_4$ photocatalysts by the polyacrylamide gel method exhibits high photocatalytic activity. The results

TABLE 2 | The photocatalytic activity of MAl_2O_4 photocatalyst.

Samples	Dye	Lamp	$C_{catalyst}$ (g L^{-1})	C_{dye} (mg L^{-1})	Irradiation time (min)	D% (%)	References
$MgAl_2O_4$	Reactive Red Me 4BL dye	UV illumination	2	10	350	90.00	Nassar et al. (2014)
		Sunlight				95.45	
Amorphous Earth-abundant	Methylene bule	300 w Xe lamp	1	10	240	81.01	Qian et al. (2017)
$MgAl_2O_4$	Phenol			50		40.01	
Mixed Amorphous and crystalline $MgAl_2O_4$ nanopowders	Methylene bule	350 W Xe-lamp	0.75	10	100	99.5	Li et al. (2011)
$MgAl_2O_4$	Methyl orange	high pressure mercury lamp	5	12	120	21	Jiang et al. (2014)
	Acid red B					23	
	Reactive brilliant red K-2G					21	
$MgAl_2O_4$	Malachite green	lamp (300 W)	0.3125 5	100	40	100	Parvarinezhad et al. (2019)
$MgAl_2O_4$	Methylene bule	150 W Xe-lamp	1	5	180	89.6	Wang et al. (2019a)
$BaAl_2O_4$	Methylene bule	100 W high pressure mercury lamp	1	5	240	79	Wang et al. (2019d)

TABLE 3 | The photocatalytic activity of metal ion doped MAl_2O_4(M = Mg, Sr, and Ba) photocatalyst.

Samples	Dye	Lamp	$C_{catalyst}$ (g L^{-1})	C_{dye} (mg L^{-1})	Irradiation time (min)	D%	References
$Mg_{1-x}Zn_xAl_2O_4$	Methylene bule	A Hg lamp	2	10	240	99	Li et al. (2016)
Cu^{2+} engrafted $MgAl_2O_4$	Methylene bule	Sunlight	1.5	10	240	98.5	Mukherjee et al. (2020)
Mg_{1-x} $Co_xAl_2O_4$	Methylene bule	150 W Xe-lamp	1	5	120	98	Wang et al. (2019c)
$MgAl_2O_4$: Ce	Rhodamine B	150-W/m^2 xenon lamp	1.5	5	180	88.2	Chen et al. (2019)
Mn-codoped $MgAl_2O_4$: Ce	Methylene blue	150-W/m^2 xenon lamp	1	5	180	85	Wang et al. (2019e)
Eu^{2+}, Dy^{3+}-doped $SrAl_2O_4$	H_2O	A high pressure Hg lamp	1	400 ml	100	0.78 mmol/h.g	Park, (2018)
Bismuth doped $SrAl_2O_4$	Methylene blue	high pressure mercury lamp	0.428	25	120	78	García et al. (2018)
	Congo red			10		100	
$SrAl_2O_4$:xCu	Congo red	lamp (300 W)	0.6	15	120	100	Berlanga et al. (2017)
$SrAl_2O_4$: Ce: Mn	Congo red	200 W/m^2 xenon lamp	0.5	10	300	80	Shifa Wang et al. (2020)
Rare earth doped $SrAl_2O_4$	Methylene orange	Solar	1	25	240	22.8	Deepika and Kumar, (2020)
Nd^{3+} doped $BaAl_2O_4$	Methylene blue	100 mW/cm^2 Newport solar simulator	1	15	180	99%	Mumanga et al. (2021)
$BaAl_2O_4$: Ce: Mn	Methylene blue	150 W/m^2 xenon lamp	1	5	240	79.85	Wang et al. (2020c)

show that the photocatalytic activity of MAl_2O_4 synthesized by different preparation methods is different.

Photocatalytic Activity of Metal Ion Doped MAl_2O_4(M = Mg, Sr, and Ba) Photocatalysts

Metal ion doping can effectively change the band gap value of aluminate photocatalyst so as to enhance its photocatalytic activity. Different doping ions have different regulation on the band gap of aluminate, so different metal ions doped aluminate show different photocatalytic activity. **Table 3** shows the photocatalytic activity of metal ion doped MAl_2O_4(M = Mg, Sr, and Ba) photocatalyst. Li et al. 2(016) synthesized the $Mg_{1-x}Zn_xAl_2O_4$ spinel nanoparticles by the chemical coprecipitation method have a high photocatalytic activity. The photocatalytic activity of $Mg_{1-x}Zn_xAl_2O_4$ spinel nanoparticles increased with the increasing of x value as shown in **Figure 3**. When Cu^{2+} ions were engrafted onto $MgAl_2O_4$ nanoparticles by a highly adaptable and energy efficient chemical process, the photocatalytic activity of the system was greatly improved (Mukherjee et al., 2020). The photocatalytic activity of $MgAl_2O_4$ can also be improved by introducing Co (Wang et al., 2019c) or Ce (Chen et al., 2019)

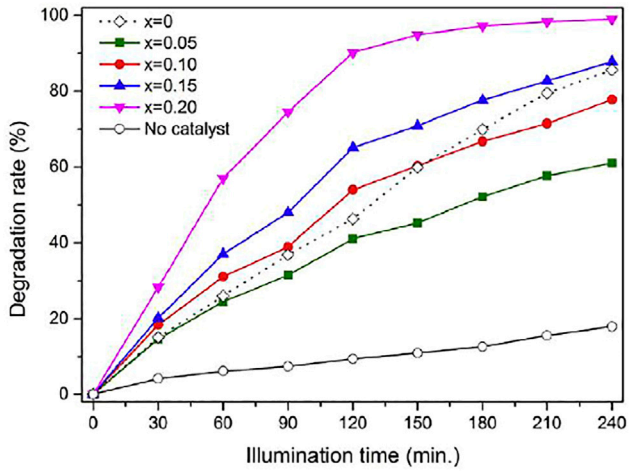

FIGURE 3 | Degradation rate curve with x value of $Mg_{1-x}Zn_xAl_2O_4$ spinel nanoparticles (Li et al., 2016). Adapted from ref. (Li et al., 2016). Copyright © 2016 Elsevier Masson SAS.

ions into $MgAl_2O_4$. Ce and Mn co-doped $MgAl_2O_4$ can further improve the photocatalytic activity of $MgAl_2O_4$ (Wang et al., 2019e). Metal ion doping in $SrAl_2O_4$ has also been widely used, through Eu^{2+} and Dy^{3+} (Park, 2018), Bi (García et al., 2018), Cu (Berlanga et al., 2017), Ce and Mn (Shifa Wang et al., 2020), and rare earth ion (Deepika and Kumar, 2020) doping $SrAl_2O_4$, all enhance the photocatalytic activity of $SrAl_2O_4$. Similarly, Nd^{3+} (Mumanga et al., 2021) and Ce and Mn (Wang et al., 2020c) ions are also used in the doping of $BaAl_2O_4$, and their photocatalytic activity is greatly improved compared with that of single-phase $BaAl_2O_4$.

Photocatalytic Activity of MAl_2O_4(M = Mg, Sr, and Ba) Based Multivariate Heterojunction Photocatalysts

The construction of multiple heterojunction composite is beneficial to combine the advantages of multiple semiconductor materials and enhance the photocatalytic activity of the system. The MAl_2O_4 (M = Mg, Sr, and Ba) photocatalyst has a relatively large band gap, which makes it difficult to respond to visible light. Therefore, the semiconductor materials that can respond to visible light are preferentially selected for the construction of heterojunction. **Table 4** shows the photocatalytic activity of MAl_2O_4(M = Mg, Sr, and Ba) based multivariate heterojunction photocatalysts. $MgAl_2O_4$ based photocatalyst was constructed by combining various semiconductor materials, and its photocatalytic activity was confirmed to be enhanced (Abbasi Asl et al., 2019; Abbasi Asl et al., 2020; Wang et al., 2021d). Meanwhile, $MgAl_2O_4/CeO_2/Mn_3O_4$ ternary heterojunction photocatalyst was constructed by combining CeO_2 and Mn_3O_4, showing high photocatalytic activity for the degradation of methylene blue dye (Li et al., 2021). Aluminate is a very good phosphor base material, the introduction of activated ions will make aluminate luminescence as phosphor. Recently, researchers have found that aluminate activated by metal ions as photocatalysts also have high photocatalytic activity. The photocatalytic activity of $SrAl_2O_4$ was greatly enhanced by the construction of multi-component composite $SrAl_2O_4$ photocatalysts (García et al., 20162016; Xiao et al., 2018; Liu et al., 2019; Zargoosh and Moradi Aliabadi, 2019; Mavengere and Kim, 2020; Aliabadi et al., 2021). The construction of the heterojunction provides a technical

TABLE 4 | The photocatalytic activity of MAl_2O_4(M = Mg, Sr, and Ba) based multivariate heterojunction photocatalysts.

Samples	Dye	Lamp	$C_{catalyst}$ (g L^{-1})	C_{dye} (mg L^{-1})	Irradiation time (min)	D % (%)	References
$Bi_7O_9I_3$-$MgAl_2O_4$	Methylene bule	Sunlight	0.5	10	120	95.9	Abbasi Asl et al. (2019)
$MgAl_2O_4$-AC nanophotocatalys	Methylene blue	Solar light	1	30	140	96	Abbasi Asl et al. (2020)
$CeO_2/MgAl_2O_4$	Methylene blue	150 W Xe-lamp	1	5	180	78	Wang et al. (2021d)
$MgAl_2O_4/CeO_2/Mn_3O_4$ heterojunction photocatalyst	Methylene blue	150 W Xe-lamp	1	5	180	94.6	Li et al. (2021)
g-C_3N_4–WO_3–Bi_2WO_6/$SrAl_2O_4$: Eu^{2+},Dy^{3+} nanocomposite	Basic blue 41	400 watt metal halide lamp	0.1	1	60	98	Aliabadi et al. (2021)
CdS-sheathed, $SrAl_2O_4$:Eu^{2+}, Dy^{3+} nanocomposites	Methyl orange	300 W Xenon lamp		10	30	96.3	Xiao et al. (2018)
g-C_3N_4/$SrAl_2O_4$:Eu,Dy/SiO_2	Methylene bule	300 W Xe lamp	1	5	60	90	Mavengere and Kim, (2020)
(Eu,Dy)-doped strontium aluminate/ aluminosilicate	Methylene bule	75 W Xenon lamp	0.3	30 mmol	300	100	(García et al., 20162016)
g-C_3N_4@Au@$SrAl_2O_4$:Eu^{2+},Dy^{3+} Composite	Rhodamine B	300 W Xe lamp	0.05	10	120	80	Liu et al. (2019)
$SrAl_2O_4$:Eu^{2+}: Dy^{3+}/WO_3/polyester nanocomposite	Methylene blue	lamp (300 W)	0.15	15	90	99	Zargoosh and Moradi Aliabadi, (2019)
Ag/$BaAl_2O_4$	Gaseous toluene	150 W Xe-lamp	1	5	240	88	Zhu et al. (2015)
$TiO_2/BaAl_2O_4$: Eu^{2+}, Dy^{3+}	Gaseous benzene	10 W UV lamps	0.1	—	300	40	Li et al. (2009)

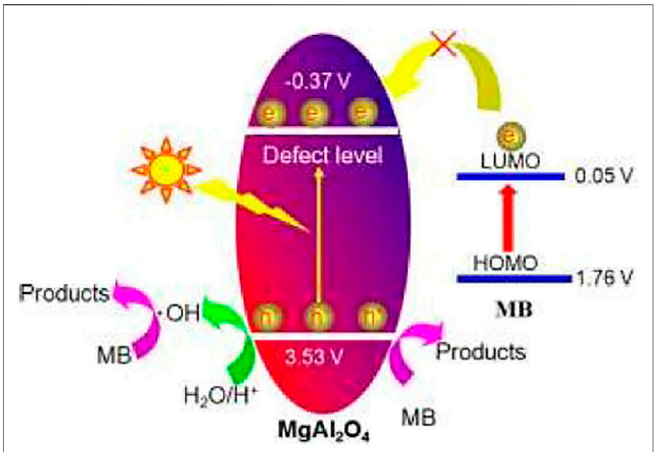

FIGURE 4 | Photocatalytic mechanism of $MgAl_2O_4$ photocatalyst (Qian et al., 2017). Adapted from ref. (Qian et al., 2017). Copyright © 2017 Royal Society of Chemistry.

reference for the subsequent study of other aluminate photocatalysts. The photocatalytic activity of aluminate modified by noble metal particles can be greatly improved by plasma resonance effect. However, the modification of Silver particles on the surface of $MgAl_2O_4$ easily leads to the hydrolysis of $MgAl_2O_4$, which greatly affects the application of $MgAl_2O_4$ as a photocatalyst. Zhu et al. (2015) synthesized the $Ag/BaAl_2O_4$ photocatalyst shows high photocatalytic activity for the degradation of Gaseous toluene. When the silver content is low, the hydrolysis of $BaAl_2O_4$ is inhibited and it can be used as a photocatalyst. Li et al. (2009) constructed the $TiO_2/BaAl_2O_4$: Eu^{2+}, Dy^{3+} photocatalyst exhibits high photocatalytic activity. These successful applications provide a new idea for the use of wide-band gap semiconductors as photocatalysts in future research.

PHOTOCATALYTIC MECHANISM OF MAL_2O_4(M = MG, SR, AND BA) BASED PHOTOCATALYSTS

Different types of photocatalysts have slightly different photocatalytic mechanisms. The photocatalytic mechanism of single component aluminate photocatalyst, ion doped aluminate photocatalyst and heterogeneous aluminate photocatalyst was compared and analyzed.

Photocatalytic Mechanism of MAl_2O_4 Photocatalysts

Due to the large band gap value of a single component aluminate, it is difficult to respond directly to visible light. When single component aluminate is synthesized by a special method, it is easy to introduce defects such as oxygen vacancy into the aluminate, so that it has visible photocatalytic activity.

Figure 4 shows the photocatalytic mechanism of $MgAl_2O_4$ photocatalyst. When a beam of light hits the surface of $MgAl_2O_4$, electrons jump from its valence band to the conduction band, and leaving holes in the valence band. It is difficult for electrons to jump directly to the conduction band without the action of defect levels. Therefore, the defect level plays an important role in the whole photocatalytic process. Combined with the band theory analysis, it is found that the degradation of methylene blue dye is difficult to take place in the photosensitization process. Therefore, the whole process is mainly photocatalytic degradation, the valence band electrons and conduction band holes are involved in the reaction, and the final generation of non-toxic and harmless products. The related chemical reactions can be described as follows (Shifa Wang et al., 2020):

(1) The creation of electron hole pairs.

$$MAl_2O_4 + h \rightarrow MAl_2O_4 \rightarrow e^- + h^+ \quad (4)$$

(2) The production of hydroxyl radicals

$$h^+ + OH^- \rightarrow [MS1_2O_4] - \bullet OH \quad (5)$$

(3) The production of superoxide radicals

$$e^- + O_2 \rightarrow \bullet O^{2-} \quad (6)$$

$$\bullet O^2 + 2H^+ + e^- \rightarrow H_2O_2 \quad (7)$$

$$2e^- + O_2 + 2H^+ \rightarrow H_2O_2 \quad (8)$$

$$e^- + H_2O_2 \rightarrow \bullet OH + OH^- \quad (9)$$

$$\bullet O^{2-} + H_2O_2 \rightarrow \bullet OH + OH^- + O_2 \quad (10)$$

(4) Dye degradation

$$\bullet OH + dye \rightarrow CO_2 + H_2O + non - toxic\ products \quad (11)$$

Photocatalytic Mechanism of MAl_2O_4 Based Heterojunction Photocatalysts

During the construction of the multiple heterostructure, the semiconductor material enhancing the photocatalytic activity of visible light is regarded as the defect level, so the other half of the aluminate heterojunction acts as the defect level. However, multiple heterojunction photocatalysts introduce new semiconductor materials and have great influence on the phase purity of the whole system. Therefore, the photocatalytic mechanism is different from that of a single component photocatalyst. **Figure 5** shows the photocatalytic mechanism of $MgAl_2O_4/CeO_2/Mn_3O_4$ heterojunction photocatalyst. $MgAl_2O_4$, CeO_2, and Mn_3O_4 form a double p-n heterojunction structure among each other, which facilitates the transfer and separation of electron hole pairs, thus enhancing the photocatalytic activity of the system. The separation of electron and hole pairs accelerates the oxidation or reduction reactions of each, which then reacts with the dye to produce non-toxic and harmless products.

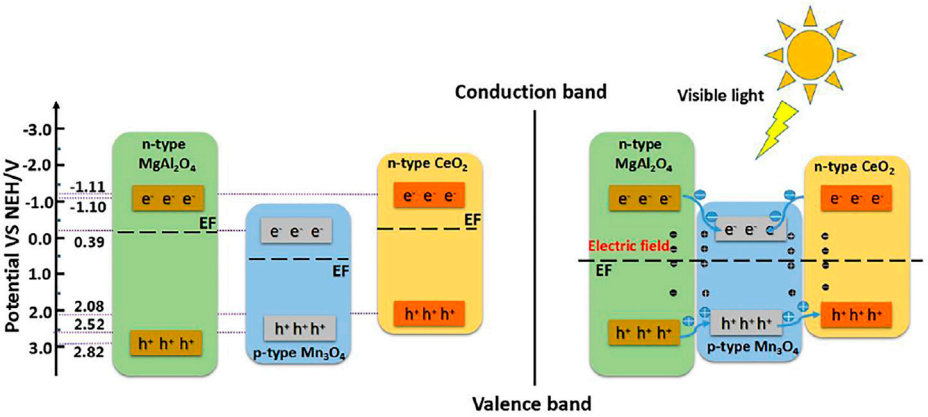

FIGURE 5 | Photocatalytic mechanism of $MgAl_2O_4/CeO_2/Mn_3O_4$ heterojunction photocatalyst (Li et al., 2021). Adapted from ref. (Li et al., 2021). Copyright © 2020 Elsevier Ltd.

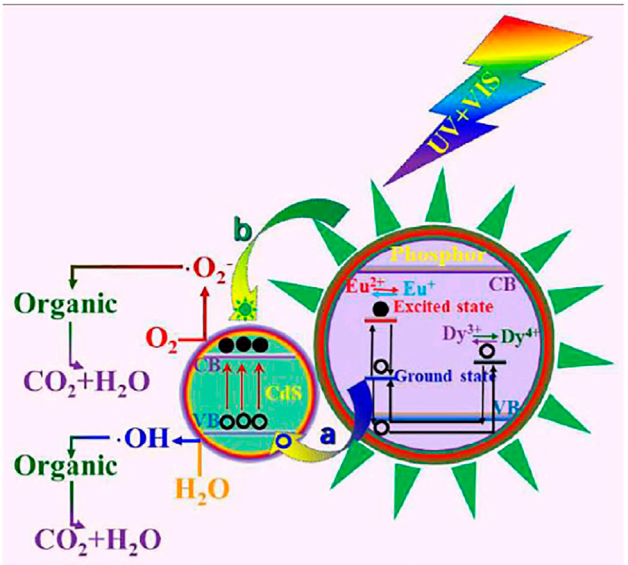

FIGURE 6 | Photocatalytic mechanism of CdS-sheathed $SrAl_2O_4$: Eu^{2+}, Dy^{3+} heterojunction photocatalysts (Xiao et al., 2018). Adapted from ref. (Xiao et al., 2018). Copyright © 2018 Royal Society of Chemistry.

Photocatalytic Mechanism of Metal Ion Doped MAl_2O_4 Based Heterojunction Photocatalysts

Activated ions induce aluminate luminescence, which is its advantage when used as a photocatalyst. **Figure 6** shows the photocatalytic mechanism of CdS-sheathed $SrAl_2O_4$: Eu^{2+}, Dy^{3+} heterojunction photocatalysts. When $SrAl_2O_4$: Eu^{2+}, Dy^{3+} is used as phosphors, the recombination of electron and hole pairs in the system is accelerated. However, when it combines with other semiconductor materials to form heterojunction photocatalyst, the energy absorbed by it can promote the electron transition in the whole system, thus accelerating the separation of electron and hole pairs in the system. The non-meeting of electrons and holes on CdS causes each to react with the dye to form CO_2, H_2O and other small molecular organics.

CONCLUSION AND OUTLOOK

Aluminate based photocatalyst is a kind of photocatalyst developed rapidly in recent years. Despite it have a very large band gap, researchers have always found ways to promote the transfer and separation of electrons and hole pairs, and thereby improving their photocatalytic activity. For the single-component aluminate photocatalysts, defects are introduced to provide defect levels to promote electron transition to aluminate conduction band under extreme conditions such as high temperature and high pressure, so as to enhance the photocatalytic activity of visible light. Similarly, impurity ions can be introduced into the lattice of aluminate by ion doping to improve the migration and separation efficiency of electron hole pairs and improve the photocatalytic activity of aluminate. The construction of special heterojunction structure is a simple method with relatively mature technology. By introducing other semiconductor materials with excellent performance, the construction of multiple heterojunction aluminate based photocatalyst has become a hot research field.

There are seven development trends of aluminate based photocatalysts in the future 1) The hydrolysis of aluminate is still one of the key problems to be solved. When silver particles are used to modify aluminate photocatalyst, aluminate will produce different degree of hydrolysis, which has been a difficult problem for researchers. The development of new synthetic pathways may solve this problem. 2) New application of aluminate based heterojunction phosphors in photocatalysis. When aluminate phosphor is combined with other semiconductor photocatalysts, the photocatalytic activity of the whole system will be greatly improved. However, the research of aluminate based phosphor in the field of photocatalysis is still in its infancy, and further research is

needed. 3) The photocatalytic mechanism needs further study. The newly developed aluminate photocatalyst will face the problem that the existing mechanism cannot explain, so it is necessary to develop a new explanation mechanism. 4) The effect of different morphologies of aluminate photocatalysts on photocatalytic activity needs further study. The specific surface area of aluminate photocatalysts with different morphologies was different, and their degradation activity to dyes was obviously different. 5) The photocatalytic activity of aluminate photocatalyst modified by lanthanide metal particles is worth further study. There is no evidence that the modification of aluminate photocatalyst by lanthanide metal particles will lead to hydrolysis, so it is also worth studying. 6) Modification of aluminate photocatalyst by organic macromolecular network. The modification of aluminate photocatalyst by organic macromolecular network is beneficial to provide electron transport carrier for aluminate, thus enhancing the photocatalytic activity of aluminate. 7) New applications of photocatalysts are worth exploring. Novel photocatalysts may induce new interpretation mechanisms, thus promoting the application of these photocatalysts in new fields.

AUTHOR CONTRIBUTIONS

All authors listed have made a substantial, direct, and intellectual contribution to the work and approved it for publication.

FUNDING

This work was supported by thethe Provincial Natural Science Key Foundation of Anhui University (KJ 2019A0522, KJ 2021A0668), General Project of AnhuiProvince (1908085ME150), and Industry-University Cooperation Collaborative Education Projects by Ministry of Education of China (202102227037, 202102538045)

REFERENCES

Abbasi Asl, E., Haghighi, M., and Talati, A. (2020). Enhanced Simulated Sunlight-Driven Magnetic MgAl2O4-AC Nanophotocatalyst for Efficient Degradation of Organic Dyes. *Separat. Purif. Technol.* 251, 117003. doi:10.1016/j.seppur.2020.117003

Abbasi Asl, E., Haghighi, M., and Talati, A. (2019). Sono-solvothermal Fabrication of Flowerlike Bi7O9I3-MgAl2O4 P-N Nano-Heterostructure Photocatalyst with Enhanced Solar-Light-Driven Degradation of Methylene Blue. *Solar Energy* 184, 426–439. doi:10.1016/j.solener.2019.04.012

Alam, M. W., Kumar, V. G. D., Ravikumar, C. R., Prashantha, S. C., Murthy, H. C. A., and Kumar, M. R. A. (2022). Chromium (III) Doped Polycrystalline MgAl2O4 Nanoparticles for Photocatalytic and Supercapacitor Applications. *J. Phys. Chem. Sol.* 161, 110491. doi:10.1016/j.jpcs.2021.110491

Aliabadi, H. M., Zargoosh, K., Afshari, M., Dinari, M., and Maleki, M. H. (2021). Synthesis of a Luminescent G-C3n4-WO3-Bi2WO6/SrAl2O4:Eu2+,Dy3+ Nanocomposite as a Double Z-Scheme Sunlight Activable Photocatalyst. *New J. Chem.* 45 (10), 4843–4853. doi:10.1039/D0NJ05529H

Bao, H., Zhu, S., Zhou, L., Fu, H., Zhang, H., and Cai, W. (2020). Mars-van-Krevelen Mechanism-Based Blackening of Nano-Sized white Semiconducting Oxides for Synergetic Solar Photo-Thermocatalytic Degradation of Dye Pollutants. *Nanoscale* 12 (6), 4030–4039. doi:10.1039/C9NR09534A

Basyrova, L., Bukina, V., Balabanov, S., Belyaev, A., Drobotenko, V., Dymshits, O., et al. (2021). Synthesis, Structure and Spectroscopy of Fe2+:MgAl2O4 Transparent Ceramics and Glass-Ceramics. *J. Lumin.* 236, 118090. doi:10.1016/j.jlumin.2021.118090

Berlanga, A., Garcia-Diaz, R., Garcia, C. R., Oliva, J., Romero, M. T., and Diaz-Torres, L. A. (2017). Photocatalytic Activity of SrAl2O4:xCu Powders under Solar Irradiation. *Nhc* 16, 63–66. doi:10.4028/www.scientific.net/nhc.16.63

Bhavani, P., Manikandan, A., Jaganathan, S. K., Shankar, S., and Antony, S. A. (2018). Enhanced Catalytic Activity, Facile Synthesis and Characterization Studies of Spinel Mn-Co Aluminate Nano-Catalysts. *j nanosci nanotechnol* 18 (2), 1388–1395. doi:10.1166/jnn.2018.14112

Boudiaf, S., Nasrallah, N., Mellal, M., Belabed, C., Belhamdi, B., Meziani, D., et al. (2020). Synthesis and Characterization of Semiconductor CoAl2O4 for Optical and Dielectric Studies: Application to Photodegradation of Organic Pollutants under Visible Light. *Optik* 219, 165038. doi:10.1016/j.ijleo.2020.165038

Canaza-Mamani, E. A., Cano, N. F., Mosqueira-Yauri, J., Rao, T. K. G., Aynaya-Cahui, S. C., Gonsalez-Vasquez, A. J., et al. (2021). TL and EPR Characteristics of SrAl2O4 Phosphor Prepared by Solid-state Reaction Method. *J. Lumin.*, 118585. doi:10.1016/j.jlumin.2021.118585

Chellammal Gayathri, R., Elakkiya, V., and Sumathi, S. (2021). Effect of Method of Preparation on the Photocatalytic Activity of NiAl2O4. *Inorg. Chem. Commun.* 129, 108634. doi:10.1016/j.inoche.2021.108634

Chen, C., Li, Q., Zhang, Q., Li, Y., Wei, Y., and Wang, S. (2019). "Artificial Neural Network Algorithm for Predict the Photocatalytic Activity of the Mn Co-doped MgAl2O4: Ce Composite Photocatalyst," in 2019 IEEE International Conference on Signal, Information and Data Processing (ICSIDP), Chongqing, China, 11-13 Dec. 2019 (IEEE), 1–5.

Chen, W., Huang, J., He, Z.-C., Ji, X., Zhang, Y.-F., Sun, H.-L., et al. (2021). Accelerated Photocatalytic Degradation of Tetracycline Hydrochloride over CuAl2O4/g-C3n4 P-N Heterojunctions under Visible Light Irradiation. *Separat. Purif. Technol.* 277, 119461. doi:10.1016/j.seppur.2021.119461

Chen, X. Y., Ma, C., Zhang, Z. J., and Li, X. X. (2009). Structure and Photoluminescence Study of Porous Red-Emitting MgAl2O4:Eu3+ Phosphor. *Microporous mesoporous Mater.* 123 (1-3), 202–208. doi:10.1016/j.micromeso.2009.04.002

Cheng, T., Gao, H., Li, R., Wang, S., Yi, Z., and Yang, H. (2021). Flexoelectricity-induced Enhancement in Carrier Separation and Photocatalytic Activity of a Photocatalyst. *Appl. Surf. Sci.* 566, 150669. doi:10.1016/j.apsusc.2021.150669

Cheng, T., Gao, H., Sun, X., Xian, T., Wang, S., Yi, Z., et al. (2021). An Excellent Z-Scheme Ag2MoO4/Bi4Ti3O12 Heterojunction Photocatalyst: Construction Strategy and Application in Environmental Purification. *Adv. Powder Technol.* 32 (3), 951–962. doi:10.1016/j.apt.2021.01.039

Cheng, T., Gao, W., Gao, H., Wang, S., Yi, Z., Wang, X., et al. (2021). Piezocatalytic Degradation of Methylene Blue, Tetrabromobisphenol A and Tetracycline Hydrochloride Using Bi4Ti3O12 with Different Morphologies. *Mater. Res. Bull.* 141, 111350. doi:10.1016/j.materresbull.2021.111350

Ching, W. Y., Xu, Y.-N., and Brickeen, B. K. (2001). Comparative Study of the Electronic Structure of Two Laser Crystals: BeAl2O4andLiYF4. *Phys. Rev. B* 63 (11), 115101. doi:10.1103/PhysRevB.63.115101

Deepika, P., and Kumar, C. A. (2020). Photocatalytic Properties of Persistent Luminescent Rare Earth Doped $SrAl_2O_4$ Phosphor under Solar Radiation. *Nanosystems-Physics Chem. Maths.* 11 (5), 590–594.

Feng, H., He, C., Ma, G., and Zhiani, R. (2021). Imidazolium Ionic Liquid Functionalized Nano Dendritic CuAl2O4 for Visible Light-Driven Photocatalytic Degradation of Dye Pollutant. *Inorg. Chem. Commun.* 132, 108818. doi:10.1016/j.inoche.2021.108818

Forouzesh, M., Ebadi, A., and Abedini, F. (2021). Thermocatalytic Persulfate Activation for Metronidazole Removal in the Continuous Operation. *Separat. Purif. Technol.* 258, 118055. doi:10.1016/j.seppur.2020.118055

Ganesh, I., Srinivas, B., Johnson, R., Saha, B. P., and Mahajan, Y. R. (2004). Microwave Assisted Solid State Reaction Synthesis of MgAl2O4 Spinel

Powders. *J. Eur. Ceram. Soc.* 24 (2), 201–207. doi:10.1016/S0955-2219(03)00602-2

Gao, H. J., Wang, S. F., Fang, L. M., Sun, G. A., Chen, X. P., Tang, S. N., et al. (2021). Nanostructured Spinel-type M(M = Mg, Co, Zn)Cr2O4 Oxides: Novel Adsorbents for Aqueous Congo Red Removal. *Mater. Today Chem.* 22, 100593. doi:10.1016/j.mtchem.2021.100593

Gao, H., Yang, H., Wang, S., Li, D., Wang, F., Fang, L., et al. (2018). A New Route for the Preparation of CoAl2O4 Nanoblue Pigments with High Uniformity and its Optical Properties. *J. Sol-gel Sci. Technol.* 86 (1), 206–216. doi:10.1007/s10971-018-4609-y

Gao, H., Yu, C., Wang, Y., Wang, S., Yang, H., Wang, F., et al. (2022). A Novel Photoluminescence Phenomenon in a SrMoO4/SrWO4 Micro/nano Heterojunction Phosphors Obtained by the Polyacrylamide Gel Method Combined with Low Temperature Calcination Technology. *J. Lumin.* 243, 118660. doi:10.1016/j.jlumin.2021.118660

García, C. R., Diaz-Torres, L. A., Oliva, J., Romero, M. T., and Salas, P. (20162016). Photocatalytic Activity and Optical Properties of Blue Persistent Phosphors under UV and Solar Irradiation. *Int. J. Photoenergy* 2016, 1–8. doi:10.1155/2016/1303247

García, C. R., Oliva, J., Arroyo, A., Garcia-Lobato, M. A., Gomez-Solis, C., and Torres, L. A. D. (2018). Photocatalytic Activity of Bismuth Doped SrAl2O4 Ceramic Powders. *J. Photochem. Photobiol. A: Chem.* 351, 245–252. doi:10.1016/j.jphotochem.2017.10.039

Ghalei, S., and Handa, H. (2022). A Review on Antibacterial Silk Fibroin-Based Biomaterials: Current State and Prospects. *Mater. Today Chem.* 23, 100673. doi:10.1016/j.mtchem.2021.100673

Gholami, T., Salavati-Niasari, M., and Varshoy, S. (2016). Investigation of the Electrochemical Hydrogen Storage and Photocatalytic Properties of CoAl2O4 Pigment: Green Synthesis and Characterization. *Int. J. Hydrogen Energ.* 41 (22), 9418–9426. doi:10.1016/j.ijhydene.2016.03.144

Habibi, N., Wang, Y., Arandiyan, H., and Rezaei, M. (2017). Low-temperature Synthesis of Mesoporous Nanocrystalline Magnesium Aluminate (MgAl2O4) Spinel with High Surface Area Using a Novel Modified Sol-Gel Method. *Adv. Powder Technol.* 28 (4), 1249–1257. doi:10.1016/j.apt.2017.02.012

Han, M., Wang, Z., Xu, Y., Wu, R., Jiao, S., Chen, Y., et al. (2018). Physical Properties of MgAl 2 O 4 , CoAl 2 O 4 , NiAl 2 O 4 , CuAl 2 O 4 , and ZnAl 2 O 4 Spinels Synthesized by a Solution Combustion Method. *Mater. Chem. Phys.* 215, 251–258. doi:10.1016/j.matchemphys.2018.05.029

Ibrahim, Y., Meslam, M., Eid, K., Salah, B., Abdullah, A. M., Ozoemena, K. I., et al. (2022). A Review of MXenes as Emergent Materials for Dye Removal from Wastewater. *Separat. Purif. Technol.* 282, 120083. doi:10.1016/j.seppur.2021.120083

Ivashchenko, A. N., Tedeeva, M. A., Kartavova, K. E., Aimaletdinov, T. R., Pribytkov, P. V., and Kustov, A. L. (2021). Oxidative Dehydrogenation of Ethane in the Presence of CO2 on CrOx/SiO2 Catalysts. *Russ. J. Phys. Chem.* 95 (12), 2417–2421. doi:10.1134/S0036024421120104

Jiang, Y. Y., Zhang, J. W., Hu, Z. Q., and Liu, J. X. (2014). Synthesis and Visible Light Photocatalytic Activity of Spinel MAl2O4 (M=Mg, Zn, Cu). *Amm* 455, 99–105. doi:10.4028/www.scientific.net/AMM.455.99

Kharlanov, A. N., Pankina, G. V., and Lunin, V. V. (2019). Physicochemical Properties of Potassium-Promoted Fe-Containing Catalysts for the Hydrogenation of CO over Magnesium Aluminum Spinels: IR Spectroscopy. *Russ. J. Phys. Chem.* 93 (12), 2356–2364. doi:10.1134/S0036024419120136

Kim, K. O., Evdokimenko, N. D., Pribytkov, P. V., Tedeeva, M. A., Borkov, S. A., and Kustov, A. L. (2021). Synthesis of Methanol from CO2 on Cu-Zn/xAl2O3-(1 - x)SiO2 Catalysts. Effect of Support Composition. *Russ. J. Phys. Chem.* 95 (12), 2422–2425. doi:10.1134/S0036024421120128

Kiryakov, A. N., Zatsepin, A. F., and Osipov, V. V. (2021). Optical Properties of Polyvalent Iron Ions and Anti-site Defects in Transparent MgAl2O4 Ceramics. *J. Lumin.* 239, 118390. doi:10.1016/j.jlumin.2021.118390

Kumar, A., and Luxmi, V. (2021). Development of an Efficient Eco-Friendly Photo-Catalyst Using Agro-Waste Turmeric Leaves and its Characterizations. *Optik* 242, 167057. doi:10.1016/j.ijleo.2021.167057

Lahiri, S. K., Zhang, C., Sillanpää, M., and Liu, L. (2022). Nanoporous NiO@SiO2 Photo-Catalyst Prepared by Ion-Exchange Method for Fast Elimination of Reactive Dyes from Wastewater. *Mater. Today Chem.* 23, 100677. doi:10.1016/j.mtchem.2021.100677

Li, F.-t., Zhao, Y., Liu, Y., Hao, Y.-j., Liu, R.-h., and Zhao, D.-s. (2011). Solution Combustion Synthesis and Visible Light-Induced Photocatalytic Activity of Mixed Amorphous and Crystalline MgAl2O4 Nanopowders. *Chem. Eng. J.* 173 (3), 750–759. doi:10.1016/j.cej.2011.08.043

Li, H., Liu, Y., Tang, J., and Deng, Y. (2016). Synthesis, Characterization and Photocatalytic Properties of Mg1−xZnxAl2O4 Spinel Nanoparticles. *Solid State Sci.* 58, 14–21. doi:10.1016/j.solidstatesciences.2016.05.007

Li, J., Wang, S., Sun, G., Gao, H., Yu, X., Tang, S., et al. (2021). Facile Preparation of MgAl2O4/CeO2/Mn3O4 Heterojunction Photocatalyst and Enhanced Photocatalytic Activity. *Mater. Today Chem.* 19, 100390. doi:10.1016/j.mtchem.2020.100390

Li, S., Wang, W., Chen, Y., Zhang, L., Guo, J., and Gong, M. (2009). Fabrication and Characterization of TiO2/BaAl2O4: Eu2+, Dy3+ and its Photocatalytic Performance towards Oxidation of Gaseous Benzene. *Catal. Commun.* 10 (7), 1048–1051. doi:10.1016/j.catcom.2008.12.064

Li, X.-Y., Xu, J., Cheng, J.-P., Feng, L., Shi, Y.-F., and Ji, J. (2017). TiO2-SiO2/GAC Particles for Enhanced Electrocatalytic Removal of Acid orange 7 (AO7) Dyeing Wastewater in a Three-Dimensional Electrochemical Reactor. *Separat. Purif. Technol.* 187, 303–310. doi:10.1016/j.seppur.2017.06.058

Liu, H., Wang, S., Gao, H., Yang, H., Wang, F., Chen, X., et al. (2022). A Simple Polyacrylamide Gel Route for the Synthesis of MgAl2O4 Nanoparticles with Different Metal Sources as an Efficient Adsorbent: Neural Network Algorithm Simulation, Equilibrium, Kinetics and Thermodynamic Studies. *Separat. Purif. Technol.* 281, 119855. doi:10.1016/j.seppur.2021.119855

Liu, X., Chen, X., Li, Y., Wu, B., Luo, X., Ouyang, S., et al. (2019). A G-C3N4@Au@SrAl2O4:Eu2+,Dy3+ Composite as an Efficient Plasmonic Photocatalyst for Round-The-Clock Environmental Purification and Hydrogen Evolution. *J. Mater. Chem. A.* 7 (32), 19173–19186. doi:10.1039/C9TA06423K

Liu, X., Wang, S., Yu, X., Tang, S., Fang, L., and Lei, L. (2020). Fabrication and Photoluminescence Properties of $MgAl_2O_4$: Mg Phosphors. *Chin. J. Mater. Res.* 34 (10), 784–792. doi:10.11901/1005.3093.2020.072

Mathew, M., Rad, M. A., Mata, J. P., Mahmodi, H., Kabakova, I. V., Raston, C. L., et al. (2022). Hyperbranched Polymers Tune the Physicochemical, Mechanical, and Biomedical Properties of Alginate Hydrogels. *Mater. Today Chem.* 23, 100656. doi:10.1016/j.mtchem.2021.100656

Mavengere, S., and Kim, J.-S. (2020). Photocatalytic Properties of G-C3n4-Supported on the SrAl2O4:Eu,Dy/SiO2. *Coatings* 10 (10), 917. doi:10.3390/coatings10100917

Mkhalid, I. A. (2022). Hydrogen Evolution over Sol-Gel Prepared Visible-Light-Responsive Ag2O/SrAl2O4/CNT Ternary Photocatalyst. *Ceramics Int.* 48 (2), 1542–1549. doi:10.1016/j.ceramint.2021.09.233

Moirangthem, N. S., Lisham, P. C., Barua, A. G., and Gartia, R. K. (2019). Electron Life Time (τ) in Trap Levels of Dy3+ Activated Calcium Aluminate: Implications in TL Dosimetry. *J. Phys. Conf. Ser.* 1330 (1), 012009. doi:10.1088/1742-6596/1330/1/012009

Mu, H.-Y., Li, F.-T., An, X.-T., Liu, R.-H., Li, Y.-L., Qian, X., et al. (2017). One-step Synthesis, Electronic Structure, and Photocatalytic Activity of Earth-Abundant Visible-Light-Driven FeAl2O4. *Phys. Chem. Chem. Phys.* 19 (14), 9392–9401. doi:10.1039/C7CP01007A

Mukherjee, A., Adak, M. K., Dhak, P., and Dhak, D. (2020). A Simple Chemical Method for the Synthesis of Cu2+ Engrafted MgAl2O4 Nanoparticles: Efficient Fluoride Adsorbents, Photocatalyst and Latent Fingerprint Detection. *J. Environ. Sci.* 88, 301–315. doi:10.1016/j.jes.2019.09.004

Mumanga, T. J., Díaz-Torres, L. A., and Gómez-Solís, C. (2021). Nd3+ Doped BaAl2O4 for Enhanced Photocatalytic Degradation of Methylene Blue. *Mater. Lett.* 292, 129664. doi:10.1016/j.matlet.2021.129664

Musa, M. A., Xu, D., Sun, F., Shao, H., Dong, X., Azis, R. A. S., et al. (2021). Electrospun ZnFe2O4/Al: ZnFe2O4 Nanofibers for Degradation of RhB via Visible Light Photocatalysis and Photo-Fenton Processes. *J. Mater. Sci. Mater. Electron.*, 1–11. doi:10.1007/s10854-021-07443-8

Nair, I. I. J., and Pillai, R. K. V. (2021). "Growth of BaAl2O4 Nanoparticles by Auto-Ignition Combustion Method and its Characterization," in AIP Conference Proceedings 2379, 030006, International Conference on Recent Trends in Theoretical and Applied Physics, 12 July 2021 (AIP Publishing).

Nassar, M. Y., Ahmed, I. S., and Samir, I. (2014). A Novel Synthetic Route for Magnesium Aluminate (MgAl2O4) Nanoparticles Using Sol-Gel Auto Combustion Method and Their Photocatalytic Properties. *Spectrochimica Acta A: Mol. Biomol. Spectrosc.* 131, 329–334. doi:10.1016/j.saa.2014.04.040

Park, B.-G. (2018). Characteristics of Eu2+, Dy3+-Doped SrAl2O4 Synthesized by Hydrothermal Reaction and its Photocatalytic Properties. *Msce* 06 (02), 12–21. doi:10.4236/msce.2018.62002

Parvarinezhad, S., Salehi, M., and Khademinia, S. (2019). Solid State Synthesis of $MgAl_2O_4$ Nanomaterials and Solar Light-Induced Photocatalytic Removal of Malachite Green. *Int. J. Nano Dimension* 10 (1), 89–104. Available at: http://www.iaujournals.ir/article_660987.html?lang=en.

Piriyanon, J., Takhai, P., Patta, S., Chankhanittha, T., Senasu, T., Nijpanich, S., et al. (2021). Performance of Sunlight Responsive WO3/AgBr Heterojunction Photocatalyst toward Degradation of Rhodamine B Dye and Ofloxacin Antibiotic. *Opt. Mater.* 121, 111573. doi:10.1016/j.optmat.2021.111573

Potbhare, A. K., Chauke, P. B., Zahra, S., Sonkusare, V., Bagade, R., Ummekar, M., et al. (2019). Microwave-mediated Fabrication of Mesoporous Bi-doped CuAl2O4 Nanocomposites for Antioxidant and Antibacterial Performances. *Mater. Today Proc.* 15, 454–463. doi:10.1016/j.matpr.2019.04.107

Pu, X., Wang, C., Chen, X., Jin, J., Li, W., and Chen, F. (2021). Synthesis and Photocatalytic Degradation of Water to Produce Hydrogen from Novel Cerium Dioxide and Silver-Doped Cerium Dioxide Fiber Membranes by the Electrospinning Method. *Front. Mater.* 8, 414. doi:10.3389/fmats.2021.776817

Qian, X., Li, B., Mu, H.-y., Ren, J., Liu, Y., Hao, Y.-j., et al. (2017). Deep Insight into the Photocatalytic Activity and Electronic Structure of Amorphous Earth-Abundant MgAl2O4. *Inorg. Chem. Front.* 4 (11), 1832–1840. doi:10.1039/C7QI00478H

Rajabathar, J. R., Arunachalam, P., Issa, Z. A., and Ahmed M, T. (2020). Synthesis and Characterization of Novel Metal Chalcogenide Modified Ni-Co-MnO2 Nanofibers Rolled with Graphene Based Visible Light Active Catalyst for nitro Phenol Degradation. *Optik* 224, 165538. doi:10.1016/j.ijleo.2020.165538

Salehabadi, A., Salavati-Niasari, M., Sarrami, F., and Karton, A. (2017). Sol-Gel Auto-Combustion Synthesis and Physicochemical Properties of BaAl2O4 Nanoparticles; Electrochemical Hydrogen Storage Performance and Density Functional Theory. *Renew. Energ.* 114, 1419–1426. doi:10.1016/j.renene.2017.07.119

Sera, M., Yamamoto, M., Tomita, K., Yabara, Y., Izawa, S., Hiramoto, M., et al. (2021). Morphology Control and Synthesis of Afterglow Materials with a SrAl2O4 Framework Synthesized by Surfactant-Template and Hydrothermal Methods. *Chem. Phys. Lett.* 780, 138916. doi:10.1016/j.cplett.2021.138916

Shang-Pan, H., Zhi-Qiang, W., Xiao-Juan, W., and Ji-Wen, S. (2020). Optical Properties of Cr Doped ZnAl2O4 Nanoparticles with Spinel Structure Synthesized by Hydrothermal Method. *Mater. Res. Express* 7 (1), 015025. doi:10.1088/2053-1591/ab6125

Sharma, S. K., Gourier, D., Viana, B., Maldiney, T., Teston, E., Scherman, D., et al. (2014). Persistent Luminescence of AB2O4:Cr3+ (A=Zn, Mg, B=Ga, Al) Spinels: New Biomarkers for *In Vivo* Imaging. *Opt. Mater.* 36 (11), 1901–1906. doi:10.1016/j.optmat.2014.06.020

Shifa Wang, S., Gao, H., Sun, G., Wang, Y., Fang, L., Yang, L., et al. (2020). Synthesis of Visible-Light-Driven SrAl2O4-Based Photocatalysts Using Surface Modification and Ion Doping. *Russ. J. Phys. Chem.* 94, 1234–1247. doi:10.1134/S003602442006031X

Sriram, B., Baby, J. N., Wang, S.-F., George, M., Joseph, X. B., and Tsai, J.-T. (2020). Surface Engineering of Three-dimensional-like Hybrid AB2O4 (AB = Zn, Co, and Mn) Wrapped on Sulfur-Doped Reduced Graphene Oxide: Investigation of the Role of an Electrocatalyst for Clioquinol Detection. *ACS Appl. Electron. Mater.* 3 (1), 362–372. doi:10.1021/acsaelm.0c00906

Szroeder, P., Sahalianov, I., Radchenko, T., Tatarenko, V., and Prylutskyy, Y. (2019). The Strain- and Impurity-dependent Electron States and Catalytic Activity of Graphene in a Static Magnetic Field. *Opt. Mater.* 96, 109284. doi:10.1016/j.optmat.2019.109284

Taazayet, W. B., Zouari, I. M., Hosni, N., Dkhil, B., and Mliki, N. T. (2021). Facile Synthesis of Pure BiFeO3 and Bi2Fe4O9 Nanostructures with Enhanced Photocatalytic Activity. *J. Mater. Sci. Mater. Electron.*, 1–16. doi:10.1007/s10854-021-07459-0

Takebuchi, Y., Fukushima, H., Nakauchi, D., Kato, T., Kawaguchi, N., and Yanagida, T. (2020). Scintillation and Dosimetric Properties of Ce-Doped MgAl2O4 Single Crystals. *J. Lumin.* 223, 117139. doi:10.1016/j.jlumin.2020.117139

Wang, S., Chen, C., Li, Y., Zhang, Q., Li, Y., and Gao, H. (2019). Synergistic Effects of Optical and Photoluminescence Properties, Charge Transfer, and Photocatalytic Activity in MgAl2O4:Ce and Mn-Codoped MgAl2O4:Ce Phosphors. *J. Elec Materi* 48 (10), 6675–6685. doi:10.1007/s11664-019-07479-x

Wang, S., Gao, H., Chen, C., Wei, Y., and Zhao, X. (2019). Irradiation Assisted Polyacrylamide Gel Route for the Synthesize of the Mg1-xCoxAl2O4 Nano-Photocatalysts and its Optical and Photocatalytic Performances. *J. Sol-gel Sci. Technol.* 92 (1), 186–199. doi:10.1007/s10971-019-05062-8

Wang, S., Gao, H., Fang, L., Hu, Q., Sun, G., Chen, X., et al. (2021). Synthesis of Novel CQDs/CeO2/SrFe12O19 Magnetic Separation Photocatalysts and Synergic Adsorption-Photocatalytic Degradation Effect for Methylene Blue Dye Removal. *Chem. Eng. J. Adv.* 6, 100089. doi:10.1016/j.ceja.2021.100089

Wang, S., Gao, H., Fang, L., Wei, Y., Li, Y., and Lei, L. (2019). Synthesis and Characterization of BaAl2O4 Catalyst and its Photocatalytic Activity towards Degradation of Methylene Blue Dye. *Z. für Physikalische Chem.* 233 (8), 1161–1181. doi:10.1515/zpch-2018-1308

Wang, S., Gao, H., Li, J., Wang, Y., Chen, C., Yu, X., et al. (2021). Comparative Study of the Photoluminescence Performance and Photocatalytic Activity of CeO2/MgAl2O4 Composite Materials with an N-N Heterojunction Prepared by One-step Synthesis and Two-step Synthesis Methods. *J. Phys. Chem. Sol.* 150, 109891. doi:10.1016/j.jpcs.2020.109891

Wang, S., Gao, H., Wei, Y., Li, Y., Yang, X., Fang, L., et al. (2019). Insight into the Optical, Color, Photoluminescence Properties, and Photocatalytic Activity of the N-O and C-O Functional Groups Decorating Spinel Type Magnesium Aluminate. *CrystEngComm* 21 (2), 263–277. doi:10.1039/c8ce01474d

Wang, S., Gao, H., Yu, H., Li, P., Li, Y., Chen, C., et al. (2020). Optical and Photoluminescence Properties of the MgAl2O4:M (M = Ti, Mn, Co, Ni) Phosphors: Calcination Behavior and Photoluminescence Mechanism. *Trans. Indian Ceram. Soc.* 79 (4), 221–231. doi:10.1080/0371750X.2020.1817789

Wang, S., Gao, H., Yu, X., Tang, S., Wang, Y., Fang, L., et al. (2020). Nanostructured SrTiO3 with Different Morphologies Achieved by mineral Acid-Assisted Hydrothermal Method with Enhanced Optical, Electrochemical, and Photocatalytic Performances. *J. Mater. Sci. Mater. Electron.* 31 (20), 17736–17754. doi:10.1007/s10854-020-04328-0

Wang, S., Li, D., Yang, C., Sun, G., Zhang, J., Xia, Y., et al. (2017). A Novel Method for the Synthesize of Nanostructured MgFe2O4 Photocatalysts. *J. Sol-gel Sci. Technol.* 84 (1), 169–179. doi:10.1007/s10971-017-4471-3

Wang, S., Wang, Y., Gao, H., Li, J., Fang, L., Yu, X., et al. (2020). Synthesis and Characterization of BaAl2O4: Ce and Mn-Ce- Co-doped BaAl2O4 Composite Materials by a Modified Polyacrylamide Gel Method and Prediction of Photocatalytic Activity Using Artificial Neural Network (ANN) Algorithm. *Optik* 221, 165363. doi:10.1016/j.ijleo.2020.165363

Wang, S., Wei, X., Gao, H., and Wei, Y. (2019). Effect of Amorphous Alumina and α-alumina on Optical, Color, Fluorescence Properties and Photocatalytic Activity of the MnAl2O4 Spinel Oxides. *Optik* 185, 301–310. doi:10.1016/j.ijleo.2019.03.147

Wang, Y., Gao, H., Wang, S., Fang, L., Chen, X., Yu, C., et al. (2021). Facile Synthesis of BaMoO4 and BaMoO4/BaWO4 Heterostructures with Type -I Band Arrangement and Enhanced Photoluminescence Properties. *Adv. Powder Technol.* 32 (11), 4186–4197. doi:10.1016/j.apt.2021.09.028

Wang, Y., Sun, X., Xian, T., Liu, G., and Yang, H. (2021). Photocatalytic Purification of Simulated Dye Wastewater in Different pH Environments by Using BaTiO3/Bi2WO6 Heterojunction Photocatalysts. *Opt. Mater.* 113, 110853. doi:10.1016/j.optmat.2021.110853

Xiao, Y., Luo, B., Cheng, B., Huang, Q., Ye, Y., Fang, L., et al. (2018). Enhanced Visible Light Catalysis Activity of CdS-Sheathed SrAl2O4: Eu2+,Dy3+ Nanocomposites. *Dalton Trans.* 47 (24), 7941–7948. doi:10.1039/C8DT01151F

Zargoosh, K., and Moradi Aliabadi, H. (2019). SrAl2O4:Eu2+: Dy3+/WO3/Polyester Nanocomposite as a Highly Efficient and Environmentally Friendly Photocatalyst for Removal of Dyes from Industrial Wastes. *Environ. Nanotechnology, Monit. Manage.* 12, 100273. doi:10.1016/j.enmm.2019.100273

Zawrah, M. F., Hamaad, H., and Meky, S. (2007). Synthesis and Characterization of Nano MgAl2O4 Spinel by the Co-precipitated Method. *Ceramics Int.* 33 (6), 969–978. doi:10.1016/j.ceramint.2006.02.015

Zhang, M., Chen, X., Zu, M., Tang, Y., Liu, C., Li, W., et al. (2022). Synthesis of Fibrous Micro-nano Hierarchical Porous Cerium Dioxide Materials by the

Impregnation and thermal Decomposition Method and Is Enhanced Photocatalytic Activity. *Front. Mater.* 8, 502. doi:10.3389/fmats.2021.775027

Zhu, Z., Li, X., Li, H., Li, Y., Sun, C., and Cao, Y. (2012). Synthesis and Characterization of BaAl2O4 Nanorods by a Facile Solvothermal Method. *Mater. Lett.* 86, 1–4. doi:10.1016/j.matlet.2012.06.093

Zhu, Z., Liu, F., and Zhang, W. (2015). Fabricate and Characterization of Ag/BaAl2O4 and its Photocatalytic Performance towards Oxidation of Gaseous Toluene Studied by FTIR Spectroscopy. *Mater. Res. Bull.* 64, 68–75. doi:10.1016/j.materresbull.2014.12.026

Conflict of Interest: The authors declare that the research was conducted in the absence of any commercial or financial relationships that could be construed as a potential conflict of interest.

Publisher's Note: All claims expressed in this article are solely those of the authors and do not necessarily represent those of their affiliated organizations, or those of the publisher, the editors and the reviewers. Any product that may be evaluated in this article, or claim that may be made by its manufacturer, is not guaranteed or endorsed by the publisher.

Copyright © 2022 Han, Sun, Chai, Li, Wu and Sun. This is an open-access article distributed under the terms of the Creative Commons Attribution License (CC BY). The use, distribution or reproduction in other forums is permitted, provided the original author(s) and the copyright owner(s) are credited and that the original publication in this journal is cited, in accordance with accepted academic practice. No use, distribution or reproduction is permitted which does not comply with these terms.

frontiers | Frontiers in Materials

ORIGINAL RESEARCH
published: 14 April 2022
doi: 10.3389/fmats.2022.889499

Construction of Molybdenum Disulfide/Biological Structure Carbon Composite Photocatalysts and Their Photocatalytic Hydrogen Production

Shujing Wang[1], Jiajing Ding[1], Chencheng Wang[1], Wanfei Li[2], Zhigang Chen[1], Chengbao Liu[1] and Feng Chen[1]**

[1]School of Materials Science and Engineering, Suzhou University of Science and Technology, Suzhou, China, [2]Suzhou Key Laboratory for Nanophotonic and Nanoelectronic Materials and Its Devices, Suzhou University of Science and Technology, Suzhou, China

OPEN ACCESS

Edited by:
Zao Yi,
Southwest University of Science and Technology, China

Reviewed by:
Luhua Lu,
China University of Geosciences, China
Fei Wang,
Sichuan University, China
Yuxiang Yan,
Nanjing University, China

***Correspondence:**
Chengbao Liu
lcb@mail.usts.edu.cn
Feng Chen
ujschenfeng@163.com

Specialty section:
This article was submitted to Semiconducting Materials and Devices, a section of the journal Frontiers in Materials

Received: 04 March 2022
Accepted: 17 March 2022
Published: 14 April 2022

Citation:
Wang S, Ding J, Wang C, Li W, Chen Z, Liu C and Chen F (2022) Construction of Molybdenum Disulfide/Biological Structure Carbon Composite Photocatalysts and Their Photocatalytic Hydrogen Production. Front. Mater. 9:889499. doi: 10.3389/fmats.2022.889499

The hydrothermal calcination method using bamboo leaves as the biological template, thiourea as the sulfur source, and molybdenum chloride as the molybdenum source was employed to synthesize the molybdenum disulfide/biological structure carbon (MoS_2/C) photocatalytic composites with different concentrations of molybdenum chloride. The thermal decomposition behavior, surface morphology, phase structure, BET specific surface area, optical and photoluminescence properties, and photocatalytic activity of MoS_2/C photocatalytic composites with different concentrations of molybdenum chloride were studied. The results showed that the optimal temperature for synthesizing MoS_2/C photocatalytic composites is 700°C. Scanning electron microscopy (SEM) and transmission electron microscopy (TEM) observations show that the hydrothermal calcination method can be used to load MoS_2 onto the biological carbon and form a structurally stable composite system. Analysis of optical and photoluminescence properties shows that the MoS_2/C composites prepared by the hydrothermal calcination method with the concentration of molybdenum chloride of 0.20 mol/L exhibit a high charge transfer and separation efficiency. Photocatalytic experiments show that the MoS_2/C composites prepared by the hydrothermal calcination method with the concentration of molybdenum chloride of 0.20 mol/L have a high photocatalytic activity and cyclic stability. This excellent synthesis strategy can be used to synthesize other photocatalytic hydrogen production materials.

Keywords: hydrothermal calcination method, molybdenum disulfide, biological structure carbon, photoluminescence properties, photocatalytic activity

INTRODUCTION

With the development of world economy, non-renewable resources are gradually exhausted, so it is necessary to develop renewable resources to meet the needs of human life (Gouma et al., 2016; Wang et al., 2021a; Wang et al., 2021b; Cheng et al., 2021; Jia et al., 2021; Li et al., 2021; Zhang et al., 2021). Photocatalytic hydrogen production is an effective technology for the utilization of renewable resources and has attracted extensive attention from researchers all over the world (Kais et al., 2019; Luo et al., 2019; Ravishankar et al., 2019; Chen et al., 2019; Wang et al., 2020a). Molybdenum

disulfide (MoS_2) is a potential photocatalyst for photocatalytic decomposition of water to produce hydrogen, which has been applied in this field (Zhang et al., 2019). MoS_2 is the main component of molybdenite in nature. Block MoS_2 is made up of a large number of single or small layers of MoS_2 combined with interlayer van der Waals force and stacked. According to the different stacking modes and layers in the crystal, layered MoS_2 can be divided into three types, namely, 1T, 2H, and 3R, where the number represents the layers of the unit cell MoS_2; T, H, and R are trigonal, hexagonal, and rhombohedral, respectively (Zhang et al., 2018). 1T-MoS_2 and 3R-MoS_2 are metastable, while 2H-MoS_2 is stable and exhibits excellent semiconductor properties (Sarno and Ponticorvo, 2019).

Single or small layer MoS_2 material is a direct band gap semiconductor; its band gap width is 1.82 eV, so it can produce optical response to the visible light in the sunlight (Rumyantsev et al., 2007). However, it is easy to form folds and clusters due to the high surface activity of MoS_2 material, which greatly reduces the surface area of MoS_2 semiconductors and increases the composite probability of the photogenerated electron–hole pair. In addition, there is a significant photocorrosion effect in MoS_2 semiconductors, which limits the further improvement of photocatalytic semiconductor materials. To solve these problems, researchers put forward a variety of solutions. Yuan et al. (Qi et al., 2019) prepared MoS_2/reduced graphene oxide (rGO) composite catalytic material, whose excellent photocatalytic performance can be attributed to graphene acting as an electron transfer bridge to improve the transfer of charge carriers. Li et al. (2014) conjugated MoS_2 nanosheets to (graphite phase carbon nitride) g-C_3N_4 through an easy ultrasonic chemical method to form the MoS_2/C_3N_4 heterostructure. In this structure, MoS_2 is used as an electron trap to prolong the life of the separated electron–hole pair and can be used for the photodegradation of organic dyes. Meng and his team (Meng et al., 2013) deposited 5–20 nm p-type MoS_2 nanosheets on n-type nitrogen-doped reduced graphene oxide (N-rGO) nanosheets to form multiple p-n junctions on each rGO nanosheet. The p-MOS_2/N-rGO heterostructure greatly enhanced charge generation and inhibited charge recombination and showed high photocatalytic activity for hydrogen evolution reaction in the wavelength range from ultraviolet to near-infrared light. Generally, bamboo leaves are used as a biological template to prepare semiconductor oxide materials with a special structure, which can enhance the physical and chemical properties of the semiconductor oxide materials (Li et al., 2007; Wang et al., 2018). It is of great significance to develop a new synthesis route using bamboo leaves as biological templates to prepare MoS_2 and enhance its charge-carrier migration and separation efficiency.

In this study, we proposed to use bamboo leaves as biological templates to prepare biostructured carbon and to prepare MoS_2/biological structure carbon (C) composites with four concentration gradients by the hydrothermal calcination method. The thermal decomposition behavior, surface morphology, phase structure, BET specific surface area, optical and photoluminescence properties, and photocatalytic activity of MoS_2/C composites with different concentrations of molybdenum chloride were comparatively studied by using various instruments. Simultaneously, the cyclic stability experiment of photocatalytic hydrogen production was performed. The MoS_2/C composites prepared by the hydrothermal calcination method with the concentration of molybdenum chloride of 0.20 mol/L exhibit lowest emission intensity, high charge transfer, and separation efficiency, as well as high photocatalytic activity.

MATERIALS AND METHODS

Preparation of MoS_2/C Composite Photocatalysts

Thiourea and molybdenum chloride, with the molar ratio of 1:1, were accurately weighed. Four solutions with different concentrations of molybdenum chloride with 0.05, 0.10, 0.15, and 0.20 mol/L were prepared. The bamboo leaves are pretreated in a tubular furnace under a nitrogen atmosphere at a sintering temperature of 800°C. Four 20 g pretreated bamboo leaf biological templates were weighed and completely immersed in the aforementioned solution. After immersing for 24 h, the templates were transferred to the reaction kettle with teflon lining. The reactor was transferred to a drying oven and held at 160°C for 6 h to obtain four concentrations of precursors. The precursors were transferred to quartz tubes in a tubular furnace, and the MoS_2/C composite photocatalysts were obtained by heating the precursors from room temperature to 800°C at a rate of 5°C/min under the exposure of nitrogen protection gas.

Material Characterization

The thermogravimetric analysis (TG) and differential scanning calorimetry (DSC) of precursors were characterized by using the SDT Q600 simultaneous thermal analyzer (TA instruments, Inc. United States) under the exposure of nitrogen protection gas. The heating rate, the air flow rate, the injection volume, and the temperature range are 20 K/min, 100 ml/min, 2 mg, and 25–800°C, respectively. The microstructures of the MoS_2/C composite photocatalysts were observed by scanning electron microscopy, while the fibers and particles constituting membranes were characterized by using an Apollo 300 scanning electron microscope (SEM) and Libra 200 type transmission electron microscope (TEM) produced by Carl Zeiss IRTS, Germany. The MoS_2/C composite photocatalysts were characterized by using a Brook D8 Advance X-Ray diffractometer with the scanning angle of 20–80°, the scanning step length of 0.02°, and using Cu target Kα (λ = 0.154056 nm) radiation with the working voltage of 40 kV and current of 40 mA. UV-visible absorption spectra of the MoS_2/C composite photocatalysts were measured by using an ultraviolet and visible spectrophotometer. The fluorescence spectra of the MoS_2/C composite photocatalysts were collected in a confocal Raman system using a He-Cd laser with the RGB laser system (325 nm, NovaPro 30 mW, Germany) at room temperature. Nitrogen adsorption experiments are performed through nitrogen adsorption equipment.

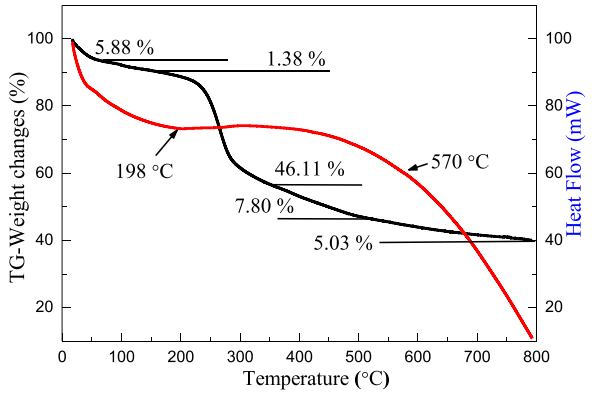

FIGURE 1 | TG–DSC curves of precursors of MoS_2/C composites with the concentrations of molybdenum chloride of 0.20 mol/L prepared by the hydrothermal calcination method.

Photocatalytic Experiments

In order to investigate the photocatalytic properties of the prepared MoS_2/C composite photocatalysts, they were applied to the reaction of photocatalytic degradation of water to produce hydrogen and compared with the pure MoS_2. The Labsolar H_2 photolysis system was developed by Beijing Perfectlight Technology Co., Ltd., and the detection device was a Shanghai Tianmei GC7900 gas chromatograph produced by Shandong Jinpu Analytical Instrument Co. Ltd., with a Microsolar 300 high-performance analog daylight xenon lamp which was used as the simulation light source. For the experiment, 100 mg sample was added to 100 ml deionized water, and sodium sulfite was added as the sacrificial agent to carry out photocatalytic hydrogen production. The hydrogen production of each material was compared after 6 h of illumination.

RESULTS AND DISCUSSION

TG-DSC Analysis

Figure 1 shows the thermogravimetry (TG) and differential scanning thermal curves (DSC) of the precursor of MoS_2/C composites with the concentrations of molybdenum chloride of 0.20 mol/L prepared by the hydrothermal calcination method. The weight loss process of the precursor is divided into five stages. As the samples were dried at 40°C, the content of free water in the precursor was slightly lower, and the weight loss ratio of free water precipitation to evaporation was 5.88% (Artiaga et al., 2005; Hsu and Lin, 2009). Hydrothermal and drying processes can effectively reduce the free water content of the precursor, and the weight loss is only 1.38% in the heating range of 100–198°C, and the release and heat dissipation of free water and bound water are energy dissipation reactions, corresponding to an obvious endothermic process on the energy curve (Saldo et al., 2002; Tahmasebi et al., 2014). The third weightless stage mainly occurs in the range of 200–400°C, which is the main concentrated range of slow thermal decomposition of cellulose (Szcześniak et al., 2008; Kristanto et al., 2021). A large number of groups in cellulose decomposition, accompanied by the pyrolysis and recombination of functional groups of lignin, and the biological structure carbon begins to generate in large quantities (Mikheeva et al., 2021). After 400°C, a small amount of cellulose cleaves to produce small molecules, the groups continue to decompose, carbon elements rearrange, and hemicellulose enters the carbonization stage and undergoes strong decomposition until 450°C basically ends (Yadav et al., 2021; Zhao et al., 2021). The main reason of 7.80% weight loss was the fracture of old bonds and the formation of new bonds in lignin. At the final weightlessness stage of the precursor, cellulose completes the carbonization reaction, and the benzene ring in lignin is first unchained and then aromatized, forming an amorphous carbon biological structure (Krueger et al., 2021; Xia et al., 2021). The hemicellulose eventually forms the biological carbon (Kabachkov et al., 2020). In addition, during the heating process of 200–570°C, the energy curve of the precursor does not decrease significantly with the pyrolysis and carbonization rearrangement of organic matter but is in dynamic equilibrium. The phenomenon can be ascribed to the release of energy, and organic carbon absorption energy of the grain growth is roughly the same, so the energy changes in a dynamic balance. Based on the analysis of weight loss in the thermal decomposition stages mentioned previously, the weight stabilizes at 800°C.

Scanning Electron Microscopy Analysis

Figures 2A–H shows the SEM images of MoS_2/C composites prepared by the hydrothermal calcination method with the different concentrations of molybdenum chloride including 0.05, 0.10, 0.15, and 0.20 mol/L at different magnifications. At low magnification, the organic matter in the leaves could be transformed into biological carbon, and the microscopic morphology of the original template was completely preserved. The composite system is based on biological structure carbon, and MoS_2 particles are loaded on the thin layer of carbon. The obtained biological structure carbon material has two main functions: First, it can provide support for the loading of MoS_2 particles so that the material can resist the deformation caused by clusters or Oswald curing during high temperature calcination and avoid the collapse phenomenon. Second, a firm bond is formed between biological carbon and MoS_2 under the action of high temperature, and the photogenerated electrons in the semiconductor are transferred to the surface of biological carbon for the reduction reaction, reducing the possibility of photogenerated electron–hole pair recombination. After the calcination process, a cluster phenomenon of MoS_2 nanoparticles was formed by the hydrothermal process under thermal action and presented a spherical structure; the diameter of spherical particles is about 2–5 μm. As the concentration of the sulfur source and molybdenum source increases in the hydrothermal process, the number of MoS_2 nanoparticles increases successively, and the cluster size increases with the concentration change. According to SEM observation, it can be inferred that the complex system has a high photocatalytic performance when

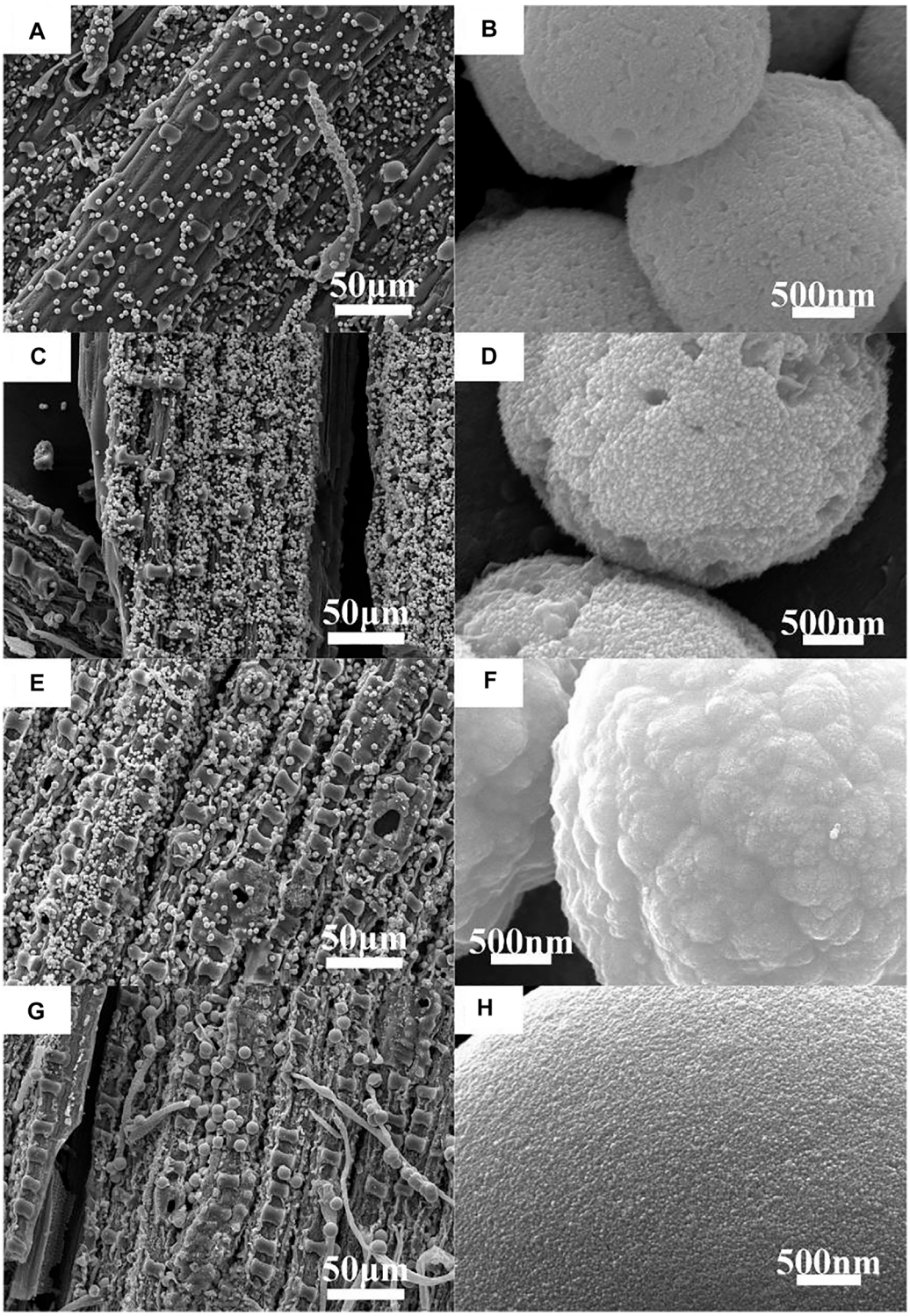

FIGURE 2 | SEM images and enlarged SEM images of MoS_2/C composites with the different concentrations of molybdenum chloride prepared by the hydrothermal calcination method. **(A,B)** 0.05 mol/L, **(C,D)** 0.10 mol/L, **(E,F)** 0.15 mol/L, and **(G,H)** 0.20 mol/L.

the molybdenum chloride concentration is 0.2 mol/L. This conclusion needs to be proven by photocatalytic experiments.

Transmission Electron Microscopy Analysis

Figure 3 shows the TEM and HRTEM images of MoS_2/C composites prepared by the hydrothermal calcination method

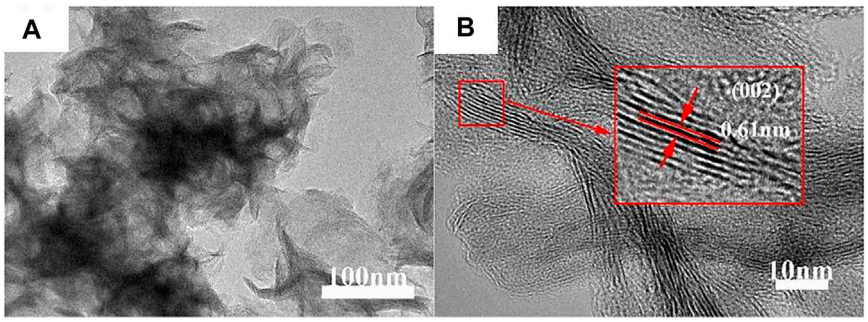

FIGURE 3 | (A) TEM and **(B)** HRTEM images of MoS_2/C composites prepared by the hydrothermal calcination method with the concentrations of molybdenum chloride of 0.20 mol/L.

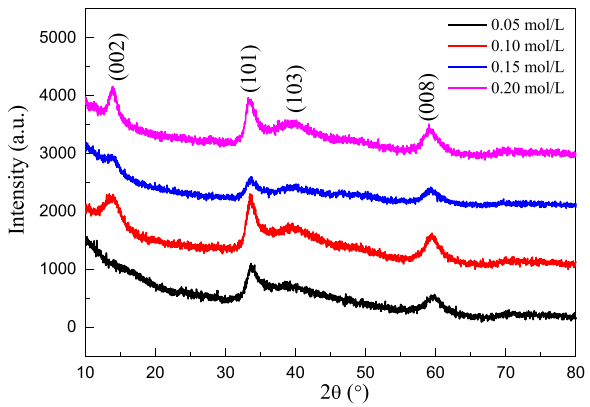

FIGURE 4 | XRD patterns of MoS_2/C composites prepared by the hydrothermal calcination method with the different concentrations of molybdenum chloride including 0.05, 0.10, 0.15, and 0.20 mol/L.

with the concentrations of molybdenum chloride of 0.20 mol/L. As can be seen from **Figure 3A**, a large number of MoS_2 nanoparticles are loaded on the a thin layer of the biological structure of carbon, indicating that the MoS_2 nanoparticles form clusters and undergo accumulation when loaded on the surface of carbon material, which is consistent with the SEM observation. **Figure 3B** was obtained by magnifying the edge of the TEM image by 10 times. From the figure, it can be found that the MoS_2 particles forming clusters are nanoscale with a particle size of about 15 nm. The crystal lattice fringe of the particles is obvious. TEM professional software is used to calculate the spacing of exposed crystal planes in the figure, and the value is 0.61 nm, corresponding to the (002) crystal plane of MoS_2 in the β-phase. Similarly, the biological structure of carbon obtained by this method is layered carbon, which further proves that high-temperature calcination is more beneficial to enhance the crystallinity of the layered carbon.

XRD Analysis

Figure 4 shows the XRD patterns of MoS_2/C composites prepared by the hydrothermal calcination method with the different concentrations of molybdenum chloride including 0.05, 0.10, 0.15, and 0.20 mol/L. A series of characteristic peaks were observed at similar locations for the four products with different concentrations, and they all corresponded to the (002), (101), (103), and (008) crystal planes of β phase MoS_2 (JCPDS card no. 41-1049) at 2θ = 13.92, 33.43, 39.77, and 59.25°, respectively. In addition, there were no redundant miscellaneous peaks in the pattern, indicating that the prepared MoS_2 nanocrystal is of high purity. The crystallinity of the material increases with the increase in the concentration, and the crystal plane with the sharpest diffraction intensity is (101). The half-peak width of the main characteristic peak of the material is wide, indicating that the average coherent scattering size of the material is small, and the concentration has no significant effect on the coherent scattering size of the material.

Optical Properties

Figure 5A shows the UV–Vis absorption spectra of molybdenum disulfide/biological structure carbon composites prepared by the hydrothermal calcination method with the different concentrations of molybdenum chloride including 0.05, 0.10, 0.15, and 0.20 mol/L. For the products obtained by the hydrothermal calcination method, the composite system absorbs all the light sources of the whole band because the color of MoS_2 is black, and the material absorbs all the light sources of the whole band. However, the composite system absorbs the infrared light source but does not respond due to the limitation of the band gap. The concentration had no significant effect on the UV–Vis absorption capacity of the composite system. The band gap energy (Eg) values of molybdenum disulfide/biological structure carbon composites were prepared by the hydrothermal calcination method with the different concentrations of molybdenum chloride including 0.05, 0.10, 0.15, and 0.20 mol/L obtained by the UV–Vis absorption spectra using the Tauc relation (Gao et al., 2018; Gao H. J. et al., 2021; Wang et al., 2021c; Wang et al., 2022) from **Figure 5B**.

$$(F(R)h\nu)^n = A\left(h\nu - E_g\right), \quad (1)$$

where ν, A, and n are the frequency, the absorption coefficient, and 2, respectively. The E_g values of molybdenum disulfide/

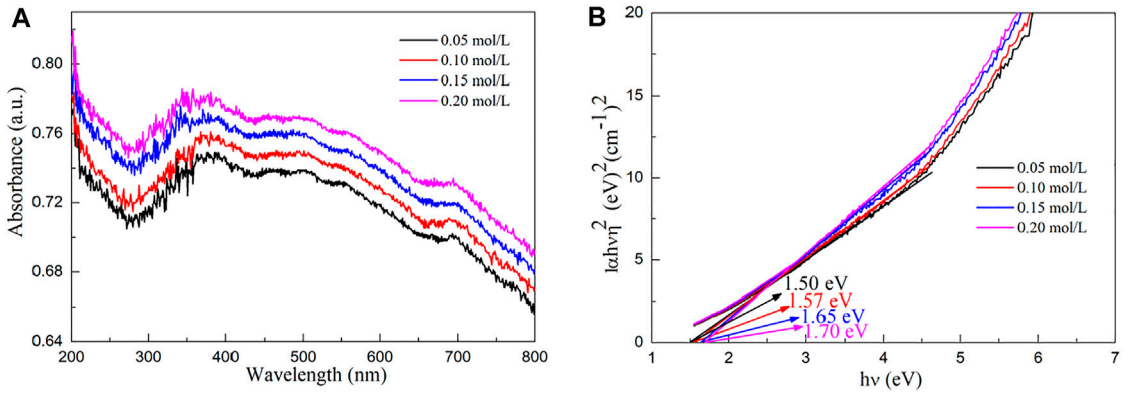

FIGURE 5 | (A) UV–Vis absorption spectra and **(B)** Eg values of molybdenum disulfide/biological structure carbon composites prepared by the hydrothermal calcination method with the different concentrations of molybdenum chloride including 0.05, 0.10, 0.15, and 0.20 mol/L.

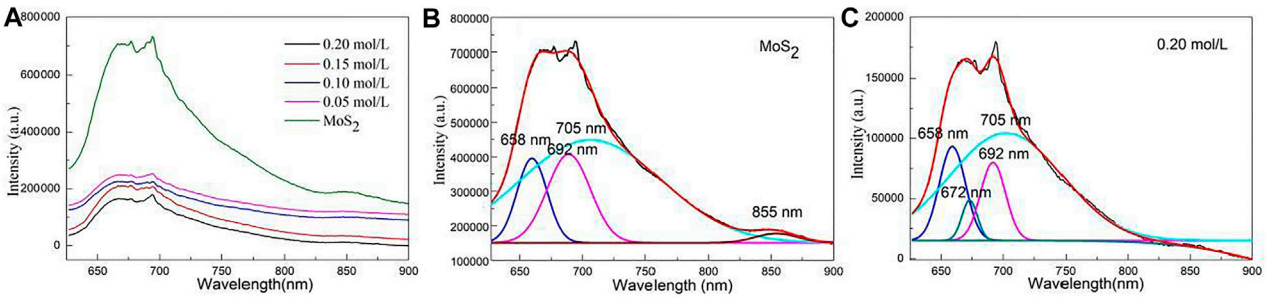

FIGURE 6 | (A) Emission spectra of MoS_2/C composites prepared by the hydrothermal calcination method with the different concentrations of molybdenum chloride including 0, 0.05, 0.10, 0.15, and 0.20 mol/L. **(B)** Emission spectrum of pure MoS_2 could be resolved into three Gaussian peaks with the maxima at 658, 692, 705, and 855 nm. **(C)** Emission spectrum of MoS_2/C composites with the concentration of molybdenum chloride of 0.20 mol/L could be resolved into four Gaussian peaks with the maxima at 658, 672, 692, and 705 nm.

biological structure carbon composites prepared by the hydrothermal calcination method with the different concentrations of molybdenum chloride including 0.05, 0.10, 0.15, and 0.20 mol/L are obtained by a simple intercept method. The Eg values of molybdenum disulfide/biological structure carbon composites prepared by the hydrothermal calcination method with the different concentrations of molybdenum chloride including 0.05, 0.10, 0.15, and 0.20 mol/L are 1.50, 1.57, 1.65, and 1.70 eV, respectively. The Eg value of molybdenum disulfide/biological structure carbon composites increases with the increasing molybdenum chlorate content. The Eg value of molybdenum disulfide/biological structure carbon composites decreases slightly than that of pure monolayer MoS_2 (1.80 eV). These results suggest that the molybdenum disulfide/biological structure carbon composites can respond to visible light.

Photoluminescence Properties

Figure 6A shows the emission spectra of MoS_2/C composites prepared by the hydrothermal calcination method with the different concentrations of molybdenum chloride including 0, 0.05, 0.10, 0.15, and 0.20 mol/L. The emission peak of pure MoS_2 is mainly concentrated in the range of 575–900 nm and has the highest emission peak intensity compared with other samples. The intensity of emission peak decreases with the increase in the molybdenum chloride content. The MoS_2/C composites prepared by the hydrothermal calcination method with the concentrations of molybdenum chloride of 0.20 mol/L have the lowest emission intensity indicating that the sample exhibits the highest charge transfer and separation efficiency. Its high charge transfer and separation efficiency result in high photocatalytic activity for splitting water to produce hydrogen.

Figure 6B shows the emission spectrum of pure MoS_2 that could be resolved into three Gaussian peaks with the maxima at 658, 692, 705, and 855 nm. The peaks at 658 and 692 nm can be ascribed to the intrinsic luminescence peak of MoS_2, which is mainly composed of the photon energy radiated by the recombination of photogenerated electron–hole pairs in the MoS_2 semiconductor. The peaks at 705 and 855 nm can be assigned to the defect luminescence peak, which is mainly composed of fluorescence radiation generated by the sulfur lattice vacancy capturing electrons in the MoS_2 semiconductor

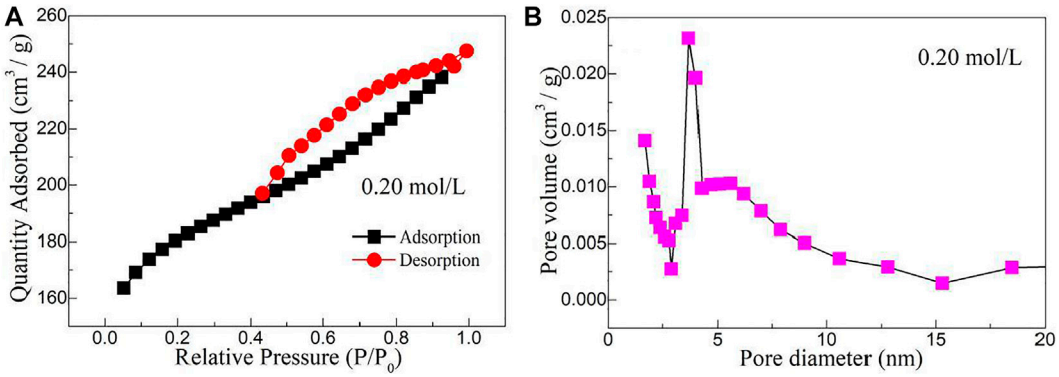

FIGURE 7 | (A) Nitrogen adsorption–desorption isotherm and **(B)** pore size distribution of molybdenum disulfide/biological structure carbon composites prepared by the hydrothermal calcination method with the concentration of molybdenum chloride of 0.20 mol/L.

and then recombination with photogenerated holes (Tang et al., 2020; Wang et al., 2020b; Wang and Tian, 2020; Gao H. et al., 2021; Wang S. F. et al., 2021).

Figure 6C shows the emission spectrum of MoS_2/C composites with the concentration of molybdenum chloride of 0.05 mol/L could be resolved into four Gaussian peaks with the maxima at 658, 672, 692, and 705 nm. This result differs from MoS_2 in two ways: one new peak at 672 nm can be observed, and the fluorescence emission peak at 855 nm is quenched. The peak at 672 nm can be ascribed to the interface defect formed by MoS_2 coupling with biological structure carbon particles. The quenching of the fluorescence emission peak at 855 nm may be due to the formation of MoS_2/C heterojunction which greatly enhances the separation and transportation of photogenerated carriers (Zhao et al., 2020; Chi et al., 2021). The intensity of the luminescent peak decreases with the increase in the content of molybdenum chloride. Generally, the charge carrier transfer and separation efficiency decrease with the increase in the luminescence intensity. The MoS_2/C composites with the concentrations of molybdenum chloride of 0.20 mol/L exhibit lowest emission intensity. Therefore, the results confirm that the MoS_2/C composites prepared by hydrothermal calcination method with the concentrations of molybdenum chloride of 0.20 mol/L have the highest charge transfer and separation efficiency.

Adsorption-Desorption Isotherm and Pore Size Distribution

Figure 7A shows the nitrogen adsorption–desorption isotherm of molybdenum disulfide/biological structure carbon composites prepared by the hydrothermal calcination method with the concentration of molybdenum chloride of 0.20 mol/L. Combined with the IUPAC classification method, the nitrogen adsorption–desorption isotherms belong to a typical type IV. When the relative pressure is at a low pressure (0–0.1), monolayer adsorption is carried out, and the adsorption capacity of the system increases gently. When the relative pressure is in the middle range (0.1–0.4), multilayer adsorption takes place, and nitrogen molecules are adsorbed on the interlayer channels of the biological structure of carbon and the slit mesopores formed by the folds of MoS_2 nanosheets. Under the relative high pressure (0.4–1.0), capillary condensation is mainly carried out in the system, and the adsorption–desorption saturation equilibrium is achieved at a p/p0 of 1.0. The H_3-type hysteresis ring formed under high pressure indicates that there are a lot of slit pore mesoporous structures formed by the accumulation of sheet MoS_2 and biological structure carbon layer in the system. Combined with the related literature studies, the causes of the H_3 hysteresis loop due to the adsorption of composite material are because of the hole wall of multilayer adsorption and condensation, two factors in the hole, by the action of the stripping process caused only by capillary condensation. Given the multilayer structure for a parallel state, Kelvin radius changes constantly, thus resulting in the H_3-type hysteresis phenomenon. The BET (Brunauer–Emmett–Teller) equation was used to analyze the data, and its specific surface area was 568.35 m^2/g. **Figure 7B** shows the pore size distribution of molybdenum disulfide/biological structure carbon composites prepared by the hydrothermal calcination method with the concentration of molybdenum chloride of 0.20 mol/L. It can be concluded from the figure that the nano-pore size of the composite is between 2 and 20 nm, which further proves that the material is a mesoporous system. It was observed that the ratio of 4 nm mesopores in the material system was high, which was caused by the coordination between pores in the carbon mesosphere of biological structure and flake MoS_2.

Photocatalytic Decomposition of Water to Produce Hydrogen

Figure 8 shows the hydrogen evolution of MoS_2/C composites prepared by the hydrothermal calcination method with the different concentrations of molybdenum chloride including 0.05, 0.10, 0.15, and 0.20 mol/L under visible light irradiation for three cycles. In addition to four samples with different concentrations of molybdenum chloride, pure MoS_2 was also tested in the photocatalytic decomposition of water to produce

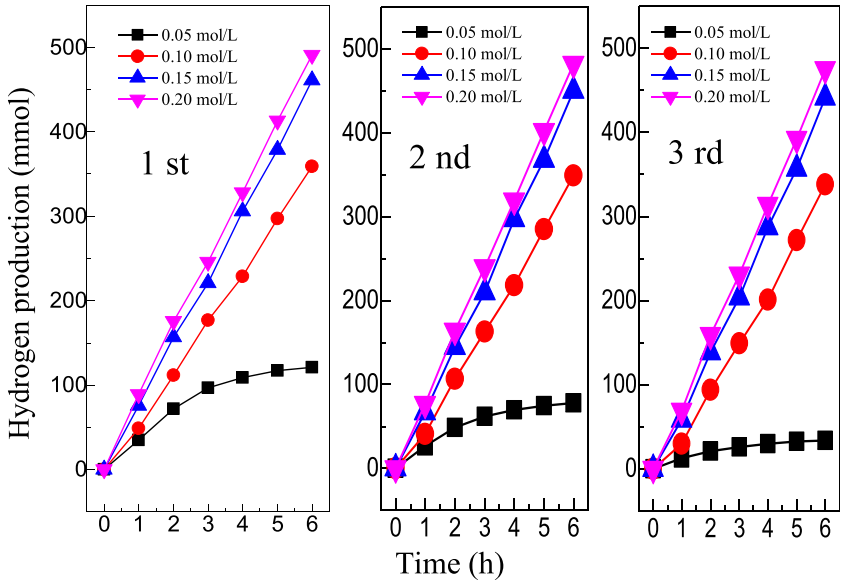

FIGURE 8 | Hydrogen evolution of MoS_2/C composites prepared by the hydrothermal calcination method with the different concentrations of molybdenum chloride including 0.05, 0.10, 0.15, and 0.20 mol/L under visible light irradiation for three cycles.

hydrogen. The experimental results show that MoS_2 can hardly decompose water to produce hydrogen. The photocatalytic performance of the composite system with a higher concentration (0.10, 0.15, and 0.20 mol/L) was better than that of the composite system with a lower concentration (0.05 mol/L) in each cycle experiment. After 6 h of illumination, the hydrogen production of low concentration MoS_2 composites tended to be gentle, while the hydrogen production of the three high concentration composites showed an upward trend. Comparing the results of three cycles, it can be found that the hydrogen production of the MoS_2 sample with the concentration of 0.05 mol/L decreases significantly with the increase of the number of cycles, while the photocatalytic hydrogen production of composite materials with other concentrations still reaches a stable high value after multiple cycles. This is because MoS_2 has a more serious photocorrosion phenomenon when the concentration is low, which limits the continuous photocatalytic reaction. After 6 h of illumination in the first cycle, the photocatalytic decomposition of hydrogen in aquatic products with four concentrations were 120.85, 358.95, 464.02, and 492.12 μmol, respectively. The hydrogen production of MoS_2/C composites prepared by the hydrothermal calcination method with the different concentrations of molybdenum chloride including 0.05, 0.10, 0.15, and 0.20 mol/L were 32.61, 336.40, 443.27, and 475.14 μmol, respectively, after 6 h of illumination in the third cycle.

Due to the low band gap value of MoS_2 and the introduction of biological structure carbon particles, the band gap value of the system is further reduced so that when the light shines on the surface of the composite material, the electrons in the MoS_2 band are easy to undergo transition to the conduction band of MoS_2 under the action of biological structure carbon (Wang and Zhao, 2019; Li et al., 2020; Deng et al., 2021; Ibrayev et al., 2021; Pu et al., 2021; Sharma et al., 2021; Syed et al., 2021; Xiu et al., 2021; Yang et al., 2021; Wang et al., 2021d). Biological structure carbon accelerates the transfer rate of charge carriers between the conduction band and the valence band of MoS_2, thus enhancing the transfer and separation efficiency of charge carriers in the system. Therefore, the photocatalytic activity of MoS_2/C composites was mainly attributed to the high charge transfer and separation efficiency of the system. The photogenerated electron in MoS_2/C composites can effectively reduce the water molecule to produce OH^- and give off H_2 (Yu et al., 2011; Zhang et al., 2013). In addition, the water molecule can be oxidized by hole to produce H^+ and to release O_2 (Zhang et al., 2013). It is also possible as the competition between the recombination of the electron–hole pair and the charge transfer and separation reaction occur in pure water. The backreaction between H_2 and O_2 produces water on the surface of MoS_2/C composites (Husin et al., 2011). The change of the band gap value continuously regulates the electron migration and recombination rate of MoS_2/C composites and then influences its hydrogen production ability.

CONCLUSION

Four kinds of MoS_2/C photocatalytic composites with different concentrations of molybdenum chloride were prepared by the hydrothermal calcination method using bamboo leaves as the biological template, thiourea as the sulfur source, and molybdenum chloride as the molybdenum source. TG-DSC, XRD, SEM, TEM, UV-VIS DRS, PL, and gas chromatograph were used to systematically study the thermal decomposition behavior, phase purity, surface morphology, optical properties, photoluminescence properties, and photocatalytic decomposition

of water to produce hydrogen of MoS_2/C photocatalytic composites with different concentrations of molybdenum chloride. The experimental results show that the hydrothermal calcination method can be used to load MoS_2 onto the biological carbon and form a structurally stable composite system. The MoS_2/C composites prepared by the hydrothermal calcination method with the concentration of molybdenum chloride of 0.20 mol/L exhibits a high charge transfer and separation efficiency. With the increase in the concentration, the photocatalytic activity of the material was significantly improved, and it showed excellent photocorrosion resistance and recyclability, which provided an effective synthesis approach for the preparation of MoS_2/C composites with a stable photocatalytic performance.

DATA AVAILABILITY STATEMENT

The original contributions presented in the study are included in the article/Supplementary Material, further inquiries can be directed to the corresponding authors.

AUTHOR CONTRIBUTIONS

SW and JD were responsible for synthesis experiments and the TG–DSC test. CW was responsible for performance tests and data analysis. WL was responsible for the analysis and guidance of XRD, SEM, and TEM. ZC was responsible for analyzing the reaction mechanism. CL and FC were responsible for the experimental design and manuscript revision.

FUNDING

This work was supported by the National Natural Science Foundation of China (21773291), the Natural Science Foundation of Jiangsu Province (BK20180103), the Qing Lan Project of Jiangsu Province, and the innovation and entrepreneurship training Program for students of the Suzhou University of Science and Technology.

REFERENCES

Artiaga, R., Naya, S., García, A., Barbadillo, F., and García, L. (2005). Subtracting the Water Effect from DSC Curves by Using Simultaneous TGA Data. *Thermochim. Acta* 428 (1-2), 137–139. doi:10.1016/j.tca.2004.11.016

Chen, Y., Li, J., and Liang, Y. (2019). Synthesis and Photocatalytic Activity of BiOBr with Different Exposed Facets and Morphology. *Russ. J. Phys. Chem.* 93 (7), 1406–1410. doi:10.1134/S0036024419070318

Cheng, T., Gao, H., Li, R., Wang, S., Yi, Z., and Yang, H. (2021). Flexoelectricity-induced Enhancement in Carrier Separation and Photocatalytic Activity of a Photocatalyst. *Appl. Surf. Sci.* 566, 150669. doi:10.1016/j.apsusc.2021.150669

Chi, Q., Zhu, G., Jia, D., Ye, W., Wang, Y., Wang, J., et al. (2021). Built-in Electric Field for Photocatalytic Overall Water Splitting through a TiO2/BiOBr P-N Heterojunction. *Nanoscale* 13 (8), 4496–4504. doi:10.1039/D0NR08928A

Deng, P., Liu, Y., Shi, L., Cui, L., Si, W., and Yao, L. (2021). Enhanced Visible-Light H2 Evolution Performance of Nitrogen Vacancy Carbon Nitride by Improving Crystallinity. *Opt. Mater.* 120, 111407. doi:10.1016/j.optmat.2021.111407

Gao, H. J., Wang, S. F., Fang, L. M., Sun, G. A., Chen, X. P., Tang, S. N., et al. (2021). Nanostructured Spinel-type M(M = Mg, Co, Zn)Cr2O4 Oxides: Novel Adsorbents for Aqueous Congo Red Removal. *Mater. Today Chem.* 22, 100593. doi:10.1016/j.mtchem.2021.100593

Gao, H., Wang, Y., Gao, Q., Pan, X., Wang, S., Yang, H., et al. (2021). Phase Evolution and Photoluminescence Behavior of MMoO4 (M = Mg, Ca, Sr) Phosphors. *Optik* 241, 167040. doi:10.1016/j.ijleo.2021.167040

Gao, H., Yang, H., Wang, S., and Zhao, X. (2018). Optical and Electrochemical Properties of Perovskite Type MAlO3 (M=Y, La, Ce) Pigments Synthesized by a Gamma-ray Irradiation Assisted Polyacrylamide Gel Route. *Ceramics Int.* 44 (12), 14754–14766. doi:10.1016/j.ceramint.2018.05.105

Gouma, P. I., Simon, S. R., and Stanacevic, M. (2016). Nano- Sensing and Catalysis Technologies for Managing Food-Water-Energy (FEW) Resources in Farming. *Mater. Today Chem.* 1-2, 40–45. doi:10.1016/j.mtchem.2016.10.004

Hsu, C.-H., and Lin, S.-Y. (2009). Rapid Examination of the Kinetic Process of Intramolecular Lactamization of Gabapentin Using DSC-FTIR. *Thermochim. Acta* 486 (1-2), 5–10. doi:10.1016/j.tca.2008.12.008

Husin, H., Su, W.-N., Chen, H.-M., Pan, C.-J., Chang, S.-H., Rick, J., et al. (2011). Photocatalytic Hydrogen Production on Nickel-Loaded LaxNa1−xTaO3 Prepared by Hydrogen Peroxide-Water Based Process. *Green. Chem.* 13 (7), 1745–1754. doi:10.1039/C1GC15070G

Ibrayev, N. K., Seliverstova, E. V., Sadykova, A. E., and Serikov, T. M. (2021). Synthesis, Structure, and Physical Properties of a Nanocomposite Based on Graphene Oxide and TiO2. *Russ. J. Phys. Chem.* 95 (4), 747–753. doi:10.1134/S0036024421040105

Jia, P., Ma, Y., Song, F., Liu, C., Hu, L., and Zhou, Y. (2021). Renewable Atom-Efficient Dendrimer-like Acetate: from Toxic Tung Oil to Non-toxic Plasticizers. *Mater. Today Chem.* 21, 100518. doi:10.1016/j.mtchem.2021.100518

Kabachkov, E. N., Kurkin, E. N., Vershinin, N. N., Balikhin, I. L., Berestenko, V. I., and Shul'ga, Y. M. (2020). Surface State of Catalysts of CO Oxidation, Obtained by Depositing Platinum on Powder of Plasma-Chemical Titanium Nitride. *Russ. J. Phys. Chem.* 94 (3), 538–543. doi:10.1134/S0036024420030127

Kais, H., Mezenner, N. Y., Trari, M., and Madjene, F. (2019). Photocatalytic Degradation of Rifampicin: Influencing Parameters and Mechanism. *Russ. J. Phys. Chem.* 93 (13), 2834–2841. doi:10.1134/S0036024419130119

Kristanto, J., Azis, M. M., and Purwono, S. (2021). Multi-distribution Activation Energy Model on Slow Pyrolysis of Cellulose and Lignin in TGA/DSC. *Heliyon* 7 (7), e07669. doi:10.1016/j.heliyon.2021.e07669

Krueger, B. C., Fowler, G. D., Templeton, M. R., and Septien, S. (2021). Faecal Sludge Pyrolysis: Understanding the Relationships between Organic Composition and thermal Decomposition. *J. Environ. Manage.* 298, 113456. doi:10.1016/j.jenvman.2021.113456

Li, B., Harlepp, S., Gensbittel, V., Wells, C. J. R., Bringel, O., Goetz, J. G., et al. (2020). Near Infra-red Light Responsive Carbon Nanotubes@mesoporous Silica for Photothermia and Drug Delivery to Cancer Cells. *Mater. Today Chem.* 17, 100308. doi:10.1016/j.mtchem.2020.100308

Li, J., Shi, X., Wang, L., and Liu, F. (2007). Synthesis of Biomorphological Mesoporous TiO2 Templated by Mimicking Bamboo Membrane in Supercritical CO2. *J. Colloid Interf. Sci.* 315 (1), 230–236. doi:10.1016/j.jcis.2007.06.065

Li, J., Wang, S., Sun, G., Gao, H., Yu, X., Tang, S., et al. (2021). Facile Preparation of MgAl2O4/CeO2/Mn3O4 Heterojunction Photocatalyst and Enhanced Photocatalytic Activity. *Mater. Today Chem.* 19, 100390. doi:10.1016/j.mtchem.2020.100390

Li, Q., Zhang, N., Yang, Y., Wang, G., and Ng, D. H. L. (2014). High Efficiency Photocatalysis for Pollutant Degradation with MoS2/C3N4 Heterostructures. *Langmuir* 30 (29), 8965–8972. doi:10.1021/la502033t

Luo, J., Yang, H., Liu, Z., Li, F., Liu, S., Ma, J., et al. (2019). Organic-inorganic Hybrid Perovskite - TiO2 Nanorod Arrays for Efficient and Stable Photoelectrochemical Hydrogen Evolution from HI Splitting. *Mater. Today Chem.* 12, 1–6. doi:10.1016/j.mtchem.2018.11.001

Meng, F., Li, J., Cushing, S. K., Zhi, M., and Wu, N. (2013). Solar Hydrogen Generation by Nanoscale P-N Junction of P-type Molybdenum Disulfide/

n-type Nitrogen-Doped Reduced Graphene Oxide. *J. Am. Chem. Soc.* 135 (28), 10286–10289. doi:10.1021/ja404851s

Mikheeva, N. N., Zaikovskii, V. I., Larichev, Y. V., and Mamontov, G. V. (2021). Toluene Abatement on Ag-CeO2/SBA-15 Catalysts: Synergistic Effect of Silver and Ceria. *Mater. Today Chem.* 21, 100530. doi:10.1016/j.mtchem.2021.100530

Pu, X., Wang, C., Chen, X., Jin, J., Li, W., and Chen, F. (2021). Synthesis and Photocatalytic Degradation of Water to Produce Hydrogen from Novel Cerium Dioxide and Silver-Doped Cerium Dioxide Fiber Membranes by the Electrospinning Method. *Front. Mater.* 8, 414. doi:10.3389/fmats.2021.776817

Qi, K., Yuan, Z., Hou, Y., Zhao, R., and Zhang, B. (2019). Facile Synthesis and Improved Li-Storage Performance of Fe-Doped MoS2/reduced Graphene Oxide as Anode Materials. *Appl. Surf. Sci.* 483, 688–695. doi:10.1016/j.apsusc.2019.04.021

Ravishankar, T. N., de O. Vaz, M., Ramakrishnappa, T., Teixeira, S. R., and Dupont, J. (2019). Ionic Liquid-Assisted Hydrothermal Synthesis of Nb/TiO2 Nanocomposites for Efficient Photocatalytic Hydrogen Production and Photodecolorization of Rhodamine B under UV-Visible and Visible Light Illuminations. *Mater. Today Chem.* 12, 373–385. doi:10.1016/j.mtchem.2019.04.001

Rumyantsev, B. M., Berendyaev, V. I., Golub', A. S., Lenenko, N. D., Novikov, Y. N., Klimenko, I. V., et al. (2007). The Role of Interface in Photo Processes in Photoconductive Heterophase Composites Based on Monolayer Dispersions of Molybdenum Disulfide. *Russ. J. Phys. Chem.* 81 (11), 1870–1876. doi:10.1134/S0036024407110271

Saldo, J., Sendra, E., and Guamis, B. (2002). Changes in Water Binding in High-Pressure Treated Cheese, Measured by TGA (Thermogravimetrical Analysis). *Innovative Food Sci. Emerging Tech.* 3 (3), 203–207. doi:10.1016/S1466-8564(02)00047-4

Sarno, M., and Ponticorvo, E. (2019). High Hydrogen Production Rate on RuS2@MoS2 Hybrid Nanocatalyst by PEM Electrolysis. *Int. J. Hydrogen Energ.* 44 (9), 4398–4405. doi:10.1016/j.ijhydene.2018.10.229

Sharma, S. K., Gupta, R., Sharma, G., Vemula, K., Koirala, A. R., Kaushik, N. K., et al. (2021). Photocatalytic Performance of Yttrium-Doped CNT-ZnO Nanoflowers Synthesized from Hydrothermal Method. *Mater. Today Chem.* 20, 100452. doi:10.1016/j.mtchem.2021.100452

Syed, A., Elgorban, A. M., and Al Kheraif, A. A. (2021). High Performance Nanohybrid CeO2@2D CdO Plates with Suppressed Charge Recombination: Insights of Photoluminescence, Visible-Light Photocatalysis, Intrinsic Mechanism and Antibacterial Activity. *Opt. Mater.* 121, 111510. doi:10.1016/j.optmat.2021.111510

Szcześniak, L., Rachocki, A., and Tritt-Goc, J. (2008). Glass Transition Temperature and thermal Decomposition of Cellulose Powder. *Cellulose* 15 (3), 445–451. doi:10.1007/s10570-007-9192-2

Tahmasebi, A., Yu, J., Su, H., Han, Y., Lucas, J., Zheng, H., et al. (2014). A Differential Scanning Calorimetric (DSC) Study on the Characteristics and Behavior of Water in Low-Rank Coals. *Fuel* 135, 243–252. doi:10.1016/j.fuel.2014.06.068

Tang, S., Wang, S., Yu, X., Gao, H., Niu, X., Wang, Y., et al. (2020). Gamma-Ray Irradiation Assisted Polyacrylamide Gel Synthesis of Scheelite Type BaWO 4 Phosphors and its Colorimetric, Optical and Photoluminescence Properties. *ChemistrySelect* 5 (34), 10599–10606. doi:10.1002/slct.202002429

Wang, B., and Zhao, B. (2019). Carbon Dots/CoFe2O4 Mesoporous Nanosphere Composites as a Magnetically Separable Visible Light Photocatalyst. *Russ. J. Phys. Chem.* 93 (2), 393–399. doi:10.1134/S0036024419020043

Wang, C., Chen, F., Tang, Y., Chen, X., Qian, J., and Chen, Z. (2018). Advanced Visible-Light Photocatalytic Property of Biologically Structured Carbon/ceria Hybrid Multilayer Membranes Prepared by Bamboo Leaves. *Ceramics Int.* 44 (6), 5834–5841. doi:10.1016/j.ceramint.2017.11.027

Wang, S., Gao, H., Sun, G., Wang, Y., Fang, L., Yang, L., et al. (2020a). Synthesis of Visible-Light-Driven SrAl2O4-Based Photocatalysts Using Surface Modification and Ion Doping. *Russ. J. Phys. Chem.* 94 (6), 1234–1247. doi:10.1134/S003602442006031X

Wang, S., Gao, H., Yu, H., Li, P., Li, Y., Chen, C., et al. (2020b). Optical and Photoluminescence Properties of the MgAl2O4:M (M = Ti, Mn, Co, Ni) Phosphors: Calcination Behavior and Photoluminescence Mechanism. *Trans. Indian Ceram. Soc.* 79 (4), 221–231. doi:10.1080/0371750X.2020.1817789

Wang, S. F., Chen, X. Y., Gao, H. J., Fang, L. M., Hu, Q. W., Sun, G. A., et al. (2021). A Comparative Study on the Phase Structure, Optical and NIR Reflectivity of BaFe12O19 Nano-Pigments by the Traditional and Modified Polyacrylamide Gel Method. *JNanoR* 67, 1–14. doi:10.4028/www.scientific.net/jnanor.67.1

Wang, S., Gao, H., Fang, L., Hu, Q., Sun, G., Chen, X., et al. (2021d). Synthesis of Novel CQDs/CeO2/SrFe12O19 Magnetic Separation Photocatalysts and Synergic Adsorption-Photocatalytic Degradation Effect for Methylene Blue Dye Removal. *Chem. Eng. J. Adv.* 6, 100089. doi:10.1016/j.ceja.2021.100089

Wang, S., Gao, H., Li, J., Wang, Y., Chen, C., Yu, X., et al. (2021b). Comparative Study of the Photoluminescence Performance and Photocatalytic Activity of CeO2/MgAl2O4 Composite Materials with an N-N Heterojunction Prepared by One-step Synthesis and Two-step Synthesis Methods. *J. Phys. Chem. Sol.* 150, 109891. doi:10.1016/j.jpcs.2020.109891

Wang, S., Tang, S., Gao, H., Chen, X., Liu, H., Yu, C., et al. (2021a). Microstructure, Optical, Photoluminescence Properties and the Intrinsic Mechanism of Photoluminescence and Photocatalysis for the BaTiO3, BaTiO3/TiO2 and BaTiO3/TiO2/CeO2 Smart Composites. *Opt. Mater.* 118, 111273. doi:10.1016/j.optmat.2021.111273

Wang, S., Tang, S., Gao, H., Fang, L., Hu, Q., Sun, G., et al. (2021c). Modified Polyacrylamide Gel Synthesis of CeO2 Nanoparticles by Using Cerium Sulfate as Metal Source and its Optical and Photoluminescence Properties. *J. Mater. Sci. Mater. Electron.* 32 (8), 10820–10834. doi:10.1007/s10854-021-05740-w

Wang, S., Tang, S., Yang, H., Wang, F., Yu, C., Gao, H., et al. (2022). A Novel Heterojunction ZnO/CuO Piezoelectric Catalysts: Fabrication, Optical Properties and Piezoelectric Catalytic Activity for Efficient Degradation of Methylene Blue. *J. Mater. Sci. Mater. Electron.* 33, 7172–7190. doi:10.1007/s10854-022-07899-2

Wang, Y., and Tian, H. (2020). Study on the Construction of YMnO3/CeO2 Composite Photocatalyst Heterostructure and Photocatalytic Degradation of Methyl Red. *Optik* 201, 163524. doi:10.1016/j.ijleo.2019.163524

Xia, M., Chen, W., Wu, J., Chen, Y., Yang, H., Chen, X., et al. (2021). Organic Salt-Assisted Pyrolysis for Preparation of Porous Carbon from Cellulose, Hemicellulose and Lignin: New Insight from Structure Evolution. *Fuel* 291, 120185. doi:10.1016/j.fuel.2021.120185

Xiu, Z., Zhang, D., and Wang, J. (2021). Direct Z-Scheme Photocatalytic System: Ag2CO3/g-C3N4 Organic-Inorganic Hybrid with Superior Activity through Built-In Electric Field Transfer Mechanism. *Russ. J. Phys. Chem.* 95 (6), 1255–1268. doi:10.1134/S0036024421060273

Yadav, N., Adolfsson, K. H., and Hakkarainen, M. (2021). Carbon Dot-Triggered Photocatalytic Degradation of Cellulose Acetate. *Biomacromolecules* 22 (5), 2211–2223. doi:10.1021/acs.biomac.1c00273

Yang, L., Wang, P. Y., and Wang, T. (2021). Performance Simulation of a 5 kW Hall Thruster. *Front. Mater.* 8, 418. doi:10.3389/fmats.2021.754479

Yu, J., Hai, Y., and Jaroniec, M. (2011). Photocatalytic Hydrogen Production over CuO-Modified Titania. *J. Colloid Interf. Sci.* 357(1), 223–228. doi:10.1016/j.jcis.2011.01.101

Zhang, F.-J., Li, X., Sun, X.-Y., Kong, C., Xie, W.-J., Li, Z., et al. (2019). Surface Partially Oxidized MoS2 Nanosheets as a Higher Efficient Cocatalyst for Photocatalytic Hydrogen Production. *Appl. Surf. Sci.* 487, 734–742. doi:10.1016/j.apsusc.2019.04.258

Zhang, P., Zhao, L., and Zhou, W. (2021). Effects of Heat Treatment on Crystallinity, Hydrophilicity, and Photocatalytic Activity of Cd0.2Zn0.8S Solid Solution. *Russ. J. Phys. Chem.* 95 (2), 262–269. doi:10.1134/S0036024421020291

Zhang, X., Du, Z., Luo, X., Sun, A., Wu, Z., and Wang, D. (2018). Template-free Fabrication of Hierarchical MoS 2/MoO 2 Nanostructures as Efficient Catalysts for Hydrogen Production. *Appl. Surf. Sci.* 433, 723–729. doi:10.1016/j.apsusc.2017.10.105

Zhang, Y. J., Liu, L. C., and Chen, D. P. (2013). Synthesis of CdS/bentonite Nanocomposite Powders for H2 Production by Photocatalytic Decomposition of Water. *Powder Techn.* 241, 7–11. doi:10.1016/j.powtec.2013.02.031

Zhao, H., Guo, L., Xing, C., Liu, H., and Li, X. (2020). A Homojunction-Heterojunction-Homojunction Scaffold Boosts Photocatalytic H2 Evolution over Cd0.5Zn0.5S/CoO Hybrids. *J. Mater. Chem. A.* 8 (4), 1955–1965. doi:10.1039/C9TA11915A

Zhao, N., Ma, H., Yao, E., Yu, Z., An, T., Zhao, F., et al. (2021). Influence of Tailored CuO and Al/CuO Nanothermites on the Thermocatalytic Degradation of Nitrocellulose and Combustion Performance of AP/HTPB Composite Propellant. *Cellulose* 28 (13), 8671–8691. doi:10.1007/s10570-021-04060-w

Conflict of Interest: The authors declare that the research was conducted in the absence of any commercial or financial relationships that could be construed as a potential conflict of interest.

Publisher's Note: All claims expressed in this article are solely those of the authors and do not necessarily represent those of their affiliated organizations, or those of the publisher, the editors, and the reviewers. Any product that may be evaluated in this article, or claim that may be made by its manufacturer, is not guaranteed or endorsed by the publisher.

Copyright © 2022 Wang, Ding, Wang, Li, Chen, Liu and Chen. This is an open-access article distributed under the terms of the Creative Commons Attribution License (CC BY). The use, distribution or reproduction in other forums is permitted, provided the original author(s) and the copyright owner(s) are credited and that the original publication in this journal is cited, in accordance with accepted academic practice. No use, distribution or reproduction is permitted which does not comply with these terms.

frontiers | Frontiers in Materials

REVIEW
published: 23 May 2022
doi: 10.3389/fmats.2022.914905

Preparation and Photocatalytic and Antibacterial Activities of Micro/Nanostructured TiO_2-Based Photocatalysts for Application in Orthopedic Implants

Liang Qi[1], Binghua Guo[1], Qing Lu[2], Hanghui Gong[3], Min Wang[1], Jinlong He[1], Bin Jia[1], Jing Ren[1], Shicheng Zheng[1] and Yufeng Lu[1]*

[1]Department of Orthopedics Combined TCM with Western Medicine, Honghui Hospital, Xi'an Jiaotong University, Xi'an, China, [2]Department of Orthopaedics, Honghui Hospital, Xi'an Jiaotong University, Xi'an, China, [3]Medical School of Yan'an University, Yan'an, China

OPEN ACCESS

Edited by:
Hua Yang,
Lanzhou University of Technology, China

Reviewed by:
Yi Li,
China Academy of Space Technology, China
Zuming He,
Changzhou University, China
Tao Xian,
Qinghai Normal University, China

***Correspondence:**
Binghua Guo
395128339@qq.com

Specialty section:
This article was submitted to Semiconducting Materials and Devices, a section of the journal Frontiers in Materials

Received: 07 April 2022
Accepted: 20 April 2022
Published: 23 May 2022

Citation:
Qi L, Guo B, Lu Q, Gong H, Wang M, He J, Jia B, Ren J, Zheng S and Lu Y (2022) Preparation and Photocatalytic and Antibacterial Activities of Micro/Nanostructured TiO_2-Based Photocatalysts for Application in Orthopedic Implants. Front. Mater. 9:914905. doi: 10.3389/fmats.2022.914905

Micro/nanostructured TiO_2, ion-doped TiO_2, and heterojunction TiO_2 composite photocatalysts have low toxicity, high biocompatibility, and high photocatalytic and antibacterial activities and have broad applications in the fields of photocatalytic, antibacterial, and orthopedic implants. The photocatalytic and antibacterial activities of TiO_2 and TiO_2-based photocatalysts depend on their preparation methods. In this review, the preparation methods of TiO_2, ion-doped TiO_2, and heterojunction TiO_2 composite photocatalysts and their effects on photocatalytic and antibacterial activities were reviewed. Based on the excellent physical and chemical properties of TiO_2, ion-doped TiO_2, and heterojunction TiO_2-based photocatalysts, their applications in the field of orthopedic implants were reviewed. Meanwhile, the development trend of the photocatalyst in the fields of photocatalysis, bacteriostasis, and medicine was prospected. The purpose of this review was to point out the direction for further study on photocatalytic and antibacterial activities and related applications of TiO_2 and TiO_2-based photocatalysts.

Keywords: TiO_2, heterojunction, photocatalytic activity, antibacterial activity, orthopedic implants

1 INTRODUCTION

The development of global economy has brought comfortable material living conditions and various conveniences to the people of the world, but at the same time, it has caused great pressure on the environment (Tiwari et al., 2022). Dyes are closely related to the clothes people wear, the paper they use, and the packaging of food and medicine. The use of these dyes discharges a large amount of organic dye wastewater into rivers, resulting in water pollution (Chow et al., 2021; Feng et al., 2021; Liu et al., 2022a). The most effective method to kill the pollution of organic dye is at the source, to solve the pollution of organic dye wastewater. Therefore, the development of new technical means to degrade organic dyes has become an urgent task to solve water pollution and has received extensive attention from all over the world.

In order to solve the problem of environmental pollution, the world's developed countries associated together at all costs to solve this problem. Through unremitting efforts, many effective

means have been developed to solve the problem of water pollution (Wang et al., 2019; Wang et al., 2020a; Wang et al., 2020b; Shifa Wang et al., 2020; He et al., 2021a; Wang et al., 2021a; Cheng et al., 2021; Mateo et al., 2021; Saheed et al., 2021; Han et al., 2022; He et al., 2022), including 1) the thermal catalysis technique driven by thermal energy; 2) the electrocatalytic technology driven by electricity; 3) the photocatalysis technique driven by light energy; 4) the ultrasonic catalytic technology driven by mechanical energy; 5) the biodegradation technology, which uses microbial degradation; 6) adsorption techniques, using physical or chemical properties or diffusion; and 7) the new catalytic technology using heat, light, electricity, and other methods. Among these catalytic technologies, the photocatalytic technology is a green catalytic technology that uses sunlight to achieve degradation of organic dyes. In order to realize the effective degradation of organic dyes, the selection of a suitable photocatalyst is very important.

Among many photocatalysts, TiO_2 photocatalysts have the longest research history (Fujishima and Rao, 1997). TiO_2 has three phases: tetragonal, orthogonal, and monoclinic phases. It has an optical band gap of 3.2 eV, can respond to ultraviolet light, and is a good ultraviolet photocatalyst, which has a wide range of applications in the industrial degradation of organic dyes (Wu and Yu, 2004). Meanwhile, it has high antibacterial activity and also has a wide range of applications in the fields of photocatalytic and antibacterial implants (Skorb et al., 2008). However, due to its large optical band gap value, it is difficult to respond to visible light, and the visible light occupies the majority of sunlight, which limits its application in the field of photocatalysis or photocatalytic and antibacterial implants (Dalton et al., 2002). Therefore, researchers have adopted many methods to improve the photocatalytic and antibacterial activities of TiO_2. 1) TiO_2 photocatalysts with a special defect structure were synthesized under extreme conditions. TiO_2 photocatalysts synthesized under such extreme conditions have a high specific surface area, which introduces a large number of defects and makes it have a high surface active site, thus enhancing its photocatalytic and antibacterial activities (Qu and Kroes, 2007; Li et al., 2017; Li et al., 2021a). 2) An atom with a similar radius to the Ti atom is selected for doping, and the optical band gap value of TiO_2 is reduced to achieve the purpose of responding to visible light. This method allows the atom to be doped to occupy the position of the Ti atom, but not many atoms can be doped. If the synthesis method is not chosen correctly, it can easily form composites (Colón et al., 2006; Cong et al., 2007; Zaleska, 2008). 3) Special preparation technology to construct a special heterojunction structure or surface-modified TiO_2 photocatalysts to enhance the photocatalytic or antibacterial activity of TiO_2 photocatalysts was developed (Chen et al., 2010; Bai et al., 2015; Martins et al., 2016). This method does not change the optical band gap value of TiO_2, and it combines one or more excellent physical and chemical properties of semiconductors so that the new TiO_2-based photocatalyst combined together has enhanced or novel physical and chemical properties.

In this study, the preparation methods of TiO_2, ion-doped TiO_2, and TiO_2-based composite photocatalysts are reviewed, and the effects of preparation methods on the physicochemical properties of TiO_2-based photocatalysts are summarized. Meanwhile, the photocatalytic and bacteriostatic activities of TiO_2, ion-doped TiO_2, and TiO_2-based composite photocatalysts in degradation of organic pollutants and antibacterials were reviewed. Based on the review of photocatalytic and antibacterial activities of TiO_2-based photocatalysts, the photocatalytic and antibacterial mechanisms and application of TiO_2-based photocatalysts in orthopedic implants were summarized. This review puts forward the future development direction of TiO_2-based photocatalysts and provides corresponding technical reference for expanding the study of other photocatalysts.

2 PREPARATION OF MICRO/NANOSTRUCTURED TIO_2-BASED PHOTOCATALYSTS

The photocatalytic and bacteriostatic activities of the micro/nanostructured TiO_2-based photocatalyst strongly depend on the preparation method (Nakata and Fujishima, 2012; Daghrir et al., 2013; Guo et al., 2019). TiO_2-based photocatalysts synthesized by using different preparation methods may have the advantages of large specific surface area, large surface defect concentration, and high charge carrier transfer and separation efficiency, thus greatly improving the photocatalytic and antibacterial activities of the system (Zhang et al., 1998; Choi et al., 2010).

2.1 Preparation of Micro/Nanostructured TiO_2 Photocatalysts

With the rapid development of technology, the preparation method of TiO_2 has also been in rapid development. But, really summed up, there are only two methods: physical and chemical methods. Physical methods mainly include the solid phase sintering method, vacuum evaporation, vapor phase transfer deposition, and sputtering method. Pure TiO_2 prepared by using the physical method is mainly in the form of a film, and as a photocatalyst, it has the disadvantages of having a small contact area and low photocatalytic efficiency. Chemical methods mainly include the gas-phase and liquid-phase preparation method. The commonly used gas-phase methods for the preparation of TiO_2 include gas fuel combustion, gas phase oxidation, and the atmospheric microwave plasma gas-phase method. The liquid phase methods include the sol–gel method, inorganic salt hydrolysis method, solvothermal method, micro-emulsion method, hydrolysis, hydrothermal method, HCl–water volatilization-assisted precipitation method, and polyacrylamide gel method (Macwan et al., 2011; Yu et al., 2009; Fan et al., 2009). Ren et al. (2022) prepared the TiO_2 nanoparticles by using the HCl–water volatilization-assisted precipitation method, which exhibit high photocatalytic

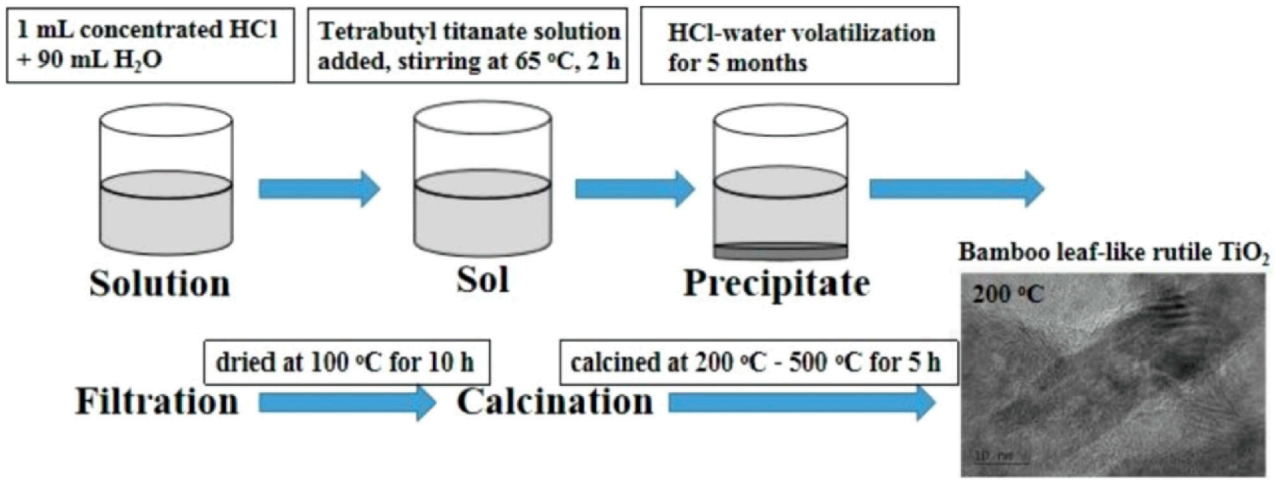

FIGURE 1 | Preparation flow chart of pure TiO_2 nanoparticles prepared by the HCl–water volatilization-assisted precipitation method. Adapted from Ren et al. (2022). Copyright © 2021 Elsevier B.V.

activity for the degradation of methyl orange. **Figure 1** shows the preparation flow chart of pure TiO_2 nanoparticles prepared by using the HCl–water volatilization-assisted precipitation method. TiO_2 nanoparticles prepared by using this method have a one-dimensional structure, which greatly enhances its specific surface area and improves its photocatalytic activity. The polyacrylamide gel method is also a common method used to prepare TiO_2 nanoparticles. The nanoparticles prepared by this method are uniformly dispersed with almost no adhesion agglomeration and are widely used in the preparation of metal oxide semiconductor materials and multiple heterojunction composite semiconductor materials (Xian et al., 2013; Gao et al., 2021a; Gao et al., 2021b; He et al., 2021b; Li et al., 2021b; Liang et al., 2021; Tang et al., 2022a; Liu et al., 2022b; Fu et al., 2022; Gao et al., 2022; Wang et al., 2022). Lu et al. (2022) prepared the TiO_2 nanotube photocatalysts, which exhibit high photocatalytic activity for the degradation of patulin in simulated juice. This special structure enables TiO_2 to achieve new applications in the degradation of cold drugs.

2.2 Preparation of Micro/Nanostructured Ion-Doped TiO_2 Photocatalysts

Ion doping mainly includes metal ion doping and non-metal ion doping. Metal ion doping mainly introduces metal ions such as alkali metals, transition metals, and rare earth metals into the crystal structure of pure TiO_2, making metal ions become the receiver pole of photogenerated electrons or the defect that can capture photogenerated electrons, thus improving the separation of the photogenerated charge carrier and correspondingly improving the photocatalytic capacity of photocatalysts. Non-metallic ion doping generally involves doping B, N, C, S, and other non-metallic elements close to O elements into TiO_2 photocatalysts. It is generally believed that the hybridization of p orbital and 2p orbital of O in the non-metal leads to an upward shift in the valence band width of TiO_2, which reduces the band gap width and enables TiO_2 to absorb visible light.

The key to the synthesis of ion-doped TiO_2 is to control the composition and content of doped ions and element substitution for the position of Ti. Researchers usually adopt physical and chemical methods to enhance the photocatalytic activity of TiO_2 by doping metal ions or non-metal ions in the lattice position of Ti or modifying the surface of TiO_2. Generally, it is easy to modify TiO_2 with metal ions, and the photocatalytic and bacteriostatic activities of TiO_2 can be greatly improved by chemical experiments. Ellouzi et al. (2021) synthesized silver-doped TiO_2 nanoparticles by the glucose-assisted ball-milling method, which exhibit high photocatalytic activity for efficient photodegradation of rhodamine B. The preparation flow chart of silver-doped TiO_2 nanoparticles prepared by using the glucose-assisted ball-milling method is shown in **Figure 2**. As can be seen from the figure, it is easier to modify Ag particles to the surface of TiO_2 nanoparticles by the glucose-assisted ball-milling method, thus improving the uniformity of the entire sample particles. Venkatachalam et al. prepared Mg^{2+}- and Ba^{2+}-doped TiO_2 nanoparticles by using the sol–gel method (Venkatachalam et al., 2007). The band gap value of nano-TiO_2 doped with Mg^{2+} and Ba^{2+} is higher than that of pure nano-TiO_2, but the photocatalytic activity of 4-chlorophenol degradation is higher than that of pure nano-TiO_2 and commercial Degussa P25. Hu et al. (2022) synthesized Ni-doped TiO_2 nanotubes by using the anodic oxidation method, which exhibit high electrocatalytic activity for the degradation of phenol wastewater. Zhou et al. (2019) prepared a photocatalyst doped with six different types of rare earth (RE) ions (La, Ce, Pr, Nd, Eu, or Gd) by using the microwave hydrothermal treatment method. The results showed that the structure and chemical properties of nanocomposites are related to the radius of Re^{3+}. Since the radius of Re^{3+} is much larger than that of Ti^{4+}, Ti^{4+} can replace Re^{3+} in the lattice of Re_2O_3 in the form of Ti^{3+}, and it produces charge imbalance due to its small ionic radius.

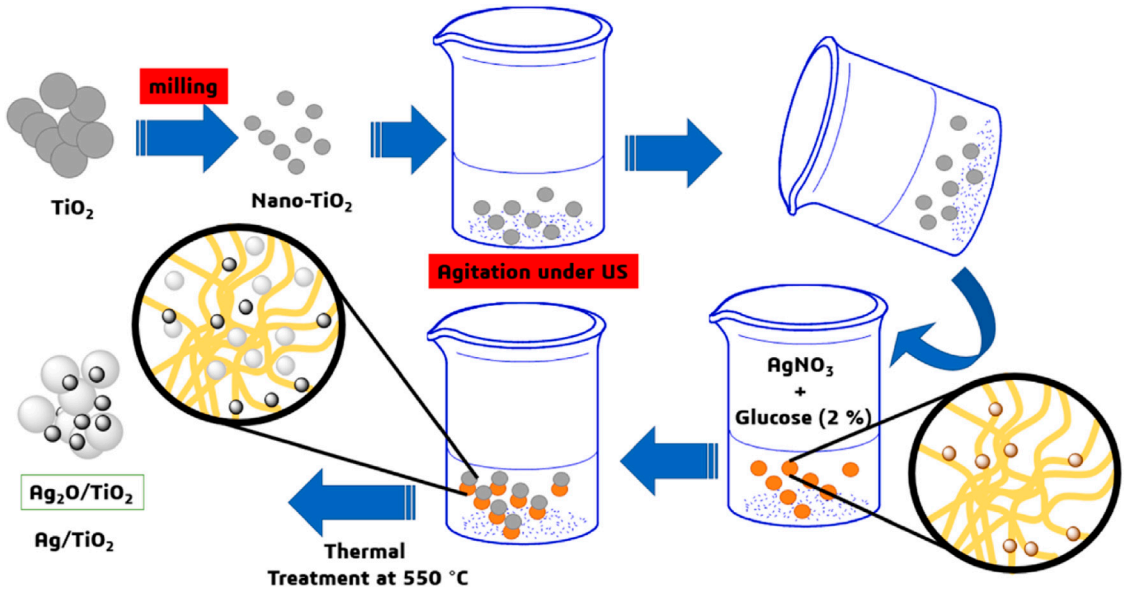

FIGURE 2 | Preparation flow chart of silver-doped TiO_2 nanoparticles prepared by the glucose-assisted ball-milling method. Adapted from Ellouzi et al. (2021). Copyright © 2021 Elsevier B.V.

Boningari et al. (2018) successfully prepared N-doped TiO_2 by using a new single-step flame spraying method. The results showed that the N atom is effectively doped into the crystal structure of TiO_2. The combination of the N atom and TiO_2 crystal structure changed the electronic band structure of TiO_2, formed a new middle gap energy state N 2p band in the O 2p valence band, reduced the band gap width of TiO_2, and transferred the optical absorption of TiO_2 to the visible region. The results showed that the N-doped TiO_2 improved TiO_2's solar energy utilization rate. Zhang et al. (2015) continuously deposited TiO_2 using monodispersed cationic polystyrene microspheres as templates by using the directional self-assembly method and then removed cationic polystyrene microspheres by calcination at 450°C to obtain C-doped hollow TiO_2. Under visible light irradiation, C-doped hollow anatase TiO_2 has better photocatalytic activity than commercial P25.

2.3 Preparation of Micro/Nanostructured TiO_2-Based Composite Photocatalysts

The TiO_2-based composite photocatalysts mainly show two states: one is the formation of heterojunction, and the other is mixed together in a simple way. Semiconductor heterostructures are usually constructed by coupling two or more semiconductors with different band gap widths to widen the light response range of wide-gap semiconductors and improve the separation efficiency of photogenerated electron hole pairs. If two or more semiconductor materials are simply combined, a simple one-step synthesis can be performed by many chemical processes. When two or more semiconductor materials are combined in a heterojunction, special preparation methods are required to couple them together. Some special morphologies, such as the hierarchical structure and core-shell structure, were constructed to promote the separation of photogenerated electron holes from the built-in electric field, thus improving the photocatalytic efficiency of the photocatalyst.

There are many methods for heterostructure construction, including the sol–gel method, electrostatic spinning method, hydrothermal method, solvothermal method, spin-coating method, and facile solid–liquid adsorption template technology, followed by calcination process. **Table 1** shows the preparation method of micro/nanostructured TiO_2-based composite photocatalysts. Based on the different uses of TiO_2 composite photocatalyst, different methods can be used to regulate and synthesize heterojunction composites with different morphologies. Wang et al. (2021b) prepared SiO_2-TiO_2@PDMS by the spray method, which exhibited excellent repellent effect toward organic dye droplets and good mechanical stability. Xu et al. (2022) synthesized the core-shell C@TiO_2 microspheres by using a three-step method, which exhibit high electrochemical property. **Figure 3** shows the preparation flow chart of core-shell C@TiO_2 microspheres prepared by using a three-step method. Uniform core-shell C@TiO_2 microspheres can be obtained by this method. However, in order to increase the photocatalytic or bacteriostatic activity of TiO_2-based composite photocatalysts, defects, impurity levels, and transport carrier of charge carriers should be introduced into the composite. As the companion of TiO_2 heterojunction, the selection of the other half plays a crucial role in the photocatalytic and antibacterial activities of TiO_2 catalysts. Improper selection of another semiconductor may result in the reduced photocatalytic or bacteriostatic activity of the entire system. Therefore, the

TABLE 1 | Preparation method of micro/nanostructured TiO_2-based composite photocatalysts.

Catalyst	Preparation method	Reference
MAO/TiO_2	Spin-coating method	Zhang et al. (2022)
SiO_2-TiO_2@PDMS	Spray method	Wang et al. (2021b)
Si@TiO_2/C	Facile solid–liquid adsorption template technology followed by the calcination process	Xiang et al. (2020)
Core-shell C@TiO_2	Three-step method	Xu et al. (2022)
Ag_2O/TiO_2	Two-step method	Gao and Wang, (2021)
Polymeric carbon nitride/TiO_2	Template method	Wu et al. (2022)
Black hollow TiO_2 nanotube-coated PDA@Ag_2S	Hydrothermal and *in situ* polymerization methods	Jiang et al. (2022)
rGO-ZnS-TiO_2	Ultrasonic irradiation method	Kale et al. (2020)
ZnO/TiO_2/ZrO_2	Continuous-wave laser irradiation method	Abrinaei and Aghabeygi, (2022)
TiO_2@Y_2O_3	Sol–gel method and high-temperature calcination reduction	Jiang et al. (2021)
TiO_2/g-C_3N_4	Hard template approach	Li et al. (2021c)
$Li_4Ti_5O_{12}$–TiO_2	Solvothermal technique	Santhoshkumar et al. (2022)
SiO_2/TiO_2	Facile grinding and the calcination process	Sun et al. (2020)
TiO_2/SiO_2	Facile spraying method	Wu et al. (2021)
Pt/TiO_2/γ-Al_2O_3	Electrospinning-coated $NaBH_4$ reduction method	Zhu et al. (2022a)

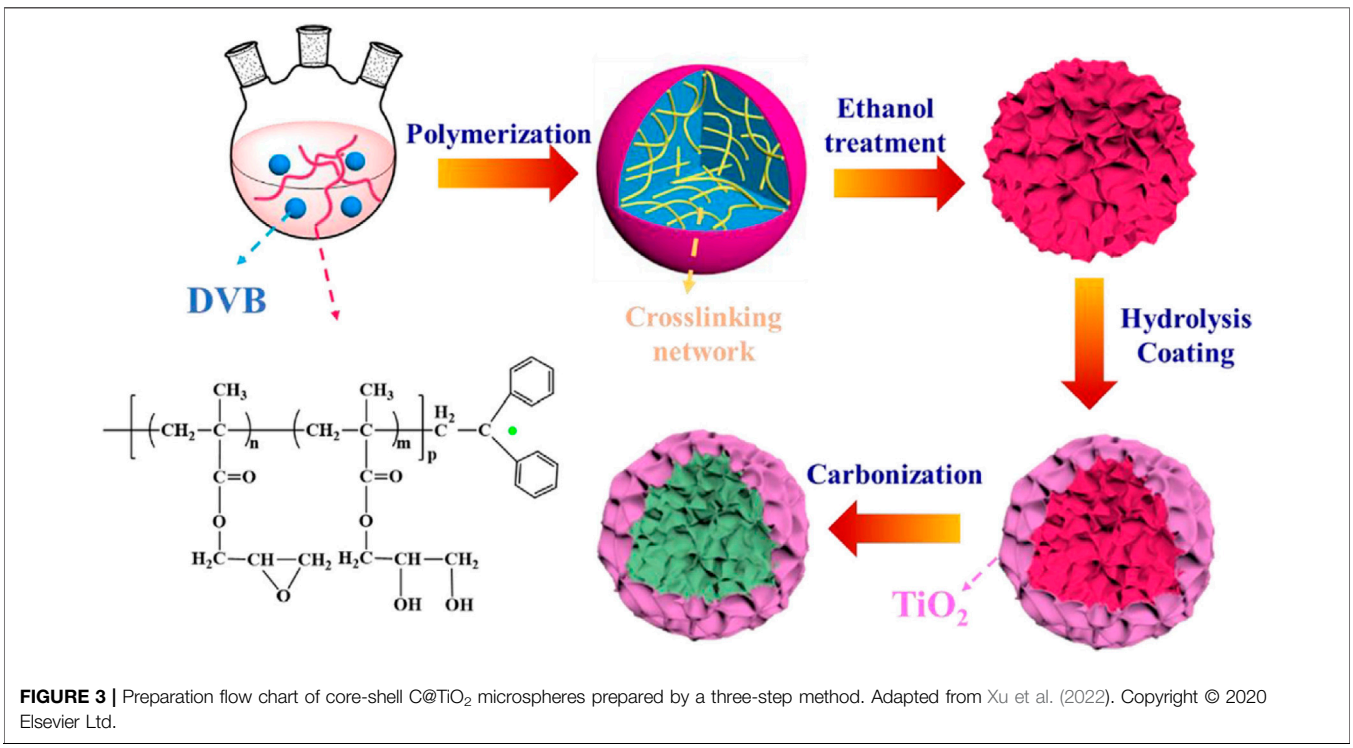

FIGURE 3 | Preparation flow chart of core-shell C@TiO_2 microspheres prepared by a three-step method. Adapted from Xu et al. (2022). Copyright © 2020 Elsevier Ltd.

preparation method is only one of the important factors affecting the photocatalytic and antibacterial activities of TiO_2-based composite photocatalysts.

3 PHOTOCATALYTIC ACTIVITY OF MICRO/NANOSTRUCTURED TiO_2-BASED PHOTOCATALYSTS

3.1 Photocatalytic Activity of Micro/Nanostructured TiO_2 Photocatalysts

The photocatalytic activity of TiO_2 strongly depends on its preparation method. TiO_2 with different morphologies can be obtained by using different preparation methods, including nanoparticles, nanoflowers, nanosheets, nanoribbons, microspheres, and nanotrees. For pure phase TiO_2, it can only respond to ultraviolet light and can degrade different kinds of dyes, drugs, and some pollutants that are difficult to degrade. Due to the small composition of ultraviolet light in natural light, this greatly limits the application of TiO_2 photocatalyst in the field of photocatalysis. The recombination rate of photogenerated carriers in TiO_2 is much higher than its mobility, which makes the photogenerated carriers to migrate to the surface of TiO_2 and participate in very few photocatalytic reactions. At present, commonly used TiO_2 photocatalysts are mainly powdered nanoparticles, which makes it difficult to separate,

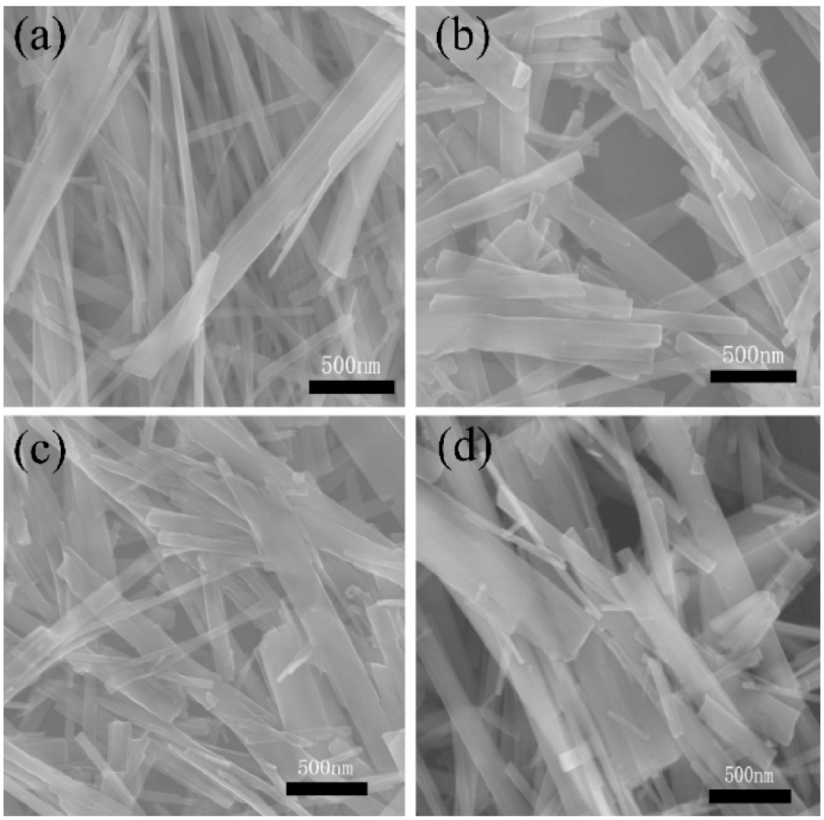

FIGURE 4 | SEM images of **(A)** TiO_2 nanobelts, **(B)** TiO_2 nanobelts calcined at 400°C for 3 h in air, **(C)** TiO_2 nanobelts with 30 mg $NaBH_4$, and **(D)** TiO2 nanobelts annealed at 400°C for 3 h under a H_2/Ar atmosphere. Adapted from Xie et al. (2021). Copyright © 2021 Capital Normal University. Published by Elsevier B.V.

recycle, and reuse from liquid after the photocatalytic reaction. On the one hand, it causes waste of photocatalysts; on the other hand, it is easy to cause secondary pollution, which limits its large-scale use. However, as a catalyst for industrial use, TiO_2 has contributed a lot.

For pure phase TiO_2 catalysts, many researchers used special preparation methods to construct defects or special morphology to enable TiO_2 to respond to visible light, thus expanding the application of TiO_2 photocatalyst in the field of photocatalysis. Xie et al. (2021) synthesized the TiO_2 nanobelts by a molten salt method with the $NaBH_4$ or H_2/Ar atmosphere and exhibits high photocatalytic activity. **Figure 4** shows the SEM images of TiO_2 nanobelts, TiO_2 nanobelts calcined at 400°C for 3 h in air, TiO_2 nanobelts with 30 mg $NaBH_4$, and TiO_2 nanobelts annealed at 400°C for 3 h under a H_2/Ar atmosphere. TiO_2 nanobelts have different concentrations of oxygen vacancies and special electronic structures through different treatment methods, thus enhancing the transfer and separation efficiency of electrons and holes in TiO_2 and finally achieving the purpose of enhancing the photocatalytic activity of TiO_2 nanoribbons. Therefore, a variety of extreme conditions are used to construct TiO_2 surface defects, regulate the electronic structure of TiO_2, and enable it to have high oxidation or reduction capacity, thus achieving the purpose of degrading dyes. However, this approach often has the disadvantages of high equipment requirements, high cost, and unsafe, and the concentration of surface defects cannot be accurately controlled, which further limits the development of this technology. Kaushik et al. (2019) transformed 2D TiO_2 to mesoporous hollow 3D TiO_2 spheres by using the solvothermal strategy followed by thermal treatment, which exhibit high photocatalytic and antibacterial activities. This strategy provides a new idea for the follow-up study of TiO_2.

3.2 Photocatalytic Activity of Micro/Nanostructured Ion-Doped TiO_2 Photocatalysts

Ion doping is one of the effective ways to enhance the photocatalytic activity of the TiO_2 photocatalyst. The optical band gap value of TiO_2 can be effectively improved by doping different ions. The reduction of its optical band gap value enables it to respond to visible light, expanding its application in the field of photocatalysis. The ultimate goal is to prevent the recombination of electron–hole pairs inside TiO_2 so that electrons react with dyes in its conduction band, and the holes in the valence band react with dyes to generate

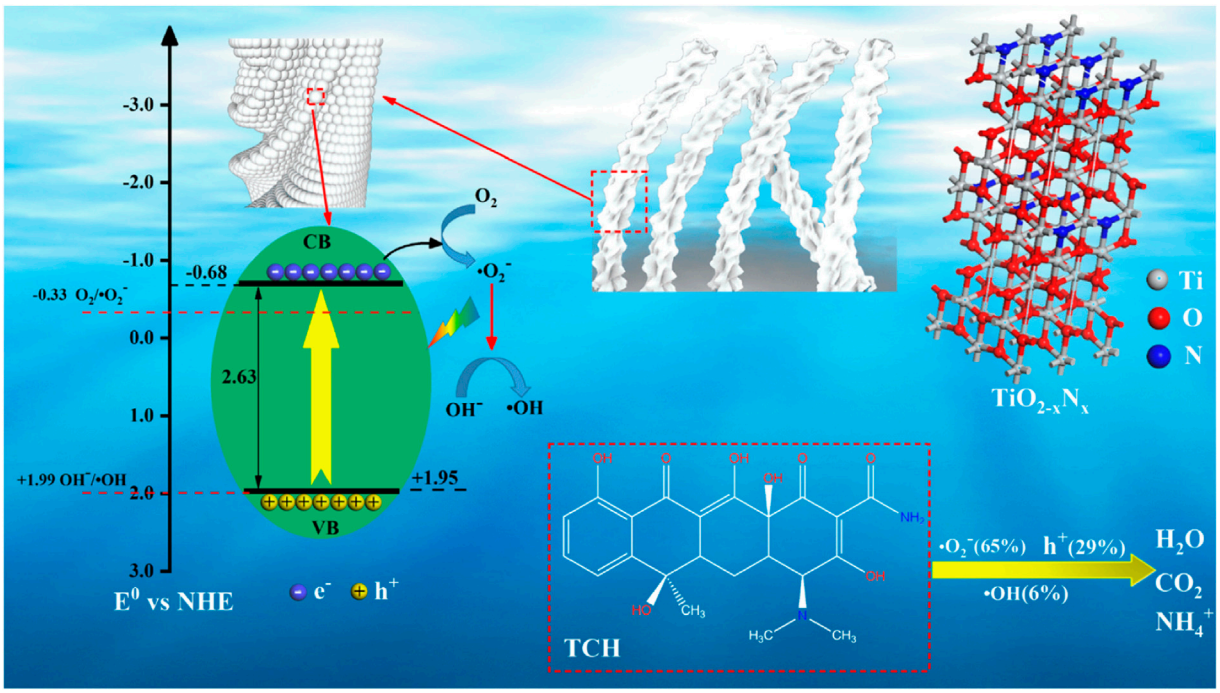

FIGURE 5 | Photocatalytic mechanism diagram of C-modified and N-doped TiO_2 photocatalysts. Adapted from Zhu et al. (2022b). Copyright © 2022 Elsevier B.V.

non-toxic and harmless products. Ion doping is divided into metal doping and non-metal doping, and metal doping is mainly performed by doping rare earth ions and transition metal ions (Santos et al., 2022). As for noble metal ions, they are easy to exist in the elemental form, so TiO_2 is mostly modified on the surface of noble metal particles to enhance the photocatalytic activity of TiO_2 (Phromma et al., 2022). The photocatalytic activity of ion-doped TiO_2 is also affected by the surface morphology, oxygen vacancy, electronic structure, and optical band gap value.

Unlike metal ion doping, non-metal ion–doped TiO_2 can be sintered at high temperature to remove non-metal ions. Therefore, it is necessary to control the appropriate sintering temperature to keep non-metal ions. This will bring a new problem: the content of non-metallic ions cannot be controlled. However, non-metallic ion doping does solve the shortcoming that TiO_2 cannot respond to visible light, which enables it to have high visible light photocatalytic activity. Zhu et al. (2022b) reported that the C-modified and N-doped TiO_2 photocatalysts prepared by the hydrothermal method using tetrabutyl titanate (TBOT) and feathers of chicken as the precursor exhibit high photocatalytic activity for the degradation of tetracycline hydrochloride under visible light irradiation. **Figure 5** shows the photocatalytic mechanism diagram of C-modified and N-doped TiO_2 photocatalysts. Carbon acts as a carrier of charge carriers in the whole system, separating photogenerated electrons and holes in space. Nitrogen doping can make TiO_2 respond to visible light.

3.3 Photocatalytic Activity of Micro/Nanostructured TiO_2-Based Composite Photocatalysts

TiO_2 composite photocatalysts can overcome the shortcoming of uncontrollable doping content of non-metal ions. Combining the advantages of two or more kinds of semiconductor materials, the whole system has physical and chemical properties that a single component does not have at the same time, which is the key to the design of TiO_2-based composite photocatalysts (Perales-Martínez et al., 2015; Hao et al., 2016; Sotelo-Vazquez et al., 2017). This design method will not only change the optical band gap value of TiO_2 but also will introduce surface defects or oxygen vacancies at the interface of the two semiconductors. Therefore, the study of the interface characteristics of two or more semiconductors is conducive to insight into the photocatalytic mechanism of TiO_2-based complex photocatalyst. In addition to metal oxides that can form heterojunctions with TiO_2, some polymers and sulfides can also form heterojunctions with TiO_2 in special ways to enhance the photocatalytic activity of TiO_2 (Vorontsov et al., 2001; Liao et al., 2010; Antoniadou et al., 2011; Riaz et al., 2015). Therefore, there are many kinds of TiO_2-based photocatalysts, but the ultimate goal is to make TiO_2

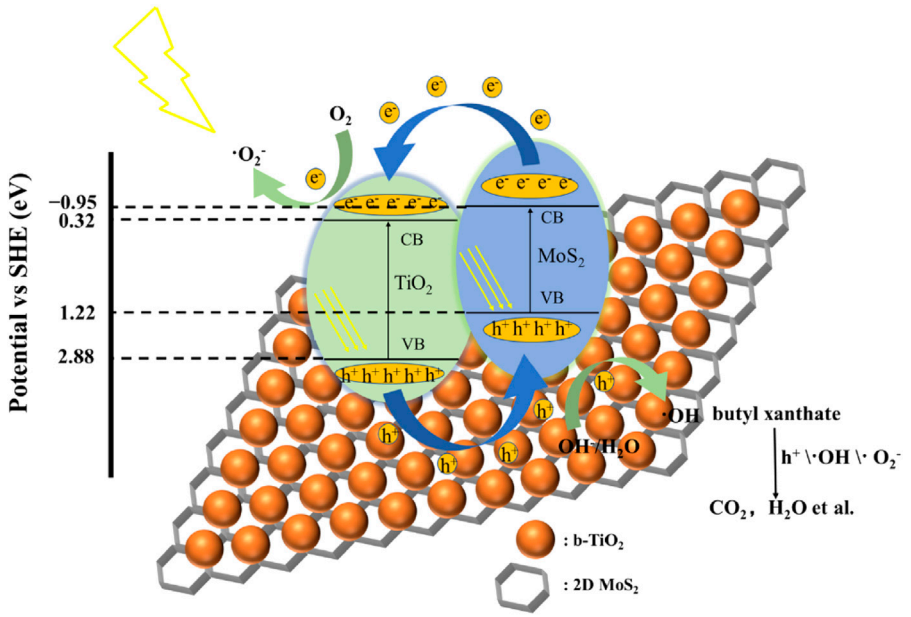

FIGURE 6 | Photocatalytic mechanism diagram of b-TiO_2 @MoS_2 photocatalysts. Adapted from Tang et al. (2022b). Copyright © 2022 Elsevier B.V.

exhibit high visible light photocatalytic activity or show new physical and chemical properties.

To summarize, there are four main ways to form a heterojunction (Schuettfort et al., 2009; Low et al., 2017; Guo et al., 2021): one is that the conduction band of a semiconductor is located in the conduction band and valence band of another semiconductor. The other is that the conduction band and valence band of one kind of semiconductor are located in the interior of another kind of semiconductor. Third, the conduction band and valence band of the two kinds of semiconductor are completely separated. Fourth, there is no conduction band and valence band between metal particles and semiconductor heterojunction. Tang et al. (2022b) reported that the b-TiO_2 @MoS_2 photocatalysts synthesized by an ultrasound technique coupled with the sol–gel method at low temperature exhibit high visible light photocatalytic activity. A photocatalytic mechanism diagram of b-TiO_2 @MoS_2 photocatalysts is shown in **Figure 6**. As can be seen from the figure, the valence band of MoS_2 is located inside the conduction band and valence band of TiO_2. Such a structure facilitates the relaxation of electrons from the more negative conduction band of MoS_2 to the conduction band of TiO_2, and the transition of holes from the more positive valence band of TiO_2 to the valence band of MoS_2, thus promoting the separation of electrons and holes. At present, the construction of special heterojunction TiO_2-based composite photocatalysts has become the most popular effective way to enhance the photocatalytic activity of TiO_2 photocatalysts.

4 ANTIBACTERIAL ACTIVITY OF MICRO/NANOSTRUCTURED TIO_2-BASED PHOTOCATALYSTS

4.1 Antibacterial Activity of Micro/Nanostructured TiO_2 Photocatalysts

The high antibacterial properties of orthopedic implants are an effective way to avoid infection during surgery, which will reduce the incidence of amputation or death due to infection. Generally, antibacterial materials can be divided into natural antibacterial materials, organic antibacterial materials, and inorganic antibacterial materials (Li et al., 2020). Inorganic antibacterial materials can be divided into two categories: one is the prepared antibacterial materials containing copper, silver, zinc, and other metal antibacterial ions; the second is photocatalytic antibacterial materials represented by TiO_2; such inorganic antibacterial materials can play an antibacterial role under the condition of ultraviolet light irradiation, water, or oxygen (Chen et al., 2017; Wang et al., 2020c). TiO_2 is a widely studied orthopedic implant material with high photocatalytic antibacterial activity. Titanium dioxide has become the most common photocatalytic antibacterial material because of its low toxicity, high safety, and no irritation to skin. Silver antibacterial materials take about 24 h to exert the antibacterial effect, while the oxide ingots only take about an hour. Moreover, the antibacterial effect of the dioxide ingot is carried out through photocatalysis, and it itself will not be consumed in the antibacterial process so that the antibacterial material of dioxide ingot has a more lasting antibacterial performance.

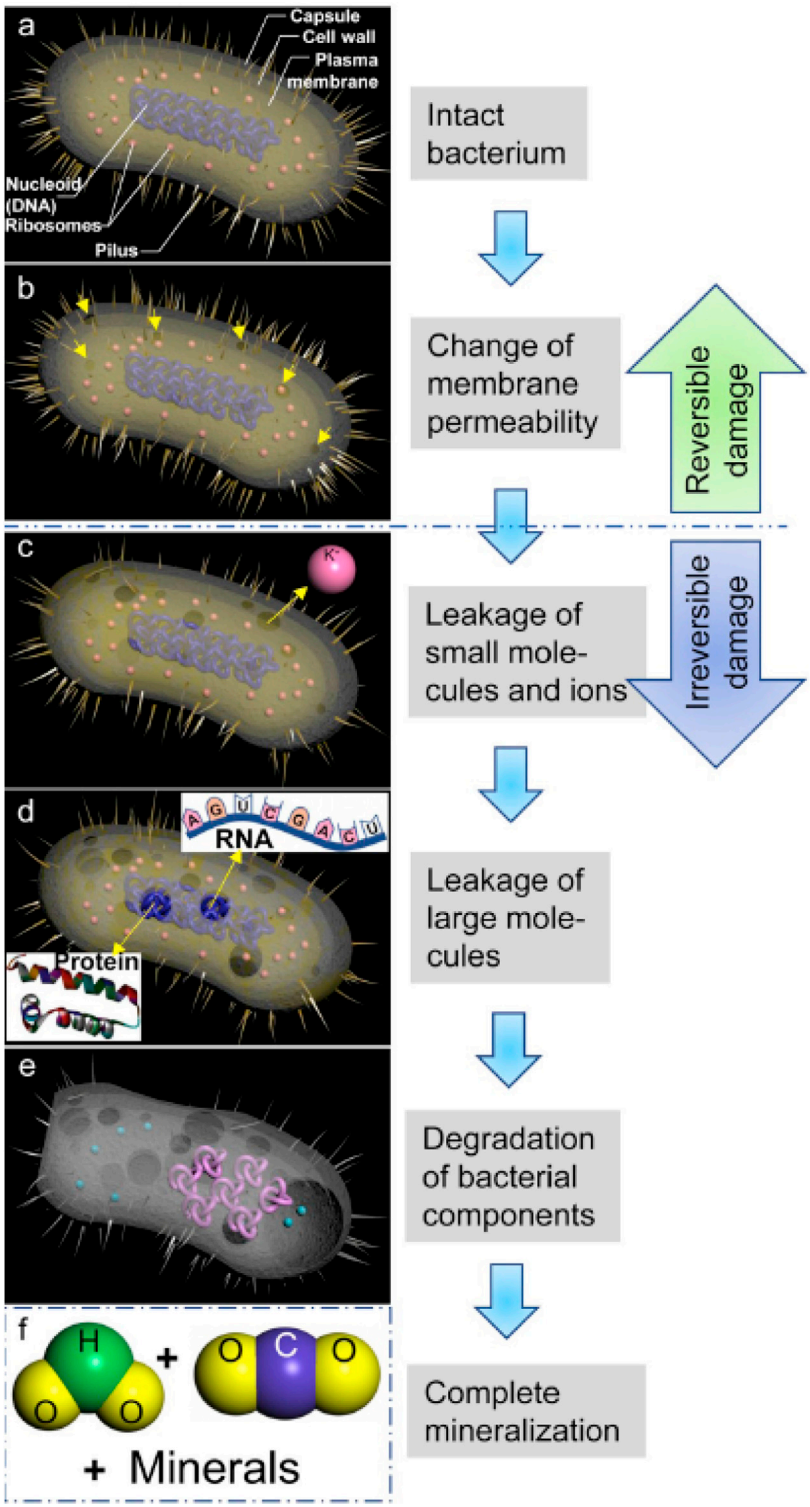

FIGURE 7 | Photocatalytic bactericidal process of TiO_2 photocatalysts. Adapted from Ge et al. (2019). Copyright © 2020 Production and hosting by Elsevier B.V. **(A)** An intact bacterium; **(B)** Bacterial oxidized by TiO_2 photocatalysis; **(C)** The bacterium leak small molecules and ions; **(D)** Leakage of higher molecular weight components; **(E)** Degradation of bacterial internal components; **(F)** The bacterium was completely mineralized.

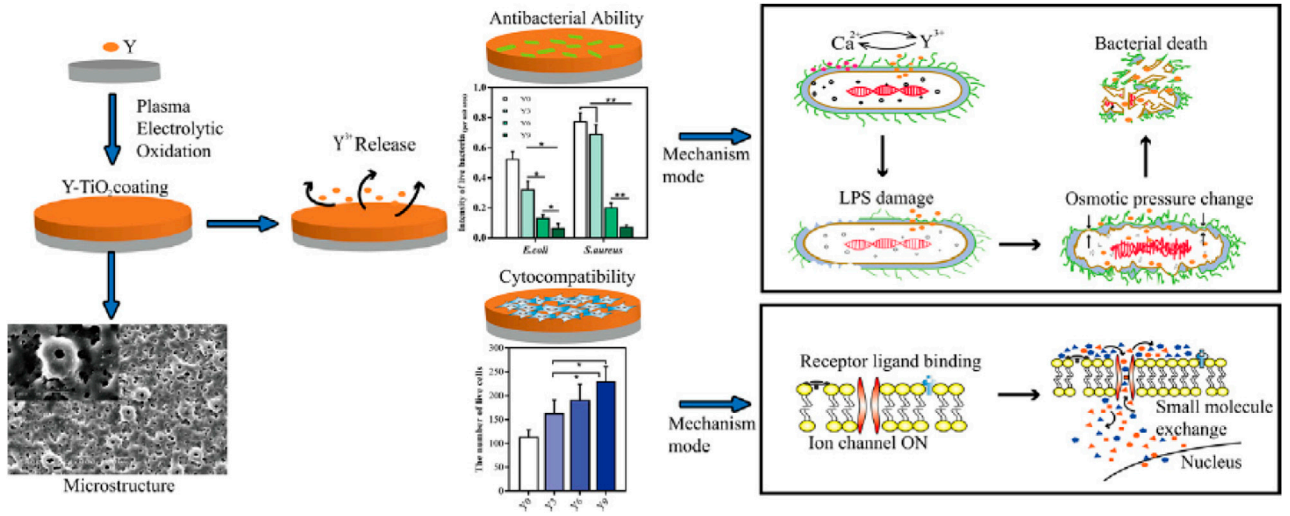

FIGURE 8 | Preparation flow chart and antibacterial mechanism of Y-doped TiO_2 photocatalysts. Adapted from Zhang et al. (2020). Copyright © 2020 Published by Elsevier Ltd.

The antibacterial mechanism of titanium dioxide is similar to its photocatalytic mechanism, and the resulting hydroxyl radicals can react with biological macromolecules, damage the structure of biological cells, and then lead to cell death. **Figure 7** shows the photocatalytic bactericidal process of TiO_2 photocatalysts. Bacteria eventually mineralize H_2O, CO_2, and other small molecular organics under the action of TiO_2 (Ge et al., 2019). Similarly, the antibacterial activity of TiO_2 is affected by its morphology, surface defects, oxygen vacancy concentration, and electronic structure (Mazare et al., 2016). At the same time, the crystal type of titanium dioxide also has a great influence on its antibacterial activity. TiO_2 has high antibacterial activity under ultraviolet light irradiation, but TiO_2 is powerless under visible light irradiation due to the limitation of its own optical band gap value. Therefore, researchers are committed to improving the photocatalytic antibacterial mechanism of TiO_2 through ion doping and heterostructure construction.

4.2 Antibacterial Activity of Micro/Nanostructured Ion-Doped TiO_2 Photocatalysts

In the process of using the antibacterial activity of titanium dioxide, the photoresponse range of titanium dioxide is narrow, and the photoelectron–hole pair is easy to compound. To solve such problems, TiO_2 photocatalytic materials can be modified structurally or on the surface so as to increase the light response range. This modification process can also reduce the recombination probability of carriers and improve the quantum efficiency, thus enhancing the photocatalytic bacteriostatic effect of TiO_2. Recently, the application of TiO_2 in the field of antibacterial materials has achieved remarkable results. With the continuous development and utilization of antibacterial performance of the TiO_2 photocatalyst, glass, ceramics, metal products, coatings, fibers, plastics, and other antibacterial products can be produced by plating on the surface of materials or doping in other materials (Mori, 2005; Tung and Daoud, 2011).

Ion-doped TiO_2 photocatalysts have been widely used in the bacteriostatic field. Similar to the photocatalytic activity of the TiO_2 photocatalyst, ion-doped TiO_2 can be divided into metal ion doping and non-metal ion doping when studying the antibacterial activity of ion-doped TiO_2. Zhang et al. (2020) reported that the Y-doped TiO_2 photocatalysts prepared by the plasma electrolytic oxidation method exhibit high bacteriostatic activity. **Figure 8** shows the preparation flow chart and antibacterial mechanism of Y-doped TiO_2 photocatalysts. The result shows that the Y-doped TiO_2 photocatalysts possess excellent bacteriostatic activity against *Staphylococcus aureus* and *Escherichia coli* and outstanding biocompatibility and antibacterial capacity. Yadav et al. (2014) prepared nickel-doped TiO_2 nanoparticles by using the sol–gel method, which show the high photocatalytic inactivation and lower recombination rate of photogenerated charge carriers. Similarly, non-metallic doping can also greatly improve the antibacterial activity of TiO_2. Cao et al. (2014) reported that the N-doped TiO_2 thin films coated on stainless steel brackets exhibit high antibacterial activity against *Lactobacillus acidophilus* and *Candida albicans*.

4.3 Antibacterial Activity of Micro/Nanostructured TiO_2-Based Composite Photocatalysts

The construction of heterojunction will greatly improve the surface oxygen vacancy concentration and interface

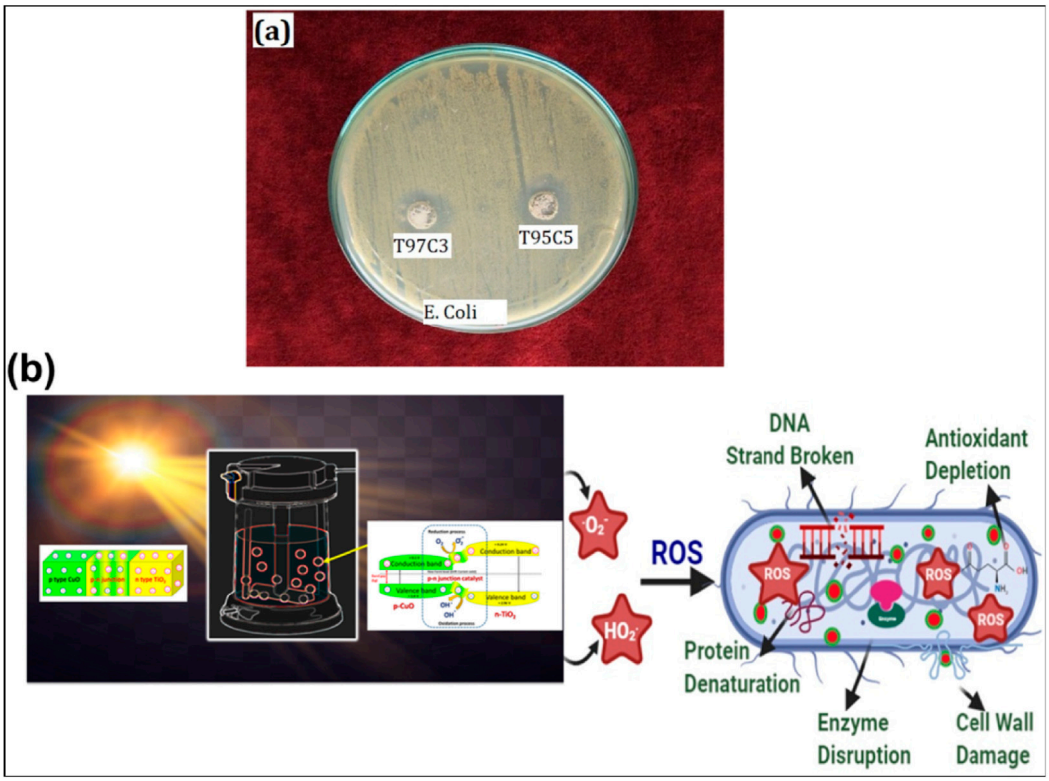

FIGURE 9 | (A) Antibacterial activity and **(B)** antibacterial mechanism of the p-n junction TiO_2/CuO heterojunction composite photocatalysts. Adapted from Gnanasekaran et al. (2021). Copyright © 2021 Elsevier Ltd.

characteristics of TiO_2 so that it has a high antibacterial activity and a potential application prospect in orthopedic implants. Similar to the study on the photocatalytic activity of TiO_2, its antibacterial activity has received unprecedented attention. The construction of heterojunction can form microspheres, mesoporous structures, layered structures, nanotubes, nanosheets, nanoribbons, nanotrees, and various flower-like structures (Wu et al., 2014; Lou et al., 2019; Murthy, 2019). These special morphologies will make TiO_2-based composite photocatalysts have high antibacterial activity. Combining the advantages of a variety of semiconductors will expand the application of TiO_2 in different fields, which is the absolute advantage of heterogeneous structure construction (Ma et al., 2015). Therefore, TiO_2-based heterojunction composite photocatalysts are widely favored by researchers.

Gnanasekaran et al. (2021) reported that p-n junction TiO_2/CuO heterojunction composite photocatalysts synthesized by the sol–gel method, followed by chemical precipitation methods, exhibit high photocatalytic and antibacterial activities. **Figure 9A** shows the antibacterial activity of p-n junction TiO_2/CuO heterojunction composite photocatalysts. The results indicate that the p-n junction TiO_2/CuO heterojunction composite photocatalysts possess high bacteriostatic activity. The antibacterial mechanism of the p-n junction TiO_2/CuO heterojunction composite photocatalysts is shown in **Figure 9B**. The conduction band and valence band of CuO are completely located inside TiO_2. However, due to the spatial separation of charge carriers, CuO and CuO have high transfer and separation efficiency, thus enhancing the antibacterial activity of TiO_2. At present, researchers focus on how to apply the prepared TiO_2-based heterojunction composite photocatalysts to orthopedic implants, hoping to move the research of TiO_2 from laboratory to practical application.

5 TiO_2-BASED PHOTOCATALYSTS FOR APPLICATION IN ORTHOPEDIC IMPLANTS

5.1 TiO_2 Photocatalysts for Application in Orthopedic Implants

Biomaterials implanted in the body will induce a series of reactions, including postoperative infection, inflammatory reaction (acute inflammatory reaction and chronic inflammatory reaction), and fibrous tissue hyperplasia, which can prolong the treatment period and increase the treatment cost of patients at one level or lead to amputation or even death of patients due to infection (Anderson, 1993; Lin et al., 2014; Zhang et al., 2021). The mechanism of infection around orthopedic implants is that bacteria adhere to the implant surface and form

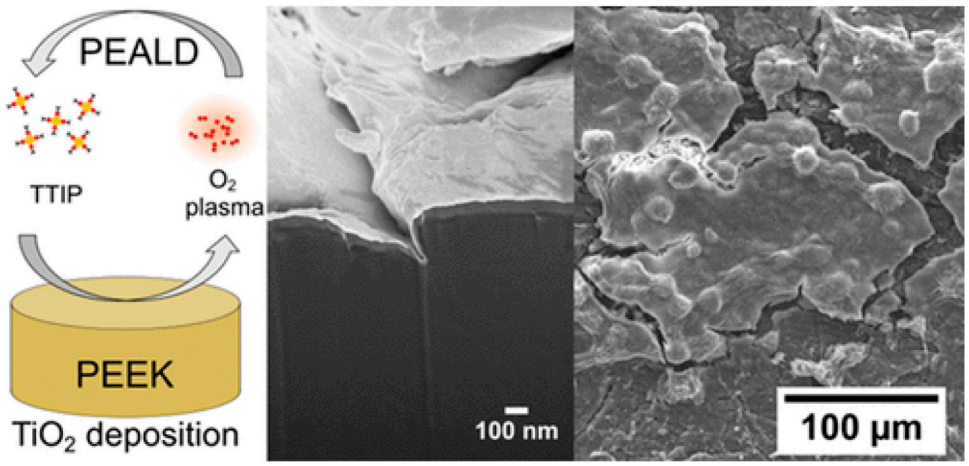

FIGURE 10 | Deposition mechanism and SEM images of TiO_2 thin films. Adapted from Blendinger et al. (2021). Copyright © 2021 The Authors. Published by the American Chemical Society.

biofilms. Deposition, adhesion, and growth are three main processes of biofilm formation. Therefore, orthopedic implants need to have high biocompatibility and bacteriostatic activity. TiO_2 has low toxicity, high biocompatibility, and high bacteriostatic activity, so it can be used as orthopedic implants in the medical field.

Blendinger et al. (2021) deposited TiO_2 thin films on the orthopedic implant material polyetheretherketone (PEEK) by plasma enhanced atomic layer deposition, which exhibit high biocompatibility and osteogenic properties. **Figure 10** shows the deposition mechanism and SEM images of TiO_2 thin films. This method provides a new idea for studying the biocompatibility and bacteriostatic properties of TiO_2 orthopedic implants. Antibiotics such as vancomycin, gentamicin, amoxicillin, and berberine were used in the study of pit bacteria coating on the titanium implant surface, among which gentamicin and vancomycin were the most commonly used. Popat et al. (2007) prepared TiO_2 nanotubes by using the anodic oxidation method and then loaded gentamicin into TiO_2 nanotubes. Experimental results showed that the gentamicin-loaded TiO_2 nanotubes could inhibit bacterial reproduction with good biocompatibility, but the release of antibiotics was faster. Due to the limitation of physical and chemical properties of pure TiO_2, its application in orthopedic implants is limited. In order to break through this limitation, ion doping and heterostructure construction are necessary effective methods to expand the application of TiO_2 in orthopedic implants.

5.2 Ion-Doped TiO_2 Photocatalysts for Application in Orthopedic Implants

In antibacterial agents, silver antibacterial agents have a wide range of antibacterial ability; can fight against Gram-negative bacteria, fungi, and even viruses; have low cytotoxicity, good stability, and low effective concentration; and are not easy to produce drug resistance and other advantages. Compared with eukaryotic cells, silver has greater toxicity to prokaryotic cells, so silver has excellent inhibition of microbial growth and proliferation and low cytotoxicity to biological somatic cells. Nanoscale silver particles have a high specific surface area, high contact probability with bacteria, and strong chemical activity. Atoms on the surface of silver particles are easy to bond with other chemical groups, and their antibacterial effect is much stronger than that of micron silver particles. Therefore, Ag-doped TiO_2 can improve the antibacterial activity and biocompatibility of TiO_2, which can be used in orthopedic implants. Zhao et al. (2013) used the anodic oxidation method and hydrothermal method in titanium implant surface preparation of Ag- and Sr-doped TiO_2 nanotubes, by changing the process parameters for different structures of TiO_2 nanotubes, as well as the precursor concentration change of Ag and Sr, and antibacterial performance and characterization of the biological activity of TiO_2 was improved. According to the results, TiO_2 coatings doped with Ag and Sr have good antibacterial activity and cytocompatibility. Amin Yavari et al. (2016) prepared TiO_2 nanotubes on the surface of 3D-printed porous titanium, then loaded the nanotubes with Ag nanoparticles, obtained a composite coating loaded with silver antibacterial factors on the surface of porous titanium, and studied the killing ability of silver ions on *Staphylococcus aureus*.

Lv et al. (2021) reported that the Zn-modified TiO_2 photocatalysts prepared by the micro-arc oxidation technique exhibit high cytocompatibility and bactericidal ability for orthopedic implants. **Figure 11** shows the pathological photographs of Zn-modified TiO_2 photocatalysts. The result indicates that the Zn-modified TiO_2 coating produced by the micro-arc oxidation technique benefits the application in the orthopedic implanted devices. Due to technical limitations, ion-doped TiO_2 is rarely used in orthopedic implants. At the same time, this is due to the fact that simple particles in the air are easy to be oxidized or easy to dissolve in water solution and release

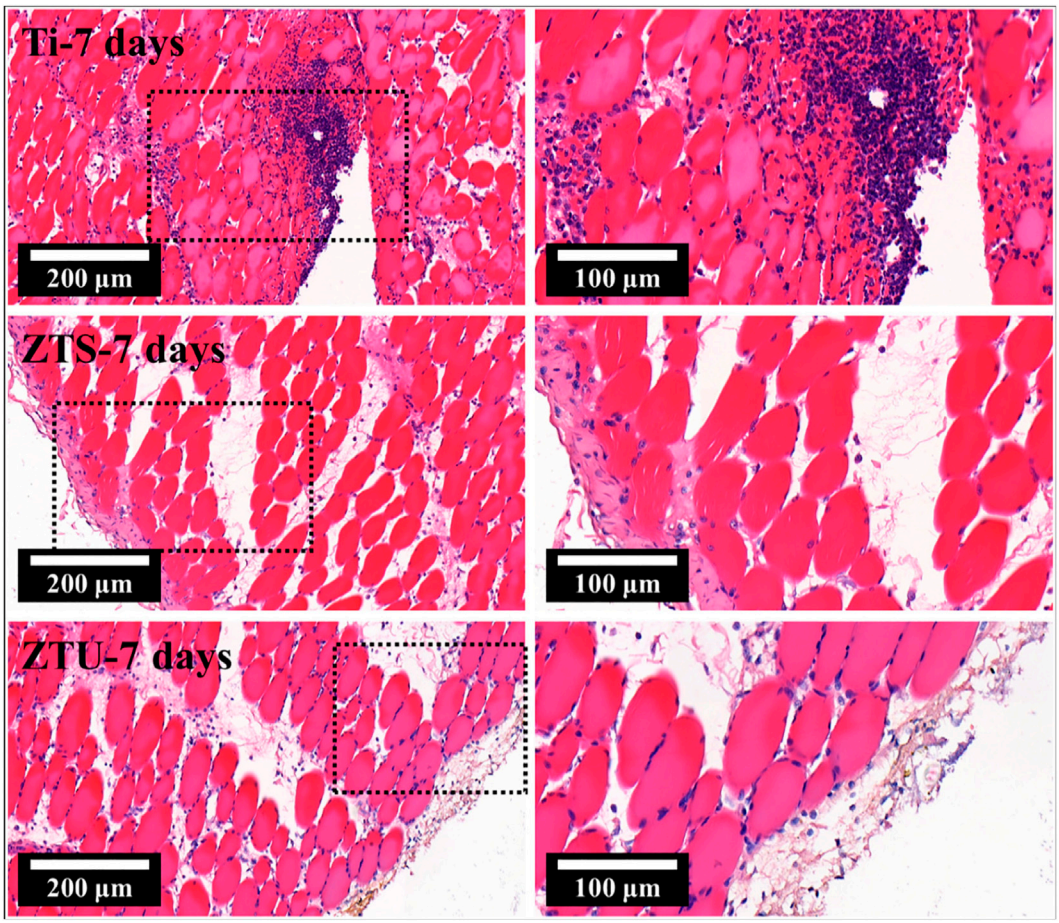

FIGURE 11 | Pathological photographs of Zn-modified TiO_2 photocatalysts. Adapted from Lv et al. (2021). Copyright © 2021 Elsevier B.V.

metal ions, resulting in high concentration of silver ions and fine toxicity. The aforementioned problems also occur when the elemental particles are combined or doped with TiO_2, thus limiting the application of ion-doped TiO_2 photocatalysts in orthopedic implants.

5.3 TiO_2-Based Composite Photocatalysts for Application in Orthopedic Implants

In order to overcome two or many kinds of antibacterial materials used alone, materials with excellent antibacterial properties, by putting other excellent antibacterial materials and two titanic oxide composite photocatalytic antibacterial materials, not only make it photocatalytic and antibacterial under strong light conditions but also in the dark under the condition of using other antibacterial effects of antibacterial materials (Etacheri et al., 2013; Sood et al., 2016; Mousa et al., 2021). The synergistic antibacterial effect of inorganic antibacterial materials was obtained. On the other hand, compared with traditional linear, blocky, spherical and tubular materials, multistage structural materials have better antibacterial effect because of their close contact with cells. The construction of multiple heterojunction TiO_2 composite photocatalysts can be effectively applied in the field of orthopedic implants.

Vandana et al. (2021) reported that the TiO_2-Nb_2O_5 nanoporous mixed metal oxide bone implant materials were assessed by using *in vitro* and *in vivo* methods and exhibit high biocompatibility. The result indicates that the TiO_2-Nb_2O_5 nanoporous mixed metal oxide bone implant materials are non-cytotoxic, non-hemolytic, and biocompatible. **Figure 12** shows the orthopedic applications for the TiO_2-Nb_2O_5 nanoporous mixed metal oxide bone implant materials. The results suggesting that the TiO_2-Nb_2O_5 nanoporous mixed metal oxide bone implant materials can be used safely for orthopedic applications. A variety of heterojunction composite TiO_2-based photocatalysts are widely used in the field of orthopedic implants. Therefore, its research is a very popular topic but also a fruitful topic. With the development of science and technology, the application of TiO_2-based composite photocatalysts in orthopedic implants will develop rapidly.

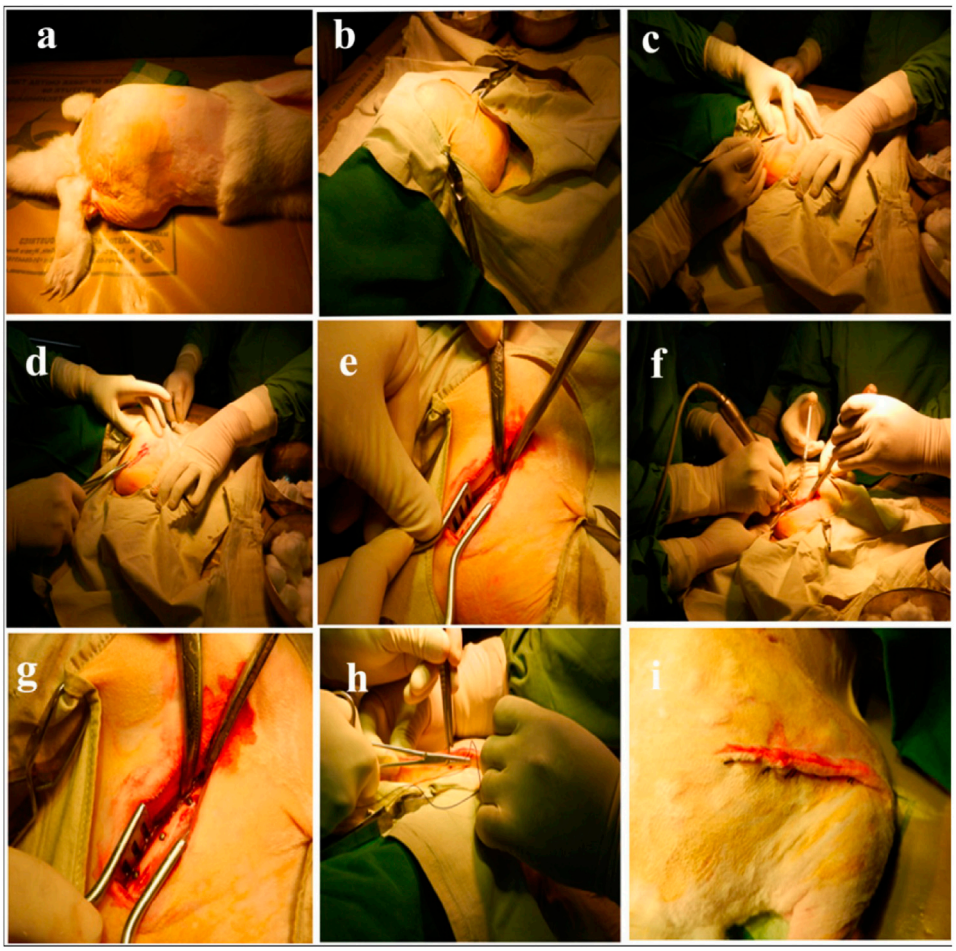

FIGURE 12 | Orthopedic applications for the TiO_2-Nb_2O_5 nanoporous mixed metal oxide bone implant materials. Adapted from Vandana et al. (2021). Copyright © 2020 Elsevier B.V. **(A, B)** Animals that lie on their side, **(C, D)** The exposed femoral cortex, **(E)** Three holes spaced 1 cm apart, **(F, G)** Material implanted, **(H, I)** Suture with sterile stitches.

6 CONCLUSION AND OUTLOOK

6.1 Conclusion

TiO_2 with three crystal structures has the characteristics of non-toxic and excellent physical and chemical properties and has been applied in many fields. Due to the large optical band gap value of TiO_2 and the influence of its particle size, crystal structure, and crystal defect on the photocatalytic and antibacterial activities of TiO_2, research of single-component TiO_2 in photocatalytic and medical fields is greatly limited. Therefore, using special means to develop metal ion–doped and non-metal ion–doped TiO_2 photocatalysts can expand the light response range of TiO_2 so that TiO_2 has an important application in the field of photocatalysis and bacteriostatic activities. Meanwhile, the development of heterojunction TiO_2-based composite photocatalysts can overcome the shortcomings of non-metal ion–doped TiO_2 and obtain novel physical and chemical properties so that the heterojunction TiO_2-based composite photocatalyst has broad application prospects in a variety of fields. It is worth noting that TiO_2, ion-doped TiO_2, and heterojunction TiO_2-based composite photocatalysts have low toxicity, high biocompatibility, high photocatalytic activity, and antibacterial activity, enabling them with unprecedented applications in orthopedic implants. Although TiO_2 and TiO_2-based photocatalysts have been widely used in the fields of photocatalysis and antibacterial and orthopedic implants, related technologies are still developing, which makes them have potential application prospects in many fields.

6.2 Outlook

The shortcomings of TiO_2 and TiO_2-based photocatalysts are being overcome by researchers, which have been applied in various fields. Nevertheless, there are still many topics worthy of study in the fields of photocatalysis, bacteriostasis, and orthopedic implants. 1) With the continuous development of science and technology, people are not only satisfied with

the use of TiO_2 and TiO_2-based photocatalysts to degrade organic dyes but also toward more complex fields such as insoluble and difficult-to-degrade pollutants and drug degradation. 2) To develop special preparation methods to synthesize TiO_2 and TiO_2-based photocatalysts with a special defective structure and improve the application of the catalyst in the fields of photocatalysis, bacteriostasis, and orthopedic implants. 3) The TiO_2-based photocatalyst combines excellent optical, magnetic, mechanical, and electrical properties of semiconductor materials and makes the properties of the system with special optical, magnetic, mechanical, or electrical properties and the internal connection mechanism of photocatalytic and bacteriostatic activities and aforementioned properties a topic worth studying. 4) The combination of ion-doped TiO_2 and heterojunction TiO_2-based composite photocatalysts will produce new physical and chemical properties, which is also a topic worthy of study.

AUTHOR CONTRIBUTIONS

All authors listed have made a substantial, direct, and intellectual contribution to the work and approved it for publication.

REFERENCES

Abrinaei, F., and Aghabeygi, S. (2022). Optimization on Preparation Conditions to Improve the Nonlinear Optical Response of ZnO/TiO2/ZrO2 Ternary Nanocomposites under Continuous-Wave Laser Irradiation. *Optik* 255, 168720. doi:10.1016/j.ijleo.2022.168720

Amin Yavari, S., Loozen, L., Paganelli, F. L., Bakhshandeh, S., Lietaert, K., Groot, J. A., et al. (2016). Antibacterial Behavior of Additively Manufactured Porous Titanium with Nanotubular Surfaces Releasing Silver Ions. *ACS Appl. Mat. Interfaces* 8 (27), 17080–17089. doi:10.1021/acsami.6b03152

Anderson, J. M. (1993). Chapter 4 Mechanisms of Inflammation and Infection with Implanted Devices. *Cardiovasc. Pathol.* 2 (3), 33–41. doi:10.1016/1054-8807(93)90045-4

Antoniadou, M., Daskalaki, V. M., Balis, N., Kondarides, D. I., Kordulis, C., and Lianos, P. (2011). Photocatalysis and Photoelectrocatalysis Using (CdS-ZnS)/TiO_2 Combined Photocatalysts. *Appl. Catal. B Environ.* 107 (1-2), 188–196. doi:10.1016/j.apcatb.2011.07.013

Bai, S., Liu, H., Sun, J., Tian, Y., Chen, S., Song, J., et al. (2015). Improvement of TiO2 Photocatalytic Properties under Visible Light by WO3/TiO2 and MoO3/TiO2 Composites. *Appl. Surf. Sci.* 338, 61–68. doi:10.1016/j.apsusc.2015.02.103

Blendinger, F., Seitz, D., Ottenschläger, A., Fleischer, M., and Bucher, V. (2021). Atomic Layer Deposition of Bioactive TiO2 Thin Films on Polyetheretherketone for Orthopedic Implants. *ACS Appl. Mat. Interfaces* 13 (3), 3536–3546. doi:10.1021/acsami.0c17990

Boningari, T., Inturi, S. N. R., Suidan, M., and Smirniotis, P. G. (2018). Novel One-step Synthesis of Nitrogen-Doped TiO2 by Flame Aerosol Technique for Visible-Light Photocatalysis: Effect of Synthesis Parameters and Secondary Nitrogen (N) Source. *Chem. Eng. J.* 350, 324–334. doi:10.1016/j.cej.2018.05.122

Cao, S., Liu, B., Fan, L., Yue, Z., Liu, B., and Cao, B. (2014). Highly Antibacterial Activity of N-Doped TiO2 Thin Films Coated on Stainless Steel Brackets under Visible Light Irradiation. *Appl. Surf. Sci.* 309, 119–127. doi:10.1016/j.apsusc.2014.04.198

Chen, C., Cai, W., Long, M., Zhou, B., Wu, Y., Wu, D., et al. (2010). Synthesis of Visible-Light Responsive Graphene Oxide/TiO2 Composites with P/n Heterojunction. *ACS Nano* 4 (11), 6425–6432. doi:10.1021/nn102130m

Chen, R., Han, Z., Huang, Z., Karki, J., Wang, C., Zhu, B., et al. (2017). Antibacterial Activity, Cytotoxicity and Mechanical Behavior of Nano-Enhanced Denture Base Resin with Different Kinds of Inorganic Antibacterial Agents. *Dent. Mat. J.* 36 (6), 693–699. doi:10.4012/dmj.2016-301

Cheng, L., Huang, D., Zhang, Y., and Wu, Y. (2021). Preparation and Piezoelectric Catalytic Performance of HT-Bi2MoO6 Microspheres for Dye Degradation. *Adv. Powder Technol.* 32 (9), 3346–3354. doi:10.1016/j.apt.2021.07.021

Choi, S. K., Kim, S., Lim, S. K., and Park, H. (2010). Photocatalytic Comparison of TiO2 Nanoparticles and Electrospun TiO2 Nanofibers: Effects of Mesoporosity and Interparticle Charge Transfer. *J. Phys. Chem. C* 114 (39), 16475–16480. doi:10.1021/jp104317x

Chow, L. K. M., Ghaly, T. M., and Gillings, M. R. (2021). A Survey of Sub-inhibitory Concentrations of Antibiotics in the Environment. *J. Environ. Sci.* 99, 21–27. doi:10.1016/j.jes.2020.05.030

Colón, G., Maicu, M., Hidalgo, M. S., and Navío, J. A. (2006). Cu-doped TiO_2 Systems with Improved Photocatalytic Activity. *Appl. Catal. B Environ.* 67 (1-2), 41–51. doi:10.1016/j.apcatb.2006.03.019

Cong, Y., Zhang, J., Chen, F., and Anpo, M. (2007). Synthesis and Characterization of Nitrogen-Doped TiO2 Nanophotocatalyst with High Visible Light Activity. *J. Phys. Chem. C* 111 (19), 6976–6982. doi:10.1021/jp0685030

Daghrir, R., Drogui, P., and Robert, D. (2013). Modified TiO2 for Environmental Photocatalytic Applications: A Review. *Ind. Eng. Chem. Res.* 52 (10), 3581–3599. doi:10.1021/ie303468t

Dalton, J. S., Janes, P. A., Jones, N. G., Nicholson, J. A., Hallam, K. R., and Allen, G. C. (2002). Photocatalytic Oxidation of NO X Gases Using TiO 2 : a Surface Spectroscopic Approach. *Environ. Pollut.* 120 (2), 415–422. doi:10.1016/s0269-7491(02)00107-0

Ellouzi, I., Bouddouch, A., Bakiz, B., Benlhachemi, A., and Abou Oualid, H. (2021). Glucose-assisted Ball Milling Preparation of Silver-Doped Biphasic TiO2 for Efficient Photodegradation of Rhodamine B: Effect of Silver-Dopant Loading. *Chem. Phys. Lett.* 770, 138456. doi:10.1016/j.cplett.2021.138456

Etacheri, V., Michlits, G., Seery, M. K., Hinder, S. J., and Pillai, S. C. (2013). A Highly Efficient TiO2-xCx Nano-Heterojunction Photocatalyst for Visible Light Induced Antibacterial Applications. *ACS Appl. Mat. Interfaces* 5 (5), 1663–1672. doi:10.1021/am302676a

Fan, X., Liang, X., Guo, G., Wang, R., and Li, J. (2009). "Preparation of Nano-TiO_2 Powder by Polyacrylamide Gel Method," in Second International Conference on Smart Materials and Nanotechnology in Engineering, Weihai China, 20 October 2009 (Weihai, China: International Society for Optics and Photonics), 749362. doi:10.1117/12.840137

Feng, S., Yan, X., Sun, H., Feng, Y., and Liu, H. X. (2021). Intelligent Driving Intelligence Test for Autonomous Vehicles with Naturalistic and Adversarial Environment. *Nat. Commun.* 12 (1), 1–14. doi:10.1038/s41467-021-21007-8

Fu, M., Yang, J., Luo, W., Tian, Q., Li, Q., Zhao, Z., et al. (2022). Preparation of Gd2Zr2O7 Nanopowders by Polyacrylamide Gel Method and Their Sintering Behaviors. *J. Eur. Ceram. Soc.* 42 (4), 1585–1593. doi:10.1016/j.jeurceramsoc.2021.12.038

Fujishima, A., and Rao, T. N. (1997). Recent Advances in Heterogeneous TiO2 Photocatalysis. *J. Chem. Sci.* 109 (6), 471–486. doi:10.1007/bf02869207

Gao, H. J., Wang, S. F., Fang, L. M., Sun, G. A., Chen, X. P., Tang, S. N., et al. (2021). Nanostructured Spinel-type M(M = Mg, Co, Zn)Cr2O4 Oxides: Novel Adsorbents for Aqueous Congo Red Removal. *Mater. Today Chem.* 22, 100593. doi:10.1016/j.mtchem.2021.100593

Gao, H., Tang, S., Chen, X., Yu, C., Wang, S., Fang, L., et al. (2021). Facile Synthesis of Cobalt Tungstate with Special Defect Structure with Enhanced Optical, Photoluminescence, and Supercapacitive Performances. *Russ. J. Phys. Chem. A* 95 (2), S288–S295. doi:10.1134/s0036024421150103

Gao, H., Wang, S., Wang, Y., Yang, H., Wang, F., Tang, S., et al. (2022). CaMoO4/CaWO4 Heterojunction Micro/nanocomposites with Interface Defects for Enhanced Photocatalytic Activity. *Colloids Surfaces A Physicochem. Eng. Aspects* 642, 128642. doi:10.1016/j.colsurfa.2022.128642

Gao, Y., and Wang, T. (2021). Preparation of Ag2O/TiO2 Nanocomposites by Two-step Method and Study of its Degradation of RHB. *J. Mol. Struct.* 1224, 129049. doi:10.1016/j.molstruc.2020.129049

Ge, X., Ren, C., Ding, Y., Chen, G., Lu, X., Wang, K., et al. (2019). Micro/nano-structured TiO2 Surface with Dual-Functional Antibacterial Effects for Biomedical Applications. *Bioact. Mater.* 4, 346–357. doi:10.1016/j.bioactmat.2019.10.006

Gnanasekaran, L., Pachaiappan, R., Kumar, P. S., Hoang, T. K. A., Rajendran, S., Durgalakshmi, D., et al. (2021). Visible Light Driven Exotic P (CuO) - N (TiO2)

Heterojunction for the Photodegradation of 4-chlorophenol and Antibacterial Activity. *Environ. Pollut.* 287, 117304. doi:10.1016/j.envpol.2021.117304

Guo, L., Chen, Y., Ren, Z., Li, X., Zhang, Q., Wu, J., et al. (2021). Morphology Engineering of Type-II Heterojunction Nanoarrays for Improved Sonophotocatalytic Capability. *Ultrason. Sonochemistry* 81, 105849. doi:10.1016/j.ultsonch.2021.105849

Guo, Q., Zhou, C., Ma, Z., and Yang, X. (2019). Fundamentals of TiO 2 Photocatalysis: Concepts, Mechanisms, and Challenges. *Adv. Mat.* 31 (50), 1901997. doi:10.1002/adma.201901997

Han, X., Sun, M., Chai, X., Li, J., Wu, Y., and Sun, W. (2022). Progress in Synthesis and Photocatalytic Activity of MAl2O4(M=Mg, Sr, Ba) Based Photocatalysts. *Front. Mat.* 9, 40. doi:10.3389/fmats.2022.845664

Hao, R., Wang, G., Tang, H., Sun, L., Xu, C., and Han, D. (2016). Template-free Preparation of Macro/mesoporous G-C 3 N 4/TiO 2 Heterojunction Photocatalysts with Enhanced Visible Light Photocatalytic Activity. *Appl. Catal. B Environ.* 187, 47–58. doi:10.1016/j.apcatb.2016.01.026

He, Z., Siddique, M. S., Yang, H., Xia, Y., Su, J., Tang, B., et al. (2022). Novel Z-Scheme In2S3/Bi2WO6 Core-Shell Heterojunctions with Synergistic Enhanced Photocatalytic Degradation of Tetracycline Hydrochloride. *J. Clean. Prod.* 339, 130634. doi:10.1016/j.jclepro.2022.130634

He, Z., Yang, H., Su, J., Xia, Y., Fu, X., Kang, L., et al. (2021). Polyacrylamide Gel Synthesis and Photocatalytic Performance of CuCo2O4 Nanoparticles. *Mater. Lett.* 288, 129375. doi:10.1016/j.matlet.2021.129375

He, Z., Yang, H., Su, J., Xia, Y., Fu, X., Wang, L., et al. (2021). Construction of Multifunctional Dual Z-Scheme Composites with Enhanced Photocatalytic Activities for Degradation of Ciprofloxacin. *Fuel* 294, 120399. doi:10.1016/j.fuel.2021.120399

Hu, C., Zhao, Q., Zang, G.-L., Luo, J.-T., and Liu, Q. (2022). Preparation and Characterization of a Novel Ni-Doped TiO2 Nanotube-Modified Inactive Electrocatalytic Electrode for the Electrocatalytic Degradation of Phenol Wastewater. *Electrochimica Acta* 405, 139758. doi:10.1016/j.electacta.2021.139758

Jiang, J., Chen, Z., Wang, P., Gu, P.-Y., Liu, J., Zhang, Z., et al. (2022). Preparation of Black Hollow TiO2 Nanotube-Coated PDA@Ag2S Heterostructures for Efficient Photocatalytic Reduction of Cr(VI). *J. Solid State Chem.* 307, 122865. doi:10.1016/j.jssc.2021.122865

Jiang, X., Peng, Z., Gao, Y., You, F., and Yao, C. (2021). Preparation and Visible-Light Photocatalytic Activity of Ag-Loaded TiO2@Y2O3 Hollow Microspheres with Double-Shell Structure. *Powder Technol.* 377, 621–631. doi:10.1016/j.powtec.2020.09.030

Kale, D. P., Deshmukh, S. P., Shirsath, S. R., and Bhanvase, B. A. (2020). Sonochemical Preparation of Multifunctional rGO-ZnS-TiO2 Ternary Nanocomposite and its Application for CV Dye Removal. *Optik* 208, 164532. doi:10.1016/j.ijleo.2020.164532

Kaushik, R., Vineeth Daniel, P., Mondal, P., and Halder, A. (2019). Transformation of 2-D TiO2 to Mesoporous Hollow 3-D TiO2 Spheres-Comparative Studies on Morphology-dependent Photocatalytic and Anti-bacterial Activity. *Microporous Mesoporous Mater.* 285, 32–42. doi:10.1016/j.micromeso.2019.04.068

Li, D., Gao, X., Huang, X., Liu, P., Xiong, W., Wu, S., et al. (2020). Preparation of Organic-Inorganic Chitosan@silver/sepiolite Composites with High Synergistic Antibacterial Activity and Stability. *Carbohydr. Polym.* 249, 116858. doi:10.1016/j.carbpol.2020.116858

Li, G., Sun, Y., Zhang, Q., Gao, Z., Sun, W., and Zhou, X. (2021). Ag Quantum Dots Modified Hierarchically Porous and Defective TiO2 Nanoparticles for Improved Photocatalytic CO2 Reduction. *Chem. Eng. J.* 410, 128397. doi:10.1016/j.cej.2020.128397

Li, J., Li, F., Zhu, X., Lin, D., Li, Q., Liu, W., et al. (2017). Colossal Dielectric Permittivity in Hydrogen-Reduced Rutile TiO2 Crystals. *J. Alloys Compd.* 692, 375–380. doi:10.1016/j.jallcom.2016.09.044

Li, J., Wang, S., Sun, G., Gao, H., Yu, X., Tang, S., et al. (2021). Facile Preparation of MgAl2O4/CeO2/Mn3O4 Heterojunction Photocatalyst and Enhanced Photocatalytic Activity. *Mater. Today Chem.* 19, 100390. doi:10.1016/j.mtchem.2020.100390

Li, Z., He, J., Ma, H., Zang, L., Li, D., Guo, S., et al. (2021). Preparation of Heterogeneous TiO2/g-C3n4 with a Layered Mosaic Stack Structure by Use of Montmorillonite as a Hard Template Approach: TC Degradation, Kinetic, Mechanism, Pathway and DFT Investigation. *Appl. Clay Sci.* 207, 106107. doi:10.1016/j.clay.2021.106107

Liang, S., Wang, C., Li, Y., Xu, M., and Jia, H. (2021). Microfluidic Fabrication of ZrO2 Microspheres Using Improved External Gelation Aided by Polyacrylamide Networks. *Ceram. Int.* 47 (15), 21576–21581. doi:10.1016/j.ceramint.2021.04.169

Liao, G., Chen, S., Quan, X., Chen, H., and Zhang, Y. (2010). Photonic Crystal Coupled TiO2/Polymer Hybrid for Efficient Photocatalysis under Visible Light Irradiation. *Environ. Sci. Technol.* 44 (9), 3481–3485. doi:10.1021/es903833f

Lin, T.-h., Tamaki, Y., Pajarinen, J., Waters, H. A., Woo, D. K., Yao, Z., et al. (2014). Chronic Inflammation in Biomaterial-Induced Periprosthetic Osteolysis: NF-Kb as a Therapeutic Target. *Acta biomater.* 10 (1), 1–10. doi:10.1016/j.actbio.2013.09.034

Liu, H., Huo, W., Zhang, T. C., Ouyang, L., and Yuan, S. (2022). Photocatalytic Removal of Tetracycline by a Z-Scheme Heterojunction of Bismuth Oxyiodide/exfoliated G-C3n4: Performance, Mechanism, and Degradation Pathway. *Mater. Today Chem.* 23, 100729. doi:10.1016/j.mtchem.2021.100729

Liu, H., Wang, S., Gao, H., Yang, H., Wang, F., Chen, X., et al. (2022). A Simple Polyacrylamide Gel Route for the Synthesis of MgAl2O4 Nanoparticles with Different Metal Sources as an Efficient Adsorbent: Neural Network Algorithm Simulation, Equilibrium, Kinetics and Thermodynamic Studies. *Sep. Purif. Technol.* 281, 119855. doi:10.1016/j.seppur.2021.119855

Lou, S., Zhao, Y., Wang, J., Yin, G., Du, C., and Sun, X. (2019). Ti-Based Oxide Anode Materials for Advanced Electrochemical Energy Storage: Lithium/Sodium Ion Batteries and Hybrid Pseudocapacitors. *Small* 15 (52), 1904740. doi:10.1002/smll.201904740

Low, J., Yu, J., Jaroniec, M., Wageh, S., and Al-Ghamdi, A. A. (2017). Heterojunction Photocatalysts. *Adv. Mat.* 29 (20), 1601694. doi:10.1002/adma.201601694

Lu, X., Yue, Z., and Peng, B. (2022). Preparation of TiO2-Nanotube-Based Photocatalysts and Degradation Kinetics of Patulin in Simulated Juice. *J. Food Eng.* 323, 110992. doi:10.1016/j.jfoodeng.2022.110992

Lv, Y., Sun, S., Zhang, X., Lu, X., and Dong, Z. (2021). Construction of Multi-Layered Zn-Modified TiO2 Coating by Ultrasound-Auxiliary Micro-arc Oxidation: Microstructure and Biological Property. *Mater. Sci. Eng. C* 131, 112487. doi:10.1016/j.msec.2021.112487

Ma, S., Zhan, S., Jia, Y., and Zhou, Q. (2015). Superior Antibacterial Activity of Fe3O4-TiO2 Nanosheets under Solar Light. *ACS Appl. Mat. Interfaces* 7 (39), 21875–21883. doi:10.1021/acsami.5b06264

Macwan, D. P., Dave, P. N., and Chaturvedi, S. (2011). A Review on Nano-TiO2 Sol-Gel Type Syntheses and its Applications. *J. Mater Sci.* 46 (11), 3669–3686. doi:10.1007/s10853-011-5378-y

Martins, N. C. T., Ângelo, J., Girão, A. V., Trindade, T., Andrade, L., and Mendes, A. (2016). N-doped Carbon Quantum dots/TiO2 Composite with Improved Photocatalytic Activity. *Appl. Catal. B Environ.* 193, 67–74. doi:10.1016/j.apcatb.2016.04.016

Mateo, D., Cerrillo, J. L., Durini, S., and Gascon, J. (2021). Fundamentals and Applications of Photo-Thermal Catalysis. *Chem. Soc. Rev.* 50 (3), 2173–2210. doi:10.1039/D0CS00357C

Mazare, A., Totea, G., Burnei, C., Schmuki, P., Demetrescu, I., and Ionita, D. (2016). Corrosion, Antibacterial Activity and Haemocompatibility of TiO 2 Nanotubes as a Function of Their Annealing Temperature. *Corros. Sci.* 103, 215–222. doi:10.1016/j.corsci.2015.11.021

Mori, K. (2005). Photo-Functionalized Materials Using Nanoparticles: Photocatalysis [Translated]†. *Kona* 23, 205–214. doi:10.14356/kona.2005023

Mousa, H. M., Alenezi, J. F., Mohamed, I. M. A., Yasin, A. S., Hashem, A.-F. M., and Abdal-hay, A. (2021). Synthesis of TiO2@ZnO Heterojunction for Dye Photodegradation and Wastewater Treatment. *J. Alloys Compd.* 886, 161169. doi:10.1016/j.jallcom.2021.161169

Murthy, H. (2019). Nanoarchitectures as Photoanodes. *Interfacial Eng. Funct. Mater. Dye-Sensitized Sol. Cells* 7, 35–77. doi:10.1002/9781119557401.ch3

Nakata, K., and Fujishima, A. (2012). TiO2 Photocatalysis: Design and Applications. *J. Photochem. Photobiol. C Photochem. Rev.* 13 (3), 169–189. doi:10.1016/j.jphotochemrev.2012.06.001

Perales-Martínez, I. A., Rodríguez-González, V., Lee, S.-W., and Obregón, S. (2015). Facile Synthesis of InVO4/TiO2 Heterojunction Photocatalysts with Enhanced Photocatalytic Properties under UV-Vis Irradiation. *J. Photochem. Photobiol. A Chem.* 299, 152–158. doi:10.1016/j.jphotochem.2014.11.021

Phromma, S., Wutikhun, T., Kasamechonchung, P., Sattayaporn, S., Eksangsri, T., and Sapcharoenkun, C. (2022). Effects of Ag Modified TiO2 on Local Structure Investigated by XAFS and Photocatalytic Activity under Visible Light. *Mater. Res. Bull.* 148, 111668. doi:10.1016/j.materresbull.2021.111668

Popat, K. C., Eltgroth, M., LaTempa, T. J., Grimes, C. A., and Desai, T. A. (2007). Decreased *Staphylococcus epidermis* Adhesion and Increased Osteoblast Functionality on Antibiotic-Loaded Titania Nanotubes. *Biomaterials* 28 (32), 4880–4888. doi:10.1016/j.biomaterials.2007.07.037

Qu, Z.-w., and Kroes, G.-J. (2007). Theoretical Study of Stable, Defect-free (TiO2)n Nanoparticles with N = 10–16. *J. Phys. Chem. C* 111 (45), 16808–16817. doi:10.1021/jp073988t

Ren, Y. W., Guo, Y., Zhao, D. Y., Wang, H. L., Wang, N., Jiang, W. W., et al. (2022). Preparation and Characterization of Rutile TiO2 Nanoparticles by HCl-Water Volatilization-Assisted Precipitation Method. *J. Cryst. Growth* 577, 126410. doi:10.1016/j.jcrysgro.2021.126410

Riaz, U., Ashraf, S. M., and Kashyap, J. (2015). Role of Conducting Polymers in Enhancing TiO2-Based Photocatalytic Dye Degradation: A Short Review. *Polymer-Plastics Technol. Eng.* 54 (17), 1850–1870. doi:10.1080/03602559.2015.1021485

Saheed, I. O., Oh, W. D., and Suah, F. B. M. (2021). Chitosan Modifications for Adsorption of Pollutants - A Review. *J. Hazard. Mater.* 408, 124889. doi:10.1016/j.jhazmat.2020.124889

Santhoshkumar, P., Shaji, N., Sim, G. S., Nanthagopal, M., and Lee, C. W. (2022). Towards Environment-Friendly and Versatile Energy Storage Devices: Design and Preparation of Mesoporous $Li_4Ti_5O_{12}$-TiO_2 Nano-Hybrid Electrode Materials. *Appl. Surf. Sci.* 583, 152490. doi:10.1016/j.apsusc.2022.152490

Santos, E., Catto, A. C., Peterline, A. F., and Avansi Jr, W., Jr (2022). Transition Metal (Nb and W) Doped TiO2 Nanostructures: The Role of Metal Doping in Their Photocatalytic Activity and Ozone Gas-Sensing Performance. *Appl. Surf. Sci.* 579, 152146. doi:10.1016/j.apsusc.2021.152146

Schuettfort, T., Nish, A., and Nicholas, R. J. (2009). Observation of a Type II Heterojunction in a Highly Ordered Polymer−Carbon Nanotube Nanohybrid Structure. *Nano Lett.* 9 (11), 3871–3876. doi:10.1021/nl902081t

Shifa Wang, S., Gao, H., Sun, G., Wang, Y., Fang, L., Yang, L., et al. (2020). Synthesis of Visible-Light-Driven SrAl2O4-Based Photocatalysts Using Surface Modification and Ion Doping. *Russ. J. Phys. Chem.* 94 (6), 1234–1247. doi:10.1134/s003602442006031x

Skorb, E. V., Antonouskaya, L. I., Belyasova, N. A., Shchukin, D. G., Möhwald, H., and Sviridov, D. V. (2008). Antibacterial Activity of Thin-Film Photocatalysts Based on Metal-Modified TiO_2 and TiO_2: In_2O_3 Nanocomposite. *Appl. Catal. B Environ.* 84 (1-2), 94–99. doi:10.1016/j.apcatb.2008.03.007

Sood, S., Mehta, S. K., Sinha, A. S. K., and Kansal, S. K. (2016). Bi 2 O 3/TiO 2 Heterostructures: Synthesis, Characterization and Their Application in Solar Light Mediated Photocatalyzed Degradation of an Antibiotic, Ofloxacin. *Chem. Eng. J.* 290, 45–52. doi:10.1016/j.jphotochem.2019.04.02810.1016/j.cej.2016.01.017

Sotelo-Vazquez, C., Quesada-Cabrera, R., Ling, M., Scanlon, D. O., Kafizas, A., Thakur, P. K., et al. (2017). Evidence and Effect of Photogenerated Charge Transfer for Enhanced Photocatalysis in WO3/TiO2 Heterojunction Films: A Computational and Experimental Study. *Adv. Funct. Mat.* 27 (18), 1605413. doi:10.1002/adfm.201605413

Sun, S., Ding, H., Wang, J., Li, W., and Hao, Q. (2020). Preparation of a Microsphere SiO2/TiO2 Composite Pigment: The Mechanism of Improving Pigment Properties by SiO2. *Ceram. Int.* 46 (14), 22944–22953. doi:10.1016/j.ceramint.2020.06.068

Tang, S., Gao, H., Wang, S., Yu, C., Chen, X., Liu, H., et al. (2022). Temperature Dependence of the Phase Transformation and Photoluminescence Properties of Metastable ZnWO4 Nano-Phosphors with High UV Absorption and VIS Reflectance. *Russ. J. Phys. Chem.* 96 (3), 515–526. doi:10.1134/s0036024422030220

Tang, Z., Xu, L., Shu, K., Yang, J., and Tang, H. (2022). Fabrication of TiO2 @MoS2 Heterostructures with Improved Visible Light Photocatalytic Activity. *Colloids Surfaces A Physicochem. Eng. Aspects* 642, 128686. doi:10.1016/j.colsurfa.2022.128686

Tiwari, I., Sharma, P., and Nebhani, L. (2022). Polybenzoxazine - an Enticing Precursor for Engineering Heteroatom-Doped Porous Carbon Materials with Applications beyond Energy, Environment and Catalysis. *Mater. Today Chem.* 23, 100734. doi:10.1016/j.mtchem.2021.100734

Tung, W. S., and Daoud, W. A. (2011). Self-cleaning Fibers via Nanotechnology: a Virtual Reality. *J. Mat. Chem.* 21 (22), 7858–7869. doi:10.1039/c0jm03856c

Vandana, U., Nancy, D., Sabareeswaran, A., Remya, N. S., Rajendran, N., and Mohanan, P. V. (2021). Biocompatibility of Strontium Incorporated Ceramic Coated Titanium Oxide Implant Indented for Orthopaedic Applications. *Mater. Sci. Eng. B* 264, 114954. doi:10.1016/j.mseb.2020.114954

Venkatachalam, N., Palanichamy, M., and Murugesan, V. (2007). Sol-gel Preparation and Characterization of Alkaline Earth Metal Doped Nano TiO2: Efficient Photocatalytic Degradation of 4-chlorophenol. *J. Mol. Catal. A Chem.* 273 (1-2), 177–185. doi:10.1016/j.molcata.2007.03.077

Vorontsov, A. V., Savinov, E. V., Davydov, L., and Smirniotis, P. G. (2001). Photocatalytic Destruction of Gaseous Diethyl Sulfide over TiO_2. *Appl. Catal. B Environ.* 32 (1-2), 11–24. doi:10.1016/s0926-3373(01)00127-8

Wang, C. Y., Makvandi, P., Zare, E. N., Tay, F. R., and Niu, L. N. (2020). Advances in Antimicrobial Organic and Inorganic Nanocompounds in Biomedicine. *Adv. Ther.* 3 (8), 2000024. doi:10.1002/adtp.202000024

Wang, S., Gao, H., Fang, L., Hu, Q., Sun, G., Chen, X., et al. (2021). Synthesis of Novel CQDs/CeO2/SrFe12O19 Magnetic Separation Photocatalysts and Synergic Adsorption-Photocatalytic Degradation Effect for Methylene Blue Dye Removal. *Chem. Eng. J. Adv.* 6, 100089. doi:10.1016/j.ceja.2021.100089

Wang, S., Gao, H., Yu, X., Tang, S., Wang, Y., Fang, L., et al. (2020). Nanostructured SrTiO3 with Different Morphologies Achieved by Mineral Acid-Assisted Hydrothermal Method with Enhanced Optical, Electrochemical, and Photocatalytic Performances. *J. Mater Sci. Mater Electron* 31 (20), 17736–17754. doi:10.1007/s10854-020-04328-0

Wang, S., Tang, S., Yang, H., Wang, F., Yu, C., Gao, H., et al. (2022). A Novel Heterojunction ZnO/CuO Piezoelectric Catalysts: Fabrication, Optical Properties and Piezoelectric Catalytic Activity for Efficient Degradation of Methylene Blue. *J. Mater Sci. Mater Electron* 33 (9), 7172–7190. doi:10.1007/s10854-022-07899-2

Wang, S., Wang, Y., Gao, H., Li, J., Fang, L., Yu, X., et al. (2020). Synthesis and Characterization of BaAl2O4: Ce and Mn-Ce- Co-doped BaAl2O4 Composite Materials by a Modified Polyacrylamide Gel Method and Prediction of Photocatalytic Activity Using Artificial Neural Network (ANN) Algorithm. *Optik* 221, 165363. doi:10.1016/j.ijleo.2020.165363

Wang, S., Wei, X., Gao, H., and Wei, Y. (2019). Effect of Amorphous Alumina and α-alumina on Optical, Color, Fluorescence Properties and Photocatalytic Activity of the MnAl2O4 Spinel Oxides. *Optik* 185, 301–310. doi:10.1016/j.ijleo.2019.03.147

Wang, X., Ding, H., Sun, S., Zhang, H., Zhou, R., Li, Y., et al. (2021). Preparation of a Temperature-Sensitive Superhydrophobic Self-Cleaning SiO2-TiO2@PDMS Coating with Photocatalytic Activity. *Surf. Coatings Technol.* 408, 126853. doi:10.1016/j.surfcoat.2021.126853

Wu, J.-J., and Yu, C.-C. (2004). Aligned TiO2 Nanorods and Nanowalls. *J. Phys. Chem. B* 108 (11), 3377–3379. doi:10.1021/jp0361935

Wu, Y., Yan, K., Xu, G., Yang, C., and Wang, D. (2021). Facile Preparation of Super-oleophobic TiO2/SiO2 Composite Coatings by Spraying Method. *Prog. Org. Coatings* 159, 106411. doi:10.1016/j.porgcoat.2021.106411

Wu, Z., Wu, Q., Du, L., Jiang, C., and Piao, L. (2014). Progress in the Synthesis and Applications of Hierarchical Flower-like TiO2 Nanostructures. *Particuology* 15, 61–70. doi:10.1016/j.partic.2013.04.003

Wu, Z., Zhao, Y., Chen, X., Guo, Y., Wang, H., Jin, Y., et al. (2022). Preparation of Polymeric Carbon nitride/TiO2 Heterostructure with NH4Cl as Template: Structural and Photocatalytic Studies. *J. Phys. Chem. Solids* 164, 110629. doi:10.1016/j.jpcs.2022.110629

Xian, T., Yang, H., Di, L. J., Chen, X. F., and Dai, J. F. (2013). Polyacrylamide Gel Synthesis and Photocatalytic Properties of TiO2 Nanoparticles. *J. Sol-Gel Sci. Technol.* 66 (2), 324–329. doi:10.1007/s10971-013-3013-x

Xiang, J., Liu, H., Na, R., Wang, D., Shan, Z., and Tian, J. (2020). Facile Preparation of Void-Buffered Si@TiO2/C Microspheres for High-Capacity Lithium Ion Battery Anodes. *Electrochimica Acta* 337, 135841. doi:10.1016/j.electacta.2020.135841

Xie, D., Wang, Y., Yu, H., Yang, X., Geng, S., and Meng, X. (2021). Molten-salt Defect Engineering of TiO2(B) Nanobelts for Enhanced Photocatalytic Hydrogen Evolution. *JCIS Open* 4, 100031. doi:10.1016/j.jciso.2021.100031

Xu, J., Liu, Z., Wang, J., Liu, P., Ahmad, M., Zhang, Q., et al. (2022). Preparation of Core-Shell C@TiO2 Composite Microspheres with Wrinkled Morphology and

its Microwave Absorption. *J. Colloid Interface Sci.* 607, 1036–1049. doi:10.1016/j.jcis.2021.09.038

Yadav, H. M., Otari, S. V., Bohara, R. A., Mali, S. S., Pawar, S. H., and Delekar, S. D. (2014). Synthesis and Visible Light Photocatalytic Antibacterial Activity of Nickel-Doped TiO2 Nanoparticles against Gram-Positive and Gram-Negative Bacteria. *J. Photochem. Photobiol. A Chem.* 294, 130–136. doi:10.1016/j.jphotochem.2014.07.024

Yu, J., Wang, W., Cheng, B., and Su, B.-L. (2009). Enhancement of Photocatalytic Activity of Mesporous TiO2 Powders by Hydrothermal Surface Fluorination Treatment. *J. Phys. Chem. C* 113 (16), 6743–6750. doi:10.1021/jp900136q

Zaleska, A. (2008). Doped-TiO2: A Review. *Eng* 2 (3), 157–164. doi:10.2174/187221208786306289

Zhang, B., Li, B., Gao, S., Li, Y., Cao, R., Cheng, J., et al. (2020). Y-doped TiO2 Coating with Superior Bioactivity and Antibacterial Property Prepared via Plasma Electrolytic Oxidation. *Mater. Des.* 192, 108758. doi:10.1016/j.matdes.2020.108758

Zhang, D., Chen, Q., Shi, C., Chen, M., Ma, K., Wan, J., et al. (2021). Dealing with the Foreign-Body Response to Implanted Biomaterials: Strategies and Applications of New Materials. *Adv. Funct. Mat.* 31 (6), 2007226. doi:10.1002/adfm.202007226

Zhang, S., Guo, W., Liu, N., Xia, C., Wang, H., and Liang, C. (2022). *In Situ* preparation of MAO/TiO2 Composite Coating on WE43 Alloy for Anti-corrosion Protection. *Vacuum* 197, 110835. doi:10.1016/j.vacuum.2021.110835

Zhang, Y., Zhao, Z., Chen, J., Cheng, L., Chang, J., Sheng, W., et al. (2015). C-doped Hollow TiO2 Spheres: *In Situ* Synthesis, Controlled Shell Thickness, and Superior Visible-Light Photocatalytic Activity. *Appl. Catal. B Environ.* 165, 715–722. doi:10.1016/j.apcatb.2014.10.063

Zhang, Z., Wang, C. C., Zakaria, R., and Ying, J. Y. (1998). Role of Particle Size in Nanocrystalline TiO2-Based Photocatalysts. *J. Phys. Chem. B* 102 (52), 10871–10878. doi:10.1021/jp982948

Zhao, L., Wang, H., Huo, K., Zhang, X., Wang, W., Zhang, Y., et al. (2013). The Osteogenic Activity of Strontium Loaded Titania Nanotube Arrays on Titanium Substrates. *Biomaterials* 34 (1), 19–29. doi:10.1016/j.biomaterials.2012.09.041

Zhou, F., Yan, C., Sun, Q., and Komarneni, S. (2019). TiO2/Sepiolite Nanocomposites Doped with Rare Earth Ions: Preparation, Characterization and Visible Light Photocatalytic Activity. *Microporous Mesoporous Mater.* 274, 25–32. doi:10.1016/j.micromeso.2018.07.031

Zhu, G., Yang, X., Liu, Y., Zeng, Y., Wang, T., and Yu, H. (2022). One-pot Synthesis of C-Modified and N-Doped TiO2 for Enhanced Visible-Light Photocatalytic Activity. *J. Alloys Compd.* 902, 163677. doi:10.1016/j.jallcom.2022.163677

Zhu, S., Zheng, J., Xin, S., and Nie, L. (2022). Preparation of Flexible Pt/TiO2/γ-Al2O3 Nanofiber Paper for Room-Temperature HCHO Oxidation and Particulate Filtration. *Chem. Eng. J.* 427, 130951. doi:10.1016/j.cej.2021.130951

Conflict of Interest: The authors declare that the research was conducted in the absence of any commercial or financial relationships that could be construed as a potential conflict of interest.

Publisher's Note: All claims expressed in this article are solely those of the authors and do not necessarily represent those of their affiliated organizations, or those of the publisher, the editors, and the reviewers. Any product that may be evaluated in this article, or claim that may be made by its manufacturer, is not guaranteed or endorsed by the publisher.

Copyright © 2022 Qi, Guo, Lu, Gong, Wang, He, Jia, Ren, Zheng and Lu. This is an open-access article distributed under the terms of the Creative Commons Attribution License (CC BY). The use, distribution or reproduction in other forums is permitted, provided the original author(s) and the copyright owner(s) are credited and that the original publication in this journal is cited, in accordance with accepted academic practice. No use, distribution or reproduction is permitted which does not comply with these terms.

frontiers | Frontiers in Materials

ORIGINAL RESEARCH
published: 05 July 2022
doi: 10.3389/fmats.2022.934759

Sol–Gel Synthesis and Photocatalytic Activity of Graphene Oxide/$ZnFe_2O_4$-Based Composite Photocatalysts

Beibei Tong, Longfei Shi and Xiaohong Liu*

Department of Mechanical Engineering, Yellow River Conservancy Technical Institute, Kaifeng, China

ZnO (ZO), Fe_2O_3 (FO), and graphene oxide (GO)/ZO/FO/$ZnFe_2O_4$ (ZFO) composite photocatalysts have been synthesized successfully *via* a simple sol–gel method and low-temperature technology. The phase structure and microstructural analysis confirmed that the GO/ZO/FO/ZFO magnetic separation photocatalyst is composed of GO, hexagonal ZnO, rhombohedral Fe_2O_3, and spinel $ZnFe_2O_4$ without any other impurities. The GO/ZO/FO/ZFO composite photocatalysts have a high visible light optical absorption coefficient and photocatalytic activity for degrading dyes, refractory pollutants, and antibiotics. The degradation percentages of methyl orange, tetrabromobisphenol A, and oxytetracycline hydrochloride by the GO/ZO/FO/ZFO magnetic separation photocatalyst were 98% for 180 min, 99% for 150 min, and 85% for 180 min, respectively. The special synthesis path leads to the formation of a special heterojunction between GO, ZnO, Fe_2O_3, and $ZnFe_2O_4$, which does not change the optical band gap value of the main lattice Fe_2O_3, and enhances the surface defects of the GO/ZO/FO/ZFO magnetic separation photocatalyst, resulting in high charge carrier transfer and separation efficiency of the catalyst and then enhanced the photocatalytic activity of the GO/ZO/FO/ZFO magnetic separation photocatalyst.

Keywords: ZnO, Fe_2O_3, composite photocatalysts, sol–gel method, charge carrier, photocatalytic activity

OPEN ACCESS

Edited by:
Steven Wu,
University of South Dakota, United States

Reviewed by:
Tao Xian,
Qinghai Normal University, China
Zuming He,
Changzhou University, China
Zao Yi,
Southwest University of Science and Technology, China

****Correspondence:***
Beibei Tong
t66pp23@163.com

Specialty section:
This article was submitted to Semiconducting Materials and Devices, a section of the journal Frontiers in Materials

Received: *03 May 2022*
Accepted: *26 May 2022*
Published: *05 July 2022*

Citation:
Tong B, Shi L and Liu X (2022) Sol–Gel Synthesis and Photocatalytic Activity of Graphene Oxide/$ZnFe_2O_4$-Based Composite Photocatalysts. Front. Mater. 9:934759. doi: 10.3389/fmats.2022.934759

INTRODUCTION

Environmental pollution has always been a coexisting problem with human development (Rasheed, 2022). Dyes, persistent organic pollutants, and antibiotics are all powerful environmental killers (Cheng et al., 2022; He et al., 2022; Li et al., 2022). The degradation of these pollutants has become a necessary means to protect the environment. As countries around the world attach importance to environmental pollution, different technological means have been developed to degrade these pollutants (He et al., 2019a; He et al., 2021a; Wang et al., 2021a; He et al., 2021b; Wang et al., 2022a; Zhao et al., 2022). These technologies mainly include the photocatalytic technology, thermal catalytic technology, piezoelectric catalytic technology, ultrasonic catalytic technology, electrocatalytic technology, biodegradation technology, and a variety of technologies combined together to degrade pollutants (Sadrameli, 2016; Xiong et al., 2018; He et al., 2019b; He et al., 2020; Cheng et al., 2021; Dadashzadeh et al., 2021). Among these technologies, photocatalysis is a semiconductor green technology driven by light energy, which can effectively degrade pollutants, and has attracted extensive attention from researchers all over the world (Selli et al., 2008). The key

aspect of the semiconductor photocatalysis technology is to develop semiconductor materials that can respond to visible light and use sunlight efficiently (Ren et al., 2016). Therefore, the development of a semiconductor photocatalyst that can respond to visible light becomes the key to solving this problem.

The photocatalytic activity of photocatalyst also depends on its charge carrier transfer and separation efficiency (Tang et al., 2018; Chen et al., 2019a; Cao et al., 2019; Luo et al., 2019; Xiao et al., 2019; Lin et al., 2020; Tang et al., 2020; Wang et al., 2022b). Even if some semiconductor materials can respond to visible light, the transfer and separation efficiency of charge carriers is not high, and Fe_2O_3 is such a material (Kuang et al., 2017; Chong et al., 2021; Fu et al., 2021). In order to enhance the visible light response capability of semiconductor materials and the transfer and separation efficiency of charge carriers at the same time, the excellent properties of various semiconductor materials can be combined to form a new composite semiconductor photocatalyst (Chen et al., 2019b; Shanavas et al., 2019; Kormányos et al., 2020). ZnO (ZO)/Fe_2O_3(FO)/$ZnFe_2O_4$(ZFO) is considered to be such a composite that its visible light response is improved compared with any single component materials (Valenzuela et al., 2002; Karpova et al., 2013a; Karpova et al., 2013b). However, due to the lack of carriers for charge carrier transfer and separation among the three, the transfer and separation efficiency of the charge carrier is low. Graphene oxide (GO) is a common carrier of charge carrier transfer and transport and is often used to enhance the charge transfer and separation efficiency of semiconductor materials (Hosseini et al., 2019; Rahmani et al., 2020; Pei et al., 2021). Therefore, the development of GO/ZO/FO/ZFO composite photocatalysts and the study of their degradation of dyes, POPS, and antibiotics are expected to show high photocatalytic activity.

In this study, we proposed the synthesis of GO/ZO/FO/ZFO composite photocatalysts with different GO contents by a low-temperature sintering technique. The effect of GO content on the phase purity, microstructure, optical properties, and photocatalytic activity of the GO/ZO/FO/ZFO composite photocatalyst was systematically studied. Using methyl orange, tetrabromobisphenol A, and oxytetracycline hydrochloride as degradation materials, the photocatalytic activity of the GO/ZO/FO/ZFO composite photocatalyst was studied. Based on the energy band theory and experimental results, a reasonable photocatalytic mechanism of the GO/ZO/FO/ZFO composite photocatalyst is proposed.

EXPERIMENTAL SECTION

Synthesis of ZnO and Fe_2O_3

According to the stoichiometric ratio of ZnO and Fe_2O_3, zinc nitrate and ferric nitrate were dissolved in 25 ml deionized water, respectively. Solutions containing zinc nitrate and ferric nitrate are labeled as solutions A and B, respectively. After zinc nitrate and ferric nitrate were dissolved, 5 g of citric acid was added to both A and B solutions to make the citric acid react with Zn ions or Fe ions. Then, the A and B solutions were transferred to an oil bath at 300°C for 12 h to obtain a black gel. A and B gels were ground into fine powder in a mortar, and after grinding with urea for half an hour, they were transferred to the combustion network for spontaneous combustion for 2 h to obtain ZnO and Fe_2O_3 powders.

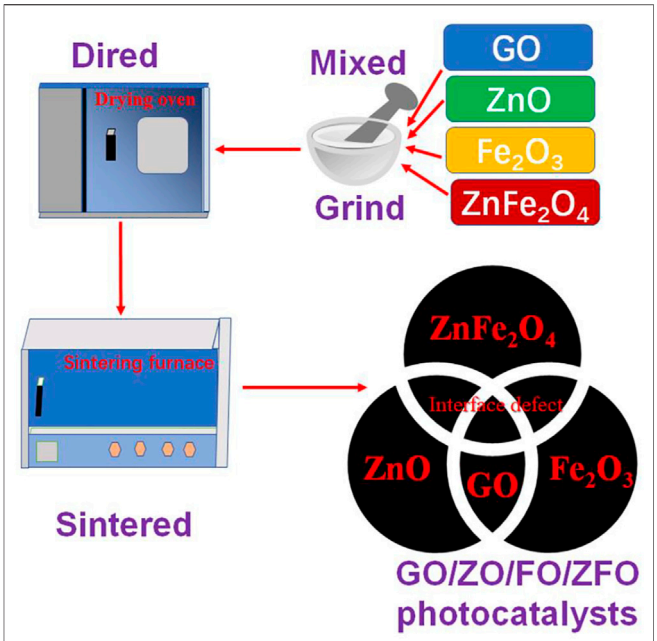

FIGURE 1 | Preparation of the flowchart of GO/ZO/FO/ZFO.

One-Step Low-Temperature Sintering Synthesis of Graphene Oxide/ZnO/Fe_2O_3/$ZnFe_2O_4$ Photocatalysts

Graphene oxide (GO) and $ZnFe_2O_4$ (ZFO) were purchased from Aladdin Reagent LTD. According to Guskos et al. (2010), ZO/FO/ZFO with the mass ratio of ZO: FO: ZFO = 20 wt%: 10 wt%: 70 wt % was obtained. Then, according to the GO mass ratios of 5 wt%, 10 wt%, 15 wt%, and 20 wt% to ZO/FO/ZFO, they are named GO/ZO/FO/ZFO1, GO/ZO/FO/ZFO2, GO/ZO/FO/ZFO3, and GO/ZO/FO/ZFO4, respectively. Finally, the samples were placed in a box furnace and sintered at 200°C for 2 h to obtain the final sample. **Figure 1** shows the preparation flowchart of GO/ZO/FO/ZFO.

Material Characterization

The phase structures of samples GO, ZnO, Fe_2O_3, GO/ZO/FO/ZFO1, GO/ZO/FO/ZFO2, GO/ZO/FO/ZFO3, and GO/ZO/FO/ZFO4 were measured by means of X-ray powder diffraction (XRD) with Cu Kα radiation. The Fourier transform infrared (FTIR) spectrophotometer with Bruker IFS 66v/S was used to study the samples GO, ZnO, Fe_2O_3, GO/ZO/FO/ZFO1, GO/ZO/FO/ZFO2, GO/ZO/FO/ZFO3, and GO/ZO/FO/ZFO4 in the wave-number range of 400–4000 cm^{-1}. The microstructures of GO/ZO/FO/ZFO1, GO/ZO/FO/ZFO2, GO/ZO/FO/ZFO3, and GO/ZO/FO/ZFO4 were investigated by field-emission scanning

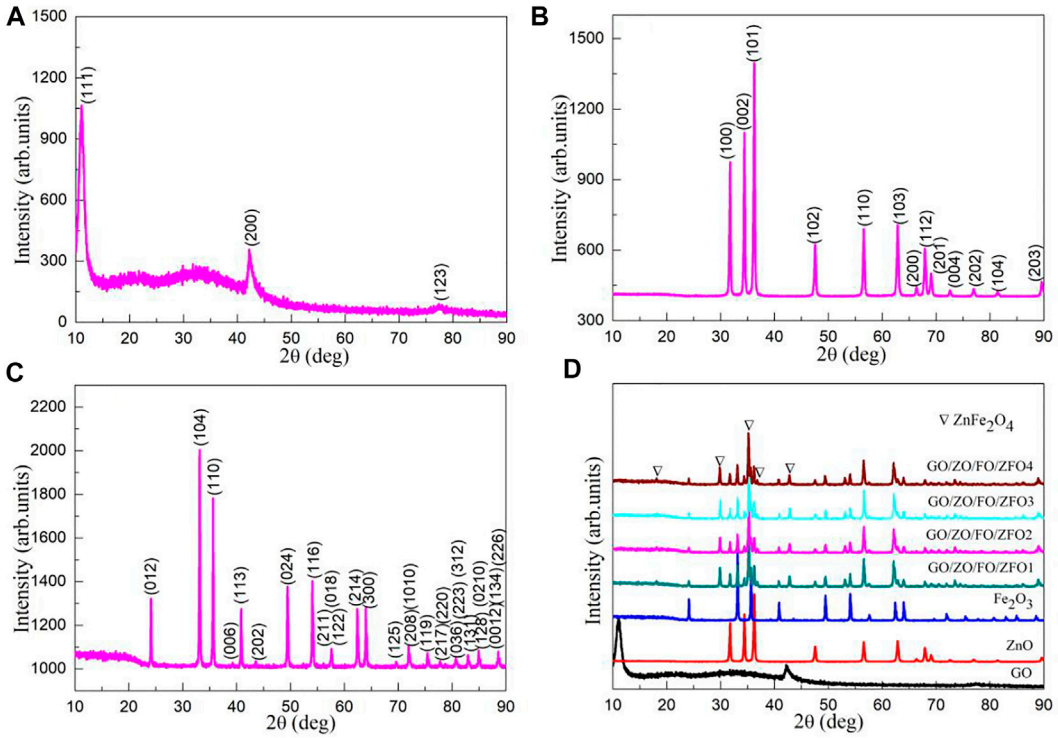

FIGURE 2 | XRD patterns of samples **(A)** GO, **(B)** ZnO, **(C)** Fe_2O_3, **(D)** GO/ZO/FO/ZFO1, GO/ZO/FO/ZFO2, GO/ZO/FO/ZFO3, and GO/ZO/FO/ZFO4.

electron microscopy (SEM) and transmission electron microscopy (TEM). Ultraviolet-visible (UV-Vis) diffuse reflectance spectra of samples GO, ZnO, Fe_2O_3, GO/ZO/FO/ZFO1, GO/ZO/FO/ZFO2, GO/ZO/FO/ZFO3, and GO/ZO/FO/ZFO4 were measured by using a UV1901 UV-Visible spectrophotometer.

Photocatalytic Experiments for the Degradation of Methyl Orange, Tetrabromobisphenol A, and Oxytetracycline Hydrochloride

The photocatalytic activity of GO/ZO/FO/ZFO composite photocatalysts was studied using methyl orange, tetrabromobisphenol A, and oxytetracycline hydrochloride as degradation materials. The light source, initial pollutant concentration, and catalyst concentration were xenon lamps with 500 W, 20 mg/L for methyl orange, 50 mg/L for tetrabromobisphenol A, and 1 g/L for oxytetracycline hydrochloride, respectively. Including adsorption experiments, samples were taken every 30 min, and each photocatalytic experiment was performed for 210 min. The removed solution was centrifuged, and its absorbance was measured by using a UV-Vis spectrophotometer. The photocatalytic degradation rate, first-order kinetic curve, and degradation percentage of the GO/ZO/FO/ZFO magnetic separation photocatalyst can be calculated based on the measured absorbance value.

RESULTS AND DISCUSSION

X-Ray Powder Diffraction Analysis

The phase structure and purity of semiconductor materials are measured by using an X-ray powder diffraction (XRD) instrument to determine whether the synthesized product is the target product. **Figure 2** shows the XRD patterns of samples GO, ZnO, Fe_2O_3, GO/ZO/FO/ZFO1, GO/ZO/FO/ZFO2, GO/ZO/FO/ZFO3, and GO/ZO/FO/ZFO4. The XRD pattern of sample GO (**Figure 2A**) shows the XRD characteristic peaks located at 10.905, 42.193, and 77.772° related to (111), (200), and (123), respectively, which is identical to the JCPDS No. 89-8489. Similarly, ZnO (**Figure 2B**) displays an XRD pattern identical to the hexagonal structural phase with the space group P63mc (186), and the XRD characteristic peaks at 31.736°, 34.378°, 36.214°, 47.483°, 56.534°, 62.775°, 66.302°, 67.886°, 69.007°, 72.462°, 76.865°, 81.268°, and 89.489° related to (100), (002), (101), (102), (110), (103), (200), (112), (201), (004), (202), (104), and (203) crystal plane ZnO corresponds to the JCPDS No. 76-0704. The sample of Fe_2O_3 (**Figure 2C**) exhibits several characteristic peaks located at 2θ of 24.149°, 33.158°, 35.631°, 39.283°, 40.862°, 43.508°, 49.462°, 54.069°, 56.159°, 57.448°, 57.597°, 62.436°, 64.000°, 66.031°, 69.595°, 71.947°, 72.281°, 75.191°, 75.455°, 77.738°, 78.776°, 79.486°, 80.582°, 80.709°, 82.953°, 84.485°, 84.934°, and 88.557°, corresponding to the (012), (104), (110), (006), (113), (202), (024), (116), (211), (122), (018), (214), (300),

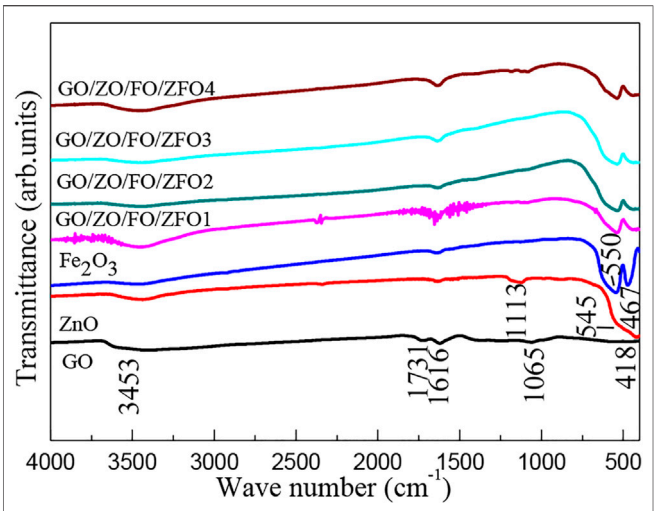

FIGURE 3 | FTIR spectra of samples GO, ZnO, Fe_2O_3, GO/ZO/FO/ZFO1, GO/ZO/FO/ZFO2, GO/ZO/FO/ZFO3, and GO/ZO/FO/ZFO4.

(125), (208), (1010), (119), (217), (220), (036), (223), (131), (312), (128), (0210), (0012), (134), and (226) crystal surfaces of rhombohedral structural Fe_2O_3 with the JCPDS No. 87-1164. When GO, ZnO, Fe_2O_3 and $ZnFe_2O_4$ are combined together, ZnO, Fe_2O_3 and $ZnFe_2O_4$ peaks appear in GO/ZO/FO/ZFO1, GO/ZO/FO/ZFO2, GO/ZO/FO/ZFO3, and GO/ZO/FO/ZFO4, as shown in **Figure 2D**. However, the diffraction peak of GO is difficult to observe. As the GO content increased to 20%, only a weak diffraction peak was observed at 10.905° of the sample GO/ZO/FO/ZFO4, further confirming that GO exists in the sample GO/ZO/FO/ZFO4.

Fourier Transform Infrared Analysis

In order to further study the phase structure and purity of semiconductor materials, FTIR was performed. **Figure 3** shows the FTIR spectra of samples GO, ZnO, Fe_2O_3, GO/ZO/FO/ZFO1, GO/ZO/FO/ZFO2, GO/ZO/FO/ZFO3, and GO/ZO/FO/ZFO4. For all samples, the peaks at 3453 and 1616 cm^{-1} can be ascribed to the absorbed water due to the use of KBr in the tablet pressing process (Gao et al., 2021; Li et al., 2021; Liu et al., 2022). For the sample GO, the peaks at 1731 and 1065 cm^{-1} can be assigned to the graphene oxide (Dat et al., 2022; Hwa et al., 2022). For ZnO, the peaks at 1113, 545, and 418 cm^{-1} are attributed to the characteristic peak of C-O and the Zn–O and Zn-O-Zn vibrations, respectively (Prabhu et al., 2018; Rammah et al., 2020; Wang et al., 2021b; Nadeem et al., 2021; Wang et al., 2022c; Tang et al., 2022). For Fe_2O_3, the peaks at 550 and 467 cm^{-1} are assigned to the Fe-O and Fe-O-Fe vibrations, respectively (Lv et al., 2010; Ratep and Kashif, 2021). For the samples GO/ZO/FO/ZFO, the intensity of the characteristic peak of GO increases with the increase in the GO content, and the characteristic peak of Fe_2O_3 is slightly shifted, especially due to the influence of the Fe-O functional group in $ZnFe_2O_4$ (can be written as $ZnO{\bullet}Fe_2O_3$), and the heterojunction between GO, ZnO, Fe_2O_3, and $ZnFe_2O_4$ is formed.

XPS Analysis

Figure 4A shows the XPS survey spectrum of the sample GO/ZO/FO/ZFO3. The survey spectra of the samples GO/ZO/FO/ZFO3 exhibit sharp peaks of C, Zn, Fe, and O elements, and no other elements are observed, indicating that the sample GO/ZO/FO/ZFO3 does not contain any impurities. **Figure 4B** shows the high-resolution XPS spectrum of Zn 2p for the sample GO/ZO/FO/ZFO3. The two bands of Zn 2p1/2 and 2p3/2 were recorded at 1044.61 and 1021.42 eV, respectively, in $ZnFe_2O_4$, while the peaks at 1024.74 and 1047.77 eV can be ascribed to Zn 2p1/2 and 2p3/2 in ZnO, respectively. The Fe 2p spectrum showed obvious peaks at 711.83 (Fe 2p3/2) and 727.24 (Fe 2p1/2) eV which may be attributed to Fe_2O_3, and the peaks at 714.03 (Fe 2p3/2) and 733.85 (Fe 2p1/2) eV can be assigned to $ZnFe_2O_4$, as shown in **Figure 4C**. The O 1s spectrum of the samples GO/ZO/FO/ZFO3 is displayed in **Figure 4D**. The O1s peak could be convoluted into five peaks at 535.75, 533.51, 531.65, 530.70, and 530.21 eV, respectively. These peaks can be ascribed to C-O, the lattice oxygen of ZnO (O-Zn-ZO), the lattice oxygen of $ZnFe_2O_4$ (O-Zn-ZFO), the lattice oxygen of Fe_2O_3 (O-Zn-FO), and the lattice oxygen of $ZnFe_2O_4$ (O-Fe-ZFO), respectively. **Figure 4E** shows the high-resolution XPS spectra of C1s for the sample GO/ZO/FO/ZFO3. Three peaks at 287.72, 285.32, and 283.49 eV can be assigned C-H, C-O, and C1s for the XPS calibration peak, respectively. The results further confirmed the successful synthesis of the GO/ZO/FO/ZFO photocatalyst by low-temperature sintering technology.

Microstructural Analysis

The microstructure of semiconductor material has a great influence on its photocatalytic activity. **Figures 5A–D** show the SEM images of samples GO/ZO/FO/ZFO1, GO/ZO/FO/ZFO2, GO/ZO/FO/ZFO3, and GO/ZO/FO/ZFO4. When the GO content is 5%, the samples are mainly composed of fine nanoparticles, with lamellar particles faintly visible, as shown in **Figure 5A**. When the content of GO increased to 10%, the agglomeration of fine particles became obvious, and the lamellar structure gradually increased, as shown in **Figure 5B**. When the content of GO further increased to 15%, fine nanoparticles gradually deposited on GO, and the lamellar structure became more obvious, as shown in **Figure 5C**. With the GO content reaching 20%, lamellar structures appear in the samples in large quantities, as shown in **Figure 5D**. **Figures 5E,F** show the TEM and HRTEM images of the sample GO/ZO/FO/ZFO3, respectively. It can be seen from **Figure 5E** that fine nanoparticles are deposited on the lamellar GO, which is consistent with the SEM observation result. The lattice planes of ZnO, Fe_2O_3, and $ZnFe_2O_4$ were (100) and (101) with a lattice space of 0.2827 and 0.2486 nm, respectively, (104) and (110) with a lattice space of 0.2699 and 0.2517 nm, respectively, and (311) with a lattice space of 0.2536 nm, respectively. The results further confirmed that the GO/ZO/FO/ZFO3 samples contained GO, ZnO, Fe_2O_3, and $ZnFe_2O_4$.

Optical Properties

The optical properties can be used to determine whether the semiconductor material has a high optical absorption

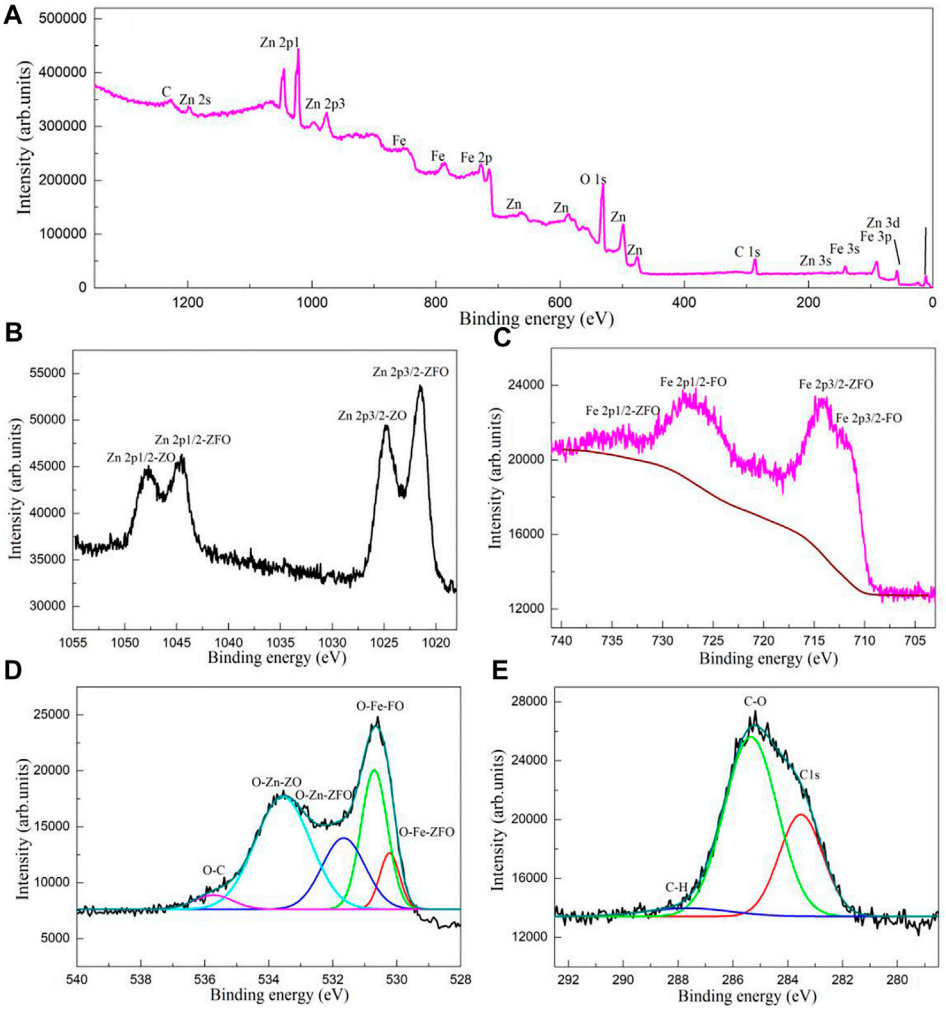

FIGURE 4 | (A) XPS survey spectrum and high-resolution XPS spectra of **(B)** Zn 2p, **(C)** Fe 2p, **(D)** O 1s, and **(E)** C 1s for the sample GO/ZO/FO/ZFO3.

coefficient and further verify whether it has high photocatalytic activity. **Figure 6A** shows the UV-Vis diffuse reflectance spectra of samples GO, ZnO, Fe_2O_3, GO/ZO/FO/ZFO1, GO/ZO/FO/ZFO2, GO/ZO/FO/ZFO3, and GO/ZO/FO/ZFO4. Fe_2O_3 has the lowest reflectivity, and ZnO has the highest reflectivity in the wavelength range of 400–800 nm, while GO tends to be almost constant in this range. When GO, ZnO, Fe_2O_3, and $ZnFe_2O_4$ are coupled, the reflectivity in the visible light range changes significantly compared with ZnO and is greatly improved. After 850 nm, the reflectivity of GO/ZO/FO/ZFO samples increases sharply with the increase in wavelength.

According to Kubelka–Munk's (K–M) formula, the UV-Vis diffuse reflectance spectrum can be transformed into the UV-Vis absorption spectrum.

$$F(R) = \frac{\alpha}{S} = \frac{(1 - R_\infty)^2}{2R} \quad (1)$$

where R is the reflectance of samples GO, ZnO, Fe_2O_3, GO/ZO/FO/ZFO1, GO/ZO/FO/ZFO2, GO/ZO/FO/ZFO3, and GO/ZO/FO/ZFO4, α is the optical absorption coefficient, and S is the scattering coefficient of samples GO, ZnO, Fe_2O_3, GO/ZO/FO/ZFO1, GO/ZO/FO/ZFO2, GO/ZO/FO/ZFO3, and GO/ZO/FO/ZFO4. **Figure 6B** shows the UV-Vis absorption spectra of samples GO, ZnO, Fe_2O_3, GO/ZO/FO/ZFO1, GO/ZO/FO/ZFO2, GO/ZO/FO/ZFO3, and GO/ZO/FO/ZFO4. ZnO exhibits a high UV absorption coefficient, indicating that it has high UV photocatalytic activity. Fe_2O_3 has the highest light absorption coefficient in the wavelength range of 190–900 nm, but its photocatalytic activity is not high because of its high charge carrier recombination rate. When GO, ZnO, Fe_2O_3 and $ZnFe_2O_4$ are coupled to form heterojunctions, the absorption coefficient of the GO/ZO/FO/ZFO sample is greatly improved in the visible light range compared with ZnO, indicating that GO/ZO/FO/ZFO samples have high visible-light photocatalytic activity.

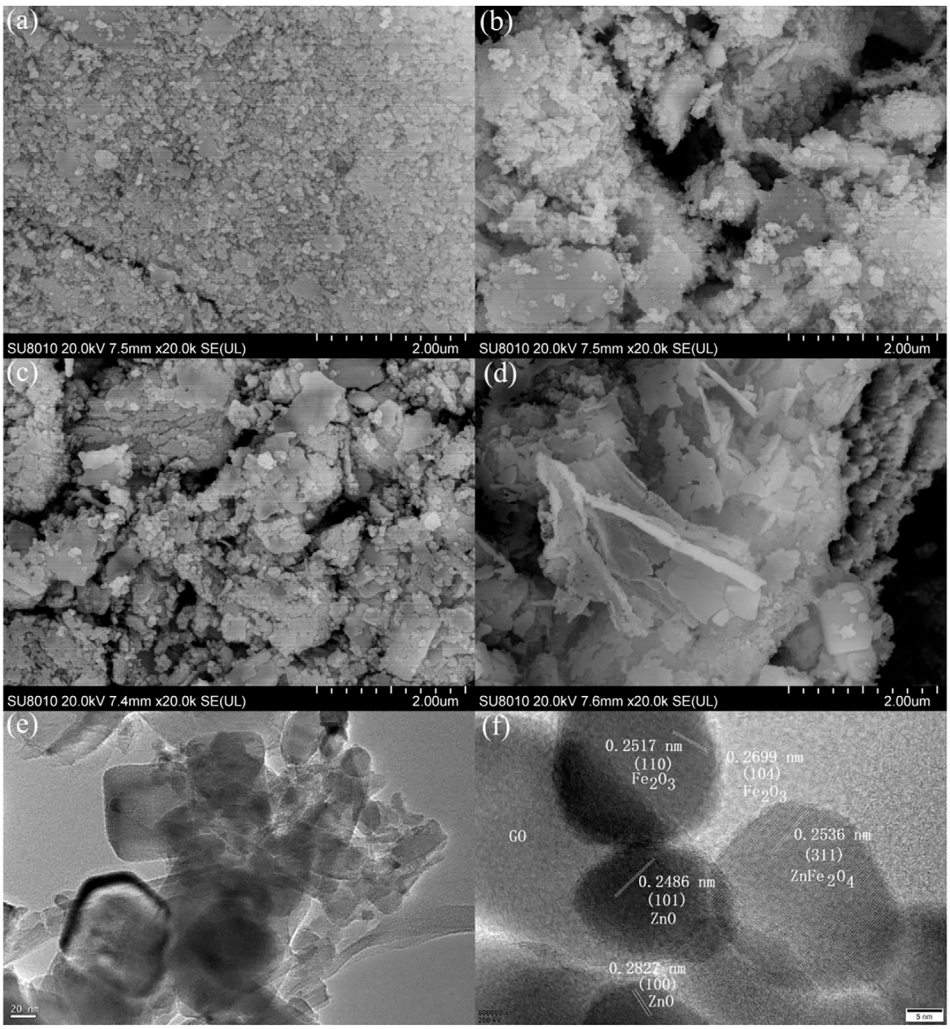

FIGURE 5 | SEM images of samples **(A)** GO/ZO/FO/ZFO1, **(B)** GO/ZO/FO/ZFO2, **(C)** GO/ZO/FO/ZFO3, and **(D)** GO/ZO/FO/ZFO4. **(E)** TEM and **(F)** HRTEM images of the sample GO/ZO/FO/ZFO3.

The first-order differential curve is calculated based on the UV-vis diffuse reflectance spectrum. The peak of the curve can be used to obtain the optical band gap (Eg) value of the semiconductor material (Gao et al., 2019; Gao et al., 2022a).

$$E_g\,(\mathrm{eV}) = \frac{hc}{\lambda_0\,(\mathrm{nm})} \approx \frac{1240}{\lambda_0\,(\mathrm{nm})} \tag{2}$$

where λ_0, h, and c are the peak of the first-order differential curve, the Plank constant, and the velocity of light, respectively. **Figures 6C–F** show the first-order differential curves of UV-Vis diffuse reflectance spectra of samples GO, ZnO, Fe_2O_3, GO/ZO/FO/ZFO1, GO/ZO/FO/ZFO2, GO/ZO/FO/ZFO3, and GO/ZO/FO/ZFO4. The Eg values of samples GO, ZnO, Fe_2O_3, GO/ZO/FO/ZFO1, GO/ZO/FO/ZFO2, GO/ZO/FO/ZFO3, and GO/ZO/FO/ZFO4 are 1.44, 3.18, 2.12, 2.11, 2.11, 2.11, and 2.11 eV, respectively. As can be seen from **Figure 5F**, when GO, ZnO, Fe_2O_3 and $ZnFe_2O_4$ are coupled, the Eg value does not change at all. According to Xue et al. (2019), Kelaidis et al. (2020), Wang et al. (2021c), Gao et al. (2022b), and Gao et al. (2022c), only defects or vacancies can be introduced, and their Eg values will not be changed after a variety of semiconductor photocatalysts are coupled to form heterojunctions. This result is consistent with the literature reports.

Photocatalytic Activity for the Degradation of Dyes

The photocatalytic activity of the sample GO/ZO/FO/ZFO was studied with dyes, pollutants, and antibiotics as target degradation materials. **Figure 7A** shows the time-dependent degradation of methyl orange in the presence of the sample GO/ZO/FO/ZFO3 under simulated solar irradiation. Before the photocatalytic degradation experiment, methyl orange was adsorbed for half an hour to exclude the influence of adsorption on photocatalytic activity. After half an hour of adsorption, the

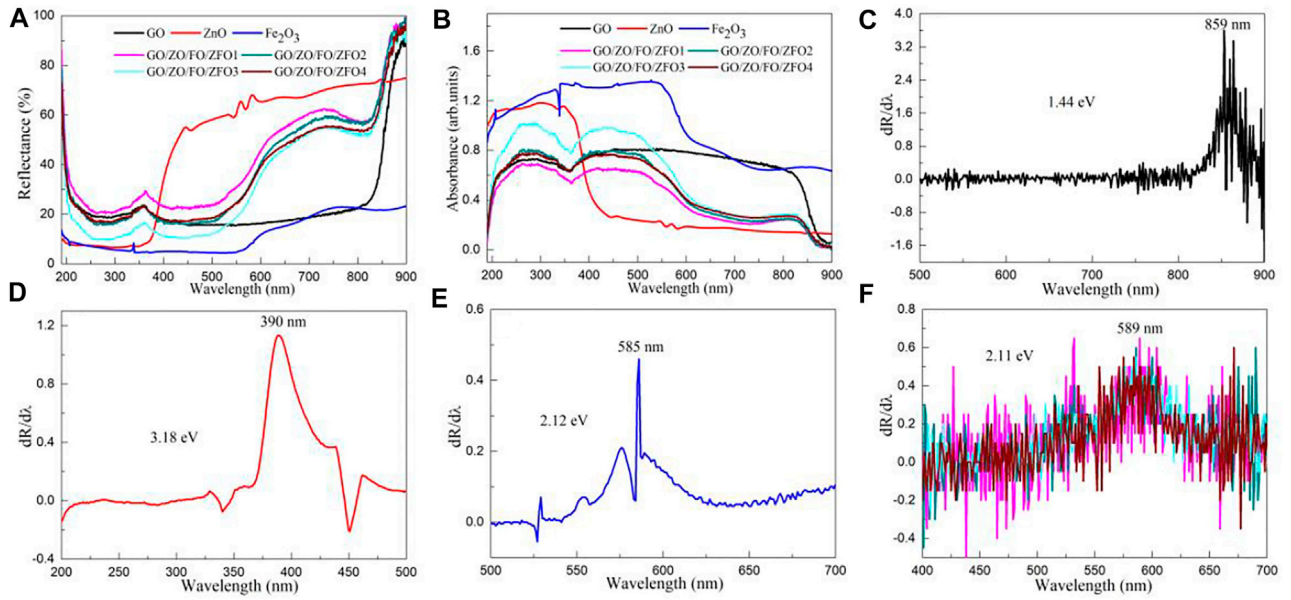

FIGURE 6 | (A) UV-Vis diffuse reflectance spectra and **(B)** UV-Vis absorption spectra of samples GO, ZnO, Fe_2O_3, GO/ZO/FO/ZFO1, GO/ZO/FO/ZFO2, GO/ZO/FO/ZFO3, and GO/ZO/FO/ZFO4. First-order differential curves of UV-Vis diffuse reflectance spectra of samples **(C)** GO, **(D)** ZnO, **(E)** Fe_2O_3, **(F)** GO/ZO/FO/ZFO1, GO/ZO/FO/ZFO2, GO/ZO/FO/ZFO3, and GO/ZO/FO/ZFO4.

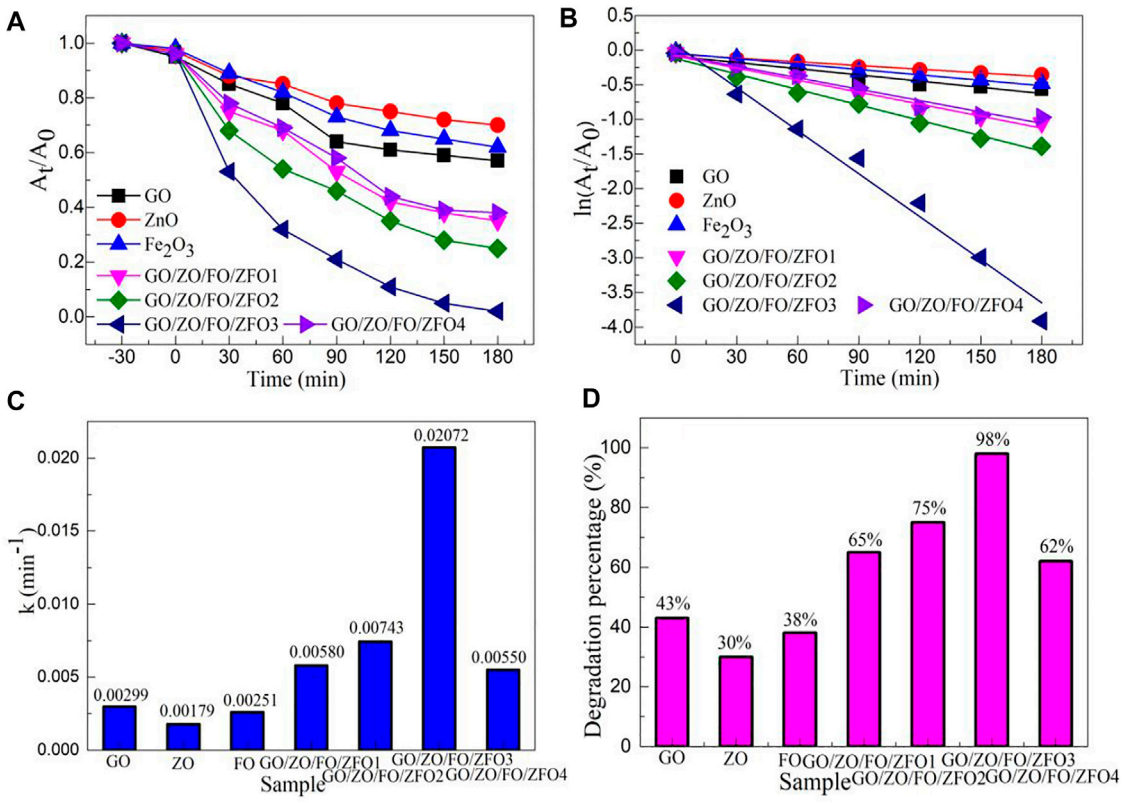

FIGURE 7 | (A) Time-dependent characteristic, **(B)** plots of ln (A_t/A_0) vs. irradiation time (t), **(C)** first-order kinetic constant (k), and **(D)** degradation percentage of degradation of methyl orange in the presence of samples GO, ZnO, Fe_2O_3, and GO/ZO/FO/ZFO under simulated solar irradiation.

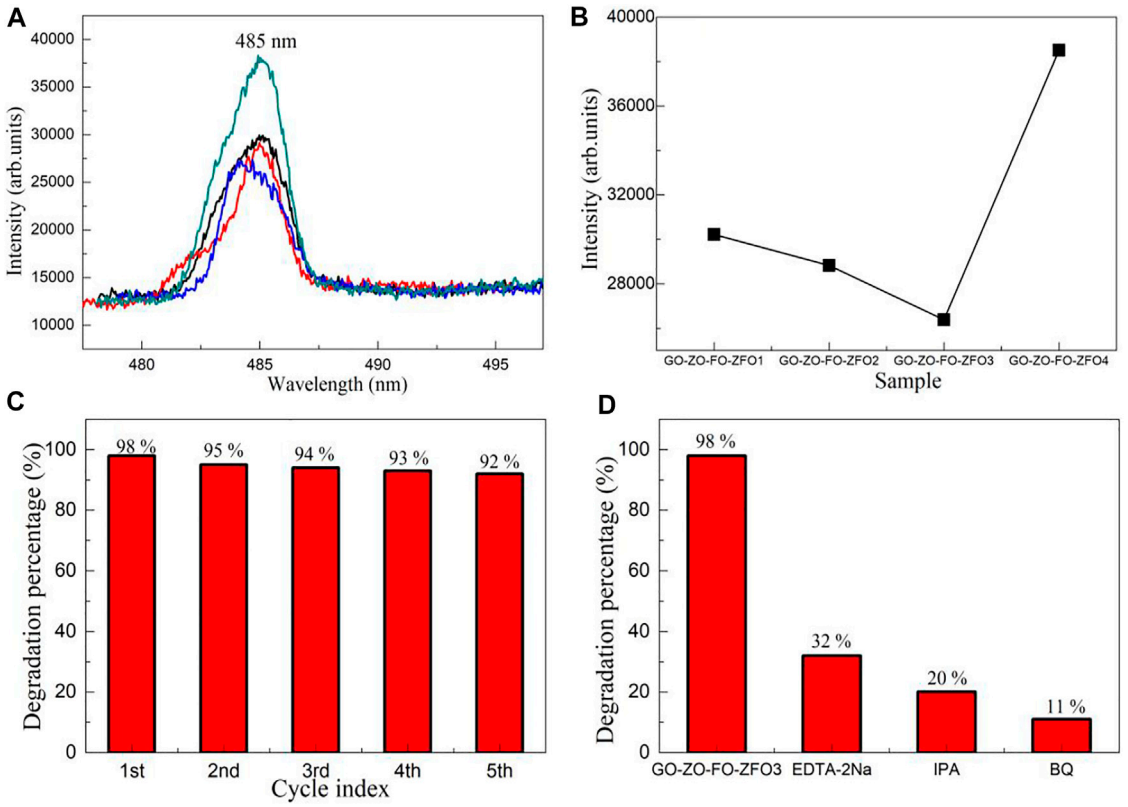

FIGURE 8 | (A) Emission spectra (λex = 300 nm) of the GO/ZO/FO/ZFO photocatalyst. **(B)** Maximum emission intensity at 485 nm of the GO/ZO/FO/ZFO photocatalyst. The **(C)** stability and **(D)** trapping experiments of the GO/ZO/FO/ZFO3 photocatalyst.

adsorption of methyl orange by GO, ZnO, Fe_2O_3, and GO/ZO/FO/ZFO is small, less than 10%. The degradation rate of all samples increased with the increase in illumination time. Under visible light irradiation, the photocatalytic degradation percentage of GO, ZnO, and Fe_2O_3 is less than 30%. The sample GO/ZO/FO/ZFO3 showed the highest photocatalytic activity, and the degradation percentage reached 98% after 3 h of degradation.

The first-order kinetic curve can directly reflect the photocatalytic activity of semiconductor materials. The first-order dynamics equation can be described as follows:

$$\ln(A_t/A_0) = -Kt, \quad (3)$$

where A_t is the absorbance of the pollutant at time t, A_0 is the absorbance of the pollutant at the initial time, k is the first-order kinetic constant, and t is the irradiation time. **Figure 7B** shows the plots of ln (A_t/A_0) vs. irradiation time of degradation of methyl orange in the presence of the sample GO/ZO/FO/ZFO3 under simulated solar irradiation. ln (A_t/A_0) for samples GO, ZnO, Fe_2O_3, and GO/ZO/FO/ZFO shows a good linear relationship with the irradiation time. **Figure 7C** shows the k values of degradation of methyl orange in the presence of samples GO, ZnO, Fe_2O_3, and GO/ZO/FO/ZFO under simulated solar irradiation. The k values of samples GO, ZnO, Fe_2O_3, GO/ZO/FO/ZFO1, GO/ZO/FO/ZFO2, GO/ZO/FO/ZFO3, and GO/ZO/FO/ZFO4 are 0.00299, 0.00179, 0.00251, 0.00580, 0.00743, 0.02072, and 0.00550 min^{-1}, respectively. The photocatalytic degradation rate of GO/ZO/FO/ZFO3 is 11.58 times that of ZnO. **Figure 7D** shows the degradation percentage of degradation of methyl orange in the presence of samples GO, ZnO, Fe_2O_3, and GO/ZO/FO/ZFO under simulated solar irradiation. The degradation percentages of samples GO, ZnO, Fe_2O_3, GO/ZO/FO/ZFO1, GO/ZO/FO/ZFO2, GO/ZO/FO/ZFO3, and GO/ZO/FO/ZFO4 are 43%, 30%, 38%, 65%, 75%, 98%, and 62%, respectively. With the increase in the GO content, the photocatalytic velocity of the GO/ZO/FO/ZFO photocatalyst first increases and then decreases. The results further confirmed that the sample GO/ZO/FO/ZFO3 had the highest photocatalytic activity.

Stability and Trapping Experiments

Figure 8A shows the emission spectra (λex = 300 nm) of the GO/ZO/FO/ZFO photocatalyst. The GO/ZO/FO/ZFO photocatalyst showed a narrow fluorescence emission peak at 485 nm, which may be caused by GO (Iliut et al., 2013; El-Hnayn et al., 2020). The maximum emission intensity at 485 nm of the GO/ZO/FO/ZFO photocatalyst is shown in **Figure 8B**. Compared with the photocatalytic activity, the emission intensity decreased with the

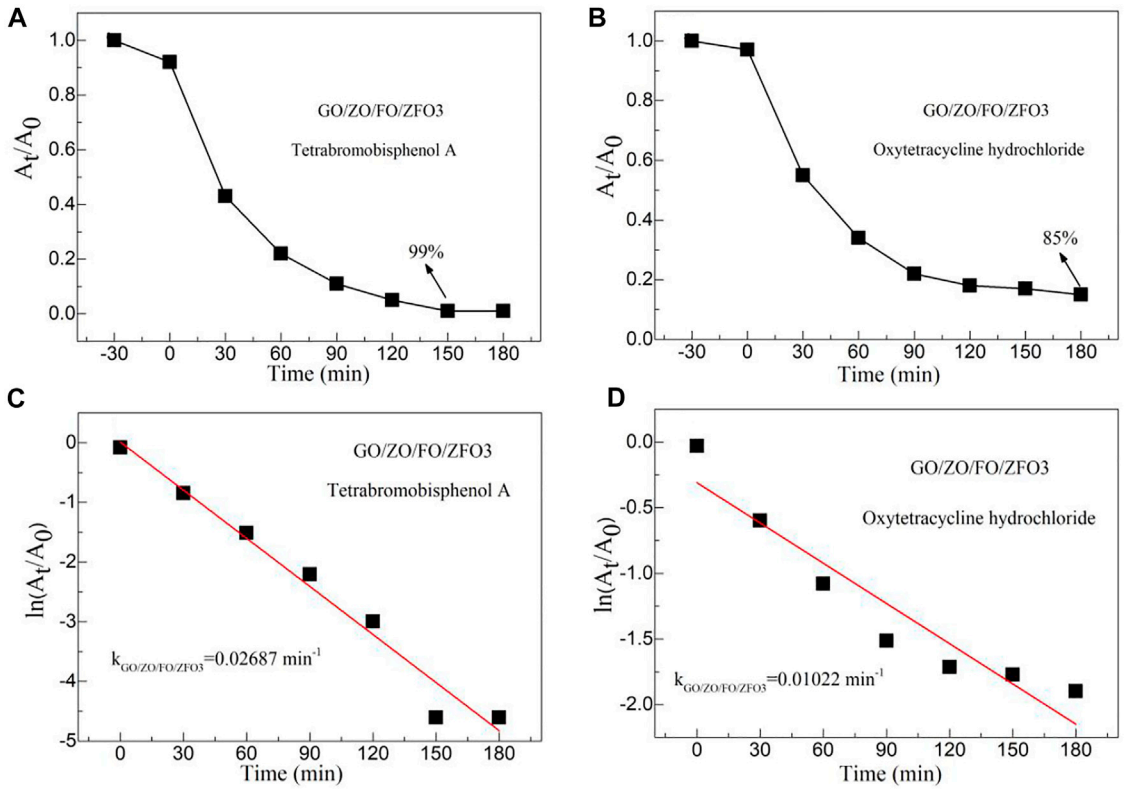

FIGURE 9 | Time-dependent degradation of **(A)** tetrabromobisphenol A and **(B)** oxytetracycline hydrochloride in the presence of the sample GO/ZO/FO/ZFO3 under simulated solar irradiation. Plots of ln (A_t/A_0) vs. irradiation time (t) for the degradation of **(C)** tetrabromobisphenol A and **(D)** oxytetracycline hydrochloride in the presence of the sample GO/ZO/FO/ZFO3.

increase in the photocatalytic activity. It can be seen from the fluorescence emission spectrum that the photocatalyst exhibits poor transfer and separation rates of photogenerated carriers with higher emission intensity. To study the stability of the GO/ZO/FO/ZFO photocatalyst, **Figure 8C** shows the stability experiments of the GO/ZO/FO/ZFO3 photocatalyst. After five cycles, the photocatalytic activity of the GO/ZO/FO/ZFO3 photocatalyst decreased by less than 6%, indicating that the GO/ZO/FO/ZFO3 photocatalyst has high stability and recycling ability. The trapping experiments of the GO/ZO/FO/ZFO3 photocatalyst are shown in **Figure 8D**. Trapping agents include the disodium ethylenediamine tetraacetic acid (EDTA-2Na), 2-propanol (IPA), and 1,4-benzoquinone (BQ), which have been used to detect the hole (h_{VB}^+), hydroxyl radical (•OH), and superoxide radical ($•O_2^-$), respectively. During each photocatalytic experiment, the amount of the trapping agent added to the reaction solution was 1 mmol/L. When EDTA-2Na, IPA, and BQ were added to the reaction solution, the photocatalytic activity of the GO/ZO/FO/ZFO3 photocatalyst decreased to 32%, 20%, and 11%, respectively. The results showed that holes, hydroxyl radicals, and superoxide radicals play important roles in the photocatalytic reaction. This will provide strong evidence for the subsequent analysis of the photocatalytic mechanism.

Photocatalytic Activity for the Degradation of Pollutants and Antibiotics

Figures 9A,B show the time-dependent degradation of tetrabromobisphenol A and oxytetracycline hydrochloride in the presence of the sample GO/ZO/FO/ZFO3 under simulated solar irradiation, respectively. The degradation percentage of GO/ZO/FO/ZFO3 to tetrabromobisphenol A reached 99% after 150 min and that of oxytetracycline hydrochloride reached 85% after 180 min. The results showed that the sample GO/ZO/FO/ZFO3 had a high photocatalytic activity for the degradation of refractory pollutants and antibiotics. **Figures 9C,D** show the plots of ln (A_t/A_0) vs. irradiation time (t) for the degradation of tetrabromobisphenol A and oxytetracycline hydrochloride in the presence of the sample GO/ZO/FO/ZFO3, respectively. The k-values of the sample GO/ZO/FO/ZFO3 for the degradation of tetrabromobisphenol A and oxytetracycline hydrochloride are 0.02687 and 0.01022 min^{-1}, respectively. The results showed that the sample GO/ZO/FO/ZFO3 had the highest photocatalytic activity for the degradation of tetrabrombisphenol A.

Photocatalytic Mechanism

In order to gain insight into the photocatalytic mechanism of GO/ZO/FO/ZFO, the conduction band potential (E_{CB}) and

TABLE 1 | Conduction band, valence band potential, electronegativity, and Eg values of GO, ZnO and Fe_2O_3, and $ZnFe_2O_4$.

Sample	Eg (eV)	X (eV)	E_{CB} (eV)	E_{VB} (eV)
GO	1.44	6.91	1.69	3.13
ZnO	3.18	5.79	−0.30	2.88
Fe_2O_3	2.12	5.89	0.33	2.45
$ZnFe_2O_4$	1.71	5.86	0.51	2.22

valence band (E_{VB}) potential of GO, ZnO, Fe_2O_3 and $ZnFe_2O_4$ were calculated based on the band theory. **Table 1** shows the conduction band, valence band potential, electronegativity, and Eg values of GO, ZnO, Fe_2O_3, and $ZnFe_2O_4$.

$$E_{CB} = X - E^e - 0.5E_g \quad (4)$$

$$E_{VB} = E_{CB} + E_g \quad (5)$$

where the Eg values of GO, ZnO,Fe_2O_3, and $ZnFe_2O_4$ are 1.44, 3.18, 2.12, and 1.71 eV (Wang et al., 2019), respectively. E^e is 4.5 eV. The absolute electronegativity (X) values of GO, ZnO, Fe_2O_3, and $ZnFe_2O_4$ are 6.91, 5.79, 5.89, and 5.86 eV, respectively, and can be evaluated by **Eqs. 4**, **5**.

$$X\left(C_4O_{2-x}(OH)_{2x}(x=0.1)\right) = \sqrt[6,3]{X^4(C)*X^{2.1}(O)*X^{0.2}(H)} \quad (6)$$

$$X(ZnO) = \sqrt[2]{X(Zn)*X(O)} \quad (7)$$

$$X(Fe_2O_3) = \sqrt[5]{X^2(Fe)*X^3(O)} \quad (8)$$

$$X(ZnFe_2O_4) = \sqrt[7]{X(Zn)*X^2(Fe)*X^4(O)} \quad (9)$$

where X (C) = 6.27 eV, X (H) = 7.18 eV, X (Zn) = 4.45 eV, X (Fe) = 4.06 eV, and X (O) = 7.54 eV.

Based on the aforementioned calculations, the energy level diagram of GO/ZO/FO/ZFO is shown in **Figure 10**. As can be seen from the figure, GO acts as a carrier of charge transfer and transmission between ZnO, Fe_2O_3, and $ZnFe_2O_4$. When light is illuminated on the surface of the GO/ZO/FO/ZFO composite, the electrons in the respective valence band undergo transition to the conduction band. Since the conduction band of GO is more negative than ZnO, Fe_2O_3 and $ZnFe_2O_4$, the electrons will relax to the conduction band of GO. The valence bands of GO are more positive than those of ZnO, Fe_2O_3, and $ZnFe_2O_4$, and the valence band holes will undergo transition to the valence bands of ZnO, Fe_2O_3, and $ZnFe_2O_4$. Such relaxation and transition will promote the separation of electron and hole pairs of the whole complex, resulting in a large increase in its photocatalytic activity. The conduction electrons will react with oxygen in the reactant solution to form superoxide radicals and with $O_2/2H^+$ to form hydroxyl radicals. Valence band holes will react with H_2O/OH^- to form hydroxyl radicals. Subsequently, hydroxyl radicals or superoxide radicals react with pollutants to form non-toxic and harmless small organic molecules. Meanwhile, the valence band holes may react directly with pollutants to form non-toxic and harmless small molecular organics. The related chemical reactions can be expressed as follows:

$$GO/ZO/FO/ZFO + hv \rightarrow e^- + h^+ \quad (10)$$

$$h^+ + OH^- \rightarrow \cdot OH \quad (11)$$

$$e^- + O_2 \rightarrow \cdot O^{2-} \quad (12)$$

$$\cdot O^{2-} + 2H^+ + e^- \rightarrow H_2O_2 \quad (13)$$

$$2e^- + O_2 + 2H^+ \rightarrow H_2O_2 \quad (14)$$

$$e^- + H_2O_2 \rightarrow \cdot OH + OH^- \quad (15)$$

$$\cdot O^{2-} + H_2O_2 \rightarrow \cdot OH + OH^- + O_2 \quad (16)$$

$$\cdot OH/\cdot O^{2-} + dye/Pollutant/antibiotics \rightarrow degradation\ products \quad (17)$$

$$h^+ + dye/pollutant/antibiotics \rightarrow degradation\ products \quad (18)$$

It can be seen that the holes, hydroxyl radicals, and superoxide radicals play important roles in the whole photocatalytic process.

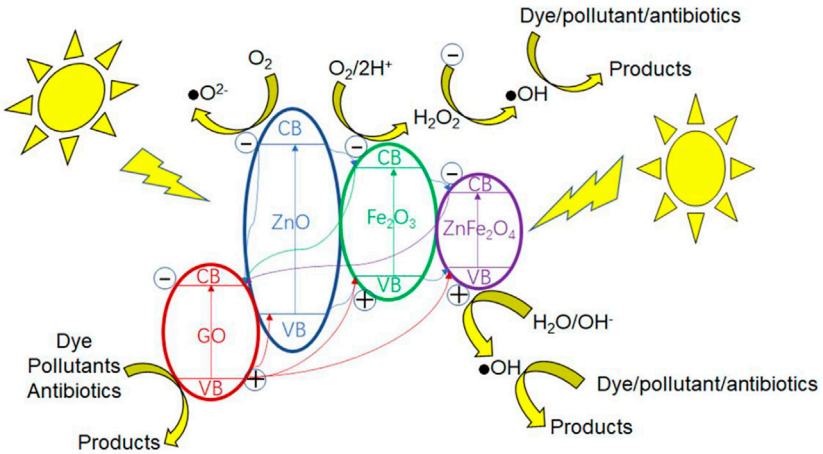

FIGURE 10 | Photocatalytic mechanism of GO/ZO/FO/ZFO.

CONCLUSION

GO/ZO/FO/ZFO composite photocatalysts with different GO contents were synthesized by a low-temperature sintering technique. The effects of the GO content on the phase purity, functional groups, microstructure, optical properties, and photocatalytic activity of GO/ZO/FO/ZFO composite photocatalysts were studied in detail. XRD, FTIR, and microstructural analysis confirmed that the GO/ZO/FO/ZFO magnetic separation photocatalyst contains four components, GO, ZnO, Fe_2O_3, and $ZnFe_2O_4$, without any other impurities. The optical property analysis shows that the GO/ZO/FO/ZFO magnetic separation photocatalyst has a high optical absorption coefficient, suggesting that it has a high visible-light photocatalytic activity, and the quadruple recombination does not change the Eg value of the main lattice of Fe_2O_3. The photocatalytic experiments confirmed that the GO/ZO/FO/ZFO magnetic separation photocatalyst had high photocatalytic activity for dyes, refractory pollutants, and antibiotics, and the degradation percentages were 98% for 180 min, 99% for 150 min, and 85% for 180 min, respectively. The special heterojunction structure promotes the transfer and separation of electrons and holes in the GO/ZO/FO/ZFO magnetic separation photocatalyst, showing high photocatalytic activity under the combined action of holes, hydroxyl radicals, and superoxide radicals.

DATA AVAILABILITY STATEMENT

The raw data supporting the conclusions of this article will be made available by the authors, without undue reservation.

AUTHOR CONTRIBUTIONS

All authors listed have made a substantial, direct, and intellectual contribution to the work and approved it for publication.

FUNDING

This work was supported by the Core Teacher Cultivating Program of the Yellow River Conservancy Technical Institute (No. 2020HYGG04).

REFERENCES

Cao, W., Lin, L., Qi, H., He, Q., Wu, Z., Wang, A., et al. (2019). *In-situ* Synthesis of Single-Atom Ir by Utilizing Metal-Organic Frameworks: An Acid-Resistant Catalyst for Hydrogenation of Levulinic Acid to γ-valerolactone. *J. Catal.* 373, 161–172. doi:10.1016/j.jcat.2019.03.035

Chen, D., Liu, Z., Guo, Z., Ruan, M., and Yan, W. (2019). 3D Branched Ca-Fe 2 O 3/Fe 2 O 3 Decorated with Pt and Co-Pi: Improved Charge-Separation Dynamics and Photoelectrochemical Performance. *ChemSusChem* 12 (14), 3286–3295. doi:10.1002/cssc.201901331

Chen, P., Liu, F., Ding, H., Chen, S., Chen, L., Li, Y.-J., et al. (2019). Porous Double-Shell CdS@C3N4 Octahedron Derived by *In Situ* Supramolecular Self-Assembly for Enhanced Photocatalytic Activity. *Appl. Catal. B Environ.* 252, 33–40. doi:10.1016/j.apcatb.2019.04.006

Cheng, T., Gao, W., Gao, H., Wang, S., Yi, Z., Wang, X., et al. (2021). Piezocatalytic Degradation of Methylene Blue, Tetrabromobisphenol A and Tetracycline Hydrochloride Using Bi4Ti3O12 with Different Morphologies. *Mater. Res. Bull.* 141, 111350. doi:10.1016/j.materresbull.2021.111350

Cheng, T., Ma, Q., Gao, H., Meng, S., Lu, Z., Wang, S., et al. (2022). Enhanced Photocatalytic Activity, Mechanism and Potential Application of Idoped-Bi4Ti3O12 Photocatalysts. *Mater. Today Chem.* 23, 100750. doi:10.1016/j.mtchem.2021.100750

Chong, R., Wang, Z., Lv, J., Rong, J., Zhang, L., Jia, Y., et al. (2021). A Hybrid CoOOH-rGO/Fe2O3 Photoanode with Spatial Charge Separation and Charge Transfer for Efficient Photoelectrochemical Water Oxidation. *J. Catal.* 399, 170–181. doi:10.1016/j.jcat.2021.05.006

Dadashzadeh, A., Moghassemi, S., and Amorim, C. A. (2021). Evaluation of PEGylated Fibrin as a Three-Dimensional Biodegradable Scaffold for Ovarian Tissue Engineering. *Mater. Today Chem.* 22, 100626. doi:10.1016/j.mtchem.2021.100626

Dat, N. M., Thinh, D. B., Huong, L. M., Tinh, N. T., Linh, N. T. T., Hai, N. D., et al. (2022). Facile Synthesis and Antibacterial Activity of Silver Nanoparticles-Modified Graphene Oxide Hybrid Material: the Assessment, Utilization, and Anti-virus Potentiality. *Mater. Today Chem.* 23, 100738. doi:10.1016/j.mtchem.2021.100738

El-Hnayn, R., Canabady-Rochelle, L., Desmarets, C., Balan, L., Rinnert, H., Joubert, O., et al. (2020). One-step Synthesis of Diamine-Functionalized Graphene Quantum Dots from Graphene Oxide and Their Chelating and Antioxidant Activities. *Nanomaterials* 10 (1), 104. doi:10.3390/nano10010104

Fu, L., Yu, H., Lin, Y., and Fang, W. (2021). Nanowheat-Like α-Fe2O3@Co-Based/Ti Foil Photoanode with Surface Defects for Enhanced Charge Carrier Separation and Photoelectrochemical Water Splitting. *Energy fuels.* 35 (21), 17956–17963. doi:10.1021/acs.energyfuels.1c02763

Gao, H. J., Wang, S. F., Fang, L. M., Sun, G. A., Chen, X. P., Tang, S. N., et al. (2021). Nanostructured Spinel-type M(M = Mg, Co, Zn)Cr2O4 Oxides: Novel Adsorbents for Aqueous Congo Red Removal. *Mater. Today Chem.* 22, 100593. doi:10.1016/j.mtchem.2021.100593

Gao, H., Wang, F., Wang, S., Wang, X., Yi, Z., and Yang, H. (2019). Photocatalytic Activity Tuning in a Novel Ag2S/CQDs/CuBi2O4 Composite: Synthesis and Photocatalytic Mechanism. *Mater. Res. Bull.* 115, 140–149. doi:10.1016/j.materresbull.2019.03.021

Gao, H., Wang, S., Wang, Y., Yang, H., Wang, F., Tang, S., et al. (2022). CaMoO4/CaWO4 Heterojunction Micro/nanocomposites with Interface Defects for Enhanced Photocatalytic Activity. *Colloids Surfaces A Physicochem. Eng. Aspects* 642, 128642. doi:10.1016/j.colsurfa.2022.128642

Gao, H., Wang, Y., Wang, S., Yang, H., and Yi, Z. (2022). A Simple Fabrication, Microstructure, Optical, Photoluminescence and Supercapacitive Performances of MgMoO4/MgWO4 Heterojunction Micro/nanocomposites. *Solid State Sci.* 129, 106909. doi:10.1016/j.solidstatesciences.2022.106909

Gao, H., Yu, C., Wang, Y., Wang, S., Yang, H., Wang, F., et al. (2022). A Novel Photoluminescence Phenomenon in a SrMoO4/SrWO4 Micro/nano Heterojunction Phosphors Obtained by the Polyacrylamide Gel Method Combined with Low Temperature Calcination Technology. *J. Luminescence* 243, 118660. doi:10.1016/j.jlumin.2021.118660

Guskos, N., Zolnierkiewicz, G., Typek, J., Sibera, D., and Narkiewicz, U. (2010). Magnetic Resonance Study of ZnO-Fe2O3-ZnFe2O4 System. *Rev. Adv. Mater. Sci.* 23, 224–228. AvaliableAt: https://www.ipme.ru/e-journals/RAMS/no_22310/guskos8.pdf.

He, Z., Siddique, M. S., Yang, H., Xia, Y., Su, J., Tang, B., et al. (2022). Novel Z-Scheme In2S3/Bi2WO6 Core-Shell Heterojunctions with Synergistic Enhanced Photocatalytic Degradation of Tetracycline Hydrochloride. *J. Clean. Prod.* 339, 130634. doi:10.1016/j.jclepro.2022.130634

He, Z., Su, J., Chen, R., and Tang, B. (2019). Fabrication of Novel P-Ag2O/n-PbBiO2Br Heterojunction Photocatalysts with Enhanced Photocatalytic

Performance under Visible-Light Irradiation. *J. Mater Sci. Mater Electron* 30 (23), 20870–20880. doi:10.1007/s10854-019-02454-y

He, Z., Su, J., Xia, Y., and Tang, B. (2020). Fabrication and Photocatalytic Performance of Bi 24 O 31 Br 10 Nanosphere by a Polyacrylamide Gel Method. *Micro & Nano Lett.* 15 (8), 499–502. doi:10.1049/mnl.2020.0016

He, Z., Xia, Y., Su, J., and Tang, B. (2019). Fabrication of Magnetically Separable NiFe2O4/Bi24O31Br10 Nanocomposites and Excellent Photocatalytic Performance under Visible Light Irradiation. *Opt. Mater.* 88, 195–203. doi:10.1016/j.optmat.2018.11.025

He, Z., Yang, H., Su, J., Xia, Y., Fu, X., Kang, L., et al. (2021). Polyacrylamide Gel Synthesis and Photocatalytic Performance of CuCo2O4 Nanoparticles. *Mater. Lett.* 288, 129375. doi:10.1016/j.matlet.2021.129375

He, Z., Yang, H., Su, J., Xia, Y., Fu, X., Wang, L., et al. (2021). Construction of Multifunctional Dual Z-Scheme Composites with Enhanced Photocatalytic Activities for Degradation of Ciprofloxacin. *Fuel* 294, 120399. doi:10.1016/j.fuel.2021.120399

Hosseini, S. A., Abbasian, A. R., Gholipoor, O., Ranjan, S., and Dasgupta, N. (2019). Adsorptive Removal of Arsenic from Real Sample of Polluted Water Using Magnetic GO/ZnFe2O4 Nanocomposite and ZnFe2O4 Nanospinel. *Int. J. Environ. Sci. Technol.* 16 (11), 7455–7466. doi:10.1007/s13762-018-2140-x

Hwa, K. Y., Santhan, A., and Sharma, T. S. K. (2022). One-dimensional Self-Assembled Co2SnO4 Nanosphere to Nanocubes Intertwined in Two-Dimensional Reduced Graphene Oxide: an Intriguing Electrocatalytic Sensor toward Mesalamine Detection. *Mater. Today Chem.* 23, 100739. doi:10.1016/j.mtchem.2021.100739

Iliut, M., Gabudean, A.-M., Leordean, C., Simon, T., Teodorescu, C.-M., and Astilean, S. (2013). Riboflavin Enhanced Fluorescence of Highly Reduced Graphene Oxide. *Chem. Phys. Lett.* 586, 127–131. doi:10.1016/j.cplett.2013.09.032

Karpova, S. S., Moshnikov, V. A., Maksimov, A. I., Mjakin, S. V., and Kazantseva, N. E. (2013). Study of the Effect of the Acid-Base Surface Properties of ZnO, Fe2O3 and ZnFe2O4 Oxides on Their Gas Sensitivity to Ethanol Vapor. *Semiconductors* 47 (8), 1026–1030. doi:10.1134/S1063782613080095

Karpova, S. S., Moshnikov, V. A., Mjakin, S. V., and Kolovangina, E. S. (2013). Surface Functional Composition and Sensor Properties of ZnO, Fe2O3, and ZnFe2O4. *Semiconductors* 47 (3), 392–395. doi:10.1134/S1063782613030123

Kelaidis, N., Bousiadi, S., Zervos, M., Chroneos, A., and Lathiotakis, N. N. (2020). Electronic Properties of the Sn1-xPbxO Alloy and Band Alignment of the SnO/PbO System: a DFT Study. *Sci. Rep.* 10 (1), 16828–8. doi:10.1038/s41598-020-73703-y

Kormányos, A., Kecsenovity, E., Honarfar, A., Pullerits, T., and Janáky, C. (2020). Hybrid FeNiOOH/α-Fe 2 O 3/Graphene Photoelectrodes with Advanced Water Oxidation Performance. *Adv. Funct. Mat.* 30 (31), 2002124. doi:10.1002/adfm.202002124

Kuang, P., Zhang, L., Cheng, B., and Yu, J. (2017). Enhanced Charge Transfer Kinetics of Fe2O3/CdS Composite Nanorod Arrays Using Cobalt-Phosphate as Cocatalyst. *Appl. Catal. B Environ.* 218, 570–580. doi:10.1016/j.apcatb.2017.07.002

Li, J., Wang, S., Sun, G., Gao, H., Yu, X., Tang, S., et al. (2021). Facile Preparation of MgAl2O4/CeO2/Mn3O4 Heterojunction Photocatalyst and Enhanced Photocatalytic Activity. *Mater. Today Chem.* 19, 100390. doi:10.1016/j.mtchem.2020.100390

Li, L., Sun, X., Xian, T., Gao, H., Wang, S., Yi, Z., et al. (2022). Template-free Synthesis of Bi2O2CO3 Hierarchical Nanotubes Self-Assembled from Ordered Nanoplates for Promising Photocatalytic Applications. *Phys. Chem. Chem. Phys.* 24 (14), 8279–8295. doi:10.1039/D1CP05952A

Lin, X., Du, S., Li, C., Li, G., Li, Y., Chen, F., et al. (2020). Consciously Constructing the Robust NiS/g-C3n4 Hybrids for Enhanced Photocatalytic Hydrogen Evolution. *Catal. Lett.* 150 (7), 1898–1908. doi:10.1007/s10562-020-03118-x

Liu, H., Wang, S., Gao, H., Yang, H., Wang, F., Chen, X., et al. (2022). A Simple Polyacrylamide Gel Route for the Synthesis of MgAl2O4 Nanoparticles with Different Metal Sources as an Efficient Adsorbent: Neural Network Algorithm Simulation, Equilibrium, Kinetics and Thermodynamic Studies. *Sep. Purif. Technol.* 281, 119855. doi:10.1016/j.seppur.2021.119855

Luo, W., Cao, W., Bruijnincx, P. C. A., Lin, L., Wang, A., and Zhang, T. (2019). Zeolite-supported Metal Catalysts for Selective Hydrodeoxygenation of Biomass-Derived Platform Molecules. *Green Chem.* 21 (14), 3744–3768. doi:10.1039/C9GC01216H

Lv, A., Hu, C., Nie, Y., and Qu, J. (2010). Catalytic Ozonation of Toxic Pollutants over Magnetic Cobalt and Manganese Co-doped γ-Fe2O3. *Appl. Catal. B Environ.* 100 (1-2), 62–67. doi:10.1016/j.apcatb.2010.07.011

Nadeem, M. S., Munawar, T., Mukhtar, F., Naveed ur Rahman, M., Riaz, M., Hussain, A., et al. (2021). Hydrothermally Derived Co, Ni Co-doped ZnO Nanorods; Structural, Optical, and Morphological Study. *Opt. Mater.* 111, 110606. doi:10.1016/j.optmat.2020.110606

Pei, J., Zhao, H., Yang, F., and Yan, D. (2021). Graphene Oxide/Fe2O3 Nanocomposite as an Efficient Catalyst for Thermal Decomposition of Ammonium Perchlorate *via* the Vacuum-Freeze-Drying Method. *Langmuir* 37 (20), 6132–6138. doi:10.1021/acs.langmuir.1c00108

Prabhu, S., Pudukudy, M., Sohila, S., Harish, S., Navaneethan, M., Navaneethan, D., et al. (2018). Synthesis, Structural and Optical Properties of ZnO Spindle/reduced Graphene Oxide Composites with Enhanced Photocatalytic Activity under Visible Light Irradiation. *Opt. Mater.* 79, 186–195. doi:10.1016/j.optmat.2018.02.061

Rahmani, S., Seyed Dorraji, M. S., Rahmani, S., Hajimiri, I., and Amani-Ghadim, A. R. (2020). Loading GO/ZnFe2O4/NiO Nanocomposite as a Hybrid Dielectric/magnetic Material into Polyurethane Foam for Induction of Radar Absorbing Properties. *J. Mater Sci. Mater Electron* 31 (7), 5107–5116. doi:10.1007/s10854-020-03071-w

Rammah, Y. S., El-Agawany, F. I., Mahmoud, K. A., El-Mallawany, R., Ilik, E., and Kilic, G. (2020). FTIR, UV-Vis-NIR Spectroscopy, and Gamma Rays Shielding Competence of Novel ZnO-Doped Vanadium Borophosphate Glasses. *J. Mater Sci. Mater Electron* 31 (12), 9099–9113. doi:10.1007/s10854-020-03440-5

Rasheed, T. (2022). MXenes as Emerging Two-Dimensional Analytical Modalities for Potential Recognition of Hazardous Environmental Contaminants. *Mater. Today Chem.* 24, 100859. doi:10.1016/j.mtchem.2022.100859

Ratep, A., and Kashif, I. (2021). X-ray Photoelectron, FTIR, and Mössbauer Spectroscopy Studied the Effect of Fe2O3/CuO Substitution on Structural and Electrical Properties of Lithium Borosilicate Glasses. *J. Mater Sci. Mater Electron* 32 (9), 12340–12347. doi:10.1007/s10854-021-05865-y

Ren, L., Li, Y., Hou, J., Bai, J., Mao, M., Zeng, M., et al. (2016). The Pivotal Effect of the Interaction between Reactant and Anatase TiO2 Nanosheets with Exposed {0 0 1} Facets on Photocatalysis for the Photocatalytic Purification of VOCs. *Appl. Catal. B Environ.* 181, 625–634. doi:10.1016/j.apcatb.2015.08.034

Sadrameli, S. M. (2016). Thermal/catalytic Cracking of Liquid Hydrocarbons for the Production of Olefins: A State-Of-The-Art Review II: Catalytic Cracking Review. *Fuel* 173, 285–297. doi:10.1016/j.fuel.2016.01.047

Selli, E., Bianchi, C., Pirola, C., Cappelletti, G., and Ragaini, V. (2008). Efficiency of 1,4-dichlorobenzene Degradation in Water under Photolysis, Photocatalysis on TiO2 and Sonolysis. *J. Hazard. Mater.* 153 (3), 1136–1141. doi:10.1016/j.jhazmat.2007.09.071

Shanavas, S., Mohana Roopan, S., Priyadharsan, A., Devipriya, D., Jayapandi, S., Acevedo, R., et al. (2019). Computationally Guided Synthesis of (2D/3D/2D) rGO/Fe2O3/g-C3n4 Nanostructure with Improved Charge Separation and Transportation Efficiency for Degradation of Pharmaceutical Molecules. *Appl. Catal. B Environ.* 255, 117758. doi:10.1016/j.apcatb.2019.117758

Tang, N., Li, Y., Chen, F., and Han, Z. (2018). *In Situ* fabrication of a Direct Z-Scheme Photocatalyst by Immobilizing CdS Quantum Dots in the Channels of Graphene-Hybridized and Supported Mesoporous Titanium Nanocrystals for High Photocatalytic Performance under Visible Light. *RSC Adv.* 8 (73), 42233–42245. doi:10.1039/C8RA08008A

Tang, S., Fu, Z., Li, Y., and Li, Y. (2020). Study on Boron and Fluorine-Doped C3N4 as a Solid Activator for Cyclohexane Oxidation with H2O2 Catalyzed by 8-quinolinolato ironIII Complexes under Visible Light Irradiation. *Appl. Catal. A General* 590, 117342. doi:10.1016/j.apcata.2019.117342

Tang, S., Gao, H., Wang, S., Fang, L., Chen, X., Yang, H., et al. (2022). Piezoelectric Catalytic, Photocatalytic and Adsorption Capability and Selectivity Removal of Various Dyes and Mixed Dye Wastewater by ZnO Nanoparticles. *Mgc* (Preprint), 1–19. doi:10.3233/MGC-210150

Valenzuela, M. A., Bosch, P., Jiménez-Becerrill, J., Quiroz, O., and Páez, A. I. (2002). Preparation, Characterization and Photocatalytic Activity of ZnO, Fe_2O_3 and $ZnFe_2O_4$. *J. Photochem. Photobiol. A Chem.* 148 (1-3), 177–182. doi:10.1016/S1010-6030(02)00040-0

Wang, S., Gao, H., Jin, Y., Chen, X., Wang, F., Yang, H., et al. (2022). Defect Engineering in Novel Broad-Band Gap Hexaaluminate MAl12O19 (M=Ca, Sr, Ba)-Based Photocatalysts Boosts Near Ultraviolet and Visible Light-Driven

Photocatalytic Performance. *Mater. Today Chem.* 24, 100942. doi:10.1016/j.mtchem.2022.100942

Wang, S., Tang, S., Gao, H., Chen, X., Liu, H., Yu, C., et al. (2021). Microstructure, Optical, Photoluminescence Properties and the Intrinsic Mechanism of Photoluminescence and Photocatalysis for the BaTiO3, BaTiO3/TiO2 and BaTiO3/TiO2/CeO2 Smart Composites. *Opt. Mater.* 118, 111273. doi:10.1016/j.optmat.2021.111273

Wang, S., Tang, S., Yang, H., Wang, F., Yu, C., Gao, H., et al. (2022). A Novel Heterojunction ZnO/CuO Piezoelectric Catalysts: Fabrication, Optical Properties and Piezoelectric Catalytic Activity for Efficient Degradation of Methylene Blue. *J. Mater Sci. Mater Electron* 33 (9), 7172–7190. doi:10.1007/s10854-022-07899-2

Wang, X., Li, S., Chen, P., Li, F., Hu, X., and Hua, T. (2022). Photocatalytic and Antifouling Properties of TiO2-Based Photocatalytic Membranes. *Mater. Today Chem.* 23, 100650. doi:10.1016/j.mtchem.2021.100650

Wang, Y., Gao, H., Wang, S., Fang, L., Chen, X., Yu, C., et al. (2021). Facile Synthesis of BaMoO4 and BaMoO4/BaWO4 Heterostructures with Type -I Band Arrangement and Enhanced Photoluminescence Properties. *Adv. Powder Technol.* 32 (11), 4186–4197. doi:10.1016/j.apt.2021.09.028

Wang, Y., Gao, J., Liu, Y., Li, M., Zhang, M., He, G., et al. (2021). Facile Fabrication of ZnO Nanorods Modified Fe3O4 Nanoparticles with Enhanced Magnetic, Photoelectrochemical and Photocatalytic Properties. *Opt. Mater.* 111, 110608. doi:10.1016/j.optmat.2020.110608

Wang, Y., Yang, L., Zhang, Y., Zhang, H., and Wei, J. (2019). Magnetic Optical Properties, and Photocatalytic Activity of the ZnFe2O4 Nanoparticles for the Degradation of the RhB Dye in Wastewater: Effects of Metal Salt and Surface Morphology. *Russ. J. Phys. Chem.* 93 (13), 2771–2781. doi:10.1134/S0036024419130314

Xiao, L., Zhang, Q., Chen, P., Chen, L., Ding, F., Tang, J., et al. (2019). Copper-mediated Metal-Organic Framework as Efficient Photocatalyst for the Partial Oxidation of Aromatic Alcohols under Visible-Light Irradiation: Synergism of Plasmonic Effect and Schottky Junction. *Appl. Catal. B Environ.* 248, 380–387. doi:10.1016/j.apcatb.2019.02.012

Xiong, X., Wang, B., Zhu, W., Tian, K., and Zhang, H. (2018). A Review on Ultrasonic Catalytic Microbubbles Ozonation Processes: Properties, Hydroxyl Radicals Generation Pathway and Potential in Application. *Catalysts* 9 (1), 10. doi:10.3390/catal9010010

Xue, J., Fujitsuka, M., and Majima, T. (2019). Shallow Trap State-Induced Efficient Electron Transfer at the Interface of Heterojunction Photocatalysts: the Crucial Role of Vacancy Defects. *ACS Appl. Mat. Interfaces* 11 (43), 40860–40867. doi:10.1021/acsami.9b14128

Zhao, W., Xie, F., Gan, M., Ma, L., Zhang, Y., Li, X., et al. (2022). Highly Graphitized Carbon-Wrapped PtFeCo Alloy with Enhanced Durability and Activity toward Methanol Electro-Oxidation. *Mater. Today Chem.* 24, 100788. doi:10.1016/j.mtchem.2022.100788

Conflict of Interest: The authors declare that the research was conducted in the absence of any commercial or financial relationships that could be construed as a potential conflict of interest.

Publisher's Note: All claims expressed in this article are solely those of the authors and do not necessarily represent those of their affiliated organizations, or those of the publisher, the editors, and the reviewers. Any product that may be evaluated in this article, or claim that may be made by its manufacturer, is not guaranteed or endorsed by the publisher.

Copyright © 2022 Tong, Shi and Liu. This is an open-access article distributed under the terms of the Creative Commons Attribution License (CC BY). The use, distribution or reproduction in other forums is permitted, provided the original author(s) and the copyright owner(s) are credited and that the original publication in this journal is cited, in accordance with accepted academic practice. No use, distribution or reproduction is permitted which does not comply with these terms.

Advantages of publishing in Frontiers

OPEN ACCESS
Articles are free to read for greatest visibility and readership

FAST PUBLICATION
Around 90 days from submission to decision

HIGH QUALITY PEER-REVIEW
Rigorous, collaborative, and constructive peer-review

TRANSPARENT PEER-REVIEW
Editors and reviewers acknowledged by name on published articles

Frontiers
Avenue du Tribunal-Fédéral 34
1005 Lausanne | Switzerland

Visit us: www.frontiersin.org
Contact us: frontiersin.org/about/contact

REPRODUCIBILITY OF RESEARCH
Support open data and methods to enhance research reproducibility

DIGITAL PUBLISHING
Articles designed for optimal readership across devices

FOLLOW US
@frontiersin

IMPACT METRICS
Advanced article metrics track visibility across digital media

EXTENSIVE PROMOTION
Marketing and promotion of impactful research

LOOP RESEARCH NETWORK
Our network increases your article's readership